Investigating Approaches to Enhance Sensing Capabilities of Nitrogen-Vacancy Centres in Nanodiamond

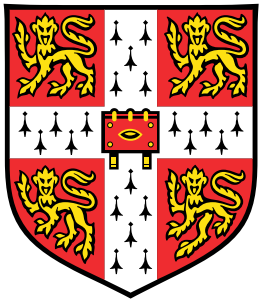

Jan David Beitner

This dissertation is submitted for the degree of

Doctor of Philosophy

at

University of Cambridge

Supervisor: Professor Mete Atatüre

Department of Physics

Jesus College

Cavendish Laboratory

April 2017

Declaration

I hereby declare that except where specific reference is made to the work of others, the contents of this dissertation are original and have not been submitted in whole or in part for consideration for any other degree or qualification in this, or any other university. This dissertation is my own work and contains nothing which is the outcome of work done in collaboration with others, except as specified in the text and acknowledgements. This dissertation contains fewer than 60,000 words including appendices, footnotes, tables and equations and has fewer than 150 figures.

Jan David Beitner

August 2017

Acknowledgements

I want to say thank you to a number of persons who have contributed profoundly to my PhD experience.

First of all, I want to acknowledge my supervisor Professor Mete Atatüre without whose inspiration and support this thesis would have never seen the light of the world. He creates a relaxed and friendly atmosphere in the group fostering discussions and research.

My first points of contact were always my two post-docs Helena Knowles and Dhiren Kara. They are both great physicists who guided me during the past three and a half years. Discussions with them were always useful and I wish them all the best for their career in academia.

Also, I wish to thank Joshua Barnes from whom I learned a lot about coding and electronics. David-Dominik Jarausch and Lucio Stefan have been great collaborators and office companions who I will certainly miss in the future. Jeffrey Holzgrafe, Quishi Gu and Ben Woodhams were great Master students and one could easily forget that particularly Jeff is not already working on his PhD. I further want to thank my collaborators Nicolas Gauriot, Angelo Di-Bernardo and the 2D materials team for their help.

In addition, my acknowledgements go to the whole AMOP group for providing such a great atmosphere and sense of camaraderie. I particularly want to highlight Benjamin Pingault with whom I had long discussions on topics ranging from research to politics and who helped to brush off some rust off my French. Outside academia, my family provided rock stable support and my college, Jesus, has always been a pleasant place to be at - may it be for dinner, sports or other social events.

Last but not least, I want to mention my funding body, the Winton Programme for the sustainability of Physics which would not exist without the generous funding provided by David Harding and the dedication of Nalin Patel who I want to thank for organising so many interesting seminars.

Abstract

The nitrogen-vacancy (NV) centre in diamond has proven to be an excellent tool to probe electro-magnetic fields and temperature. It has a number of unique features: High sensitivity and resolution, long coherence and lifetimes, the ability to operate from cryogenic temperatures to hundreds of Kelvin, chemical inertness and addressability via optics and microwaves. Recent progress includes the detection of NMR and spectroscopy of single proteins on a diamond surface and in-vivo temperature measurements.

However, while the NV centre in bulk diamond has received a lot of attention, the nitrogen-vacancy in nanodiamond has not been investigated extensively due its widely seen inferior properties. It is only very recently that problems with the stability of photoluminescence and short coherence times have been overcome. The NV centre in nanodiamond is thus increasingly seen as an interesting tool for research requiring nanoscale sensors, e.g. in cells.

The findings of this thesis facilitate applications of the NV centre in nanodiamond and demonstrate its high potential for future research. Most notably, the nuclear host spin, which is intrinsic to the point defect, can be used to enhance sensitivity and resolution of measurements. In addition, the sensitivity can be improved by time-tagging the emission from the NV centre. Furthermore, the graphite layer covering nanodiamonds can be removed by annealing. This does not have negative effects on the spin properties of the hosted NV centres but enables functionalisation of the surface and therefore advanced in-vivo measurements. Finally, the capabilities of the NV centre in nanodiamond in investigating the formation of magnetic domains are demonstrated at low temperatures.

These results enable and motivate the use of the NV centre in nanodiamond for future research, most especially in biological systems.

Table of contents

List of figures

List of tables

CHAPTER 1

Introduction and motivation

The NV centre in diamond has recently received a lot of attention after its discovery in 1965 by du Preez [46], Dyer et al. [48] and confirmation as a single photon emitter in 1997 by Gruber et al. [67]. It consists of two lattice sites in diamond of which one is vacant and the other occupied by a nitrogen atom [119, 120]. Its electron spin ($S = 1$) is optically accessible, i.e. non-resonant excitation with green light initialises the spin and can also be used to readout the spin as the fluorescence intensity is different for the $m_s = 0$ and $m_s = \pm 1$ spin states [165]. Initialisation fidelities of 80 % have been reported [166]. The initialisation and readout mechanism has been demonstrated from cryogenic temperatures to more than 600 K [195]. At cryogenic temperatures, phonon-related broadening of the transitions is reduced to an extent that resonant excitation becomes feasible enabling all-optical control [210] leading to an initialisation fidelity of 98 % and single shot readout of the spin state [166]. Furthermore, the spin can be coherently controlled with microwaves at all temperatures, i.e. universal quantum operations can be implemented.

The NV centre's attractiveness is largely due to its spin properties at ambient conditions. In bulk diamond electron spin state lifetimes of many hundreds seconds [186] and coherence times of 0.6 s have been observed in isotopically pure ^{12}C diamond at 77 K and 3.3 ms at room temperature [12].

The electron spin of the NV centre couples to strain, electro-magnetic fields and other proximal spins. As strain corresponds to a lattice displacement, temperature also affects the

transition energies of the spin sub-levels. This versatile coupling together with long coherence and lifetimes enables a wide range of applications. Amongst them are quantum information processing [62, 16, 152, 144, 8], the first loophole-free Bell test [73] electrometry [42], decoherence microscopy [31], magnetometry [10, 77, 129] and thermometry [107, 142, 195, 196, 198]. Most applications of NV centres focus on sensing electron or nuclear spins. The ultimate goal is the development of a molecular microscope enabling the positional mapping of nuclei in a molecule on the surface of diamond. NV centres close to the surface have recently received a lot of attention. Most recently, the detection of different spin species in proteins on the surface of bulk diamond has been achieved with a shallow NV centre in bulk diamond [121].

NV centres in nanodiamonds have distinct advantages due to their size, the wide range of groups their surface can be functionalised with and their non-toxicity to cells which makes them attractive for applications in biology [135, 212]. As diamond is chemically inert nanodiamonds are well-suited for in-vivo applications. For example, Kucsko et al. [107] have employed NV centres for in-vitro measurements of temperature. Current development in the field apart from efforts to employ NV centres in nanodiamond for sensing in cells includes building a magnetic force microscopy type microscope to investigate either the stray magnetic field of a sample or to perform nuclear magnetic resonance. The scanning probe either consists of a nanodiamond hosting a NV centre or (an array of) diamond pillars with NV centres implanted at the tip. Maletinsky et al. [122] have made progress towards the implementation of such a system and Dussaux et al. [47] has investigated topological magnetic defects in FeGe with nanodiamonds dispersed on the surface. In addition, research testing the quantum nature of large objects in gravity focuses on entanglement of a single spin of a nitrogen vacancy centre with the nanodiamond position [75, 80, 162, 74].

In 2013 Knowles et al. [101] discovered NV centres in nanodiamond that do not suffer from photo bleaching or blinking, i.e. loss of the NV centre or conversion to an unfavourable charge state. This discovery has overcome a major problem often expressed by NV centres hosted in nanodiamond. NV centres in nanodiamond still exhibit inferior spin properties compared to shallow implanted NV centres because of the inevitably rough surface of nanodi-

amond exposing dangling bonds and charge traps which are responsible for fast decoherence. NV centres in the favourable charge state NV^- have been found in nanodiamond only 5 nm in diameter but these exhibit coherence times in the single digit microsecond domain [21]. However, Knowles et al. [101] found NV centres hosted in nanodiamond only 17 nm in mean diameter with coherence times of up to 60 µs. This is close to the values found in bulk diamond with similar impurity concentrations. The observed lifetimes are typically hundreds of microseconds for NV centres in such nanodiamonds.

As mentioned the spin coherence of NV centres in nanodiamond is on the order of tens of microseconds limiting the sensitivity and resolution of NMR measurements. In addition, many processes in biology have timescales on the order of many milliseconds which is not within the bandwidth of current emitters. This thesis aims to find techniques to increase sensitivity, resolution and bandwidth of NV centres in nanodiamond by developing new methods and adopting concepts used in bulk diamond. While improvements can help to come to par with NV centres in bulk diamond, they also increase the competitiveness of NV centres in nanodiamond compared to other systems aimed at sensing in cells.

1.1 Alternatives to the nitrogen-vacancy centre

In this Section, we want to further explore the advantages and disadvantages of NV centres compared with other systems. This study also shines light on a number of important properties for applications not mentioned in the general introduction. NV centres are currently predominantly used for experiments to test fundamental physics requiring entanglement and for sensing electro-magnetic fields and temperature. We consider both categories separately as the competing systems are mostly non-overlapping although the advantages and disadvantages are.

Entanglement and distributed quantum networks

In this Section we consider a number of physical systems and compare them to NV centres based on the DiVincenzo requirements for quantum computation which provide guidelines

for identifying strengths and weaknesses of technologies [38]. In particular, we examine superconducting qubits including coupling to NV centres, quantum dots, defects in silicon carbide, silicon vacancy and germanium vacancy centres in diamond. Apart from superconducting qubits which can have a range of physical implementations, all other directly competing systems are single photon emitters based on a spin in solid state. Spin states are often long-lived as they are conserved under changes of other quantum numbers and many systems do not exhibit strong spin-orbit coupling.

Superconducting qubits pioneered by the Martinis group are the most advanced candidates for quantum computing [76, 13, 174]. However, until efficient microwave to photon and vice versa transducers are available such systems cannot be used for long-range communication. With NV centres, however, entanglement over distances more than 1 km has been demonstrated [73].

There are efforts to combine the high fidelities of superconducting qubits with the long coherence times of NV centres which could serve as memories. In particular, coupling to flux qubits has already been realised [215, 173]. Current research focuses on physical phenomena such as dark states [214] and how to improve entangement of NV centres with superconducting qubits [181] and the life- and coherence time of stronly coupled, i.e. hybrid, systems [43, 126].

Optically inactive quantum dots suffer from the same problem as superconducting qubits whereas optically active quantum dots provide a large number of photons per time interval compared to NV centres allowing fast entanglement generation [183]. However, unlike for NV centres the coherence times are too short to perform microwave control. Therefore, quantum gates rely on short, resonant laser pulses [54]. Other technical challenges include the reproducibility of quantum dots leading to individual transition energies for every dot.

Quantum information processing with nitrogen vacancy centres suffers particularly from problems associated with spin-photon conversion. First, only 4 % of photons are emitted into the zero-phonon line [193] and, second, spectral diffusion of the zero-phonon line poses a challenge for communication between multiple NV centres using photons [207, 55]. Third, the NV centre excited state is relatively long-lived, reducing its brightness [82]. Efforts

to overcome these problems by employing a resonant cavity have made some progress. Signal enhancement factors of up to 7.0 were observed using a photonic crystal cavity [50]. A defect in diamond, which solves all three issues, is the silicon vacancy (SiV) centre. 80 % of photons are emitted into the zero phonon line [140] which does not suffer from spectral diffusion due to the symmetry of the defect [177] and has an approximately ten to thirteen times shorter excited state lifetime [203, 177]. However, despite microwave control has been demonstrated recently [156], the spin coherence is limited due to spin-orbit coupling [155]. It has been measured to 115 ns at 4 K compared to hundreds of microseconds typically obtained for NV centres in bulk diamond [156]. By freezing out phonons at millikelvin temperatures or designing a diamond structure which does not support phonons in the respective frequency range, this problem could be overcome. Nevertheless, spin-orbit coupling limits the applications of the SiV centre in diamond. Another contender is the germanium vacancy centre in diamond which is similar to the SiV centre but has advantages in fabrication [85]. However, no technique has been developed yet to deterministically create defects in diamond with atomic precision. In addition, diamond is a difficult and brittle material to shape.

Last but not least, we want to mention the silicon vacancy defects in silicon carbite (SiC). Silicon carbite can be manufactured using well-developed CMOS processes as opposed to diamond which is difficult to process and integrate into existing circuits. In addition, the investigated defects have demonstrated high brightness [25]. However, different SiC defect types (4H, 6H and 3C) exist which can not be created on demand and more research is required to explore their potential as spin based qubits [103]. Recent experiments on the 6H-SiC have shown a spin readout contrast of only 1 % [106] as compared to 20 % for NV centres [164].

SENSING

For nanoscale sensing of electro-magnetic fields various systems exist that can detect single electrons. In this Section, we present magnetic resonance force microscopy (MRFM) and nanosized superconducting quantum interference devices (Nano-SQUIDs).

MRFM detects magnetic fields by measuring the force between a ferromagnetic cantilever and spins in a stationary sample. The cantilever creates a magnetic field gradient. By applying microwaves synchronised with the tip position spins can be addressed with spacial selectivity as only those spin contribute to the signal whose transitions, which are determined by the local magnetic field, are on resonance with the microwaves. A resolution of 25 nm for single electron spins has been shown which were as far as 100 nm away from the surface [172]. A 3D image of the proton density in a single virus has been acquired [37]. However, as phonon noise plays a major role in the detection efficiency and spin lifetimes on timescales similar to cantilever oscillation period are required, i.e. tens of Hz, MRFM typically operate at cryogenic temperatures typically below 4 K [172]. NV centres do not offer the large sensing volume of MRFM but can operate at ambient conditions, have higher sensitivity beyond the nuclear spin detection limit and offer angstrom spacial resolution. However, single nuclear spin sensitivity of MRFM is likely to be achieved in the near future [172].

While SQUIDS have been invented more than 50 years ago [87], nano-SQUIDS are have been invented only recently. SQUIDs rely on the Josephson effect and directly measure the number of magnetic flux quanta flowing through a loop. Vasyukov et al. [200] have built a SQUID with a loop diameter of 40 nm and achieve single electron sensitivity 10 nm away from the device. Typically micro and nano-SQUIDS are only capable of measuring fields out-of-plane of the sample. However, in 2014 Anahory et al. [6] present a device which can also detect in-plane fields and single electrons but operates at sensitivities one order of magnitude below the out-of-plane nano-SQUID. Both devices have a spacial resolution of 20 nm. Compared to NV centres nano-SQUIDs are an even less invasive method as no excitation laser is required. Further, their high sensitivity allows relatively fast imaging. However, they do not yet reach single nuclear spin sensitivity and must be operated at cryogenic temperatures as SQUIDs rely on superconductivity.

In conclusion, NV centres have advantages due to their high sensitivity and operation at ambient conditions.

1.2 THESIS OUTLINE

In **Chapter 2** we describe the structure and the optical and spin properties of the NV centre. Further, we present the experimental setup, take and analyse a basic set of measurements and provide a theoretical framework for parameter error estimation. In addition, we show to improve the signal-to-noise ratio by post-processing data.

The primary use case of the NV centre is sensing electro-magnetic fields and temperature with its electron spin. In **Chapter 3** we focus on the spin properties, how they are affected by the fabrication of bulk and nanodiamond and how they determine the sensitivity of the sensor. Also, we give an overview over existing measurement protocols which we employ in the subsequent chapters.

Decoherence of the spin of NV centres in nanodiamond is dominated by surface defects such as dangling bonds and charge traps. In **Chapter 4** we demonstrate that by removing graphite from the surface of nanodiamonds by annealing the sample at 445 °C for 5 h we can improve the spin properties of the hosted NV centres. In particular, we observe a change in the bath dynamics from fast to slow. This is a sign for a change of the primary noise source. The change should also enable further decoupling of the noise and hence boost sensitivity by a order of magnitude.

The NV centre in nanodiamond can be employed as a local magnetic field probe. In particular, by detecting the stray field of a magnetic material, domain formation can be investigated. By combining macroscopic DC measurements using a superconducting quantum interference device and microscopic DC and AC measurements we unravel the time dynamics of domain formation and the nature of magnetisation of a 150 nm thick PCMO ($Pr_{0.8}Ca_{0.2}MnO_3$) thin film in **Chapter 5**. Our results are consistent with previous measurements but provide additional insight into the magnetic field noise possibly caused by moving domains. In addition, we show how illumination with a green laser can lead to demagnetisation and provide multiple explanations.

The NV centre electron spin intrinsically is accompanied by a nitrogen host nuclear spin. We employ this spin in **Chapter 6** at magnetic fields above 2000 G which are aligned

with the NV centre axis to increase sensing resolution and universally to increase sensitivity of the electron spin. Two isotopes of the nuclear spin can be used. We show that the ^{14}N spin has significant advantages over the ^{15}N as it allows partial error correction. Further, we demonstrate that the coherence time of the nuclear spin is limited by the lifetime of the electron spin.

In **Chapter 7** we summarise the thesis and provide an outlook on future measurements. In particular, we consider the feasibility to sense ion concentrations in cells by employing techniques discussed in Chapter 2 and 6.

CHAPTER 2

Control and readout of the nitrogen-vacancy centre

In this Chapter, we discuss the basic properties and measurement techniques that are relevant to this thesis. The fundamental properties of NV centres such as the crystal and electronic structure along with optical transitions are introduced in Section 2.1. Sections 2.2 and 2.3 describe the experimental setup and its calibration, respectively. Next, we present the optical properties of NV centres in Section 2.4. We then demonstrate spin control of the NV centre in Section 2.5 by employing microwaves before explaining how to conduct error estimations using parameter distributions in Section 2.6. While the methods discussed in the later Section are relevant to all kinds of measurements, they are particularly important in Section 2.7 where we investigate the possibility to increase readout fidelities by post-processing acquired data.

2.1 Crystal and electronic structure

There is a large number of atomic defects in diamond of which around 100 are optically active [35]. One of them is the NV centre. It consists of a nitrogen atom which replaces a carbon atom next to a vacant site in the diamond tetrahedral lattice. The four axes in diamond result in four different orientations of the NV centre. Figure 2.1 shows the four different arrangements of atoms in diamond for the NV centre.

The local defect disturbs the electronic environment of the lattice which leads to well-localised electronic orbitals around it which are between the valance and conduction band of diamond. Thus, the NV centre can be referred to as an artificial atom.

2.1.1 Atomic structure

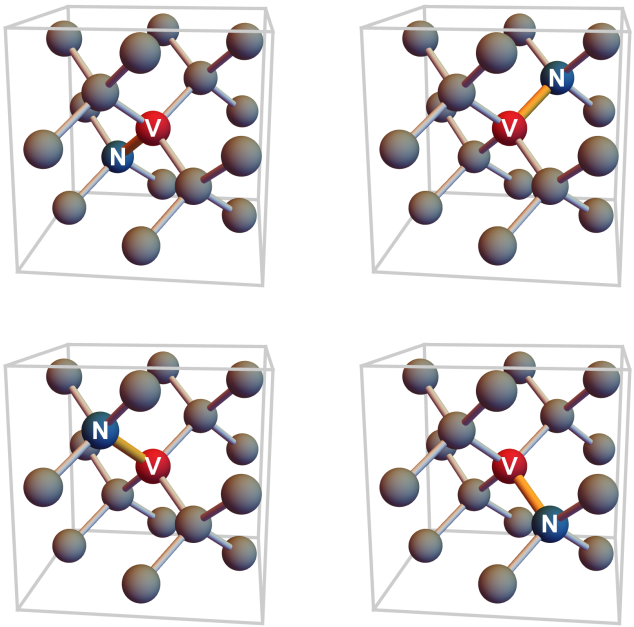

Fig. 2.1 **Axes of the NV centre in diamond**. Gray spheres illustrate carbon atoms in the diamond lattice, while the blue sphere represents a nitrogen atom and the red one a missing carbon atom.

The number of electrons which constitute the artificial atom's orbitals are determined by the Fermi energy. Two different charge states are known and a third one has been proposed while no final evidence has been reported for its existence [119, 120, 134]. The confirmed states are NV^- and NV^0 to which six and five electrons contribute, respectively. The neutral charge state NV^0 consists of two electrons from the nitrogen atom and one electron from each of the three carbon atoms next to the vacancy. In case of the negatively charged state NV^- an additional electron, captured from the vicinity of the defect, contributes to the electronic states of the NV centre [119, 120]. Changing the charge state alters the electronic structure

and the energy states of the NV centre. NV^- and NV^0 have recently been extensively investigated. However, as only the spin state of the negatively charged NV centre can be initialised and readout optically the NV^- centre has received more attention. The charge state NV^+ remains a mystery and has not yet been confirmed despite multiple claims of observation [112, 66, 88].

Study of the charge conversion process from the negative to the neutral charge state and vice versa has lead to new spin state readout mechanisms based on electronics as opposed to optics [22, 20, 176]. There is evidence that the conversion is a two-photon process where the first photon promotes the NV centre to its excited state and the second photon excites the defect state to the conduction band of diamond [78]. The charge conversion rate depends quadratically on the optical power under nonresonant excitation [15, 202, 119]. As the charge conversion destroys the spin state and the states of the NV^0 are mostly unknown, it is desirable to remain as long as possible in or quickly revert back to the negative charge state. This can be achieved by selective pumping of the NV^0 zero phonon line at 575 nm, where the absorption cross section of NV^0 exceeds that of NV^- so that NV^0 is converted to NV^- at a higher rate than vice versa through the aforementioned two photon process [178, 15]. While this does not require a fundamental change in the experimental setup or measurement protocols, it has not been realised in the work presented in this thesis. The primary reason is that, due to the relatively high concentration of nitrogen impurity atoms of approximately 50 ppm, there is a sufficient high number of electrons in the vicinity of the NV centre which can be captured to form the NV^- state. Optical spectra (Section 2.4.1) have consistently shown that the used NV centres are 10 % of the time in the NV^0 state. Characteristic switching between the charge states - NV^0 is 30 % darker than NV^- [21] - has not been observed with the nanodiamonds used. We conclude therefore that the switching is likely to be on a timescale of at most tens of milliseconds which means it is below the signal-to-noise ratio of the employed setup.

In this thesis, "NV centre" refers to a nitrogen vacancy centre in the negative charge state, i.e. NV^-, if not explicitly indicated otherwise.

2.1.2 MOLECULAR ORBITALS

The basic properties of the NV centre can be inferred by using group theory. In particular, the electronic structure, i.e. orbital shapes and their relative positions in energy, and optical transition rules can be deduced [40]. This Section summarises the previous work on the topic and the most important properties of the NV centre which were obtained by employing group theory.

The NV symmetry group is the pyramidal C_{3v}. This group has three irreducible representations which are two one-dimensional (A_1 and A_2) and one two-dimensional representations (E) [40].The Hamiltonian of the NV centre is invariant under symmetry operations of the C_{3v} group because the C_{3v} group describes the spacial symmetries of the defect in diamond which must be reflected in the Hamiltonian [191].

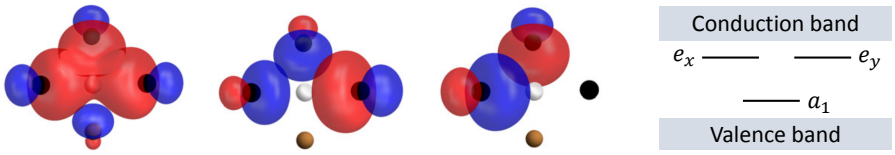

(a) a_1 (b) e_x (c) e_y (d) Energies

Fig. 2.2 **Single electron NV molecular orbitals**. (a)-(c) the orbitals and their energy positioning. (d) the diamond band gap. The color coding refers to negative (blue) and positive (red) phase contributions to the orbitals, respectively. Reprinted from Reference [40].

In 1977 Loubser and Van Wyk [119] were the first to construct orbitals for the NV centre using group theory. They are linear combinations of the nitrogen orbital and three sp^3 orbitals of the tetrahedrally positioned carbon atoms closest to the vacancy lattice site. The resulting orbitals are orthogonal to each other and by construction satisfy the symmetries of the C_{3v} group. Two symmetric orbitals $a_1(1)$ and $a_1(2)$ related to the A_1 group and two degenerate orbitals e_x and e_y related to the E group emerge [128, 115]. While these orbitals do not account for distortions in the crystal lattice or longer range interactions, they can be used to determine the ordering of the energy levels which correspond each to one orbital configuration. It was found that the $a_1(1)$ level is the lowest in energy and lies in the valance

band and, hence, is always populated by two electrons regardless of the NV state. The configurations for the ground and the excited state are $a_1^2e^2$ and $a_1^1e^3$, respectively [40]. The orbitals and their positioning in energy in the diamond band gap are shown in Figure 2.2.

For a detailed discussion of how to use the molecular orbitals to model the dependence of the corresponding energy states on electric or magnetic fields, or strain, the reader is referred to work by Doherty et al. [40], Maze et al. [128], Neumann et al. [143], Tamarat et al. [187], Batalov et al. [14] and Doherty et al. [39].

2.1.3 Fine and hyperfine structure - the NV Hamiltonian

Adding the NV electron spin results in six distinct ground states which are presented in Table 2.1 [128]. The triplet state $^3A_2$ in the $e^2(T)$ configuration is the ground state of the NV centre as depicted in Figure 2.3. It must have an anti-symmetric orbital function to minimise the Coulomb energy. The exact energy of the singlet states with respect to the triplets is still disputed. Currently, the consensus is that there are at least two singlet states E_1 and A_1 with an energy difference of 1042 nm with E_1 being lower in energy [36, 41]. Also, there is agreement over the fact that the singlet state plays an essential role in the optical initialisation and readout process of the NV spin. However, it is unknown where the singlet states in energy are located in between the excited and ground state.

The Hamiltonian describing the spin system formed by the NV centre electron and host nuclear spin is

$$\hat{H} = \hat{H}_S + \hat{H}_I + \hat{H}_{SI} + \hat{H}_B + \hat{H}_E, \tag{2.1}$$

where $\hat{H}_S$ describes the electron spin with $S = 1$, $\hat{H}_I$ the nitrogen ^{14}N or ^{15}N host spin with $I = 1$ or $I = 1/2$, respectively, and $\hat{H}_{SI}$ the interactions between the electron and nuclear spin. $\hat{H}_B$ refers to the interactions with the magnetic field and $\hat{H}_E$ to interactions with the electric field and strain. The zero-field components, which can be deduced from the canonical spin

Configuration	State			Symmetry
$e^2(T)$	$^3A_{2-}$	=	$\left\|e_x e_y - e_y e_x\right\rangle \otimes \left\|\downarrow\downarrow\right\rangle$	$E_1 + E_2$
	$^3A_{20}$	=	$\left\|e_x e_y - e_y e_x\right\rangle \otimes \left\|\uparrow\downarrow + \downarrow\uparrow\right\rangle$	A_1
	$^3A_{2+}$	=	$\left\|e_x e_y - e_y e_x\right\rangle \otimes \left\|\uparrow\uparrow\right\rangle$	$E_1 - E_2$
$e^2(S)$	$^1E_1$	=	$\left\|e_x e_x - e_y e_y\right\rangle \otimes \left\|\uparrow\downarrow - \downarrow\uparrow\right\rangle$	E_1
	$^1E_2$	=	$\left\|e_x e_y + e_y e_x\right\rangle \otimes \left\|\uparrow\downarrow - \downarrow\uparrow\right\rangle$	E_2
	$^1A_1$	=	$\left\|e_x e_x + e_y e_y\right\rangle \otimes \left\|\uparrow\downarrow - \downarrow\uparrow\right\rangle$	A_1

Table 2.1 **Orbital ground state configurations of the NV centre**. The spin triplet configuration $e^2(T)$ corresponds to the NV ground state $^3A_2$ and the singlet configuration $e^2(S)$ corresponds to the states $^1E_1$, $^1E_2$ and $^1A_1$ which sit between the excited and ground state in energy. The total spin S is denoted by the superscript, i.e. 1 for a singlet and 3 for a triplet. The letter and first part of the subscript refer to the symmetry of the state (A_1, A_2, E_1, and E_2) and the second subscript is the spin state quantum number m_s. The spins of the electrons in the quantum state are indicated by up- and downwards arrows and only the orbitals e_x and e_y are displayed as a_1 and a_2 are always fully occupied in the ground state.

Hamiltonian, are

$$\hat{H}_S = D\left[\hat{S}_z^2 + S(S+1)/3\right] \tag{2.2}$$

$$\hat{H}_I = P\left[I_z^2 - I(I+1)/3\right] \tag{2.3}$$

$$\hat{H}_{SI} = A^{\parallel}\hat{S}_z\hat{I}_z + A^{\perp}(\hat{S}_x\hat{I}_x + \hat{S}_y\hat{I}_y). \tag{2.4}$$

The form of the Hamiltonian is the same in the ground and excited state with different parameters. The electron spin Hamiltonian $\hat{H}_S$ is governed by the axial zero-field splitting (ZFS) described by the parameter D. In the ground state $D_{gs} \approx 2.87\,\text{GHz}$ [119, 120]. The host nuclear spin Hamiltonian $\hat{H}_I$ depends on the quadrupole splitting parameter $P_{gs} = -4.945\,\text{MHz}$ [180], which has not been measured in the excited state. Note, that ^{15}N is a spin $I = 1/2$ system and thus $P = 0$. While ^{14}N is the dominant nitrogen isotope with a natural abundance of 99.6 %, working with ^{15}N can reduce the number of required gates in some measurement schemes if the host nuclear spin is used as a memory. Chapter 6

elaborates on how to use this nuclear spin to increase sensitivity and resolution of AC magnetometry with NV centres. The axial and transverse components of the hyperfine constants are $A_{gs}^{\parallel} = -2.162\,\mathrm{MHz}$ [180] and $A_{gs}^{\perp} = -2.65\,\mathrm{MHz}$ [28], respectively. The operators $\hat{\mathbf{S}} = (\hat{S}_x, \hat{S}_y, \hat{S}_z)$ and $\hat{\mathbf{I}} = (\hat{I}_x, \hat{I}_y, \hat{I}_z)$ are the spin 1 (or $1/2$ in case of ^{15}N) Pauli operators. Operators are denoted by a hat and vectors are typed in bold font. h is set to 1.

The effect of magnetic and electric fields is given by

$$\begin{aligned}
\hat{H}_B =& g_S^{\parallel}\mu_B \hat{S}_z B_z + g_S^{\perp}\mu_B \left[\hat{S}_x B_x + \hat{S}_y B_y\right] && (2.5)\\
&+ g_N \mu_N \hat{\mathbf{I}} \cdot \mathbf{B} && (2.6)\\
\hat{H}_{E,gs} =& d_{gs}^{\parallel}(E_z + \delta_z)\left[\hat{S}_z^2 - S(S+1)/3\right] && (2.7)\\
&+ d_{gs}^{\perp}(E_x + \delta_x)\left[\hat{S}_x^2 - \hat{S}_y^2\right] && (2.8)\\
&+ d_{gs}^{\perp}(E_y + \delta_y)\left[\hat{S}_x\hat{S}_y - \hat{S}_y\hat{S}_x\right] && (2.9)\\
\hat{H}_{E,es} =& d_{es}^{\parallel}(E_z + \delta_z)\left[\hat{S}_z^2 - S(S+1)/3\right] && (2.10)\\
&+ \xi\left[\hat{S}_x^2 - \hat{S}_y^2\right]. && (2.11)
\end{aligned}$$

The Zeeman shift is governed by the external magnetic field $\mathbf{B}$ multiplied by the gyromagnetic ratio $\gamma_S/(2\pi) = \mu_g$. Here, μ_B is the Bohr magneton, μ_N is the nuclear magneton, $g_S^{\parallel}$ and $g_S^{\perp}$ are the longitudinal and transverse ground state electronic g-factors close to the electronic Landé factor $g_S = 2.003$ [119, 52]. Thus, the gyromagnetic ratio for the electron spin $\gamma_S/(2\pi) = g_S\mu_B \approx 2.8034\,\mathrm{MHz/G}$. For the nuclear spin the gyromagnetic ratio $\gamma_I/(2\pi) = g_I\mu_I$ depends on the nitrogen isotope and is $\gamma_I(^{14}\mathrm{N})/(2\pi) = 307.7\,\mathrm{Hz/G}$ and $\gamma_I(^{15}\mathrm{N})/(2\pi) = -431.6\,\mathrm{Hz/G}$ [9, 17], respectively. This means the shift of the nuclear energy is four orders of magnitude below that of the electron energy shift under an external magnetic field. This is a particular high ratio because the nuclear gyromagnetic ratio is almost one order below the average of all nuclei.

δ describes the strain field, typically leading to a splitting of 10 to 40 MHz in the nanodiamonds we use, and $d_{gs}^{\parallel} \approx 0.35\,\mathrm{Hzcm/V}$ and $d_{gs}^{\perp} \approx 17\,\mathrm{Hzcm/V}$ are the longitudinal and transverse ground state electric dipole strengths [199]. For NV centres in bulk diamond the strain splitting is mostly in the kHz range. The difference in strain is a result of different

fabrication methods which makes it hard to obtain nanodiamonds with negligible or even similar strain which makes characterisation of strain every single NV centre in nanodiamond a necessity [192]. Fortunately, otherwise strain does (mostly) not reduce the applicability of NV centres in nanodiamond as sensors but renders photonic coupling between NV centres in nanocrystals almost impossible. The external electric field $\mathbf{E}$ causes a splitting similar to strain because strain causes a lattice displacement which in turn creates an electric field. Therefore, strain can also be an advantage as at low magnetic fields the strain dominates the degeneracy of the two spin transitions. Hence, noise due to the magnetic field environment is reduced.

For the excited state the parameters are $D_{es} \approx 1.42\,\text{GHz}$ [182], $A_{es}^{\parallel} = -40\,\text{MHz}$ and $A_{es}^{\perp} = -23\,\text{MHz}$ [158], respectively. ξ is the splitting caused by strain and has been measured to be 70 MHz by Fuchs et al. [56] in a NV centre in bulk with 5 MHz ground state strain splitting. For the neutrally charged NV^0 the parameters for the ZFS and the hyperfine interaction differ significantly. In the excited state the ZFS was measured to be $D_{es,NV^0} = 1.685(5)\,\text{GHz}$ and the hyperfine interaction constants are $A_{es,NV^0}^{\parallel} = -35.7(3)\,\text{MHz}$ and $A_{es,NV^0}^{\perp} = -23.8(3)\,\text{MHz}$, respectively. The data was obtained by electron paramagnetic resonance (EPR) measurements which is a equivalent to NMR but involves microwaves of many GHz due to the higher energy gaps typically observed between electron spin states [61, 51].

At low temperature, six separate electron states can be resolved, one orbital doublet for each electron spin state $m_s \in \{-1, 0, +1\}$. The spin-spin interaction, strain, and spin-orbit interactions lift their degeneracy resulting in two separate branches of three states each. At higher (or room) temperature, the doublets cannot be distinguished due to orbital averaging due to phonon interactions. The averaging causes them to merge into the three states of the ^{3}E triplet which are shown in Figure 2.3.

2.1.4 Optical transition rules

One of the advantages of the NV centre is the optical addressability of its spin state. This includes all-optical preparation and readout at room temperature. This Section focuses on the lifetimes of the different NV centre states and how the spin polarisation mechanism works.

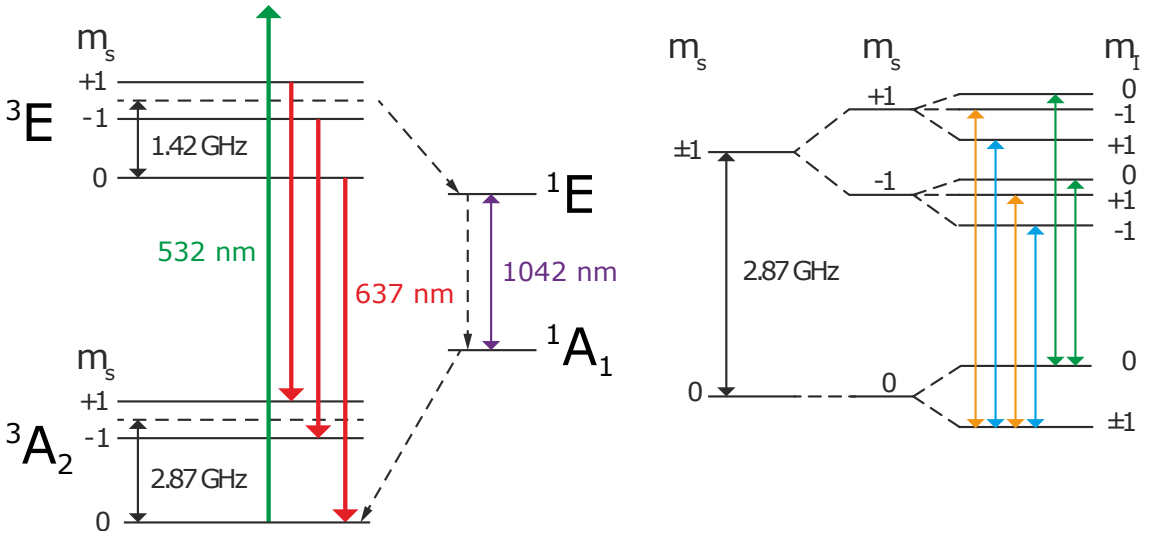

(a) All levels (b) Ground state

Fig. 2.3 **NV centre energy levels**. (a) the energy levels of the NV centre including Zeeman shifts of the electron spin states m_s related to magnetic field. Denoted are the spin states, the singlet states $^1A_1$ and ^1E of the inter-system-crossing and the triplet states $^3A_2$ and ^3E of the ground and excited state, respectively. Spin conserving non-resonant laser excitation at 532 nm and spontaneous emission at 637 nm are represented by green and red arrows, respectively. (b) the ground state including interactions with the nuclear spin. The excited state has the same structure apart from a different ZFS constant of $D_{es} = 1.42\,\text{GHz}$ as opposed to $D_{gs} = 2.87\,\text{GHz}$.

As described in the previous Sections 2.1.2 and 2.1.3 the NV centre has two triplet states $^3A_2$ (ground state) and ^3E (excited state), and two singlet states ^1E and $^1A_1$. The different decay pathways and the energy levels are displayed in Figure 2.3. Under optical excitation with light at and above the zero phonon line at 637 nm the NV centre is promoted from the ground state to the excited state while the electron and nuclear spin quantum numbers m_s and m_I are conserved. In case of non-resonant excitation the NV centre is excited to vibrational states of the ^3E triplet from where the vibrational states quickly relax. From the ^3E excited state the centre decays to the ground state $^3A_2$ and to the ^1E singlet state from which it further decays to the $^1A_1$ singlet before it reaches the ground state. The decay path from the excited state triplet $^3A_2$ to the singlet state ^1E is called the inter-system-crossing (ISC).

The direct decay path to the triplet ground state is accompanied by the emission of a photon between approximately 637 and 850 nm. A measured spectrum is shown in Figure 2.6 in Section 2.4.1. The decay paths from the excited state triplet $^3A_2$ to the singlet ^1E and from the singlet $^1A_1$ to the triplet in the ground state ^3E is non-radiative. However, a photon is emitted at 1042 nm when the state decays from singlet to singlet.

State	Lifetime (ns)	Reference
^3E, $m_s = 0$	12.7	Neumann et al. [143]
^3E, $m_s = \pm 1$	23	Neumann et al. [143]
^1E	0.9 ± 0.5	Acosta et al. [2]
$^1A_1$	371 ± 6	Robledo et al. [164]

Table 2.2 **Lifetimes of the NV excited state**. The lifetimes are grouped by electronic configuration and spin state.

In bulk the ^3E lifetime is $T_1 = 12.7$ ns and in nanodiamond this lifetime extends to $T_1 = 23$ ns because the density of states in air is lower than in diamond [82, 32]. Excitation and direct decay to the ground state are predominately spin conserving due to the lack of spin-orbit coupling. However, the chosen decay path is highly dependent on the spin state. According to Doherty et al. [41], the $m_s = 0$ state decays directly with a probability of more than 80 % while the $m_s \pm 1$ states decay non-radiatively via the ISC with a probability of approximately two third. Decay via the ISC is not spin conserving due to the spinless nature of singlet states. The singlet state $^1A_1$ relaxes non-radiatively into the $m_s = 0$ ground state with a probability of at least two third. This leads to polarisation of the spin into $m_s = 0$ of up to 96 % and a brightness difference between the $m_s = 0$ and the $m_s = \pm 1$ of up to 40 %. These percentages should be taken with care as many conflicting numbers of the precise proportion of radiative to non-radiative decay have been reported as discussed by Doherty et al. [41] who cites polarisation fidelities between 42 % and 96 %. This demonstrates the need for further research and a deeper understanding of the decay mechanism. In particular, the fraction of radiative to non-radiative decay determines the polarisability of the electron

spin under non-resonant excitation and, thus, the overall fidelity of quantum operations at room temperature.

In Robledo et al. [166] the ratio of the decay rates from the excited states with spin $m_s = 0$ and $m_s = \pm 1$ to the singlet state is defined as $\beta = k(^3\mathrm{E}, m_s = 0 \rightarrow ^1\mathrm{A}_1)/k(^3\mathrm{E}, m_s = \pm 1 \rightarrow ^1\mathrm{A}_1) < 1$. The ratio of the rates from $\left|^1\mathrm{E}\right\rangle$ into the ground states, $\left|^3\mathrm{A}_2, m_s = 0\right\rangle$ and $\left|^3\mathrm{A}_2, m_s = \pm 1\right\rangle$ has been estimated to $\alpha = k(^1\mathrm{E} \rightarrow ^3\mathrm{A}_2, m_s = \pm 1)/k(^1\mathrm{E} \rightarrow ^3\mathrm{A}_2, m_s = 0) \approx 0.8$ [166]. From the average reported spin polarisation of 80 % follows $\alpha\beta \approx 0.2$, resulting in $\beta \approx 0.2$ [41]. This means that the spin-polarisation of the nitrogen vacancy under non-resonant continuous wave excitation is governed by the decay from the excited state $^3\mathrm{E}$ into the intermediate state $^1\mathrm{A}_1$ rather than from the intermediate state $^1\mathrm{E}$ into the ground state $^3\mathrm{A}_2$. It was also found that optical spin polarisability decreases with increasing temperature [52], which at least partly explaines inconsistent values in literature [41].

Higher polarisation fidelities can be achieved by optical polarisation with light resonant with the specific spin transitions. The degeneracy of the spin energy levels rates can be only resolved at low temperatures when phonon-broadening is minimised. Employing the optically addressable transitions the spin can be polarised into the $m_s = 0$ state. In addition, single shot readout of the electron spin state becomes possible. Under resonant excitation preparation fidelities have been reported to reach 99.7 % and 99.2 % for spin $m_s = 0$ and $m_s = \pm 1$, respectively [166]. As the lines are phonon broadened at room temperature, this approach, though, does require low temperature. Spectral diffusion of the zero phonon line, which is discussed in Section 2.4.1 poses additional challenges. The brightness or readout contrast between $m_s = 0$ and $m_s = \pm 1$ is 39 % (at 100 % polarisation) between $m_s = 0$ and $m_s = \pm 1$ [123].

2.2 Confocal microscopy setup

A confocal microscope allows us to optically address NV centres less than 1 µm apart. For this technique, the excitation is focused on a point and the collection of light is spatially

filtered, typically using a pinhole which we can be replaced by the fibre aperture. The two foci of excitation and collection have to coincide. This is called the confocal configuration.

A confocal microscope has two main advantages. First, the common focal point can be chosen freely in all three dimensions which increases the contrast because the signal only comes from the point of interest. And second, the lateral resolution of a confocal microscope is increased. The Rayleigh criterion defines the resolution r_{normal} as the distance between the centre of an Airy disk and its first minimum which depends on the wavelength λ and the numerical aperture (NA). Experimentally, the resolution is determined by measuring the full width half maximum (FWHM) of the point-spread function which is proportional to the Rayleigh criterion. In a confocal configuration the FWHM is the multiplication of two Airy disks, one from the excitation and one from collection. This leads to an increase in the resolution by approximately 30 %.

$$r_{\text{normal}} \approx \frac{1.22\lambda}{2\text{NA}} \approx \frac{0.6\lambda}{\text{NA}} \tag{2.12}$$

$$r_{\text{confocal}} \approx \frac{0.4\lambda}{\text{NA}} \tag{2.13}$$

As depicted in Figure 2.4, the excitation of NV centres is driven by a 532 nm diode pumped, continuous wave, solid state laser (Ventus 532, 1 W, Laser Quantum). Its intensity is controlled and gated using two acoustic optical modulators (AOM, MT80-A1-VIS, AA Opto-Electronic) along with their drivers (MT80-A1.5-VIS, AA Opto-Electronic) which create the RF signal that drives the piezo crystal in the AOM at a fixed frequency. In an AOM, an optical grating is generated in the crystal by a driving a standing acoustic wave (in this case at 80 MHz) with a piezo crystal. This modifies the refractive index locally and causes an interference pattern to arise. Of this interference pattern, we select the light deflected into the first order by using a pinhole. The selected order is then coupled into a fibre which connects to the optical setup as shown in Figure 2.4. Typically, 85 % of the laser beam can be deflected into the first order of the grating. By tuning the RF signal amplitude the grating's transparency and therefore the power in the first order is controlled. Pulsing the RF signal creates pulsed laser pulses. The rise and fall times of these pulses are primarily limited by

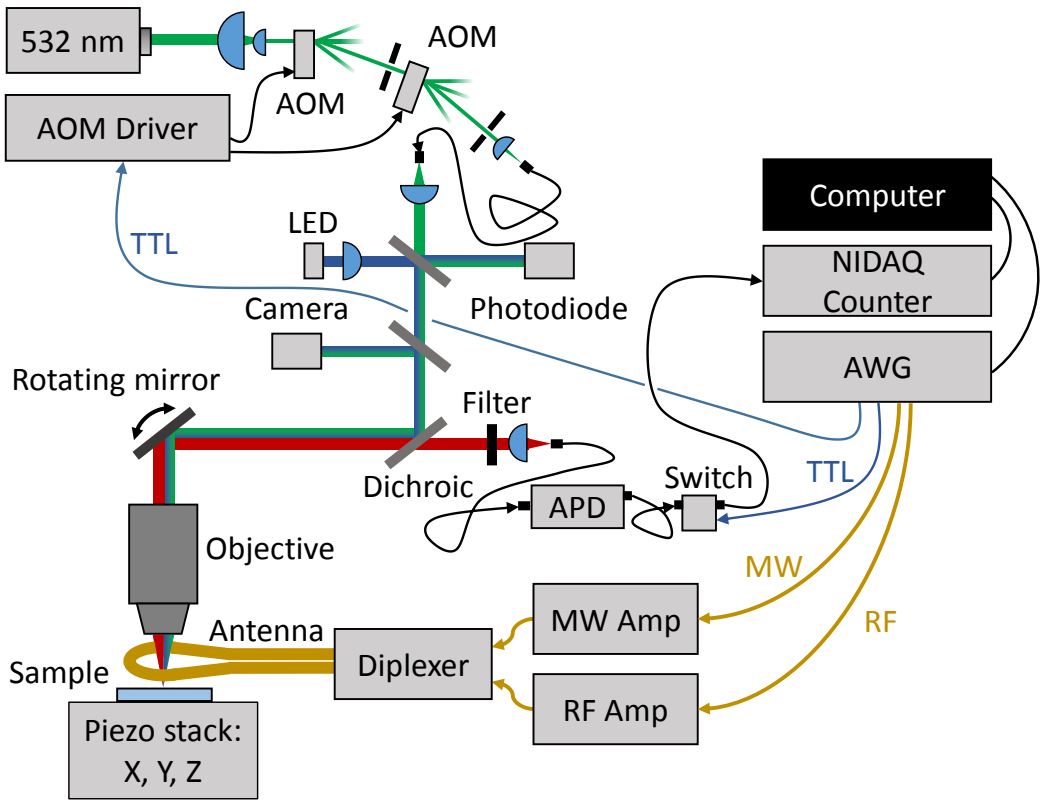

Fig. 2.4 **Schematic representation of the experimental setup**. The excitation laser beam path (green), the extracted photons (red) and LED light (blue) for wide field illumination are shown along with the optical elements needed for confocal microscopy. In addition, the equipment for microwave generation, pulsed operations, sample positioning and signal acquisition is depicted.

the time it takes phonons to travel across the laser beam diameter. Details of the pulsed operations can be found in Section 2.3. Working with two instead of one AOM increases the suppression efficiency quadratically and protects against scattered light into the first order. For the same reason, an optical telescope is used to reduce the laser beam diameter to prevent scattering into the first order at the edges of the AOM crystal. This also decreases the rise and fall times of the gated laser beam since they are determined by the time it takes a phonon to travel across the laser beam width.

To control the laser intensity 10 % of the light in the fibre is diverted by a beamsplitter and sent to a photodiode whose signal serves as a feedback to the AOM driver. The feedback

signal is used to stabilise the optical excitation power to a certain value by adjusting the AOM voltage accordingly. The same beam splitter is also used to couple a 450 nm LED (M450D3, Thorlabs) into the beam path for wide-field illumination.

In order to separate the excitation and collection beam a dichroic beamsplitter (LM01-552-25, Semrock) with a cut-off at 552 nm is inserted into the beam path.

The angle of the beam path in front of the objective (MPLFLN100X, Olympus, NA = 0.9) can be changed with a piezo controlled rotating mirror (S-334.2SL, Physik Instrumente). Altering the angle changes the position of the focused beam in the focal plane and hence allows scanning the excitation and collection beam simultaneously. A 4F configuration to avoid the barrel effect is not necessary as the angle changes are small and the position is changed by less than 20 µm. The objective aperture (4 mm) is slightly overfilled by the excitation beam to prevent underfilling when changing the rotating mirror angle. In addition to the mirror three room temperature open-loop piezo stages (ESC3030-S1-154, with ECC100 or ANC150 controller, Attocube) move the sample in the X-, Y- and Z-direction. The stages roughly align the sample in the X and Y direction and move its surface into focus by stepping in the Z direction. For scanning, the mirror is essential since the stages are too slow and cannot be moved back to a previous position with high accuracy. Yet, the mirror scanning range is limited to approximately 50 µm rendering the piezo stages indispensable.

Because the dichroic has an efficiency below 100 % we can image the focal plane of both, the excitation and the collection beams by using a camera (WAT-120N+, Watec). The same camera also serves as a tool to image the surface under wide-field illumination by the LED. This is particularly important if markers are present on the sample.

We want to extract the photons emitted by the NV centres. Under green excitation they emit broadband between 550 nm and 900 nm with a peak at approximately 680 nm. Before the green laser is reflected by the dichroic, it passes through bandpass filter (FL532-3, Thorlabs, not depicted in Figure 2.4). Because the dichroic mirror reflects only 98 % of the green light, the remaining 2 % are suppressed by two hard-coated longpass filters (FELH0550, Thorlabs) with a cut-off wavelength of 550 nm. Using two instead of one filter does not significantly diminish the collection efficiency as these filters transmit almost 98 % of light

above 550 nm. They are, however, necessary, to suppress the emission of the 532 nm laser below 550 nm sufficiently.

The extracted photons are guided into a single mode fibre (SM600, Thorlabs) whose single mode property, i.e. the fibre only supports Gaussian modes, and fibre aperture make sure only light from a specific focal plane is collected. The photons are detected using an avalanche photodiode (APD, Excelitas, SPCM-AQRH-14-FC). The APD outputs a TTL pulse for every incoming photon and is operated well below its saturation point. Dark counts are around 140 Hz. The TTL pulses are gated by a switch (ZASWA-2-50DR+, Mini-Circuits) and counted by a hardware-timed counter (NI-PCIe 6323, National Instruments). If the excitation laser is pulsed by the AOM, the signal form the APD needs to be gated in synchronisation with the laser in order to prevent dark counts dominating the total count signal. Alternatively to the APD, a spectrometer (Acton SP2570, Princeton Instruments) or a beamsplitter with two APDs in conjunction with a time-tagging unit (quTAU, quTools) for correlation measurements can be connected to the collection arm.

In addition to optical pulses to initialise and readout the NV centre state, microwave and radio frequency signals need to be applied for coherent control of the spin state. Therefore, a loop antenna is used. This loop design ensures throughput for frequencies from DC to the self-resonance frequency of the loop, i.e. smaller diameters are more desirable. The loop antenna is either made from gold evaporated through a silicon hard mask directly onto the cover slip with $r_{\text{loop}} \approx 25\,\mu\text{m}$ or made from copper from a rigid microwave cable which is not in direct contact with the sample ($r_{\text{loop,external}} \approx 650\,\mu\text{m}$). Connecting the antenna directly to the ground has shown to yield generation of stronger magnetic fields compared to 50 Ohm matched antenna circuits designed with a specialised electromagnetic simulation software (Sonnet Suite) despite the significant impedance mismatch. This can be attributed to the overall lower impedance leading to higher currents. If a wire is used instead of an antenna, connecting to the ground likewise proved to improve the efficiency of magnetic field generation.

As a large bandwidth of frequencies is required if nuclear spins should be addressed, whose transition frequencies are in the MHz range, different amplifiers are needed. Specifi-

cally, a microwave amplifier from 2 to 4 GHz with maximum power output of 16 W (ZHL-16W-43+, Mini-Circuits), a 1 W microwave amplifier from 10 MHz to 4.2 GHz (ZHL-42W+, Mini-Circuits), a 30 W radio frequency amplifier (LZY-22+, Mini-Circuits) and two 11 dBm pre-amplifiers from 300 kHz to 14 GHz (ZX60-14012L+, Mini-Circuits) are part of the setup. We choose to use either the 16 W or the 1 W amplifier at a time depending on the power and bandwidth requirements. The pre-amplifiers are necessary to reach an input power that saturates the main amplifiers. The microwave and radio frequency signals are combined by a diplexer (D02G18G1, AMTI Microwave Circuits) to minimise crosstalk between the amplifiers.

The microwave signals are generated by a two-channel 25 GHz arbitrary waveform generator (AWG70002A, Tektronix). This device has also a number of TTL outputs that control the gating of the laser and of the APD. In a previous version of the experiment, a pulse generator at 500 MHz (PulseBlaster-ESR Pro, SpinCore Technologies) and different microwave sources (SG384 from Stanford Research Instruments, SMF100A from Rhode & Schwarz, BK4064 from B&K Precision) combined with switches (ZASWA-2-50DR+, Mini-Circuits) created the pulsed microwave and TTL signals.

Further devices such as programmable and fixed attenuators, programmable voltage sources, programmable motors, etc. were employed in carrying out the experiments. All devices are controlled by custom software presented in Appendix B written in the programming language Python.

2.3 Calibration of pulse delays

Most pulsed experiments in this thesis consist of three parts. First, the NV is initialised into its ground state with a non-resonant, green laser. Second, nuclear and electron spins are manipulated by applying microwave or radio frequency fields and, third, the NV spin state is readout by sending a laser pulse from the same laser used in the initialisation step and counting the photons emitted from the NV centre. The timing of the different pulses is crucial for the success of experiments.

Three delays must be considered: The delay of the AOM which gates the laser, the delay of the switch that gates the APD counts and the delay of the microwave and radio frequency pulses. The APD is gated in order to minimise the number of background counts contributing to the measured signal from the NV centre. Sources of systematic timing mismatches are delays through the cables which deliver the signals, and device-dependent rise and fall times. While the former are relatively short as the signals travel at the speed of light, i.e. approximately 30 cm/ns, device dependent errors can be large and of the order of hundreds of nanoseconds due to complicated electronics.

We will now discuss the specific delays and how to determine them. The microwave pulse delays are set to 12 ns which corresponds to approximately 3.6 m of cables between the microwave switches or the AWG and the loop antenna. It can be safely assumed that the amplifiers and the diplexer only add a negligible amount to this delay. We will also see that 12 ns is very small compared to the delays of other devices. The next delay we want to determine is the time it takes from the detection of a photon to the voltage pulse the detector generated passing the switch which is used to gate the APD signal. The time from detection to pulse generation can be extracted from the specifications sheet of the APD and is around 240 ns. There is a jitter of approximately 350 ps on the output. The signal pulse travels another 1-2 m before it is gated by the additional switch. The rise and fall time of this switch is 10 ns according to the manufacturer. The last remaining delay concerns the AOM. We will not measure it directly (which is possible using a fast photodiode) but rather measure the delay from starting a laser pulse to detecting photons. From this measurement we subtract the APD delay to obtain the final AOM delay.

To determine the delay between the AOM TTL pulse and TTL pulse from the APD triggered by the first detected photon, we scan a short APD window over a long AOM window as shown in Figure 2.5. We choose a 1 µs window for the AOM and a fixed 15 ns window for the APD. As the typical rise and fall time of the used switches is around 10 ns, the APD window is even shorter in reality. We observe a rise in counts at 614 ns after the AOM has been triggered by the TTL pulse. This indicates a delay of the AOM of 374 ns. Furthermore, we can determine the rise and fall times of the AOM specific to the waist of

the laser beam that passes through it. A half maximum is reached at 678 ns and at 1587 ns leading to fall and rise times of 64 ns and 58 ns. However, it is important to note that the laser pulse has a long tail, and thus our estimate of the fall time is too optimistic. Furthermore, the 1000 ns TTL pulse has only lead to a 909 ns long laser pulse. It seems like the AOM responses far faster to a switch-off of the TTL signal than to a switch-on. Further, additional measurements indicate different behaviours if consecutive laser pulses are close to each other (within a few hundreds of nanoseconds). Those different responses can be explained by heating of the AOM which leads to an expansion of the piezo-driven crystal and the lack of a sufficient cool down period for the AOM if pulses are close to each other.

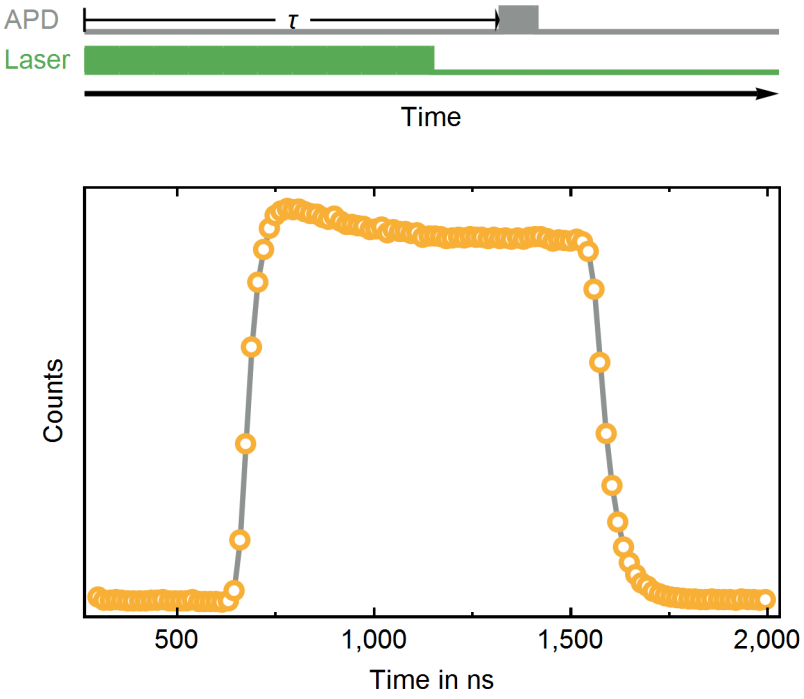

Fig. 2.5 **AOM delay**. Above, the pulse sequence for measuring the AOM delay is displayed. Below, the counts are shown for different APD window delays τ. The gray line connects the data points and serves solely as a guide to the eye.

The shape of the intensity profile in Figure 2.5 is a convolution of the NV response and the AOM laser profile. A detailed discussion can be found in Section 2.7.

One remaining delay has to be set for every pulsed experiment: The time between the laser pulse and the first microwave pulse. It is the time required to wait until the NV

centre has decayed from the excited state to its ground state. While the optical lifetime is 23 ns [82] short, undergoing ISC takes longer, as the lifetime of the $^1A_1$ singlet state is 300 ns [1], and hence determines the waiting time. We choose a "AOM buffer time" of 550 ns which is long enough to make sure that even if the NV centre has undergone ISC, $1-\exp(-550\,\text{ns}/300\,\text{ns}) = 84\,\%$ of the population is in the ground state. Given that after a couple of optical cycles the NV spin should be in the $m_s = 0$ state, the probability for undergoing ISC is very small and therefore, far more than 84 % is in the ground state after waiting 550 ns.

2.4 Optical properties

2.4.1 Spectrum

The optical spectrum of a NV centre consists of a linear combination of spectra of the NV^- and the NV^0. Depending on the environment, the defect can switch between these two charge states. In particular, Rondin et al. [169] suggest charge traps on the surface of nanodiamonds which capture the NV^- electron and as such decrease the stability of the NV^- centre.

The zero phonon lines (ZPL) of NV^- and a NV^0 are at 637 nm and 575 nm, respectively. However, the majority of photons are emitted at higher wavelengths due to phonon states in diamond as shown in Figure 2.6.

The vibrational states of the nuclei in the diamond lattice can be modelled as a harmonic oscillator, i.e. the states are equally spaced and discrete in energy. Both the excited and ground state couple to the vibrational states. Vibrational state excitations decay very rapidly and on time scales far shorter than the lifetime of the excited state. Therefore, the Stokes transitions from the excited state to the ground state are highly suppressed. The NV centre in its excited state can be always assumed to be in its vibrational ground state. When the NV centre in its excited state decays to the NV ground state modulated by the vibrational states, the decay can be accompanied by the generation of phonons. As these vibrational states are short lived, the photon emission is broadband and not discrete. The probability of decaying into the different vibrational states is governed by the Frank-Condon factor. The

transition from the NV excited state in its vibrational ground state is to the NV ground state in its second and third vibrational states has the highest probability. Thus, only 4 % of the excited state population decays into the zero phonon line and most photons are emitted into the phonon sideband [193].

Figure 2.6 shows a spectrum of a single photon emitter. Because the vibrational spectrum is assumed to be described by a harmonic oscillator, the phonon states are equally spaced in energy and exhibit a Lorentzian lineshape. The blue lines refer to contributions to the total photon emission from the NV^0 and the red lines from the NV^-. The fit indicates a NV^0-contribution of 12 % to the spectrum. The low wavelength and high frequency part of the spectrum is suppressed by a longpass filter with an edge at 559 nm which explains the deviation of the model and the data at low wavelengths. Therefore, the data points below 559 nm were not included to fit the model.

The phonon sideband cannot be suppressed at low temperatures because the transition probabilities do not change. However, the vibrational modes' broadening is reduced as their lifetime increases and, therefore, they can be better resolved [167]. In order to enhance emission into the zero phonon line one can use a photonic crystal cavity [50].

If two NV centres are to communicate via photons, the photons from each much be identical in frequency. the temperature must be lowered to resolve the spin transitions comprising the zero-phonon line. In addition, these transitions must be monitored constantly as the transitions suffer severely from spectral diffusion of the ZPL of up to 0.5 nm under non-resonant excitation which is due to a fluctuating electro-static environment causing a Stark shift [207, 55].

2.4.2 Saturation measurements

We excite the NV centre with non-resonant light and monitor the photon counts. Such saturation measurements provide crucial information about the optical saturation power and maximum photon count signal from a specific emitter. Many measurements are designed to work best with a certain excitation rate. Therefore, the saturation power is an important

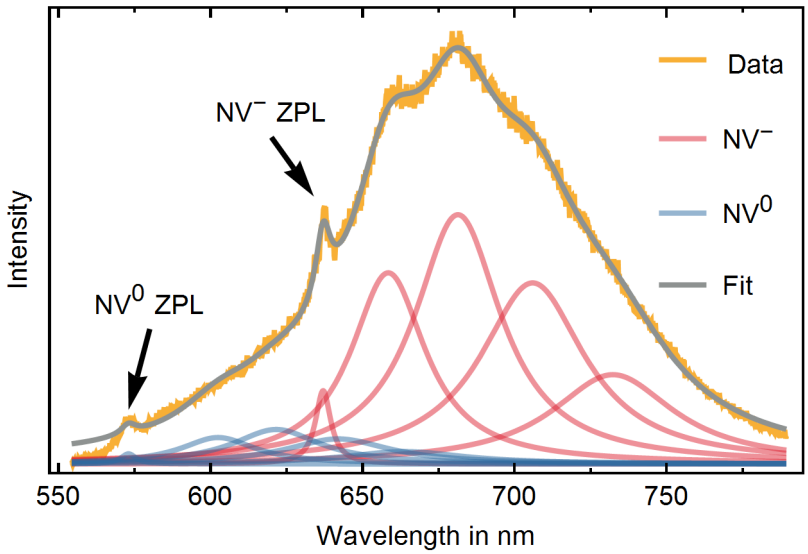

Fig. 2.6 **Spectrum of a single photon emitter**. The yellow line is plotted from the data directly obtained from the spectrometer, the gray line represents a fit to this data. The red and blue lines denote the contributions of the different phonon modes if the NV centre is in its NV^- or NV^0 charge state, respectively.

value for calibration. Moreover, from experience we know that the saturation curve very well forecasts the desirable properties of an emitter for further measurements.

In the following, we assume a simple two-level system with ground state g and excited state e to model the photon counts collected from a NV centre. The state populations p_g and p_e along with rates r_{ge} for excitation and r_{eg} for decay is governed by the rate equations

$$\begin{pmatrix} -r_{ge} & r_{eg} \\ r_{ge} & -r_{eg} \end{pmatrix} \begin{pmatrix} p_g \\ p_e \end{pmatrix} = \frac{\mathrm{d}}{\mathrm{d}t} \begin{pmatrix} p_g \\ p_e \end{pmatrix}. \tag{2.14}$$

To obtain the steady-state solution we set

$$\frac{\mathrm{d}}{\mathrm{d}t} \begin{pmatrix} p_g \\ p_e \end{pmatrix} = \begin{pmatrix} 0 \\ 0 \end{pmatrix} \tag{2.15}$$

and

$$p_g + p_e = 1. \tag{2.16}$$

The photon collection intensity $I(s)$ depends on the laser power s and is proportional to the population in the excited state p_g. Therefore, we solve the system of differential equations for p_e and obtain

$$p_e = \frac{r_{ge}}{r_{eg} + r_{ge}}. \tag{2.17}$$

s is proportional to the excitation rate r_{ge}. Thus, the saturation curve has the form

$$I(s) = I_{\max} \frac{s}{s + P_s}, \tag{2.18}$$

where $I_{\max} = \lim_{s\to\infty} I(s)$ and P_s is the half saturation power, i.e. $I(P_s) = I_{\max}/2$. In Figure 2.7 two saturation curves are depicted which are typical for emitters found on samples. Figure 2.7.a shows a saturation curve which follows Equation 2.18 while the data in Figure 2.7.b is taken in the linear regime of Equation 2.18.

Taking saturation curves has proven to be a quick and reliable method to predict NV centres, which are single photon emitters and have coherence and lifetimes above the average. Good candidates for further characterisation exhibit smooth saturation curves indicating no blinking or bleaching behaviour and half saturation power at relatively low optical excitation powers. On our setup half saturation powers of up to 500 µW (measured before the NA = 0.9, objective) and maximum count rates of 40 to 180 kHz were a good sign for single NV centres.

In practice, saturation curves very much depend on the polarisation of the laser light and the alignment of the emitter and its axis with the beam paths. This makes a direct comparison between emitters by only using their saturation curves difficult. Nevertheless, they can give a good indication of how well an emitter is suited for further experiments. Additionally, the half saturation power is required for calibration in order to compare measurements of different emitters with each other.

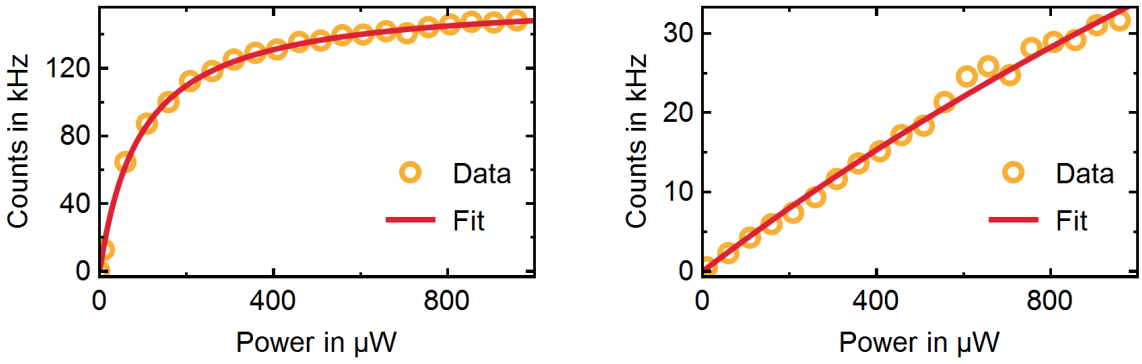

(a) Good emitter

(b) Bad emitter(s)

Fig. 2.7 **Saturation curves of two bright spots**. (a) the fit (red) for data yields a half saturation power of $I_s = 95\,\mu W$ and a maximum count rate of $I_{max} = 162\,KHz$. The laser power is measured before the objective, meaning that the actual power at the emitter is smaller as there are losses through absorption, reflection, misalignment, polarisation mismatch, and an overfilled aperture of the objective. (b) the saturation curve of emitter(s) exhibits high noise at high powers indicating extensive charge conversion leading to blinking due to the different quantum efficiency of the two charge states and optical filtering of their spectra.

2.4.3 Photon Statistics

The NV centre is a single photon emitter. Hence, only one photon at a time can be emitted when the excited state decays. This property makes the NV centre a single photon source and leaves a specific signature in the second order correlation function of the emitted photons which allows us to determine if a bright spot in a confocal scan is a single photon emitter or not.

The second order correlation function describes the correlations between photons arriving at time t and t_0. One also calls this function the autocorrelation function, $g^{(2)}$-function or coincidence function. It is defined as

$$g^{(2)}(t) = \frac{\langle I(t_0)I(t_0+t)\rangle}{\langle I(t)\rangle^2}. \tag{2.19}$$

Here, $I(t) = \mathbf{E}^*(t) \cdot \mathbf{E}(t)$ denotes the field intensity equivalent to the number of photons arriving at time t. The angled brackets $\langle\ \rangle$ denote taking the time average over t_0. Note that the $g^{(2)}$-function is normalised and therefore it represents the level of correlations compared to two identical, albeit, independent and uncorrelated emitters. Given two such emitters with field intensity $I_1(t)$ and $I_2(t)$, the correlations are $\langle I_1(t_0)I_2(t_0+t)\rangle$. Due to the independence of $I_1(t)$ and $I_2(t)$ this expression can be simplified to $\langle I_1(t)\rangle\langle I_2(t_0+t)\rangle = \langle I_1(t)\rangle^2 = \langle I(t)\rangle^2$, i.e. the normalisation expression in the denominator.

In practice, detecting all photons cannot be expected due to non-unity efficiency of the detectors and collection optics. Yet, losses do not change the number of coincidences observed at time t if the detected photons do not suffer from selection bias. For the experimental realisation we could use one detector in conjunction with a clock to record all photon arrival times. However, as the used APDs cannot detect a photon for a certain time typically on the order of hundreds of nanoseconds after having already detected a photon (also called "dead time"), a different solution is required. To circumvent the dead time of a single APD, the collection path is split by a non-polarising 50:50 beamsplitter into two so two APDs can be used. Their counts are time-tagged and subsequently correlated.

The $g^{(2)}$-function can be also interpreted in terms of probability, i.e. it is proportional to the probability of detecting a photon at time t after having recorded a detection event at time t_0. However, the $g^{(2)}$-function is not strictly a probability density function as an integral over it will always yield infinity.

Without any detailed derivations some properties of the autocorrelation function can be deduced. First, it has to be symmetric around $t = 0$ because $\langle I(t_0)I(t_0+t)\rangle = \langle I(t_0-t)I(t_0)\rangle$ and $\langle I(t)\rangle^2 = \langle I(-t)\rangle^2$. Second, for a single photon emitter, only one photon at a time is expected, i.e. $g^{(2)}(0) = 0$. This phenomenon is called anti-bunching (Figure 2.8.a). For n emitters, we expect $g^{(2)}(0) = 1 - 1/n$. However, background counts uncorrelated with the single photon emitters and detector jitter can lead to a serious overestimation of n. Therefore, only an estimate for the upper bound for the number of emitters can be inferred from the data. Third, in the limit of $t \to \infty$ the autocorrelation function $g^{(2)} \to 1$. And fourth, for intermediate times $g^{(2)}(t)$ can exceed 1 since for a NV centre there exists a long lived shelving

state (singlet $^1A_1$) in which most of the population will be stored at high power. Under high power excitation, two cases can be distinguished. Either the NV centre generates many photons as it is cycled between its ground and excited state or it is dark because it finds itself in the optically inaccessible shelving state. Once it decays from the shelving state to the ground state, photons can be generated again. This leads to a specific time determined by the lifetime of the shelving state after which the NV is re-excited. Thus, $g^{(2)}$ can rise over 1 which means that the correlations exceed those with an identical, but independent emitter. This phenomenon is called bunching and does not occur at low excitation powers when most of the population remains in the ground state as it is linked to the total population in the singlet state compared to ground state.

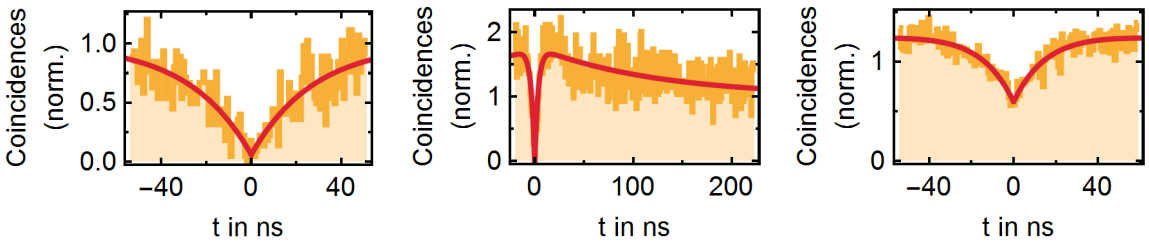

(a) 1 emitter (low power) (b) 1 emitter (high power) (c) 2.5 emitters (low power)

Fig. 2.8 **Autocorrelation measurements**. (a) characteristic drop in the autocorrelation function for a single photon emitter. (b) bunching under high power excitation. (c) $g^{(2)}$ of more than one emitter. The correlations at $t = 0$ are non-zero in this case.

We will now examine the exact functional nature of the autocorrelation function. Only one single NV centre is modelled as the autocorrelation function $g_i^{(2)}(t)$ of many single photon emitters $i = 1,\ldots,N$ is the summed and renormalised autocorrelation of all emitters

$$g^{(2)}(t) = \frac{\sum_{i=1}^{N} g_i^{(2)}(t)}{\sum_{i=1}^{N} g_i^{(2)}(\infty)}. \tag{2.20}$$

The $g^{(2)}(t)$-function can be directly inferred from the solutions to the rate equations of the NV centre. Here, a simplified model only comprised of the ground (g), the excited (e) and

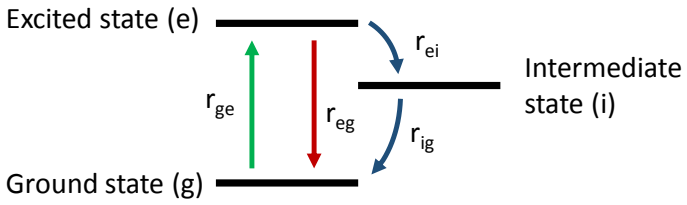

Fig. 2.9 **Simplified NV level scheme for modelling the autocorrelation function**. The NV energy levels are reduced to the ground state (g), excited state (e) and intermediate state (i). The green arrow denotes excitation, the red represents relaxation under the spontaneous emission of a photon and the blue arrows indicates relaxation from the excited to the ground state via the intermediate state without photon emission.

the intermediate singlet state (i) is used. In this case the rate equations, where the population of state n is identified by p_n, simplify to

$$\frac{\mathrm{d}}{\mathrm{d}t}\begin{pmatrix} p_g \\ p_e \\ p_i \end{pmatrix} = R \begin{pmatrix} p_g \\ p_e \\ p_i \end{pmatrix} \tag{2.21}$$

with the rate matrix R, where r_{nm} denotes the rate from state n to m (Figure 2.9) being

$$R = \begin{pmatrix} -r_{ge} & r_{eg} & r_{ig} \\ r_{ge} & -(r_{eg}+r_{ei}) & 0 \\ 0 & r_{ei} & -r_{ig} \end{pmatrix}. \tag{2.22}$$

Generally, such a system of differential equations has a solution of the form

$$\begin{pmatrix} p_g \\ p_e \\ p_i \end{pmatrix} = \begin{pmatrix} a_{11} & a_{12} & a_{13} \\ a_{21} & a_{22} & a_{23} \\ a_{31} & a_{32} & a_{33} \end{pmatrix} \begin{pmatrix} \exp(-\lambda_1 t) \\ \exp(-\lambda_3 t) \\ \exp(-\lambda_3 t) \end{pmatrix}. \tag{2.23}$$

The λ_k can be identified with the eigenvalues of the rate matrix and the coefficients a_{kl} are determined by the initial conditions and the rate matrix. The coefficients a_{kl} must, in order to conserve the total population, satisfy $\sum_{kl} a_{kl} = 1$. Because of the rate matrix is only of rank

2, the first eigenvalue $\lambda_1 = 0$. For $t \to \infty$ the populations $p_n \to \sum_l a_{nl}$, i.e. we can identify the coefficients a_{nl} with the steady state solution.

The coincidence function $g^{(2)}(t)$ is the probability to detect a photon at time t just after a photon has been emitted at time 0 compared to the probability to detect a photon at time t. Then, the autocorrelation function is directly proportional to the excited state population $p_e(t)$. As $\lim_{t\to\infty} g^{(2)}(t) = 1$, the autocorrelation function must be

$$g^{(2)}(t) = \frac{p_e(t)}{\lim_{t\to\infty} p_e(t)}. \tag{2.24}$$

Using Equation 2.23 and $\lambda_1 = 0$, it follows that

$$p_e(t) = A + Be^{\lambda_2 t} + ce^{\lambda_3 t}. \tag{2.25}$$

Initially, $p_e(0) = 0$, so that

$$A + B + C = 0 \tag{2.26}$$

$$-\lambda_2 B - \lambda_3 C = r_g e \tag{2.27}$$

With the steady state $\mathrm{d}p_n/\mathrm{d}t = 0$ for $n \in \{e, g, i\}$, $\lim_{t\to\infty} p_e(t) = A$, and $\sum_n p_n = 1$, we find for the excited state population

$$p_e(t) = K\left(1 - (s + 1/2)e^{\lambda_2 t} + (s - 1/2)e^{\lambda_3 t}\right), \tag{2.28}$$

where

$$\lambda_2 = -\frac{a+b}{2} \tag{2.29}$$

$$\lambda_3 = -\frac{a-b}{2} \tag{2.30}$$

$$s = \frac{a^2 - b^2 - 2ar_{ig}}{4r_{ig}b} \tag{2.31}$$

with

$$a = r_{ge} + r_{ge} + r_{ei} + r_{ig} \tag{2.32}$$

$$b = \sqrt{a^2 - 4(ar_{ig} + r_{ei}r_{ge} - r_{ig}^2)}. \tag{2.33}$$

and normalisation constant

$$K = \frac{r_{ge}r_{ig}}{r_{ge}(ar_{ig} + r_{ei}r_{ge} - r_{ig}^2)}. \tag{2.34}$$

The autocorrelation function can be obtained easily by dividing Equation 2.28 by its normalisation constant K. a and b are positive, and $r_{ig} \approx 1/300\,\text{ns}$ [1] and $r_{eg} \approx 1/23\,\text{ns}$ [82], i.e. $r_{ig} < r_{eg}$ and thus s will always be positive. This means $-\lambda_2 > -\lambda_3$. The greater the difference between λ_2 and λ_3, which is equivalent to a large b, the stronger is the observed bunching. The value of b is power-dependent. If r_{ge} increases, b also increases and so does the bunching signature.

Bunching arises when a significant fraction of the population is in the intermediate state. This is the case for NV centres, where some population is shelved in the singlet state $^1\text{A}_1$ whose lifetime is a few hundred nanoseconds. At high powers, no population is in the ground state. As the excited state lifetime is short compared to the time it takes to decay via the ISC to the ground state, most population is in the singlet state $^1\text{A}_1$. The NV remains dark while it is in the singlet states. If a photon is detected, there is a high likelihood that the NV was cycled one more time between ground and excited state before it was trapped in the singlet state. Therefore, bunching appears on the timescale of the excited state lifetime. At low powers, only the typical anti-bunching feature is visible in a $g^{(2)}(t)$ measurement because the population in the excited and intermediate states is negligible to the population in the ground state.

We extract r_{ge} and r_{ei} by fitting eight data sets from the same emitter but at different excitation powers shown in Figure 2.10. The values for r_{ge} and r_{ig} are taken from literature ($r_{eg} = 1/23\,\text{ns}$, $r_{ig} = 1/300\,\text{ns}$) to avoid overfitting. The value of $1/r_{ei}$ has been fitted to $1/121\,\text{ns}$ with excitation rates r_{ge} from $1/23\,\text{ns}$ to $1/422\,\text{ns}$.

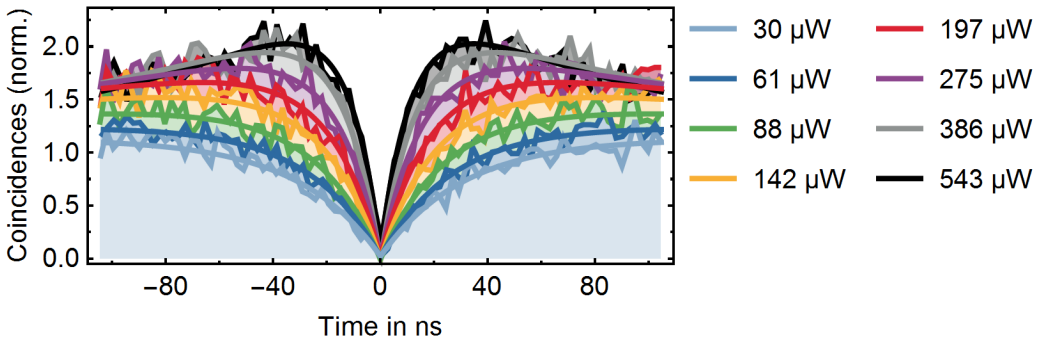

Fig. 2.10 **Coincidence counts at different excitation powers**. Autocorrelation measurements of the same emitter were taken for different excitation powers. The smooth, solid lines are fits to the data. For illustration purposes only part of the data is displayed but coincidences up to 2 µs were recorded to avoid overfitting.

2.5 Spin control

One of the main advantages of the NV centre is that its spin can be manipulated with microwaves around 2.8 GHz. Principle advantages of microwave over optical control are the ease of applying microwave signals and higher gate fidelities. Fidelities are solely depending on the spin coherence time because the spin transitions can be addressed directly without the risk of ionisation of the system. Therefore, the fidelities can be close to 100 % due to coherence times of hundreds of microseconds as discussed in Section 3.1. In contrast to optical pulsed laser sources tailored microwave sources, waveform generators, amplifiers, and switches are commercially readily available at reasonable prices. In addition, delivering microwaves only requires cables, multiplexers and loop antennas which significantly simplify the task compared to optical signals which ask for well-aligned components such as high-quality lenses, filters, tunable and stabilised lasers, etc. While optical control requires low temperatures to resolve the different spin transitions, pulses are typically on the picosecond scale as opposed to tens of nanoseconds required for microwave pulses.

2.5.1 Optically detected magnetic resonance (ODMR)

Optically detected magnetic resonance (ODMR) spectroscopy is a technique to find the transition frequencies from spin state $m_s = 0$ to $m_s = \pm 1$. A microwave signal is scanned in frequency while the counts from the NV centre are constantly monitored under non-resonant illumination with a 532 nm green laser. When the microwave signal is not resonant with one of the spin transitions, the NV centre is constantly optically pumped into its $m_s = 0$ state. The closer the microwave signal frequency is to the NV centre resonance, the more population of the $m_s = 0$ state can be transferred to the $m_s = -1$ or $m_s = +1$ state. As discussed in Section 2.1 the NV centre emits fewer photons if it is in the $m_s = \pm 1$ state as opposed to the $m_s = 0$ state. This difference in brightness gives us information about the transition frequencies of the electronic spin state.

A typical ODMR spectrum is shown in Figure 2.11. Under non-resonant, continuous excitation with a 532 nm laser, we observe intensity differences of up to 20 % between on and off resonance the spin transitions. In the absence of a static external magnetic or electric field, the transitions $m_s = 0 \leftrightarrow -1$ and $m_s = 0 \leftrightarrow +1$ are not degenerate in nanodiamonds due to the presence of strain in the crystal which is similar to an electric field. This strain field causes a splitting up to 40 MHz. It can also be the reason for unequal resonance amplitudes due mixing of the $m_s = \pm 1$ states which are addressed by orthogonal, linear polarisations of the microwave field.

If an external magnetic field is applied, the transitions are shifted due to the Zeeman effect. At higher magnetic field strain plays a lesser role in mixing the states and the imbalance in the resonance amplitudes diminishes. The splitting follows

$$\Delta\nu \approx \sqrt{\left(\frac{\gamma_S}{2\pi} B_{\text{ext}}\right)^2 + \Delta^2_{\text{strain}}} \tag{2.35}$$

if the strain splitting and the Zeeman splitting are far smaller than the ZFS. Here, Δ_{strain} is the strain induced splitting, $\gamma_S/(2\pi) \approx 2.8025\,\text{MHz/G}$ the gyromagnetic ratio of an electron and B_{ext} the external magnetic field. This functional form for the magnetic field dependence means that the NV spin splitting is primarily sensitive to electric fields at low magnetic

fields. In turn, at high magnetic fields the external magnetic field contribution to the splitting dominates.

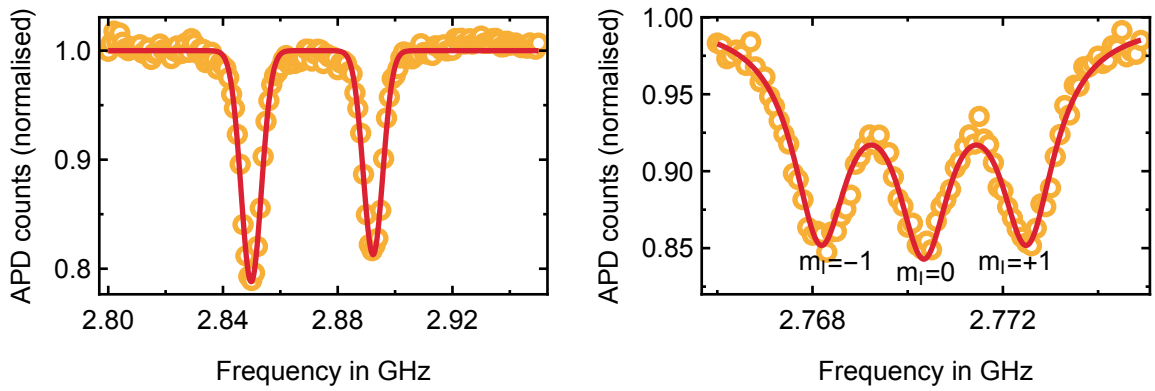

(a) ODMR

(b) Hyperfine resolved ODMR

Fig. 2.11 **ODMR measurements**. (a) typical ODMR measurement without an external magnetic field. The two spin transitions are split due to strain. (b) at moderate magnetic fields, the $m_s = 0 \leftrightarrow -1$ transition is investigated and the hyperfine interaction with the ^{14}N is resolved.

The linewidth of the resonances is governed by three different broadening mechanisms. First, $1/T_2^*$ of the spin states, also called the natural linewidth, sets the lower limit for the linewidth accessible in any measurement. Second, optically non-resonant driving of the system to reinitialise the NV centre into its $m_s = 0$ state leads to power broadening. And third, similar to optical power broadening driving the spin transition(s) by microwaves results into additional power broadening. According to Dréau et al. [44] the total linewidth is

$$\Delta\nu = \frac{\Gamma_c^\infty}{2\pi}\sqrt{\left(\frac{s}{1+s}\right)^2 + \frac{\Omega_R^2}{\Gamma_p^\infty \Gamma_c^\infty}}, \tag{2.36}$$

where Ω_R is the Rabi frequency as defined in Section 2.5.2, s is the fraction of the half saturation power as defined in Section 2.4.2,, and Γ_p^∞ and Γ_c^∞ are the rate of polarisation and optical cycling at half saturation power.

By reducing the optical pump rate and microwave power, the hyperfine interaction of the NV electron spin with its host nuclear spin of -2.162 MHz can be resolved [180]. Depending

on the isotope of the nuclear spin it has spin $I = 1$ in the case of ^{14}N or spin $I = 1/2$ in the case of ^{15}N. The hyperfine interaction allows to distinguish between the two nuclear isotopes. In Figure 2.11.b a hyperfine-resolved ODMR for a NV centre with host ^{14}N spin is displayed. We solely work with ^{14}N as it the dominant naturally occurring isotope with 99.6 % abundance.

Given the strong quadrupole interaction of the nuclear spin of $P = -4.95\,\mathrm{MHz}$ [180], the nuclear spin is pinned to the axis of the NV centre at fields below $P/\gamma_n \approx 1.61\,\mathrm{T}$, where $\gamma_n/(2\pi) \approx 3.077\,\mathrm{MHz/T}$ is the gyromagnetic ratio of the ^{14}N spin [9]. The magnetic field from the nuclear spin can, thus, be considered static on the timescale of milliseconds which is longer than most experiments carried out for this dissertation. We investigate its dynamics further in Chapter 6.

However, as the optical power has to be reduced typically by a factor of 20 to avoid power broadening the signal from the APD is very significantly decreased. In Section 2.5.3 we discuss a method to avoid optical broadening without reducing the signal-to-noise ratio by using laser and microwave pulses.

2.5.2 Rabi nutations

In order to exercise coherent control over the electronic spin by means of microwave pulses, we need to carefully characterise driving of the spins by AC magnetic fields. In particular, we want to extract times for the $\pi/2$, π, and $3\pi/2$-rotation which are needed for pulsed experiments. The $3\pi/2$-pulse length is not necessarily the sum of the lengths of the $\pi/2$ and π-pulses because of pulse errors from broadening and losses in the cables and imperfections in amplification.

We will now consider a two-level spin system with states $|1\rangle$ and $|2\rangle$, driven by a classical, monochromatic magnetic field $\mathbf{B} = \mathbf{B}_0 \cos(\omega t)$ which is on or close to resonance. This corresponds well to driving one of the NV centre spin transitions.

The Hamiltonian for such a system is

$$\hat{\mathrm{H}} = \hat{\mathrm{H}}_0 + \hat{\mathrm{H}}_\mathrm{I}(t), \tag{2.37}$$

where $\hat{\mathrm{H}}_0$ is the Hamiltonian for the unperturbed spin system and $\hat{\mathrm{H}}_\mathrm{I}(t)$ describes the time dependent interaction with the magnetic field. $\hat{\mathrm{H}}_0$ is given by

$$\hat{\mathrm{H}}_0 = \frac{\hbar\omega_0}{2}\hat{\sigma}_z, \tag{2.38}$$

where $\omega_0 = \omega_2 - \omega_1$. The frequencies ω_1 and ω_2 correspond to the energies $E_1 = \omega_1/\hbar$ and $E_2 = \omega_2/\hbar$ of the states $|1\rangle$ and $|2\rangle$ and $\hat{\sigma}_z$ is the Pauli z-operator. Solving the Schrödinger equation of the unperturbed system

$$i\hbar\frac{\partial}{\partial t}\Psi = \hat{\mathrm{H}}_0\Psi \tag{2.39}$$

yields

$$\Psi(t) = c_1 e^{-i\omega_1 t}|1\rangle + c_2 e^{-i\omega_2 t}|2\rangle. \tag{2.40}$$

Here, c_1^2 and c_2^2 correspond to the initial populations of state $|1\rangle$ and $|2\rangle$.

The interaction Hamiltonian is governed by the oscillating magnetic field $\mathbf{B}$ and is given by

$$\hat{\mathrm{H}}_\mathrm{I}(t) = -\mu\mathbf{B}_0\cos(\omega t), \tag{2.41}$$

where μ is the electron magnetic moment, $\mathbf{B}_0$ the amplitude vector of the magnetic field, and ω its oscillation frequency. Solving the Schrödinger equation for the driven system

$$i\hbar\frac{\partial}{\partial t}\Psi = (\hat{\mathrm{H}}_0 + \hat{\mathrm{H}}_\mathrm{I})\Psi \tag{2.42}$$

results in two coupled differential equations

$$i\dot{c}_1 = \Omega\cos(\omega t)e^{-i\omega_0 t}c_2 \tag{2.43}$$

$$i\dot{c}_2 = \Omega\cos(\omega t)e^{i\omega_0 t}c_1, \tag{2.44}$$

with the Rabi frequency defined as $\Omega = \langle 1|\,\mu\mathbf{B}_0\,|2\rangle/\hbar$. We assume, without loss of generality, the driving field to be only along the x-axis.

Next, we expand the cosine term into $\frac{1}{2i}(e^{i\omega t}+e^{-i\omega t})$ and neglect the fast rotating terms proportional to $\exp(i(\omega+\omega_0))$ by applying the rotating wave approximation. We define the detuning of the driving frequency from the transition frequency as $\Delta=\omega_0-\omega$. Then, the Equations 2.43 and 2.44 simplify to

$$i\dot{c}_1=\frac{\Omega}{2}e^{-i\Delta t}c_2 \tag{2.45}$$

$$i\dot{c}_2=\frac{\Omega}{2}e^{i\Delta t}c_1. \tag{2.46}$$

Finally, we use the ansatz

$$c_2(t)=\exp(i\lambda t) \tag{2.47}$$

and find

$$\lambda_\pm=\frac{1}{2}\left(\Delta\pm\sqrt{\Delta^2+\Omega^2}\right). \tag{2.48}$$

Under the assumption that the system is polarised into the $|1\rangle$ state before the driving field is switched on, i.e. $c_1(0)=1$ and $c_2(0)=0$, the general solution to the Hamiltonian $\hat{\mathrm{H}}$ is

$$c_2(t)=ie^{i\Delta t/2}\frac{\Omega}{\sqrt{\Omega^2+\Delta^2}}\sin\left(\frac{\sqrt{\Omega^2+\Delta^2}}{2}t\right). \tag{2.49}$$

Taking the norm of $c_2(t)$ yields the population for state $|2\rangle$

$$|c_2(t)|^2=\frac{\Omega^2}{\Omega^2+\Delta^2}\sin^2\left(\frac{\sqrt{\Omega^2+\Delta^2}}{2}t\right). \tag{2.50}$$

The $\sin^2$ term oscillates with frequency $\sqrt{\Omega^2+\Delta^2}$ in time. Those oscillations are called Rabi nutations and were first observed in a NV centre spin system by Jelezko et al. [90]. Increasing the detuning results in a lower amplitude but higher frequency of the signal.

The Hamiltonian $\hat{\mathrm{H}}=\hat{\mathrm{H}}_0+\hat{\mathrm{H}}_\mathrm{I}$ does not capture decoherence which is present in every real quantum system. To acquire Rabi oscillations we repeatedly apply a laser pulse for initialisation into the spin state $m_s=0$ followed by a microwave pulse whose length is scanned before the spin state is read out with a second laser pulse (Figure 2.12). The

microwave pulse is typically chosen to be resonant with the spin $m_s = 0 \leftrightarrow -1$ transition, i.e. the detuning Δ is chosen to be 0. In order to address only the $m_s = 0$ and $m_s = -1$ states, the spin transitions are split by a static, external magnetic field which causes a Zeeman splitting. If the detuning from the $m_s = 0 \leftrightarrow +1$ transition is small compared to the Rabi frequency, we drive a three level system with more complicated dynamics.

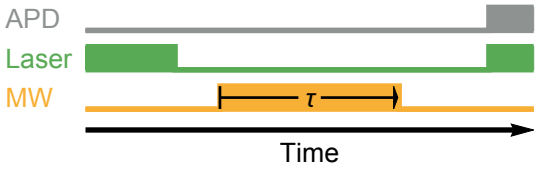

Fig. 2.12 **Pulse sequence for taking a Rabi curve**. First, the laser initialises the NV spin into $m_s = 0$, then a variable length microwave pulse is scanned before the NV state is readout.

The data acquired through this sequence is displayed in Figure 2.13. We extract a Rabi frequency of $\Omega = 2\pi \times 4.7\,\text{MHz}$ and a characteristic $1/e$ decay time of $T_{2,\text{MW}} = 6.6\,\mu\text{s}$ from the data. The characteristic decay time $T_{2,\text{MW}}$ has a lower limit set by the inhomogeneous de-phasing time T_2^*. Continuous driving of the spin transition acts as a filter to a part of the electro-magnetic noise in the environment of the NV centre and, thus, leads to $T_{2,\text{MW}} > T_2^*$. In Chapter 3 this effect is discussed in more detail. In order maximise rotation fidelities we typically drive the electron spin with the maximum available microwave power, i.e. as fast as possible to avoid dephasing. We achieve Rabi rates with the external loop antenna between 3 and 6 MHz and up to 60 MHz with an evaporated gold loop with approximately 150 µm mean radius with a 16 W amplifier.

To illustrate the power dependence, we plot squared Rabi rates as a function of the microwave power before the 16 W amplifier in Figure 2.14. We expect a linear relationship for low powers and saturation of the Rabi rates for the amplifier at higher input powers. Assuming losses of 1 dBm from the amplifier to the loop, we generate an AC field with an amplitude of 2.5 G to drive spins if the 16 W microwave amplifier is fully saturated.

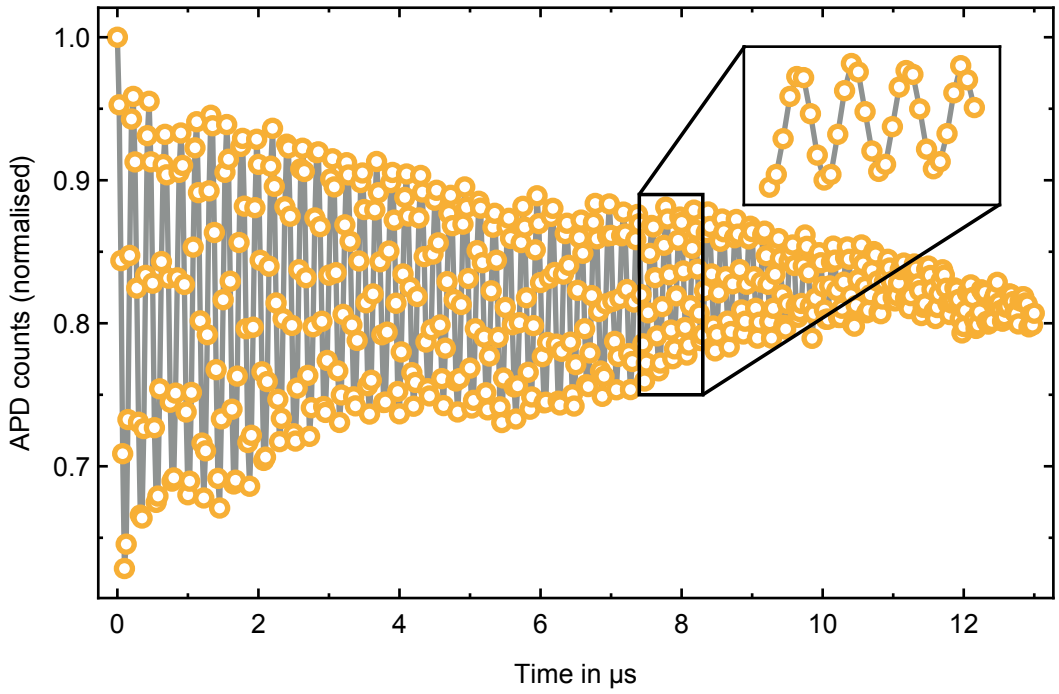

Fig. 2.13 **Rabi oscillations**. The data is acquired applying the pulse sequence in Figure 2.12. The gray line connects the data points and does not represent a fit but serves solely as a guide to the eye. A direct fit is not possible for such a number of oscillations due to pulse errors. Taking a Fourier transform of the data reveals a peak at $2\pi 4.7\,\mathrm{MHz}$ and an analysis of the exponential decay yields a characteristic $1/e$ decay time of $6.6\,\mu\mathrm{s}$.

2.5.3 Pulsed optically detected magnetic resonance

In order to access the host nuclear spin and to determine the population distribution of the nuclear spin state, using a continuous wave ODMR is inefficient. As presented in Section 2.5.1 it suffers from a small signal as the laser power must be reduced to typically 1/20 of the saturation power to resolve the hyperfine interaction according to Equation 2.36 for the ODMR linewidth. Therefore, we use a pulsed version of ODMR which circumvents the problem of having to lower the laser power. In fact, the laser is switched off during spin manipulation with microwaves.

The pulse scheme consists of a laser pulse initialising into the $m_s = 0$ state followed by a weak microwave π-pulse, whose frequency is scanned, before reading out with a second

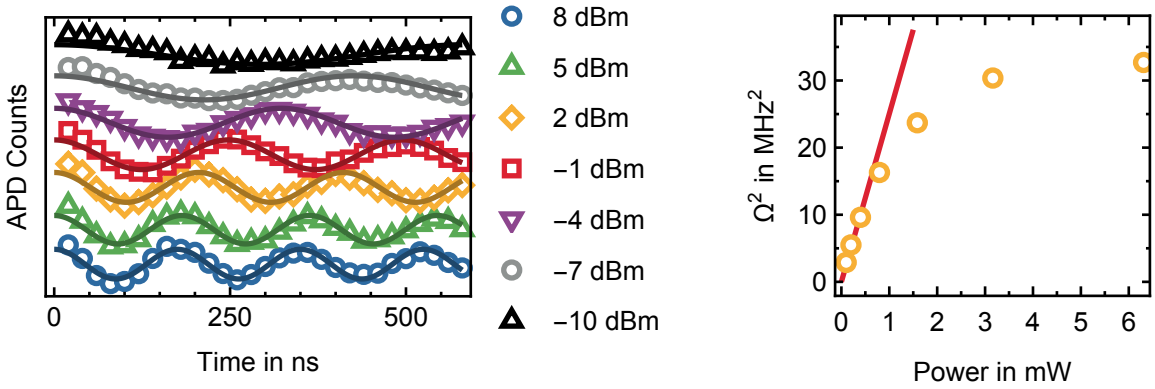

(a) Rabi curves

(b) Input power vs. Rabi rates

Fig. 2.14 **Rabi measurements at different powers**. (a) raw measurements along with their fits. (b) corresponding squared Rabi rates. For higher powers the linear relationship between squared Rabi rates and microwave power into the 16 W amplifier does not hold any more because the microwave amplifier starts to saturate.

laser pulse. The weak microwave π-pulse length is typically chosen around 550 ns which corresponds to a broadening of less than 1 MHz which in turn is sufficient to resolve the hyperfine coupling of -2.162 MHz. Various Rabi curves at different powers are taken to find a microwave power leading to such a π-pulse. Because of decoherence a too long microwave pulse is undesirable.

In Figure 2.15 a Rabi with a sufficiently low microwave power to resolve the hyperfine interaction with the nuclear spin and a pulsed ODMR measurement are displayed. Three non-degenerate resonances were detected indicating that this particular NV has a ^{14}N nucleus which is a spin $I = 1$ system.

2.6 Poisson statistics and error estimation

Two mistakes can be made when estimating parameters and their errors. First, the errors of the data are not correctly estimated. Using a least-square fit implicitly assumes Gaussian errors which is not always correct. Second, many methods often provide error estimates of their parameters θ. However, they are in often only valid if the fitted function $f(x, \theta)$ is

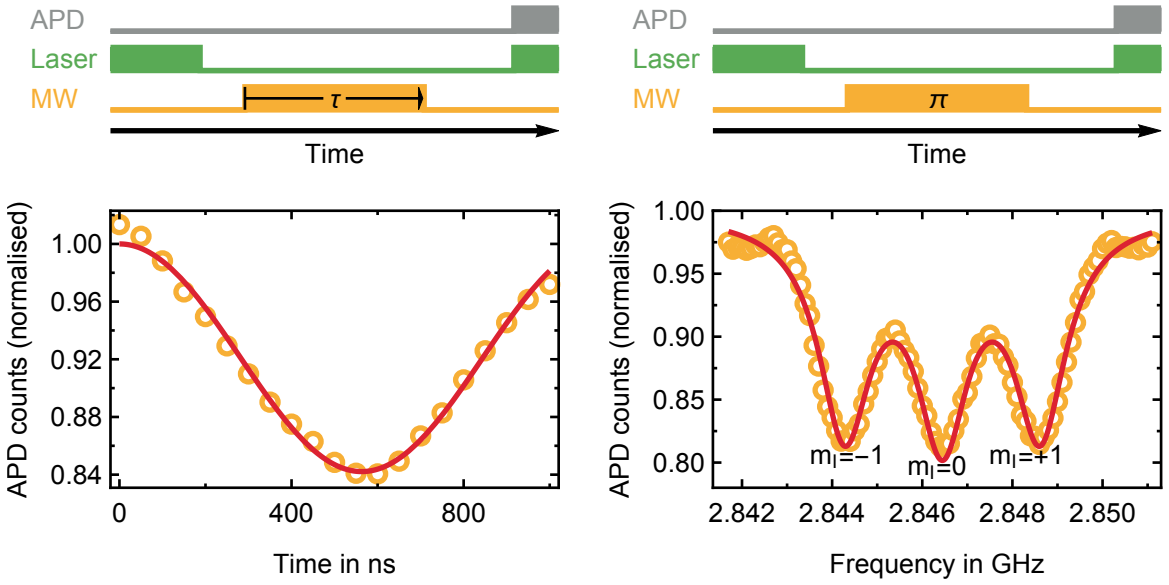

(a) Rabi

(b) Pulsed ODMR

Fig. 2.15 **Rabi oscillations and pulsed ODMR at low microwave powers**. Above the two figures the pulse sequences are displayed which were used to obtain the data. (a) one Rabi oscillation at low microwave power. As the Rabi rate is small, primarily the $m_I = 0$ subset of states is addressed leading to a reduced contrast. The extracted π-pulse length is 563 ns. (b) the microwave π-pulse is scanned in frequency to obtain a spectrum of the hyperfine resonances of the NV centre.

linear in those parameters. If the function f is non-linear in the estimated parameters, the error distribution can be heavily skewed and methods such as sampling from the likelihood distributions should be used to determine parameter errors.

In this Section we will examine the distribution of APD counts which we use to appropriately determine the errors of estimated parameters from a fit to the average photon counts. We show that the underlying statistics of the photon counts has a strong influence on the fit result and parameter errors. Using a least-square fit makes an assumption about the photon count distribution which is often not justified.

First, we motivate the usage of a Poisson distribution at low numbers of counts and a Normal distribution at high numbers of counts. Then, we investigate the sensitivity of estimated fit parameters and their errors by using Monte-Carlo simulations.

POISSON DISTRIBUTED PHOTON COUNTS

The photon emission of most physical systems will follow Poisson statistics. This follows directly from the exponential decay of excited states. Let $N(t)$ be the number of detected photons between time 0 and t, and X_i the time between the arrival of photon $i-1$ and i. The X_i are independent and have identical exponential distributions with rate parameter λ. Then, $T_n = \sum_{i=1}^{n} X_i$ is the arrival time of the i^{th} photon. In terms of probabilities this means

$$P(N(t) = n) = P(T_{n+1} > t) - P(T_n > t), \tag{2.51}$$

as the sets $\{N(t) = n\}$ and $\{T_n \leq t \leq T_{n+1}\}$ are equivalent. $P(T_n > t)$ is the Erlang distribution or the Gamma distribution where n is the shape parameter and λ the rate parameter. The connection between $P(T_n > t)$ and the Erlang distribution can be easily made using moment generating functions.

The n-th moment of a distribution with probability density function $f(x)$ is defined by $\mu_n = \mathrm{E}[X^n] = \int x^n f(x)\mathrm{d}x$. If all moments of two distributions are identical, the two distributions must be the same. The moment generating function of a random variable X is defined as $M_X(t) = \mathrm{E}[\mathrm{e}^{\mathrm{tX_i}}]$. By differentiation at $t = 0$ the moments of X can be found, i.e. $\mu_n = \frac{\mathrm{d}}{\mathrm{d}t} M_X(t)|_{t=0}$.

The moment generating function of the exponential distribution is $M_{X_i}(t) = \mathrm{E}[\mathrm{e}^{\mathrm{tX_i}}] = (1 - t/\lambda)^{-1}$. Thus, the moment generating function for T_n is $M_{T_n}(t) = \prod_{i=1}^{n} M_{X_i}(t) = (1 - t/\lambda)^{-n}$. This moment generating function is equal to the moment generating function of the Erlang distribution, and hence T_n must be Erlang distributed.

Substituting $P(T_n > t)$ with the probability density distribution of the Erlang distribution Equation 2.51 yields the Poisson distribution

$$P(N(t) = n) = \frac{\lambda^n e^{-\lambda}}{n!}. \tag{2.52}$$

This is the proof that photon counts are Poisson distributed.

Normally, we assume that the errors of photon counts follow the Normal distribution. A Poissonian distribution has a mean λ and a variance of λ from which immediately follows that even if we assume a Normal distribution of the errors, the residuals will have a variance proportional to the true value of the mean. Therefore, we can improve least square fits by weighting the data points with their value.

The use of a Normal distribution is justified for a large number of counts by the central limit theorem which states that if a random variable X is the sum of n independent and identically distributed variables X_i, X is normally distributed for $n \to \infty$.

However, for a small number of counts the central limit theorem does not hold and we must use the Poisson distribution to estimate errors correctly. One of the measurements where this is particularly important is the $g^{(2)}$ measurement. Here, for single photon emitters, we expect close to zero coincidence counts at zero time delay. In this Section, we will show how the error in estimating the number of emitters is affected by using a Poisson distribution as opposed to a Gaussian distribution.

Using a Gaussian distribution has one specific advantage over a Poissonian distribution. It incorporates already other error sources such as laser instability which induce fluctuations in the mean count rate λ in the Poissonian case. Hence, in order to model the number of counts, we would have to use a prior distribution for λ. Here, we assume that other error sources are negligible and, therefore, λ is constant.

Estimation of fit parameters and their errors

In the following we investigate how to infer the fit parameters and their errors from a photon count distribution. By comparing results from using the Gaussian and the Poisson distribution we demonstrate the shortcomings of employing the Gaussian distribution.

Parameter errors can be directly inferred from their distribution $p(\theta_i)$ computed from the likelihood function $L(\theta)$ by integration, i.e.

$$p(\theta_i) = \int_V L(\theta) \mathrm{d}\theta_{-i}. \tag{2.53}$$

Here $\theta = (\theta_1, \ldots, \theta_k)$ is the parameter vector, θ_i is one of its elements, and θ_{-i} is the parameter vector θ without θ_i, i.e. $\theta_{-i} = (\theta_1, \ldots, \theta_{i-1}, \theta_{i+1}, \ldots, \theta_k)$. The likelihood function for data (x_i, y_i), where $i = 1, \ldots, n$, using the model $y = f(x)$, is

$$L(\theta) = \prod_{i=1}^{n} \frac{1}{y_i!} f(x_i, \theta)^{y_i} e^{f(x_i, \theta)} \tag{2.54}$$

for a Poissonian distribution of counts y_i and

$$L(\theta) = \prod_{i=1}^{n} \frac{1}{\sqrt{2\pi\sigma_i}} \exp\left(-\frac{(y - f(x_i, \theta))^2}{2\sigma_i^2}\right) \tag{2.55}$$

for a Gaussian distribution. The Gaussian distribution also requires us to specify errors σ_i for all y_i. We assume, that all $\sigma_i = \sigma$ are the same and set

$$\sigma_i \equiv \sigma = \sqrt{\frac{1}{n-1} \sum_{i=1}^{n} (y - f(x_i))^2}. \tag{2.56}$$

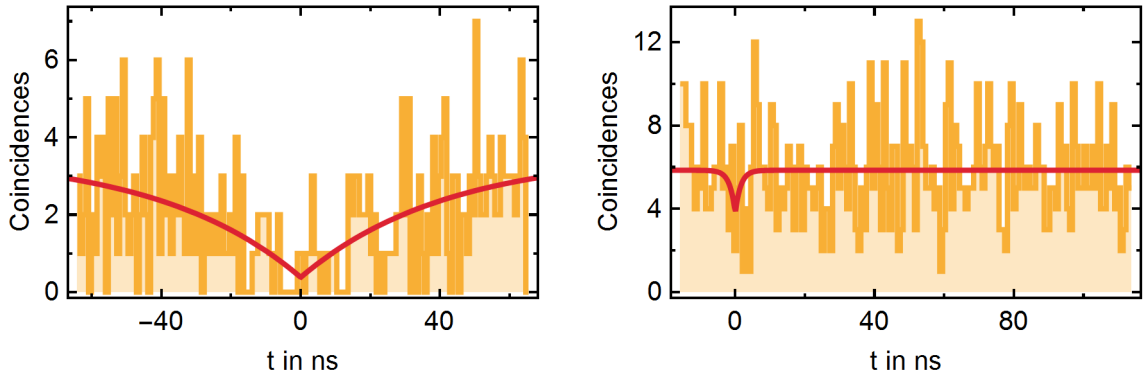

(a) Measurement 1

(b) Measurement 2

Fig. 2.16 **$g^{(2)}$ measurements with high noise levels.** Two $g^{(2)}$ measurements are shown and fitted using a least-square fit which assumes Gaussian errors. The first dataset on the left has a low signal to noise but clearly shows a single photon emitter. The second dataset is stems from a site with a high number of emitters.

Often, integrating the likelihood function is computationally too expensive and we have to resort to sampling from the likelihood distribution. We use Metropolis sampling implemented

in the Python package `pymc` which makes use of FORTRAN libraries for computational speed gains.

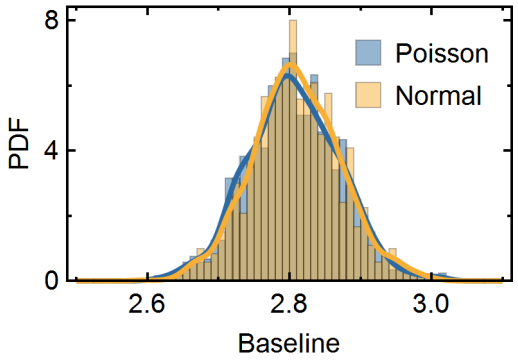

(a) Histogram for A, measurement 1

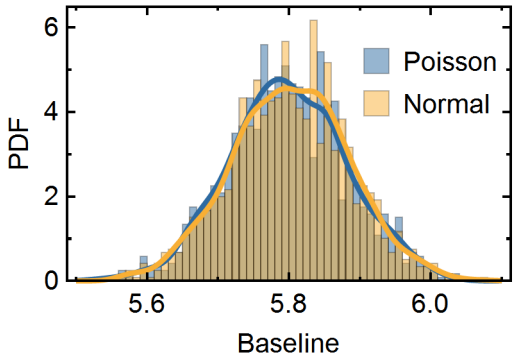

(b) Histogram for A, measurement 2

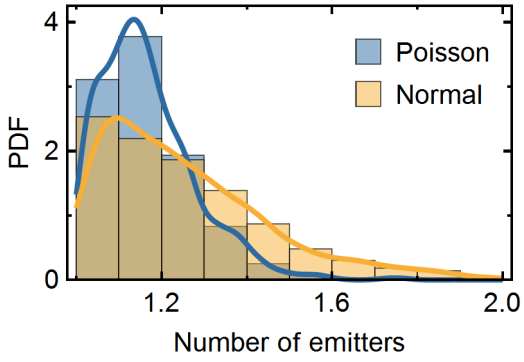

(c) Histogram for n, measurement 1

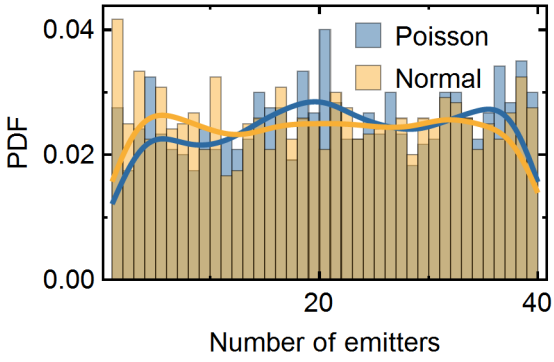

(d) Histogram for n, measurement 2

Fig. 2.17 **Histograms of selected parameters**. Histogram for the probability density functions (PDF) shown assume Poisson or Normal distributions of the signal in Figure 2.16. The solid lines represent the estimated density kernels of the distributions. For sampling, the parameters were restrained to 0-14 for the baseline A and to 1-40 for the number of emitters n. (d) this leads to an underestimation of the kernel density estimates on the (here only the right) edges of the parameter space.

For demonstrating the need of using a Poisson distribution and sampling from the likelihood, we present data in Figure 2.16 and 2.17 on two autocorrelation measurements and examine errors in the number of emitters n and the position of the baseline A. The fitted

function is based on the autocorrelation function derived in Section 2.4.3 and is given by

$$f(t) = A\left[1 - \exp\left(-\left|\frac{t-t_0}{\tau}\right|\right)/n\right], \tag{2.57}$$

where τ is the lifetime of the excited state. t_0 is the time zero in the laboratory time frame. In the measurement time frame $t_0 = 0$.

The fitting method based on minimising least-squares is greedy. For the second dataset this leads to a fit converged into a local minimum which is clearly not supported by the data. Traditional methods such as inferring the errors from the covariance matrix underestimate the fit parameter errors for measurement 2 dramatically. Sampling methods, however, do not suffer from convergence into local minima as they explore a larger part of the parameter space.

In Figure 2.17 the histograms for the parameters are displayed. The fit function is linear in A, and therefore A is normally distributed. For the baseline A there are no significant differences between assuming a Normal or Poisson distributed signal. This is not unexpected as the fit function is linear in A, all data points are relevant for the estimate and the majority of them is far away from the anti-bunching dip, i.e. they have a roughly symmetric and equal distribution.

For the number of emitters n, in general, the Gaussian approach yields too big errors as it overestimates the error on the data at a small number of total counts. Exactly these data points with small errors are the ones to which the estimate of n is most sensitive. Additionally, assuming a Normal distribution leads to overestimating the likelihood for a very small n as it assumes symmetric errors and, thus, also negative count rates.

In conclusion, a Poissonian distribution for the photon counts should be used if some part of the signal has a small number of counts. Small means less than 30 total counts as above this value the errors from the Poissonian and Normal approach can be considered equal. Least square fits can be improved by weighting the data points with their value. For parameters, in which the fitted function is non-linear, sampling from the likelihood yields their correct distributions. For parameters that are linear and uncorrelated to all non-linear

parameters, less computationally expensive methods can be employed. It should be stressed that using the same methods for parameters in which the fitting function is non-linear can lead to completely different and incorrect results.

2.7 Increasing the readout fidelity by data post-processing

The laser pulse for initialisation of the NV centre into the $m_s = 0$ spin state must not be too short to ensure, first, that the NV centre is maximally polarised into its ground state and, second, as the pulsed experiments are repeated many thousand times that all information stored in the NV state from the previous experiment is erased, i.e. the NV spin is always prepared into the same state. There is no maximum length but the longer the initialisation time is, the longer the total time taken by a single measurement and the less often a measurement can be cycled per second. In order to minimise the total acquisition time, a short initialisation window is desirable. The readout window, however, has an optimal length, which is linked to the initialisation speed. A too short length will lead to a low photon count rate, increasing the overall time needed to reach a certain ODMR signal-to-noise ratio and a too long window will lead to the acquisition of noise, directly decreasing the signal-to-noise ratio.

Choosing an optimal readout window is the process of expanding the window width until the overall signal-to-noise ratio degrades. This approach compares the total acquired signal to the total acquired noise and does not take into account that each photon has a different signal-to-noise ratio. As we optically excite the NV centre and acquire photon counts the spin state is reset to $m_s = 0$. Hence, the photons with earlier arrival after the start of excitation do carry more information than the subsequent.

In this Chapter we show that by time-tagging the photons and weighting the photon counts with their individual signal-to-noise ratios the readout efficiency can be improved by 15 %. This means that only 87 % of time is necessary to reach the same signal-noise-ratio.

2.7.1 Optimal readout window length

First, we want to introduce a direct way of determining the optimal readout window length before embarking on a different approach which uses the individual arrival times of photons. A long readout window increases the acquired counts but after a full re-initialisation of the NV spin the acquired counts do not carry any information. This means when we increase the readout window length, we should stop the moment a marginal increase in the readout window length results in a decrease of the total signal-to-noise ratio. The signal is defined by the difference in counts $n_0(t) - n_{\pm1}(t)$ from the NV centre in states $m_s = 0$ and $m_s = \pm 1$. The noise can be modelled as shot noise as dictated by the central limit theorem for a large number of counts in order to simplify calculations. This means it must be proportional to $\sqrt{N(t)}$. The signal-to-noise ratio is then

$$SN(t) \propto \frac{n_0(t) - n_{\pm1}(t)}{\sqrt{\frac{n_0(t)+n_{\pm1}(t)}{2}}}. \tag{2.58}$$

We can now carry out the experiment to determine the optimal APD window length. The pulses are illustrated in Figure 2.18. By optical pumping we first initialise the NV centre with a green laser into the $m_s = 0$. Before reading out with the laser while scanning the APD window length, we can apply a microwave π pulse to probe the $m_s = \pm 1$ state. The π pulse length was chosen using a Rabi measurement as described in Section 2.5.2. The two curves become parallel when the NV spin state has been reset to $m_s = 0$. Then, only noise but no signal is acquired (Figure 2.18.a). By applying Equation 2.58, the signal-to-noise ratio can be estimated apart from a proportionality constant (Figure 2.18.b). The optimal APD window size is at the maximum of the signal-to-noise ratio curve. In our case, 550 ns for the optimal window size was consistently measured if working at half saturation power. The exact shape of the signal-to-noise ratio curve is highly power dependent. For this reason, before acquiring any data, we always first measure a saturation curve and set the power to the half saturation point as discussed in Section 2.4.2.

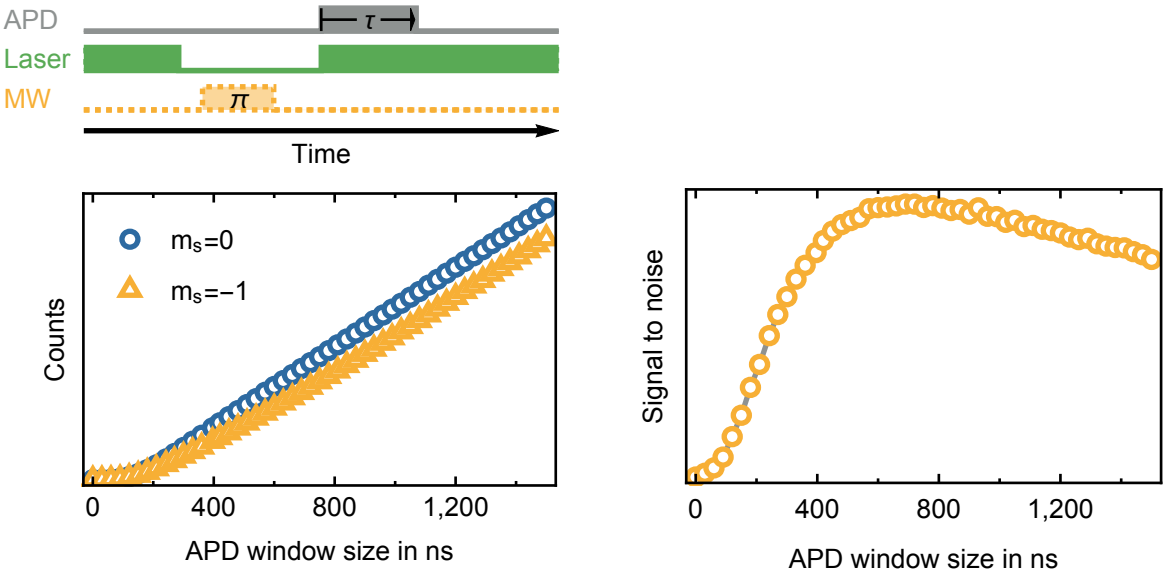

(a) Raw data

(b) Signal-to-noise extracted from raw data

Fig. 2.18 **Optimal APD window size**. (a) raw data and the corresponding pulse sequences, which is adjusted for delays, on top of the figure. The lower line has been recorded with the microwave induced π-flip and the upper line without. (b) extracted signal-to-noise ratio assuming shot noise. The maximum is at 550 ns. This is the optimal APD window.

2.7.2 Spin state readout

The NV centre electron spin state is readout by applying a green laser. To judge the amount of information available in the photon count signal, we first examine the mean counts after turning the laser on and record a photon count time-trace for the initial states $m_s = 0$ and $m_s = -1$. In the absence of transverse magnetic or electric fields, the time-traces for the $m_s = \pm 1$ states are equal. We therefore refer in the following to the $m_s = \pm 1$ states without distinguishing the two. The different states are prepared by first initialising the electron spin into $m_s = 0$ with a long laser pulse. To probe the $m_s = \pm 1$ states we then apply a microwave π-pulse. The two resulting curves are shown in Figure 2.19. If the state is a mixture of $m_s = 0$ and $m_s = \pm 1$, the measured count trace is a weighted average of the traces of $m_s = 0$ and $m_s = \pm 1$.

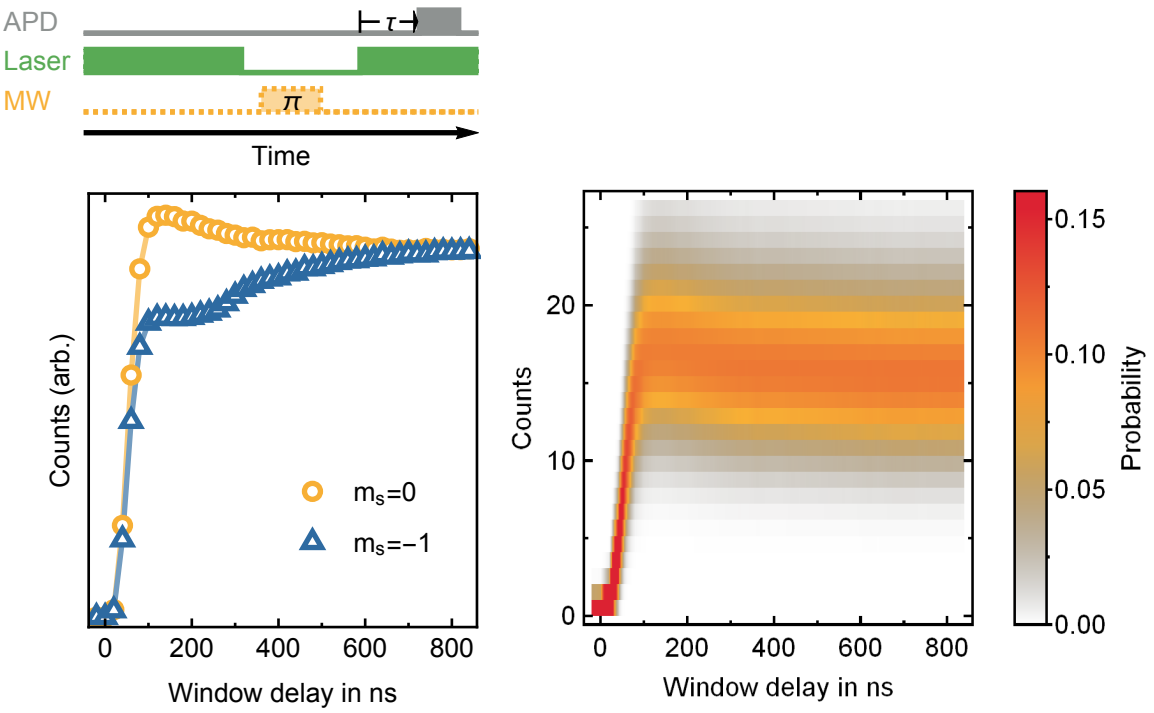

(a) Signal from $m_s = 0$ and $m_s = -1$

(b) Poissonian count distribution for $m_s = 0$

Fig. 2.19 **Photon counts and their errors during readout**. (a) an APD window of fixed length is stepped over the readout laser pulse. The two signals for states $m_s = 0$ and $m_s = -1$ are displayed whose difference constitutes the ODMR contrast. The step size for the window delay τ and the fixed APD window size are chosen to be 20 ns. However, the rise and fall time of the switches gating the TTL count signal from the APDs is on the same timescale, i.e. the effective APD window size is far smaller than 20 ns and estimated to be approximately 5 ns given the achieved count rates. (b) the probability density of counts calculated from the $m_s = 0$ curve in (a) is shown evolving over time for 15 mean counts per time bin at full polarisation of the NV centre electron spin. From the distribution of the detected count rates we can infer lower expected variance at small than at high count rates.

We can make two key observations from the data shown in Figure 2.19.a. First, after 700 ns a steady state, i.e. initialisation into $m_s = 0$, has been reached. This is an important result as we can therefore choose a 1 µs green laser pulse to reliably initialise the spin. Second, the difference between the mean counts from the two spin states is not constant which indicates that we can make significant efficiency gains by weighting the photons according to their information carried which depends on the delay τ denoted in Figure 2.19.

The exact shape of the NV centre response depends on the AOM rise profile, the decay rates of the NV centre, external electro-magnetic fields, the excitation laser power and the efficiency with which photons are extracted and successfully detected. As the resulting curves are proportional to the convolution of the AOM laser output profile and the NV centre response and as we do not know the AOM laser output profile, in the following we use a function to interpolate the values from the empirical profile instead of a simulation based on theory would most likely suffer from more inaccuracies due to the complexity of the task.

2.7.3 Fisher information of photon count statistics

Fisher information is a measure of information which is contained in an observable random variable X about a parameter θ. θ is a parameter of the distribution that models X and the observable information is a set of data points sampled from X. We want to know the amount of information available about the spin state in the time-tagged photon counts from the NV centre, i.e. the Fisher information of the spin state. An intuitive understanding of Fisher information is given by the Cramer-Rao bound which states that the variance of an unbiased estimator $\hat{\theta} = \mathrm{E}(\theta)$ is equal or larger than one over the Fisher information $\mathcal{I}$, i.e.

$$\mathrm{Var}(\theta) \geq \frac{1}{\mathcal{I}(\theta)}. \tag{2.59}$$

This is an important relation because the number we are interested in is the time for which we have to acquire data until a certain variance threshold / information level is reached.

Mathematically, the Fisher information is defined as the expectation value of the observed information

$$\mathcal{I}(\theta) = \mathrm{E}[\mathcal{J}(\theta)|\theta] = \mathrm{E}\left[\left(\frac{\partial}{\partial\theta}\log L(X,\theta)\right)^2 \middle| \theta\right], \tag{2.60}$$

where $\mathcal{J}$ is the observed information, $L(X,\theta)$ is the likelihood of the observed random variable X under the parameters θ and $\mathrm{E}[A|B]$ is the expectation value of A conditional on B. Fisher information lies in the interval $[0,\infty)$, where 0 information corresponds to no knowledge and ∞ to exact knowledge about the value of θ.

If $L(X,\theta)$ is twice differentiable with respect to θ, then the Fisher information can be also written as

$$\mathcal{I}(\theta) = -\mathrm{E}\left[\frac{\partial^2}{\partial\theta^2} l(X,\theta)\middle|\theta\right], \tag{2.61}$$

where $l(X,\theta) = \log L(X,\theta)$ is the log-likelihood. Form Equation 2.54 in Section 2.6 the log-likelihood of a Poissonian process such as the generation of photon or APD counts must be

$$l(\theta) = \sum_{i=1}^{n} y_i \log f(\tau_i,\theta) - f(\tau_i,\theta) - \log(y_i!), \tag{2.62}$$

where y_i is observed data and $f(\tau_i,\theta)$ is the expected observed data at delay τ_i under the model $f(\tau,\theta)$ with parameter θ. Then, the Fisher information is

$$\mathcal{I}(\theta) = \sum_{i=1}^{n} \mathrm{E}\left[\frac{y_i}{f(\tau_i,\theta)}\left\{\frac{1}{f(\tau_i,\theta)}\left(\frac{\partial f(\tau_i,\theta)}{\partial\theta}\right)^2 - \frac{\partial^2 f(\tau_i,\theta)}{\partial\theta^2}\right\} - \frac{\partial^2 f(\tau_i,\theta)}{\partial\theta^2}\middle|\theta\right]. \tag{2.63}$$

Let $c_0(\tau) = f(\tau,0)$ be the expected count rate when the spin state is $m_s = 0$ and $c_{\pm1}(\tau) = f(\tau,\pm1)$ when the state is $m_s = \pm1$. The expected count rate $f(\tau,\theta)$ will be linear in the spin state parameter θ because at the moment of the measurement the spin state superposition is projected into one of the states. Let $\theta = 0$ denote $m_s = 0$ and $\theta = 1$ represent $m_s = \pm1$. Then

$$f(\tau,\theta) = c_0(\tau)(1-\theta) + c_{\pm1}(\tau)\theta \tag{2.64}$$

and

$$\mathcal{I}(\theta) = \sum_{i=1}^{n} \mathrm{E}\left[\frac{y_i}{f(\tau_i,\theta)^2}\left(\frac{\partial f(\tau_i,\theta)}{\partial\theta}\right)^2 \middle| \theta\right] \tag{2.65}$$

$$= \sum_{i=1}^{n} \frac{\mathrm{E}[y_i|\theta]}{f(\tau_i,\theta)^2}\left(\frac{\partial f(\tau_i,\theta)}{\partial\theta}\right)^2 \tag{2.66}$$

$$= \sum_{i=1}^{n} \frac{f(\tau_i,\theta)}{f(\tau_i,\theta)^2}\left(\frac{\partial f(\tau_i,\theta)}{\partial\theta}\right)^2 \tag{2.67}$$

$$= \sum_{i=1}^{n} \frac{1}{f(\tau_i,\theta)}\left(\frac{\partial f(\tau_i,\theta)}{\partial\theta}\right)^2 \tag{2.68}$$

$$= \sum_{i=1}^{n} \frac{(c_0(\tau_i) - c_{\pm1}(\tau_i))^2}{c_0(\tau_i)(1-\theta) + c_{\pm1}(\tau_i)\theta}. \tag{2.69}$$

The Poisson distribution can be well approximated by a Normal distribution if more than 30 samples are available. As we typically average hundreds or thousands of counts this approximation holds. The Fisher information of the Normal distribution is

$$\mathcal{I}_{\mathrm{normal}}(\theta) = \sum_{i=1}^{n}\left(\frac{c_0(\tau) - c_{\pm1}(\tau)}{\sigma_i}\right)^2, \tag{2.70}$$

where σ_i is the standard deviation of the individual data points. In both cases the information grows linearly with the number of counts corresponding to the integration time t because $c_0(\tau) \propto t$, $c_{\pm1}(\tau) \propto t$ and $\sigma \propto \sqrt{t}$. In the following we use the Poissonian version of information and assume as in Section 2.6 that the mean of the Poissonian count statistics is constant and does not fluctuate, for example due an unstable laser source.

We can plot the information contained in each time interval by state, i.e. for $\theta = 0$ and $\theta = 1$. The information corresponds to how much we can increase our confidence to that the NV centre was in the $m_s = 0$ or $m_s = \pm1$ state. The information contained in a time interval is plotted in Figure 2.20.a. By division of this information by the mean counts in the respective interval we can deduce the information carried per photon as shown in Figure 2.20.b. Given that the information per photon is not constant or the curve has a rectangular shape, we must be able to extract more information by weighting each photon individually than choosing equal weights which corresponds to using a readout window of fixed length as explained in

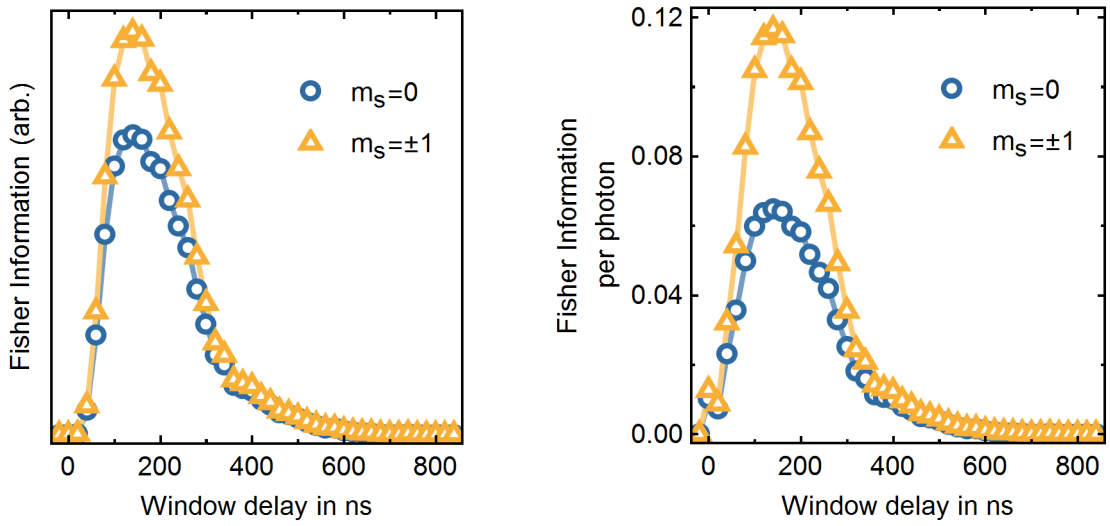

(a) Information per time interval

(b) Information per photon

Fig. 2.20 **Fisher information in the readout window**. (a) the Fisher information per time interval determined by the APD window size and the APD window delay for the $m_s = 0$ and $m_s = \pm 1$ states. (b) the information per photon. The light yellow and blue lines only serve as a guide to the eye. The underlying data is identical with that shown in Figure 2.19.

Section 2.7.1. The information per photon is not maximal for delay $\tau = 0$. This is due to finite errors in the empirical data. The discrepancy between the two states can be explained by the left skewness of the Poisson distribution, i.e. for two random variables X_1 and X_2 modelled by Poisson distributions with means λ_1 and λ_2, where $\lambda_1 < \lambda_2$, the probabilities $\mathrm{P}(X_2 < \lambda_1) < \mathrm{P}(X_1 > \lambda_2)$. Therefore, a small number of photon counts is always a stronger indication for being in the spin state $m_s = \pm 1$ than a high number of photons count is for $m_s = 0$.

2.7.4 Estimating the information gain

Estimating the information gain by weighting the photon counts instead of a fixed acquisition window leads to a shorter integration time needed to obtain the same uncertainty about the measured spin state.

The Cramer-Rao bound in Equation 2.59 can be used to translate information into integration time. For a Poisson distribution with mean λ the two sides of the Cramer-Rao equation are equal, i.e. the information is equal to the inverse of the variance. However, our signal for θ ($\theta = 0$ for the $m_s = 0$ state and $\theta = 1$ for the $m_s = \pm 1$ states) is not directly a parameter of the Poisson distribution with parameter λ. $\lambda = a\theta + b$ with constants a and b. We show that nevertheless, the equality holds as well for θ and not only for λ.

First, because of the linearity of λ in θ, $\hat{\theta}$ is an unbiased estimator of θ. Second, calculating the Fisher information yields

$$\mathcal{I}(\theta) = \mathrm{E}\left[-\frac{\partial^2}{\partial\theta^2}\log\left(\frac{[(a\theta+b)t]^X}{X}e^{-(a\theta+b)t}\right)\right] \tag{2.71}$$

$$= \mathrm{E}\left[\left(\frac{a}{a\theta+b}\right)^2 X\right] = \left(\frac{a}{a\theta+b}\right)^2 \mathrm{E}[X] = \frac{a^2 t}{a\theta+b} \tag{2.72}$$

which is the inverse of the variance of θ, i.e.

$$\mathrm{Var}[\theta] = \mathrm{E}\left[\left(\theta-\hat{\theta}\right)^2\right] = \frac{1}{(at)^2}\mathrm{E}\left[\left(X-\bar{X}\right)^2\right] = \frac{a\theta+b}{(at)^2}t = \frac{a\theta+b}{a^2 t}, \tag{2.73}$$

where t is the integration time. It directly follows that comparing information obtained after two integration times t_1 and t_2 is equivalent to comparing the integration times t_1 and t_2 to reach a specific uncertainty of θ.

We can now determine the efficiency gain by using the information obtained from weighted counts by the comparing the total available Fisher information described by Equation 2.69 and the Fisher information available for a given, fixed readout window size t_w. The latter is

$$\mathcal{I}_{\mathrm{window}}(\theta, t_w) = \frac{\left(C_0(t_w) - C_{\pm1}(t_w)\right)^2}{C_0(t_w)(1-\theta) + C_{\pm1}(t_w)\theta} \tag{2.74}$$

with

$$C_s(t_w) = \int_0^{t_w} c_s(\tau)\mathrm{d}\tau, \tag{2.75}$$

where the integral emphasises the continuity of $c_s(\tau)$.

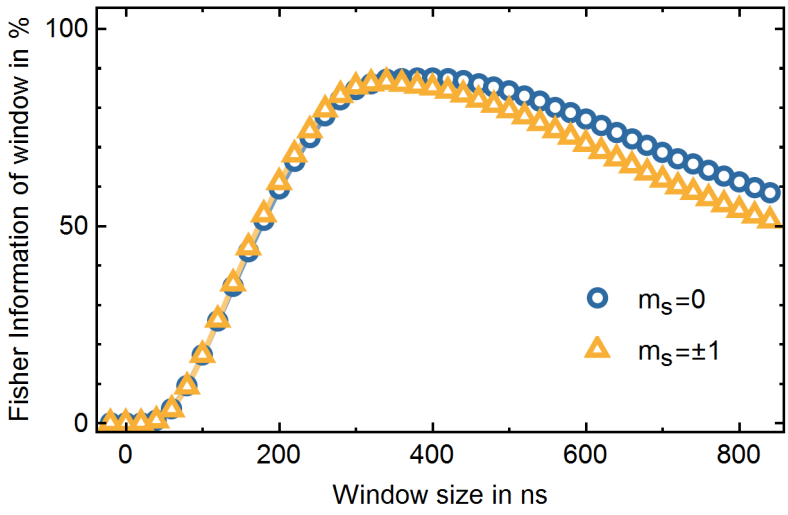

Fig. 2.21 **Fisher information in fixed readout window compared to total available information**. The Fisher relative information in a readout window of size t_w is displayed. The information values were computed according to Equation 2.74 and divided by the total Fisher information available according to Equation 2.69. The peaks are at 340 ns and 400 ns, respectively, and have a height of approximately 85 %. Taking the square root of the information yields the signal-to-noise ratio.

In Figure 2.21 the information extracted by choosing a specific window size, is presented as a fraction of the total information available. By optimising the window size, up to 87 % of the total information can be extracted which is available by individually weighting the photon counts. Further, using time tagging and post-processing data can reduce the total measurement time by 13 %.

In Figure 2.21 we obtain 400 ns and 340 ns for the optimal readout window size for the $m_s = 0$ and $m_s = \pm 1$ states, respectively. The single state lifetime is 300 ns [1] which is the minimum time it takes to polarise the NV centre into the $m_s = 0$ state. We expect a slightly longer optimal readout window given a finite excitation power and non-zero probabilities of undergoing ISC and transition from the singlet state to the $m_s = \pm 1$ states. In Section 2.7.1 we did find 500 ns as the optimal readout window. This discrepancy can be explained three-fold. First, we assumed a Normal as opposed to a Poisson distribution in Section 2.7.1. Second, the two NV centres might exhibit different decay rates and, third errors in the measurement of the

half-saturation power lead to different excitation rates. Given that the curve in Figure 2.21 has a higher absolute slope at window sizes t_w smaller than the optimal window sizes compared to the absolute slope at window sizes greater, it is recommended to choose a readout window size slightly above the calculated optimum.

2.7.5 Conclusions

Time-tagging photon count events and post-processing this data can decrease the required integration time by 15 %. If the scheme is implemented, the NV centre's optical response has to be carefully characterised which can either be achieved as displayed in Figure 2.19 or directly by time-tagging the APD TTL pulses with respect to the laser pulse start time. The average steady state count rate of the NV centre under continuous excitation needs to be estimated precisely because the final readout fidelity depends on it critically. This can be done with arbitrary precision as there is no limit to the length of the readout laser pulse.

Compared to other techniques an improvement of 15 % of the signal-to-noise ratio is a modest. Using superconducting photon detectors with almost 100 % detection efficiency can boost the ration by $\approx 35\,\%$. Before implementing time tagging and post-processing greater gains can be achieved by using solid immersion lenses and high numerical aperture oil objectives with improvements of 544 % and 242 %, respectively, assuming increases in numerical aperture from 0.9 to 2.1 and 1.4, respectively. Evanescent coupled cavities have demonstrated to reach collection efficiencies of up to 37 % corresponding to an approximately 2000 % improvement [150]. However, such cavities have been only implemented with bulk diamond, yet. Photonic crystal cavities are also suitable to enhance the emission of NV centres hosted by nanodiamonds and Englund et al. [50] have seen brightness improvements of emission into the ZPL of up to 700 %, albeit at the expense of emission into the phonon sideband which accounts for the bulk of fluorescence.

CHAPTER 3

Sensing with nitrogen-vacancy centres

A major application of NV centres is sensing magnetic and electric fields. Furthermore, temperature can be detected as temperature changes affect the crystal lattice spacings and therefore the position of nuclear spins and the shape and position of electron orbitals is modified. These changes cause a change in the electric field environment which can be measured by the NV centre.

The spin energy levels $m_s = \pm 1$ of the NV centre are sensitive to magnetic fields through the Zeeman interaction. Electric fields and temperature can be detected by observing changes in the ZFS. The NV centre is an excellent local and non-invasive sensor. It is local because it only occupies two lattice sites in diamond. Since only a single spin is involved in the sensing, the backaction on the environment is minimised. This is fundamentally different for macroscopic sensors such as SQUIDs (Chapter 5). Furthermore, its lack of need for electrical leads adds to its non-invasiveness, which is particularly important for sensing in biological systems.

Two types of measurements can be identified. These are continuous spectroscopy and pulsed interferometry experiments. Interferometry, in general, has the advantages to select specific features, i.e. to suppress noise, and to probe the system without perturbations (in this case by driving microwaves). This leads to a higher signal-to-noise ratio which allows higher sensitivity. However, continuous measurements offer the advantage of experimental simplicity. The equivalent to mirrors in optical interferometry are microwave pulses in

interferometry with a spin system. Interferometry measurements rely on probing the coherent evolution of the spin state and therefore require phase stability. Hence, sensitivity is linked to the coherence time of the spin state.

In this Chapter we first introduce the spin properties in Section 3.1 which determine the sensing capabilities of the NV centre. In Section 3.2 we compare fabrication methods for NV centres in bulk and nanodiamond. The choice of a method heavily influences the obtained spin properties. Eventually, the basics of the main application of NV centres, that is sensing, is discussed. We present sensitivities and different techniques for sensing DC electric and magnetic as well as AC magnetic fields. We do not demonstrate AC electric field sensing in this thesis and refer to Dolde et al. [42] who report a sensitivity of $203\,\mathrm{Vcm^{-1}Hz^{-1/2}}$ with a NV centre whose coherence time is roughly $100\,\mu\mathrm{s}$. The coherence and lifetime of the electron spin is short compared to nuclear spins. This is especially true for nanodiamonds as the sensing volume of nuclear spins is smaller than that of electron spins. One readily available nuclear spin for the NV centre is its host nuclear nitrogen spin. In Chapter 6 the host nuclear spin and its applications for sensing with NV centres in nanodiamonds will be discussed in detail.

3.1 SPIN PROPERTIES

Employing spins as qubits requires them to meet the DiVincenzo criteria [38]. Amongst them are a universal set of quantum gates and long coherence times. In particular, this means we need to characterise three time scales: The inhomogeneous dephasing time T_2^*, the homogeneous dephasing time T_2 and the lifetime T_1. In this Section we will examine the details of time scales by considering the noise sources they are related to.

The lifetime or relaxation time T_1 of the spin state is affected by electro-magnetic and phonon interactions. At low temperature phonon-related noise is suppressed as the acoustic modes in diamond are not populated anymore because the low Boltzmann energy k_BT, where $k_B = 86.2\,\mu\mathrm{eVK^{-1}}$ is the Boltzmann constant. At low temperatures the T_1 of NV centres in the nanodiamonds used for this work increases from hundreds of microseconds to tens of

milliseconds. In bulk diamond T_1 extends to seconds at room temperature, reaches hundreds of seconds at 40 K and at least many hours at cryogenic temperatures where measurements had to be stopped due to time constraints despite the availability of single shot readout [186]. Ultimately, it is expected to be limited by spin-lattice relaxation which is on the order of 10^4 s in diamond [11]. Therefore, phonon noise dominates at room temperature. Redman et al. [160] have investigated the relation of the spin lifetime with temperature. They find that a two-phonon Orbach process dominates at low temperatures. The two-phonon Orbach process is essentially a Raman process which consists of the absorption of a phonon, a spin-flip and the emission of a phonon. Therefore,

$$\frac{1}{T_1} \propto \frac{\Delta^3}{\exp\left(\frac{\Delta}{k_B T}\right) - 1}, \tag{3.1}$$

where k_B is the Boltzmann constant, T is the temperature and Δ the activation energy. Redman et al. [160] find $\Delta = 62.2\,\text{meV}$ which is close to the dominant phonon energy of the NV centre of 63 meV. At room temperatures Redman et al. [160] discover that the inverse lifetime follows a T^5 temperature dependence which is in line with a second order Raman process.

While relaxation causes the population to change, dephasing only affects the phase of the spin. Similar mechanisms cause both processes and the dephasing time is limited by twice the lifetime. For the NV spin system T_2 is typically far shorter than T_1 and phonon noise is a minor concern for phase coherence. We associate the inhomogeneous dephasing time with T_2^* and the homogeneous with T_2. T_2^* depends solely on the noise environment of the defect and is measured using a Ramsey sequence while T_2 is equal T_2^* if no filter is applied to the noise from the environment. Thus, T_2 depends on the specific measurement protocol. The term "coherence time" normally denotes homogeneous dephasing time. In most articles on NV centres T_2 refers to the Hahn echo dephasing time. Both the Ramsey and the Hahn echo sequence are presented in Chapter 3.

Electro-magnetic noise dominates the dephasing of NV centres. Noise is caused by magnetic interactions with the NV electron spin which are due to a bath of proximal nuclei and electrons spins. There are no direct spin flip-flops as the energy mismatch given

that the ZFS $D = 2.87\,\text{GHz}$ is far greater than the perpendicular hyperfine coupling of $A_{gs}^{\perp} = -2.65\,\text{MHz}$. However, electrons and nuclear spin in the bath flip each other and therefore cause a fluctuating magnetic field at the site of the NV centre. While ^{12}C, which is the main element of diamond, is a spin-less isotope, most impurities carry a spin. At impurity concentrations above 1 ppm noise from the electron spin bath is the main source of dephasing. Noise by electron spin flips is caused primarily by nitrogen spins ($S = 1/2$) whose concentration can be controlled at the time of diamond growth. However, the NV centre concentration also strongly depends on the number of incorporated nitrogen atoms. But if nitrogen ions are implanted, ultra-pure diamond can be used as a substrate [59]. Another technique for reducing noise caused by electron spins is applying a magnetic field to induce a large energy mismatch between the spins in the bath. If this energy mismatch exceeds the interaction time of the electron spins the noise from the bath is suppressed [72]. In contrast, matching the energy of the electron spin flip-flops with the NV centre spin transitions can cause strong decoherence or, as it has recently been shown by Knowles et al. [102], can be used to polarise proximal nitrogen electron spins. Reducing the temperature below 2 K (at a magnetic field of 8 T) is another path to polarisation of the electron spin bath. As the bath becomes polarised the coherence time increases dramatically [186]. It should be noted that in general cooling the diamond does not affect dephasing because phonons mainly affect the NV spin lifetime which is much larger than the decoherence time.

As we reduce the noise from nitrogen electron spins by polarisation or decreased impurity concentration, the interactions with nuclear spins become the limiting factor for coherence. ^{12}C and is a spin-less isotope of carbon but the $I = 1/2$ nuclear spin of ^{13}C causes a fluctuating magnetic field through interactions similar to the one produced by electron spins. The small magnetic moment of nuclear spins reduces the amplitude of this nuclear spin noise significantly. Also, as Gaebel et al. [59] write, the energy shift experienced by the nuclear spins, due to hyperfine coupling with the NV centre, is large close to the NV centre and, hence, as the law of energy conservation must be obeyed, the nuclear spins can only flip together. Given the gyromagnetic ratios of nuclear and electron spins and the 1.1 % natural abundance of ^{13}C, they calculate a sphere of frozen spins with radius 2.2 nm which yields

a coherence time in agreement with their measurement of 350 µs. Using a sophisticated decoupling sequence, i.e. a high quality noise filter, a coherence time $T_2 \approx 0.6$ s has been achieved in isotopically pure diamond at 77 K and $T_2 = 3.3$ ms at room temperature [12]. The value at 77 K could potentially be improved by further decreasing the temperature as this T_2 is limited by phonon noise. In terms of inhomogeneous dephasing times values between $T_2^* = 1.7$ µs and tens of microseconds have been observed while the later was reported for a NV centre in isotopically pure diamond [30, 11]. All aforementioned values refer to values measured in the ground state. In the excited state a value of $T_2 = 5.8$ ns has been measured [56].

Additional noise sources are charge traps and spins on the surface. This is particularly relevant for nanodiamonds that have rough surfaces with broken bonds. Most NV centres in nanocrystals have not shown coherence times beyond a few microseconds [139, 192, 110]. Nevertheless, in high purity nanodiamond as used in this work, coherence times of up to 60 µs have been observed using a CPMG sequence which is discussed in Section 3.6 [101]. However, typical values for Hahn echo are still only found in the single digit microseconds region.

Shallow implanted NV centres, which are complementary to NV centres in nanodiamonds for many applications, have recently received a lot of attention. After acid and heat treatment of the surface, coherence times of up to 100 µs have been observed for NV centres just 10 nm below the diamond-air interface [154]. This value decreases rapidly for the NV centres which are closer to the surface. Only $T_2 = 4$ µs has been achieved for defects 5 nm away from the surface without special treatment of the diamond [149].

3.2 Fabrication of nanodiamonds

In this Section, we review different fabrication methods and their respective (dis)advantages. However, first, we describe which properties of a fabrication method are desirable.

If we imagine an ideal fabrication method, it would allow the creation of strain-free isotopically pure diamonds of any size with a flat and charge trap-free surface. Nitrogen

atoms could be incorporated locally and the conversion efficiency to NV centres, whose axis could be controlled, would be 100 %. Purity, a perfectly flat surface and high conversion efficiency maximise the spin life- and coherence time of NV centres and spatial control, no or negligible strain and control over the NV axis is desirable for sample reproducibility. Long spin coherence and lifetimes are essential for the achievement of high sensitivities as outlined in Chapter 3. In Section 3.1 we discussed that solid state qubits, such as the NV centre, typically suffer from dephasing and spin flips due to their interactions with proximal spins which form a spin bath. Therefore, a high purity of the diamond hosting the NV centre is important. High conversion efficiency avoids the creation of dark nitrogen spins, which contribute to the noise environment and, hence, is advantageous.

Nanodiamonds can be fabricated in different manners which strongly affect the properties of the NV centre hosted in the crystal. Nanosized diamond crystals can be fabricated, i.e. milled, from bulk diamond synthesised in a high pressure high temperature environment (HPHT) or by chemical vapour deposition (CVD). They can also be directly created by detonation. Milling nanodiamonds from bulk diamond guarantees better control over the properties and density of hosted NV centres but induces additional strain through the forces acting on the crystal during the mechanical process [192].

Detonation nanodiamonds are created by igniting mixed explosives with a negative oxygen balance. After the detonation, crystals condense on the walls of the formed the detonation chamber from which they can be collected [68]. The crystal size distribution peaks typically in the single digit nanometre range. The peak can be shifted to up to 14 nm by selectively removing nanodiamonds by oxidation in air [148]. NV centres have been detected in detonation crystals of only 5 nm diameter [21]. Due to the nature of the creation process, which introduces a large number of defects and impurities, detonation diamonds exhibit short coherence times [110] and show blinking and photo bleaching [21, 169]. In NV centres in bulk diamond close to the surface, the Fermi level has been successfully controlled to change the charge state of the NV centres proximal to the surface to NV^- [66]. Most research and this thesis focus on the NV^- charge state which is optically addressable. Charge state conversion leads to blinking and short spin coherence times as the NV^0 is a spin $S = 1/2$ and

the NV^- is a spin $S = 1$ system. However, the band bending technique discussed by Grotz et al. [66] cannot be applied to stabilise NV centres in nanodiamond because it requires the patterning of electrodes on the diamond surface. Other band bending techniques such as surface termination have proven to significantly improve coherence times for NV centres in bulk diamond but have not been extensively studied for nanodiamond, yet [121]. In Chapter 4 we discuss the surface chemistry of nanodiamond in more detail.

HPHT and CVD diamond growth techniques have been well developed and, thus, pure diamonds with specific nitrogen contents are commercially available. HPHT mimics the natural conditions under which diamonds form, i.e. temperatures up to 2600 °C and pressures up to 6 GPa, and allows incorporation of nitrogen atoms at concentrations ranging from 20 to 200 ppm [95]. CVD directly synthesises diamond from a hydrocarbon gas mixture. By selecting the carbon isotope and controlling the nitrogen concentration in the gas mixture, isotopically pure diamond can be fabricated [11] and the impurity concentration can be very well controlled allowing nitrogen concentrations from 0.05 to 10 ppm [95].

The NV centre density depends on the nitrogen content and the number of vacant sites. Annealing increases the conversion efficiency of nitrogen defects to NV centres as increased temperature facilitates diffusion of vacant sites through the carbon lattice [36]. A combination of irradiation with electrons and annealing yields NV centre concentrations of up to 16 ppm [1]. For bulk diamond a number of methods have been developed to place NV centres locally [131] and control the direction of their axis [116, 132]. Since there are no means yet by which the orientation and shape of nanodiamonds could be controlled, these methods do not apply to them but are important to understand the methods' shortcomings. Therefore, they are presented in the following paragraph.

A technique called delta doping allows the growth of layers of nitrogen enriched diamond by CVD with a FWHM ≈ 7.5 nm which is limited by the diffusion of nitrogen atoms and the measurement technique to obtain the nitrogen profile [26]. In addition, the NV centre axis can be aligned along a preferential direction during growth [116, 132]. Lateral confinement of NV centres can be reached through selective creation of vacancies by irradiation of a delta doped diamond with electrons with sub-micron precision [131]. Confinement in all

three dimensions is obtained by irradiating with nitrogen ions, or carbon atoms [147], or electrons through patterned masks [175]. Proximity to the surface of down to 10 nm is simply achieved by etching down a diamond crystal with a layer of NV centres. However, irradiation is incompatible with the fabrication of preferentially aligned NV centres.

The main advantage of NV centres in nanodiamond is their size and potentially their large surface area. In terms of coherence and lifetimes NV centres in bulk remain uncontested by NV centres in nanodiamond until now. The nanodiamonds used in this thesis have an average diameter of 17.8 nm as shown in Section 3.3. This diameter has proven to work well with biological cells as they are small enough to be ingested but too big to be discharged [208]. The nanocrystals are milled from HPHT diamond with a nominal impurity concentration of 50 ppm. This nitrogen concentration categorises the diamond between type Ib and type IIa. No electron irradiation or other treatment has been applied. The size and nitrogen content lead to approximately one NV centre in 100 nanodiamonds. On the one hand this allows to identify single nanodiamonds with an NV centre with atomic force microscopy and on the other hand on the small number of impurities enables coherence times of up to 60 µs as observed by Knowles et al. [101]. This is a large improvement from previous work where coherence times of 1.4 to 10.9 µs were demonstrated [192, 110, 139].

3.3 NANODIAMOND SAMPLE PREPARATION

We use quartz slides (CFQ-1050, UQG Optics) with dispersed nanodiamonds on its surface. The quartz slides are 0.5 mm thick and should not be chosen thinner to avoid reflections from its back surface. Some samples were also patterned with grid markers which can serve as points of orientation to locate NV centres and return to emitters. One example is displayed in Figure 3.3. We deposit them by evaporating gold through a silicon hard mask. The marker features are on the micrometre scale which provides sufficient resolution to locate different emitters and allows avoiding lithography. Direct evaporation minimises residues of fluorescent resist which can cause additional noise into the photon count signal.

Before the deposition of nanodiamonds, the quartz slides are sonicated in deionised water, acetone and finally isopropanol for 20 minutes each.

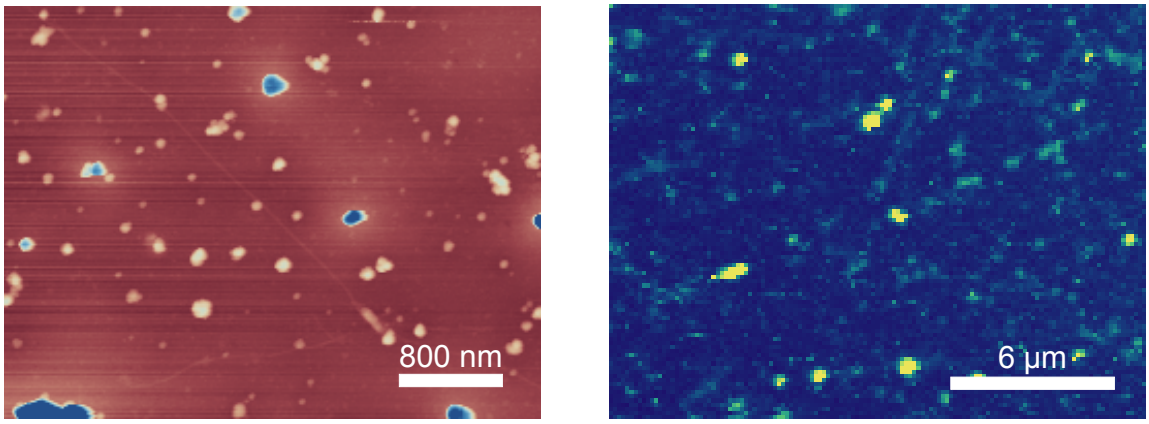

(a) AFM image

(b) Fluorescent scan

Fig. 3.1 **AFM scan and fluorescence of sample surface**. (a) AFM scan of nanodiamonds and carbon nanotubes. The size of the nanodiamonds can only be determined from their height as the lateral components of the scan are broadened because the image is a convolution of the crystal shapes with the AFM tip. (b) NV centres fluorescing under green excitation. Note the vastly different scale bars indicating that not every nanocrystal contains a NV centre

Two methods for nanodiamond deposition were used. First, the nanodiamond powder is mixed into ethanol in a ratio of 10 mg to 25 ml and sonicated for at least 1 hour to prevent clusters of diamond forming. This suspension is diluted with ethanol to obtain the right concentration of nanodiamonds for deposition. One method of deposition is to first coat the surface of the sample substrate with a single molecular layer of Polydiallyldimethylammonium chloride (PDDA). This molecule binds to the dangling bonds at the nanodiamond surface. After the surface is coated with the polymer the nanodiamond-ethanol suspension is dropcast on the sample which is rinsed after 1 min with deionised water for 1 min. Another method of depositing the nanodiamond-ethanol suspension is to use an electric mesh nebuliser, which is typically sold to asthma patients for inhalation of drugs. While no difference in background fluorescence was observed between the two methods, the second one is easier to carry out.

Some samples were characterised with an Atomic Force Microscope (AFM) and subsequently examined under a confocal microscope as described in Section 2.2. Such images can then be overlaid to identify the nanodiamonds containing NV centres. Comparing the two images, it becomes apparent that most nanodiamonds do not contain any NV centres. In fact, only around 1 in 100 diamonds hosts one or more fluorescent defects.

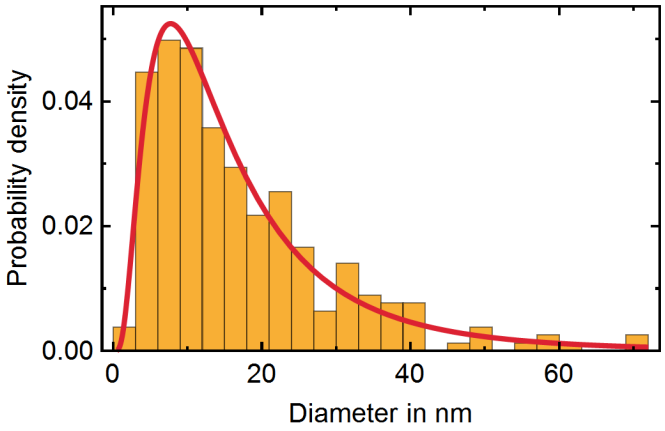

Fig. 3.2 **Histogram of nanodiamond diameters**. The red line was obtained by fitting to the cumulative distribution of a log-normal distribution. The found parameters are 17.8 nm for the mean and 15.3 nm for the standard deviation.

In order to identify single NV centres optically, they have to be separated by $0.4\lambda/0.9$ as discussed in Section 2.2. Thus, the concentration of nanodiamonds in the deposited suspension has to be carefully chosen. Any density of nanodiamonds and NV centres can be reproduced with the presented methods, making it easy to determine the right concentration for optical spectroscopy and AFM imaging.

From the AFM images a distribution for the diameters of the nanodiamonds can be obtained by extracting the height of each nanodiamond. Care was taken to not include clusters of nanodiamonds or foreign particles on the sample which could both skew the result. This distribution, shown in Figure 3.2, is a log-normal distribution with a mean of 17.8 nm and a standard deviation of 15.3 nm. Log-normal distributions of a variable X for example arise in situations where X subsequently grows by a fraction of its size and the growth rate Y follows a normal distribution, i.e. $X = \exp(Y)$. The distribution arises if multiplicative effects

are added as opposed to additive effects which lead to a normal distribution. Therefore, many particle size distributions follow the log-normal distribution. The distribution of the used nanodiamonds is not an exception. The histogram in Figure 3.2 was compiled from the measured height of 261 nanodiamonds.

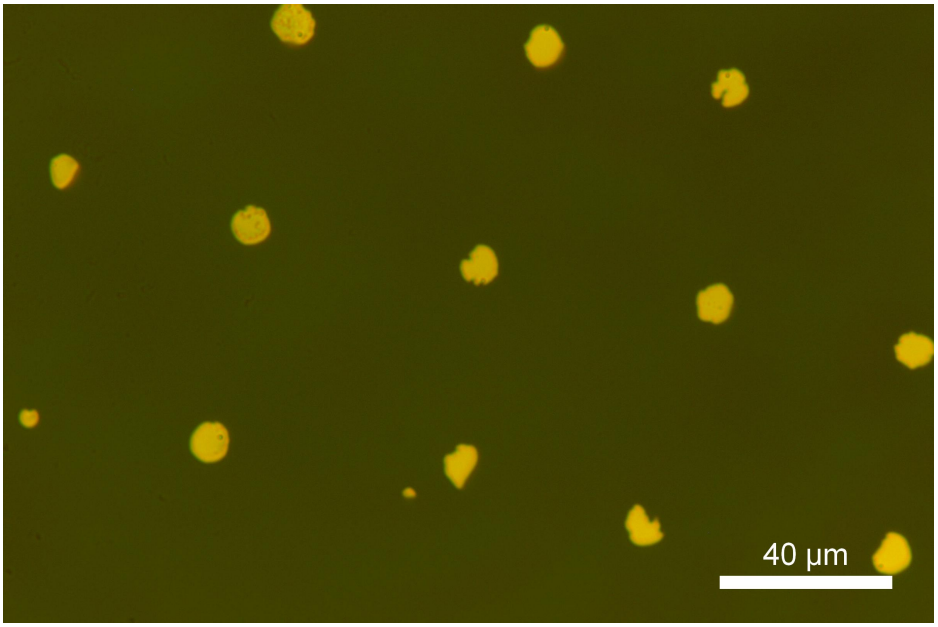

Fig. 3.3 **Grid markers on sample**. The markers create reference points on the sample and, therefore, coordinates can be associated with emitters. Hence, NV centres can be located on the surface and we can also return to them after switching samples or having explored other areas of the same sample.

3.4 DC MAGNETIC AND ELECTRIC FIELD SENSING

A DC magnetic field causes Zeeman splitting of the NV spin states, i.e. the energy levels of the spin $m_s = \pm 1$ states are shifted by $\Delta = \pm\gamma_S/(2\pi)B_{\text{ext,z}}$, where $\gamma_S/(2\pi) = 2.8034\,\text{MHz/G}$ is the gyromagnetic ratio of the electron spin and $B_{\text{ext,z}}$ is the external magnetic field along the axis of the NV centre.

Electric fields also affect the frequency of the $|m_s = 0\rangle \leftrightarrow |m_s = \pm 1\rangle$ transition. The external magnetic field perpendicular to the NV axis changes the non-linear effect of the

external electric field perpendicular to the NV axis [42]. Generally, an electric field can be seen as a perturbation of the ZFS D_{gs}, and in the case of no perpendicular components of the magnetic or electric field, the energy difference is $d_{gs}^{\parallel}\mathrm{E}_z$, where $d_{gs}^{\parallel} \approx 0.35\,\mathrm{Hzcm/V}$ is the electric dipole strength along the z-axis [199].

Strain in the diamond crystal has a similar effect on the spin states as electric field. Strain displaces the atoms. As this displacement creates an internal electric field, the shape of the NV centre orbitals changes. Therefore, strain is a more complex subject than an external electric field. Temperature modifies the atom positions in the entire crystal and affect the NV energy level structure similarly to strain. In this Section we focus on sensing DC magnetic fields before shifting to thermometry in Section 3.5.

The simplest way to determine the frequency of the $|m_s = 0\rangle \leftrightarrow |m_s = \pm 1\rangle$ transitions is continuous wave ODMR as described in Section 2.5.1. The frequency of the ODMR dip is best monitored by tuning the microwave frequency to the point of the steepest slope where the photon count rate from the emitter is most sensitive to changes in shifts of the resonance. Consequently, the resolution is limited by the linewidth and the smallest measurable frequency shift is given by

$$\Delta\nu_{\mathrm{min}} = \frac{\Gamma}{\sqrt{CT}\eta}. \tag{3.2}$$

Here, Γ is the full width at half maximum amplitude (FWHM) of the transition, C is the photon count rate, T is the acquisition time and η is the fraction changed in the count rates on and off resonance, i.e. the contrast of the resonance. By tuning the microwave and optical excitation power, the parameters can be adjusted to find the optimum. The natural linewidth Γ_n, which is equal to $1/T_2^*$ and thus is between 0.5-2 MHz in the used nanodiamonds, is broadened by both the microwave and the optical pumping of which typically the former dominates. Then, the linewidth $\Gamma = \sqrt{\Gamma_n^2 + \Omega^2}$ is limited by the Rabi frequency Ω. The higher the optical power in continuous wave ODMR, the higher the microwave power needs to be in order to achieve the same contrast η. Typical values for the parameters in Equation 3.2 are $C = 60\,\mathrm{kHz}$, $\eta = 20\,\%$ and $\Gamma = 10\,\mathrm{MHz}$. This yields a sensitivity of $\Delta\nu_{\mathrm{min}}/\gamma_S = 7\,\mu\mathrm{T}/\sqrt{\mathrm{Hz}}$, where $\gamma_S/(2\pi) = 2.8025\,\mathrm{MHz/G}$ is the gyromagnetic ratio of an electron.

If we want to avoid power broadening completely, we need to resort to interferometry. Microwave pulses correspond to beam splitters used in an optical interferometer. In most cases, only two of the three ground state electron spin levels are used. The spin state is brought into a superposition of the two selected states which, subsequently, acquires a phase while the NV centre interacts with its environment. The phase allows us to directly deduce the magnitude of the magnetic field along the NV centre axis. The time for which the phases can be acquired is limited by the coherence time of the spin state.

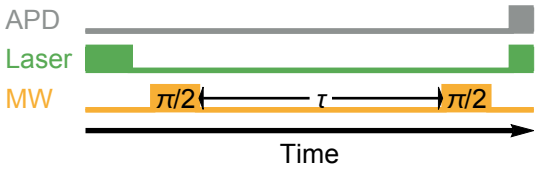

Fig. 3.4 **Pulse sequence for Ramsey interferometry**. It consists of two (off-resonant) microwave $\pi/2$-pulses whose temporal separation τ is scanned.

The most basic implementation of the interferometry measurement is a Ramsey experiment; see sequence displayed in Figure 3.4. First, the NV centre is prepared into the $|0\rangle$ state by an off-resonant green laser pulse. Then, a $\pi/2$-pulse along σ_y at the $|0\rangle \leftrightarrow |+1\rangle$ transition is applied to create the superposition state

$$\frac{1}{\sqrt{2}}(|0\rangle + |+1\rangle). \tag{3.3}$$

Choosing the transition $|0\rangle \leftrightarrow |-1\rangle$ or σ_x yields the same final result at the end. The $|+1\rangle$ state acquires a phase during the time τ in a DC magnetic field with magnitude B, leading to the state

$$\frac{1}{\sqrt{2}}\left(|0\rangle + e^{i\theta\tau}|+1\rangle\right), \tag{3.4}$$

where

$$\theta = \frac{\mu B}{\hbar}. \tag{3.5}$$

Here, the global phase due to the ZFS D_{gs} is discarded. We can readout the phase $\theta\tau$ by applying another $\pi/2$-pulse which maps the phase to a population difference. After the

second $\pi/2$-pulse the state is

$$\Psi_f = \frac{1}{\sqrt{2}}\left[\left(1+e^{i\theta\tau}\right)|0\rangle + \left(1-e^{i\theta\tau}\right)|+1\rangle\right]. \tag{3.6}$$

The final readout, i.e. converting population to photon counts, is done with a non-resonant laser pulse. The photon counts are proportional to the population in $|0\rangle$. The probability $P_{|0\rangle}(\tau)$ of the NV centre being in state $|0\rangle$. It is given by

$$\begin{aligned} P_{|0\rangle}(\tau) &= \left|\langle 0|\Psi_f\rangle\right|^2 && (3.7)\\ &= \left|\frac{1}{2}\langle 0|0\rangle\left(1+e^{i\theta\tau}\right)\right|^2 && (3.8)\\ &= \frac{1}{2}\left(1+e^{i\theta\tau}\right)\left(1+e^{-i\theta\tau}\right) && (3.9)\\ &= \frac{1}{2}\left(1+\cos(\theta\tau)\right). && (3.10) \end{aligned}$$

By varying τ and repeating the sequence multiple times an interference pattern can be obtained from the resulting counts. The Ramsey sequence is sensitive to magnetic fields from all frequencies but the effect of AC fields is eventually averaged out as a different phase is acquired every single time the sequence is run leading to a diminished T_2^*. Therefore, the Ramsey experiment is used to detect DC magnetic fields.

The achieved sensitivity is limited by T_2^*, i.e. as before the ultimate limit is the natural linewidth Γ_n. In order to achieve maximum sensitivity, one should measure the signal S at the steepest slope of the Ramsey signal, i.e. where $\frac{\mathrm{d}}{\mathrm{d}\tau}P_{|0\rangle}(\tau)$ is maximal. The signal S can be derived from the probability of being in the $m_s = 0$ state after the Ramsey sequence. S is proportional to its maximal slope which is

$$\begin{aligned} \max\left|\frac{\mathrm{d}}{\mathrm{d}\tau}P_{|0\rangle}(\tau)\right| &= \left|\frac{\mathrm{d}}{\mathrm{d}\tau}P_{|0\rangle}(\tau)\right|\Bigg|_{\tau=\tau_{\max}} && (3.11)\\ &\propto \sin(\theta\tau)\Big|_{\tau=\tau_{\max}} && (3.12)\\ &\approx \theta\tau_{\max}. && (3.13) \end{aligned}$$

For simplicity, we drop the index in the following for τ so that $\tau \equiv \tau_{\max}$. The difference in counts is the actual signal

$$S = C\theta\tau = C\frac{g\mu_B B}{\hbar}\tau \tag{3.14}$$

with C being a parameter specific to an experimental setup.

$$C = \frac{1}{\sqrt{1+1/\sigma^2}} \tag{3.15}$$

with limits

$$\lim_{\sigma\to\infty} C = 1, \tag{3.16}$$

$$\lim_{\sigma\to 0} C = 0, \tag{3.17}$$

where σ is the signal-to-noise ratio for one single measurement. It is given by

$$\sigma = \frac{n_0 - n_{+1}}{\sqrt{(n_0+n_{+1})/2}} \tag{3.18}$$

as the signal is proportional to the difference in counts $n_0 - n_{+1}$ from the spin states $|0\rangle$ and $|+1\rangle$ limited by shot noise. $n_i = t_d\gamma_i\eta$ for $i \in \{0,+1\}$ with the detection window $t_d = 500\,\text{ns}$, the decay rate $\gamma_0 = 1/23\,\text{ns} = 43\,\text{MHz}$ and $\gamma_{\pm1} = 0.6/23\,\text{ns} = 26\,\text{MHz}$ and a detection efficiency η approximately $0.5\,\%$. These parameters yield $C \approx 0.07$.

From Equation 3.14 follows that the smallest detectable magnetic field difference for one single measurement is

$$\Delta B_{\text{min,single}} = \frac{\hbar}{Cg\mu_B}\frac{1}{\tau}. \tag{3.19}$$

For N measurements, the shot noise limits $\Delta B_{\min}$ to

$$\Delta B_{\text{min,N}} = \frac{\sqrt{N}}{N}\frac{\hbar}{Cg\mu_B}\frac{1}{\tau}, \tag{3.20}$$

where $N = T_M/\tau$ and T_M is the total measurement time while τ is the time it takes to conduct a single measurement, i.e. we make the implicit assumption that the time needed for

initialisation, the microwave pulses and readout is negligible compared to the precession time τ. This is certainly true for measurements in bulk diamond where $T_2^* \gg 2\,\mu s$. The resulting sensitivity is

$$\Delta B_{\min} = \frac{\hbar}{Cg\mu_B}\sqrt{\frac{1}{T_M \tau}}. \tag{3.21}$$

We now take into account that the coherence time of the NV centre spin state is not infinite, i.e. there is an optimal value for $\tau \leq T_M$ because the signal decays exponentially as

$$S(\tau) \propto \exp\left(-\frac{\tau}{T_2^*}\right), \tag{3.22}$$

where T_2^* is the phase coherence of the NV spin. Maximising the sensitivity yields $\tau = T_2^*$ and therefore

$$\Delta B_{\min} = \frac{\hbar}{Cg\mu_B}\sqrt{\frac{1}{T_M T_2^*}}. \tag{3.23}$$

The sensitivity, that is normally quoted, is

$$\eta_{se,\text{Ramsey}} = \frac{\hbar}{Cg\mu_B}\sqrt{\frac{1}{T_2^*}} \tag{3.24}$$

which has units of $\text{T}\,\text{Hz}^{-1/2}$.

The highest sensitivity value for DC magnetometry with NV centres in nanodiamond (17 µm mean diameter) up to date is $600\,\text{nT}\,\text{Hz}^{-1/2}$ [101]. We use nanodiamonds from the same batch.

3.5 THERMOMETRY

This Section demonstrates that results obtained in bulk diamond regarding the temperature dependence of NV centres can be reproduced with NV centres in nanodiamond. First, the application of NV centres for thermometry is motivated. Second, achieved sensitivities are reviewed. And third, measurements are analysed to determine the temperature dependence of NV centres in nanodiamond in the range of 20 to 100 °C.

Applications of NV centres for temperature sensing

The NV centre is particularly interesting temperature sensor because its atomic size enables local probes. An additional advantage of NV centres is that many of them can simultaneously be readout optically to measure a large area which enables taking time resolved videos of temperature. The very wide range of temperature 0 to 700 K favours NV centres for thermometry over other methods [195, 157].

Diamond has the highest heat conductivity known which, however, depends critically on the impurity concentration [179]. In Ib HPHT diamond, similar to the nanodiamond used in this work, a value of $16\,\mathrm{W\,cm^{-1}\,K^{-1}}$ [211] was measured. Therefore, bulk diamond affects the measured temperature by acting as a heat sink, i.e. diverting heat from the source. Hence, the defects have to be either close to the surface in order to serve as a local probe or nanodiamonds must be used. But the high heat conductivity leading to an equal temperature in the entire crystal also enables the use of NV centre ensemble measurements. This is a way to increase sensitivity [107].

For biological or chemical purposes their non-toxicity, high tolerance and low reactivity is a plus. Applications include but are not limited to temperature sensing in cells enabling potential cancer therapies [107] or large range nanoscale thermometry, e.g. for the development of complex electronic circuits.

Reported temperature sensitivity

The gradient of the zero-field splitting (ZFS) D_{gs} changes with temperature as the orbitals and environment of the NV centre change under the deformation of the diamond lattice. Its absolute value and its change give information about the local temperature at the site of the NV centre.

Measuring temperatures from 0 to 700 K with NV centres has proven to be feasible [157]. The sensitivity is not only dependent on the coherence time of the spin but also on the gradient of the ZFS ΔD_{gs} and the NV centre fluorescence intensity. While, as a general rule, with increasing temperature the coherence time and the intensity decrease due to

phonon coupling, ΔD_{gs} increases. The T_2 dependence on temperature strongly depends on the impurity concentration within the diamond as it typically dominates the decoherence process even at high temperatures. The loss of intensity is very significant. For example, the intensity at 623 K is 2.5 times lower than at 373 K. This effect can be attributed to an increased non-radiative rate [157]. The temperature dependence of D_{gs} has been studied extensively at a wide range of temperatures in bulk diamond and is $80\,\mathrm{kHz/K}$ at room temperature [142, 195, 2, 29].

The highest sensitivity for temperature with a single NV centre is $5\,\mathrm{mK\,Hz^{-1/2}}$ and was achieved by Neumann et al. [142]. Neumann et al. [142] also found a sensitivity of $130\,\mathrm{mK\,Hz^{-1/2}}$ with a noise floor of 1 mK for a single NV centre in a 50 nm sized nanodiamond. Using an ensemble consisting of 500 defects in a 100 nm diameter nanodiamond, a sensitivity of $9\,\mathrm{mK\,Hz^{-1/2}}$ and 1.8 mK in absolute terms was reached [107].

The vast improvements by Toyli et al. [196] and Kucsko et al. [107] over simple ODMR measurements to determine D_{gs} are due to filtering a number of noise sources. In particular, the filtered errors include fluctuations in external magnetic field, changes in fluorescence intensity, errors in Rabi frequency and electron spin resonance contrast.

Temperature dependence of zero-field splitting for NV centres in nanodiamond

In order to measure the temperature dependence for NV centres in nanodiamond, we record ODMR lineshapes at different temperature points from which we extract the ZFS. The technical details of the experiment can be found in Appendix A. To our knowledge, this is the first characterisation of temperature dependence in nanodiamond. It confirms the current understanding that no differences between bulk and nanodiamond occur. Figure 3.5 shows the ODMR measurements and compares the change in the measured ZFS to data by Toyli et al. [195].

From the gradient of the ZFS D_{gs} at 20 °C and our DC magnetic field sensitivity using ODMR measurements, the sensitivity for temperature is $2.5\,\mathrm{K\,Hz^{-1/2}}$. Given total integration times of many minutes, this is many magnitudes better than the stability of the temperature.

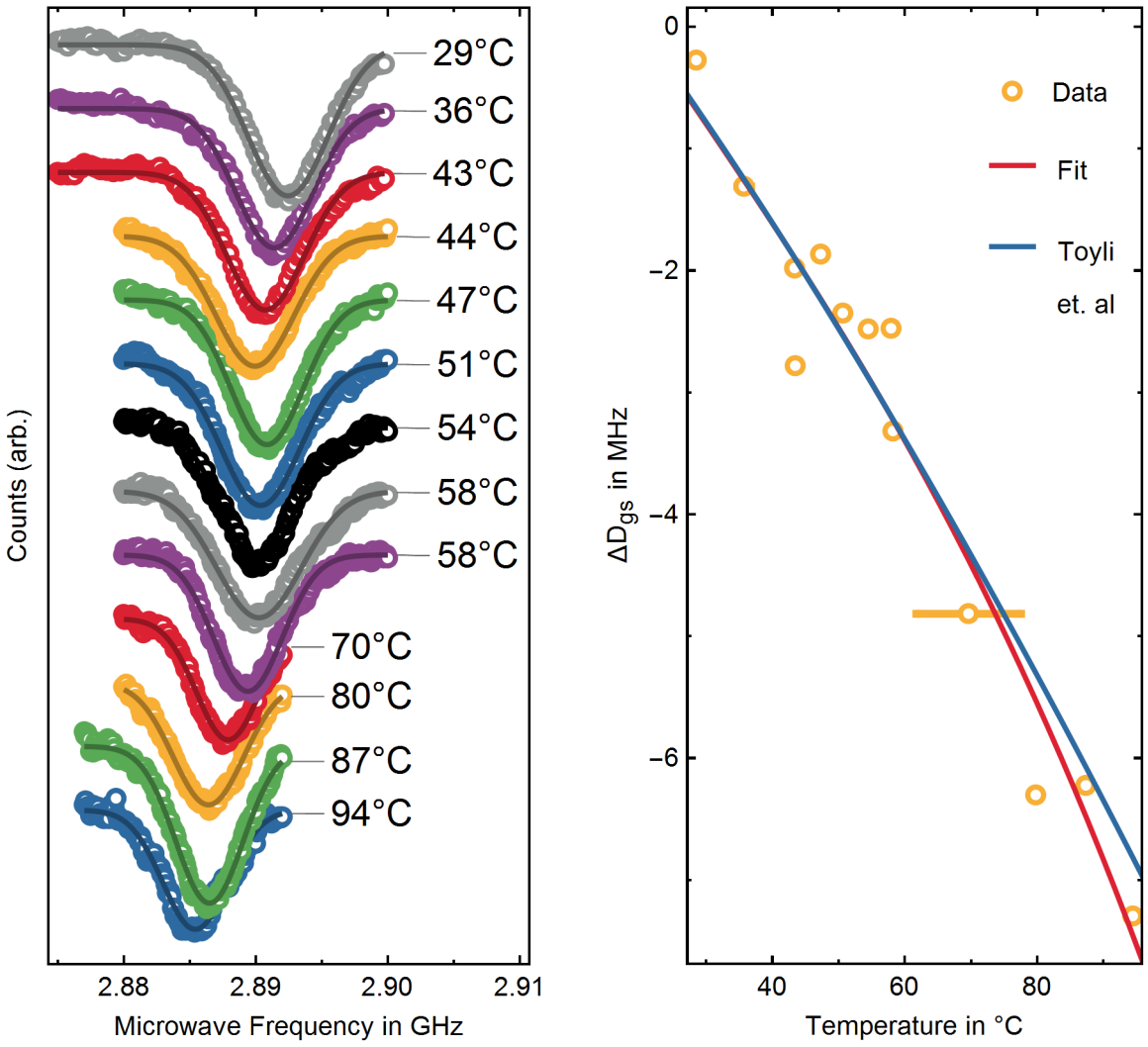

(a) ODMRs at different temperature

(b) Temperature dependence of D_{gs}

Fig. 3.5 **Temperature dependence of the ground state ZFS** D_{gs}. (a) ODMR measurements at different temperature along with fits to their Gaussian lineshapes. (b) the shift in ODMR resonance compared to 20 °C is plotted against temperature. The obtained fit is compared against the results from Toyli et al. [195] who carried out experiments in bulk diamond.

By using pulse sequences which are designed to measure solely ΔD_{gs}, the practical sensitivity should be by at least one order of magnitude below this value [107, 196]. In addition, employing ensembles of NV centres can boost the sensitivity.

3.6 AC MAGNETIC FIELD SENSING

AC magnetic field sensing always requires an interferometric approach as monitoring the ODMR experiment yields only information about the amplitude of an external field and none about its the frequency.

Through slight modifications of the Ramsey sequence, the filter function effectively applied by the interferometer on the magnetic field environment can be changed and the sequence of microwave pulses leads to a measurement highly sensitive to a specific set of frequencies. Filtering noise from the environment is often also called dynamical decoupling.

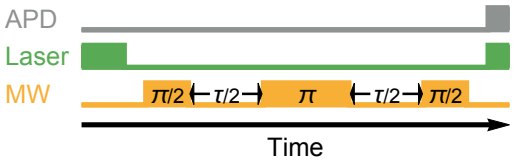

Fig. 3.6 **Hahn echo pulse sequence**. The pulse sequence is made of just three microwave pulses. The two $\pi/2$-pulses form the interferometer and the π-pulse in the middle filters noise at low frequencies. The temporal separation $\tau/2$ between the pulses is scanned to change the sensitivity of the sequence to different frequencies. Figure 3.7 shows the effect of all applied pulses on the Bloch sphere if the external magnetic field is constant.

The Hahn echo (also often called spin echo) sequence is the most basic among a large family of sequences which can be used to decouple from noise and detect magnetic AC fields for NMR measurements. The spin echo sequence is obtained from the Ramsey sequence by adding a π-pulse between the two $\pi/2$-pulses as shown in Figure 3.6. After acquisition of a phase for $\tau/2$ the state is

$$\frac{1}{\sqrt{2}}\left(|0\rangle + e^{i\theta\tau/2}|+1\rangle\right). \tag{3.25}$$

After applying the π-pulse and deducting a global phase, it becomes

$$\frac{1}{\sqrt{2}}\left(|0\rangle - e^{-i\theta\tau/2}|+1\rangle\right). \tag{3.26}$$

And after the remaining precession time $\tau/2$ has passed, the acquired phases are cancelled, i.e. the state is

$$\frac{1}{\sqrt{2}}\left(|0\rangle - |+1\rangle\right). \tag{3.27}$$

As the final state is the same as the state to start with regardless of the DC external magnetic field, the sequence perfectly filters for DC noise. The states and the gates applied at every step of the sequence are illustrated by Bloch spheres in Figure 3.7.

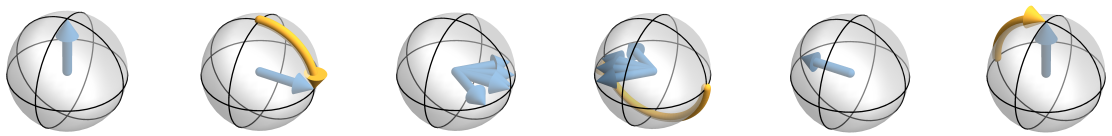

(a) Initialise (b) To equator (c) Wait $\tau/2$ (d) Flip (e) Wait $\tau/2$ (f) Project

Fig. 3.7 **Bloch spheres for different times during the Hahn echo sequence**. The Bloch arrows are calculated under the assumption that the external magnetic field is constant. (a) the state after initialisation by the green laser into $m_s = 0$. (b) a $\pi/2$ microwave pulse creates a superposition state whose phase is sensitive to magnetic fields. (c) the acquisition of a phase $\phi_1 = \psi$ and dephasing during $\tau/2$ indicated by state vectors with different phases. (d) a π-pulse is applied to the spin state. (e) assuming the external field, which causes the acquisition of the phase, is constant for time τ, the state acquires the phase $\phi_2 = -\psi$ after time $\tau/2$. The two acquired phases ϕ_1 and ϕ_2 exactly cancel. (f) When we now project the spin back on the z-axis with another $\pi/2$-pulse, all population is in spin state $m_s = 0$.

However, if the magnetic field is reversed during the π-pulse, then the acquired phases add up and the final state is

$$\frac{1}{\sqrt{2}}\left(|0\rangle - e^{-i\theta\tau}|+1\rangle\right), \tag{3.28}$$

i.e. the number of photons when reading out the spin state is reduced as $\theta \neq 0$. This is the case if the magnetic field alternates with a period of $(2n+1)\tau$ or $\tau = (2n+1)/\nu$ matches the frequency ν of the external field. For $\tau = 2n/\nu$ the spin echo signal revives completely, leading to an oscillating signal. Fourier transforming it yields the frequency spectrum of the magnetic field noise.

To estimate the sensitivity for a spin echo sequence, the sensitivity of the Ramsey measurement in Equation 3.24 needs to be multiplied by a factor $\pi/2$ [188] and the inhomogeneous coherence time T_2^* can be replaced by the far longer homogeneous coherence time T_2.

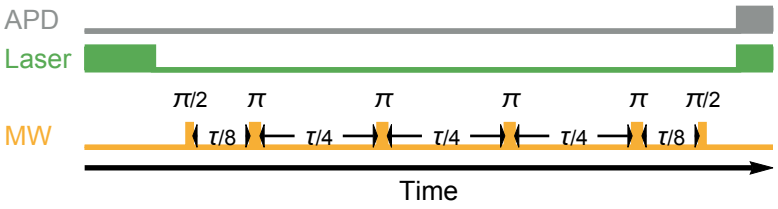

Fig. 3.8 **Carr-Purcell pulse sequence**. This sequence is similar to the spin-echo sequence but n π-pulses separated by a precession time of τ/n are applied instead of one. Here, $n = 4$ is shown.

The spin echo sequence is a rather poor filter as its bandwidth remains very limited primarily because noise is not suppressed on timescales shorter than $\tau/2$. Another problem is that the spin echo is sensitive to imperfect π-pulses. Pulse errors comprise errors in timing and pulse shape. Therefore, better sequences have been developed with more pulses which also protect against pulse errors and allow longer interrogation times as they more effectively decouple the NV centre from all other noise sources. This allows the detection of weaker magnetic fields but also fields oscillating at lower frequency. This is important as for typical pulse lengths of 20-100 ns the coherence time should be at least on the order of a couple of microseconds. The Carr-Purcell, UDD and CPMG-XY8 sequence have received most attention. The Carr-Purcell sequence is the straight forward extension of the Hahn echo sequence as n π-pulses spaced by the precession time τ/n are inserted between the two interferometry $\pi/2$-pulses as displayed in Figure 3.8. The UDD sequences is similar but only equidistant pulses are used, i.e. the precession time between the first and the second and the last and the pulse before the last is equal to the precession time between the π-pulses. Therefore, the spacing must be $\tau/(n+1)$. The family of CPMG sequences is an extension of the Carr-Purcell sequence which uses pulses around the two axes σ_x and σ_y. Rotations around two axes protect against errors in the pulses which are in practice not ideally square and have non-zero length. Timing and shape errors lead to imperfect π-rotations and non-

equal precession times while non-zero-length pulses cause additional dephasing during their application.

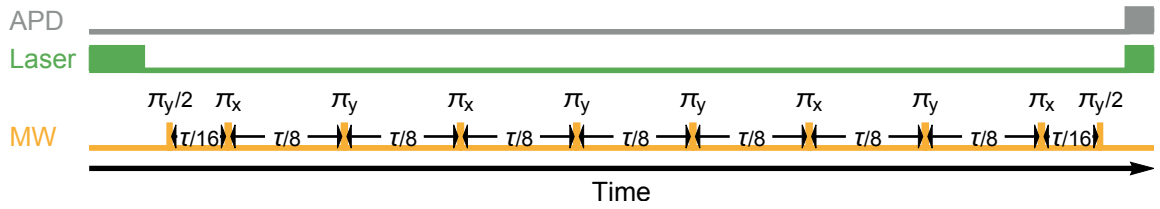

Fig. 3.9 **CPMG sequence**. The CPMG measurement uses π-pulses of different phases. The difference between the phases of π_x- and π_y-pulses is 90°. Here, the XY8 sequence is shown for $n = 1$, i.e. the XY8 sequence is only repeated once.

Wang et al. [205] and Biercuk et al. [18] find that for NV centres the CPMG-XY8 sequence shown in Figure 3.9 generally decouple from the noise environment best. The "8" stands for the number of π-pulses before the sequence is repeated n times, i.e. for $n = 2$ 16 π-pulses are necessary. Versions for XY4, XY16, XY32, etc. exist. This is because the equivalent filter function has the highest bandwidth to filter noise from the electron spin bath which is often the strongest source of decoherence. In addition, the different phases of subsequent π-pulses effectively protect against pulse errors. The XY4 sequence has shown inferior protection against pulse errors but no improvement was observed in case of the XY16 or higher order sequences. In nanodiamond the highest value for sensitivity for AC magnetometry with NV centres in nanodiamond is $140\,\mathrm{nT\,Hz^{-1/2}}$ [101] and in bulk values of up to $4.3\,\mathrm{nT\,Hz^{-1/2}}$ [11]. The sensitivities were achieved using an XY8 sequence. We use the same nanodiamond as Knowles et al. [101].

Apart from sensitivity resolution of the frequency is of importance. Resolution is limited directly by the total length of the interferometer τ and cannot be increased by averaging. Both can be enhanced by employing nuclear spins proximal to the NV centre. Nuclear spins can either be directly used to probe noise as their coherence times are longer or their spin state serves as a memory to store the electron spin phase; thus increasing the length of the interferometer to the lifetime of the nuclear spin. In particular, the nuclear host spin which is inherent to the NV centre is of interest. This is the topic of Chapter 6.

CHAPTER 4

Surface oxidation by annealing

The NV centre in nanosized crystals is by definition close to the nanodiamond surface which is covered by a graphite layer due to the manufacturing process [135]. However, spins close to dangling bonds and charge traps cause fast decoherence of the NV centre electron spin [96, 170, 137, 168, 149] and a reduction in lifetime [189] as they provide a electro-magnetic field environment with a short correlation time. In addition, surface charge traps lead to rapid charge state conversion of the NV centre whose rate increases under laser illumination as photons provide extra energy for ionisation [169, 55].

By removing the graphitic material and subsequent oxidation of the surface the electric and magnetic field noise can be significantly reduced as has been shown with shallow emitters in bulk diamond whose surface has undergone appropriate treatment [145]. The coherence time of defects 5 nm away from the surface was improved from single digit microseconds to more than $T_2 > 100\,\mu s$ and even more important, as the nature of the spin bath changes, decoupling techniques can be applied more effectively to further enhance T_2 [21, 149, 146, 168]. This improvement has enabled landmark experiments such as the detection of different species of nuclei in a single protein on the surface of diamond [121]. In addition, the accessible carbonyl groups can be functionalised for purposes such as a wide range of medical applications [135]. Nanodiamonds have shown no toxicity in a mouse model [212] which makes them an excellent candidate for medical applications [135].

An important step in improving coherence times of NV centres close to the surface in bulk diamond is acid cleaning and annealing [146, 121]. However, these methods have not yet been applied to nanodiamonds hosting NV centres. We will focus here on annealing because single nanodiamonds can be tracked throughout the process. By annealing, we can selectively burn graphite which combusts at lower temperatures than diamond. Further, annealing can be used to increase the yield of NV centres [36, 1].

In this Chapter we study the effect of annealing on NV centres in nanodiamonds and provide evidence for oxidation of the surface and reduction of electro-magnetic noise stemming from the surface. This enables enhanced sensitivity of the hosted NV centres and functionalisation of the nanodiamonds, i.e. attachment of foreign chemical groups to the surface.

In Section 4.1 we present the sample preparation and the characterisation measurements. We then determine the optimal annealing temperature in Section 4.2 and confirm successful oxidation. Finally, in Section 4.3 we show the effect of the surface treatment on the coherence time, the lifetime, the crystal size, the lattice strain and the charge state of twelve randomly selected single NV centres.

4.1 SAMPLE TREATMENT AND MEASUREMENT PROTOCOL

The sample is prepared by depositing gold markers on a cleaned quartz cover slip with a hard mask and nanodiamonds as discussed in Section 3.2. We use an external loop antenna which transmits microwaves for Rabi nutations and ODMR. This ensures maximum cleanness.

After deposition of the nanocrystals we search for nanodiamonds hosting NV centres on the surface. No particular pre-selection of NV centres was carried out apart from restricting the search to single photon emitters with "good" saturation curves as discussed in Section 2.4.2, i.e. the emitters show saturation and exhibiting stable count rates. In addition, we exclude all emitters which do not display an ODMR signal. Hence, the measurements can be expected to be representative for randomly selected NV centres in the negatively charged state. We characterise the following properties:

- Half saturation power and maximum photon counts,
- Strain splitting (by acquiring an ODMR curve without magnetic field),
- Lifetime T_1 with and without external magnetic $\approx 100\,\mathrm{G}$ field aligned with the NV axis to selectively suppress electric noise,
- Coherence time T_2 (by using a Hahn-echo sequence) with and without magnetic $\approx 100\,\mathrm{G}$ field along the NV axis to selectively suppress electric noise,
- Fraction of time spent in the NV^0 charge state by analysing optical spectra,
- Nanodiamond size (by extracting the particle height from an AFM image which is correlated with the optical raster scan to link optical and AFM measurements to the same defects).

All measurements are repeated after annealing the sample in air at 445 °C for 5 h. The next Section describes how we determined this optimal annealing temperature.

4.2 Determining the annealing temperature

Before we carefully characterise NV centres and before and after annealing the nanodiamonds, we first have to find the optimal temperature. The used nanodiamonds for these experiments and this thesis stem from the same batch, i.e. no dependence on their size was investigated. The measurements in this Section were carried out by Benjamin Woodhams, a PhD student and collaborator in the Biological and Soft Systems group in Cambridge. We want to remove as much graphite as possible without burning any nanodiamond. Therefore, three samples with very high nanodiamond density were prepared to conduct weight measurements during the heating process and Fourier transform infrared (FTIR) and Raman spectroscopy. AFM measurements are carried out using a fourth sample with lower density to reliably identify single crystals on the surface. Woodhams et al. [208] describes the details of the measurement protocols.

First, the mass while annealing the nanodiamonds in air is monitored. In Figure 4.1.a the nanodiamonds start to burn at $\approx 534\,°\mathrm{C}$. The kinks in the blue and yellow traces in Figure 4.1.a represent real data and can be attributed to different burning phases such as

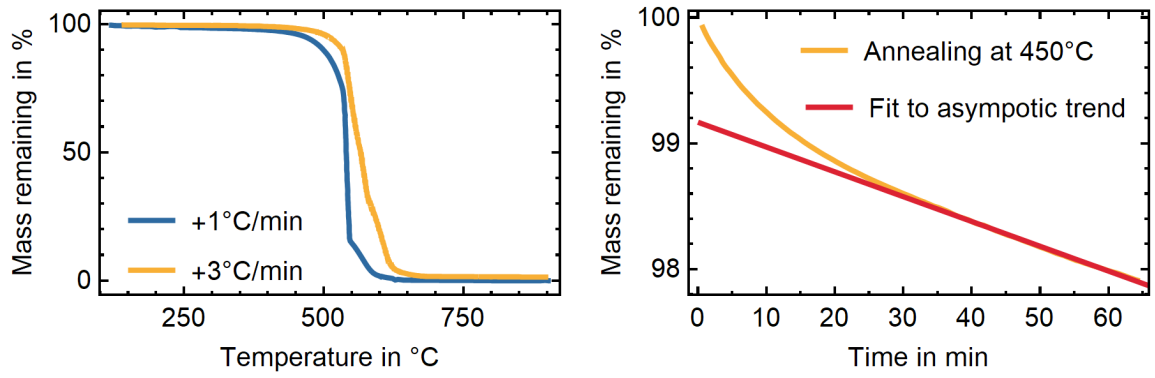

(a) Mass loss by temperature

(b) Mass loss at 450 °C

Fig. 4.1 **Mass loss depending on temperature**. (a) the nanodiamond mass is constantly monitored while the temperature is increased. Two curves for ramping temperature by 1 °C/min and 3 °C/min were acquired, respectively. (b) the mass loss during annealing at 450 °C. Data taken from [208].

an exothermic reaction at $\approx 536\,°C$ indicated by a sleep slope. However, as shown in Figure 4.1.b already at 450 °C a constant loss of mass of 1.20 %/h is observed indicating that this temperature is sufficient for oxidation of graphite but does not result into an exothermic reaction of diamond and oxygen in air. Annealing for 5 h is long enough to enter this asymptotic regime in which graphite is very slowly removed. The burning rate is expected to be proportional to the exposed diamond surface area which does not change significantly given the small amount of total mass burnt.

To confirm oxidation and removal of graphite Raman spectroscopy and FTIR absorption spectroscopy is employed. The sharp peak at $1333\,cm^{-1}$ in the Raman spectrum in Figure 4.2.a can be attributed to diamond, i.e. sp^3 bonds, and the broad peak at $1550\,cm^{-1}$ stems from graphite, i.e. sp^2 bonds. The graphite related peak is reduced by approximately 80 % after annealing for 5 h at 445 °C as evident from comparing the areas under the blue (before annealing) and the yellow (after annealing) traces. The FTIR spectroscopy curves in Figure 4.2.b show that O=C ($1710-1850\,cm^{-1}$) and O-H (($3100-3700\,cm^{-1}$) groups are formed [151]. The later is a sign for surface water absorption [151]. Both features are strong indication of oxidation of the diamond surface.

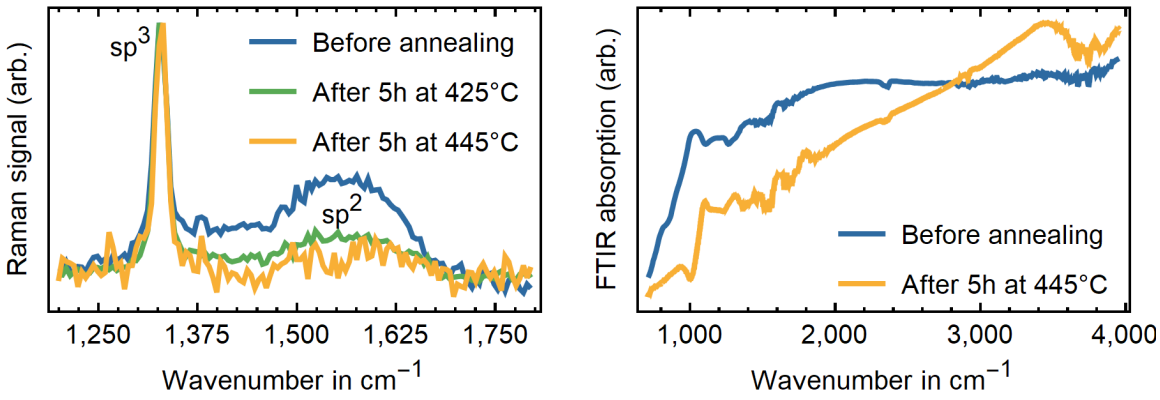

(a) Raman

(b) FTIR

Fig. 4.2 **Raman and FTIR signal before and after annealing**. (a) the blue curve represents the Raman signal of an untreated sample; the green and the orange curve correspond to annealing the samples for 5 h at 425 °C and 445 °C, respectively. (b) curves obtained by FTIR absorption spectroscopy before and after annealing. Data taken from [208].

Last but not least, AFM measurements are carried out before and after annealing at 445 °C for 5 h. Only diamonds smaller than 15 nm in size are investigated and the finding is that the two resulting histograms of nanodiamond size for before and after annealing are shifted by ≈ 0.2 nm. Assuming spherical particles, this reduction in diameter is consistent with an expected mass loss of 6 % after 5 h of annealing which is suggested by extrapolating the data displayed in Figure 4.1.b.

We conclude that choosing 445 °C as the optimal temperature for annealing leads to a reliable removal of graphite and at least partial oxidation of the diamond surface.

4.3 Impact of surface treatment

In this Section we compare results from measurements on individual NV centres and their host nanodiamonds, respectively, before and after annealing. While we started with 14 emitters, two could not be identified after the annealing procedure leading to twelve characterised emitters. The missing defects correspond to missing nanodiamonds indicating that either the

two nanodiamonds in question were completely combusted or moved to another site of the sample which is suggested by a different particle pattern in the local area of the nanocrystals.

The measurements carried out are described in Section 4.1. Correlations and results of interest are presented and discussed in this Section. In particular we consider changes in the spin coherence time, the nature of the noise bath, the spin lifetime, the crystal size, the lattice strain and the NV^0 charge state fraction.

4.3.1 SPIN COHERENCE TIME

The coherence time T_2 of the NV centre electron spin has been subject to a number of studies which have found that there is a strong dependence of the spin coherence on the distance to the diamond surface [168, 149]. In particular, electric noise due to charge traps [96] and magnetic noise due to surface spins related to dangling bonds [170] have been identified as noise sources.

Klauder and Anderson [100] investigate decoherence theoretically. They find that the homogeneous dephasing time T_2 is determined by the NV centre spin-bath coupling b and the correlation time of the bath τ_C, which depends on the interaction strength of bath spins with each other. The signal from a Hahn-echo is given by

$$E_{\text{echo}}(t) \propto \exp\left[-(b\tau_C)^2\left(\frac{t}{\tau_C} - e^{-\frac{t}{\tau_C}} + 4e^{-\frac{t}{2\tau_C}} - 3\right)\right]. \tag{4.1}$$

For fast bath dynamics such as often observed for spins close to the surface τ_C has been measured in the range of 10 ps to 10 µs [170, 137, 168]. Hence, $b\tau_C \ll 1$ and Equation 4.1 becomes

$$E_{\text{echo,fast}}(t) \propto \exp\left[-\frac{t}{T_2}\right], \tag{4.2}$$

with

$$T_2 = \frac{\tau_C}{b^2} \qquad \text{for} \qquad b\tau_C \ll 1. \tag{4.3}$$

This is equivalent to considering coupling to a bath of independent spins. In this case, Fermi's golden rule can be applied which confirms a single exponential decay of coherence or information, respectively.

However, for $b\tau_C \gg 1$, i.e. when the bath dynamics are slow and can therefore be considered quasi-static, Equation 4.1 simplifies to

$$E_{\text{echo,slow}}(t) \propto \exp\left[-\left(\frac{t}{T_2}\right)^3\right], \tag{4.4}$$

with

$$T_2 = \sqrt[3]{\frac{12\tau_C}{b^2}} \qquad \text{for} \qquad b\tau_C \gg 1. \tag{4.5}$$

Because of the slow bath dynamics the drop in coherence is reversible by employing a more sophisticated decoupling sequence because the information is still stored in the bath. Therefore, we strongly favour emitters without a simple exponential decay. By applying a strong external magnetic field larger than 100 G we increase the correlation time of the bath as the energy required to flip a single bath spin is increased. However, the applied biases in the Chapter are not sufficient to significantly affect the coherence time or even change the NV centre electron spin to bath coupling regime as we demonstrate in Section 6.4.

Combining the two approximations, the signal can be well approximated by

$$E_{\text{echo,approx}}(t) \propto \exp\left[-\left(\frac{t}{T_2}\right)^\alpha\right], \tag{4.6}$$

where $1 < \alpha < 3$. Larger α indicates fast dynamics of the bath and weak the coupling of the NV centre to the bath. For a diamond with a nitrogen impurity concentration of 50 ppm such as in this thesis, a model by Wang and Takahashi [206] suggests $\alpha \geq 2$, i.e. values of $\alpha < 2$ denote emitters limited by noise sources on the surface. Improvements in α through annealing are a sign of surface oxidation and removal of graphite which corresponds to terminated dangling bonds and removed charge traps, respectively. Also, greater α allows

the more effective application of dynamical decoupling techniques to even further increase the coherence time T_2 [18, 205].

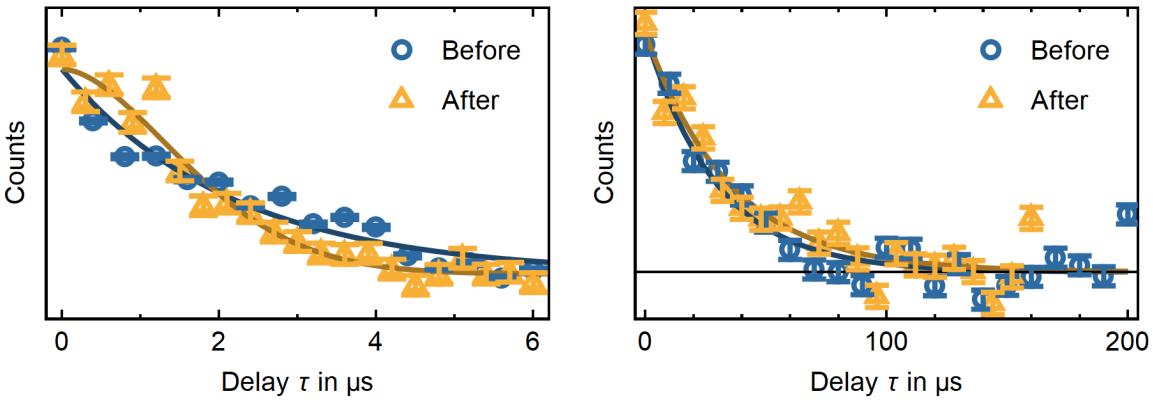

(a) Hahn-echo

(b) Lifetime

Fig. 4.3 **Coherence and lifetime of emitter "NV D"**. Raw data before and after annealing for (a) a Hahn-echo to determine the coherence time T_2 and the parameter α and (b) a lifetime measurement. Both measurements were taken without a magnetic B-field bias. The error bars denote one standard deviation.

In Figure 4.4 we present the extracted values for α and the coherence time T_2. We observe statistically significant improvements in α in eight out of twelve emitters. One of them (NV D) exhibits improvement when measured without and with an external magnetic field aligned with its axis. Seven NV centres show improvement only in one of the cases. Not a single defect has shown a reduction of α after annealing. The average change over all measurements is $\Delta\alpha = 0.18$ or 16 % with a large spread of values indicating that some NV centres are either not strongly affected by surface noise as they are not close to it or that not the entire surface of all nanodiamonds was successfully oxidised.

The improvements in α are largely reflected in improvements in the coherence time T_2 supporting the hypothesis of these improvements in α to be real. This can be inferred from Figure 4.5 which displays the change in α compared to the change in T_2.

Annealing reduces the coupling b to the magnetic spin bath because spins and charge traps are removed and it increases the inter-bath correlation time τ_C for the same reason. For $b\tau_C \ll 1$ with short τ_C and moderate values for b such as in the investigated sample, a

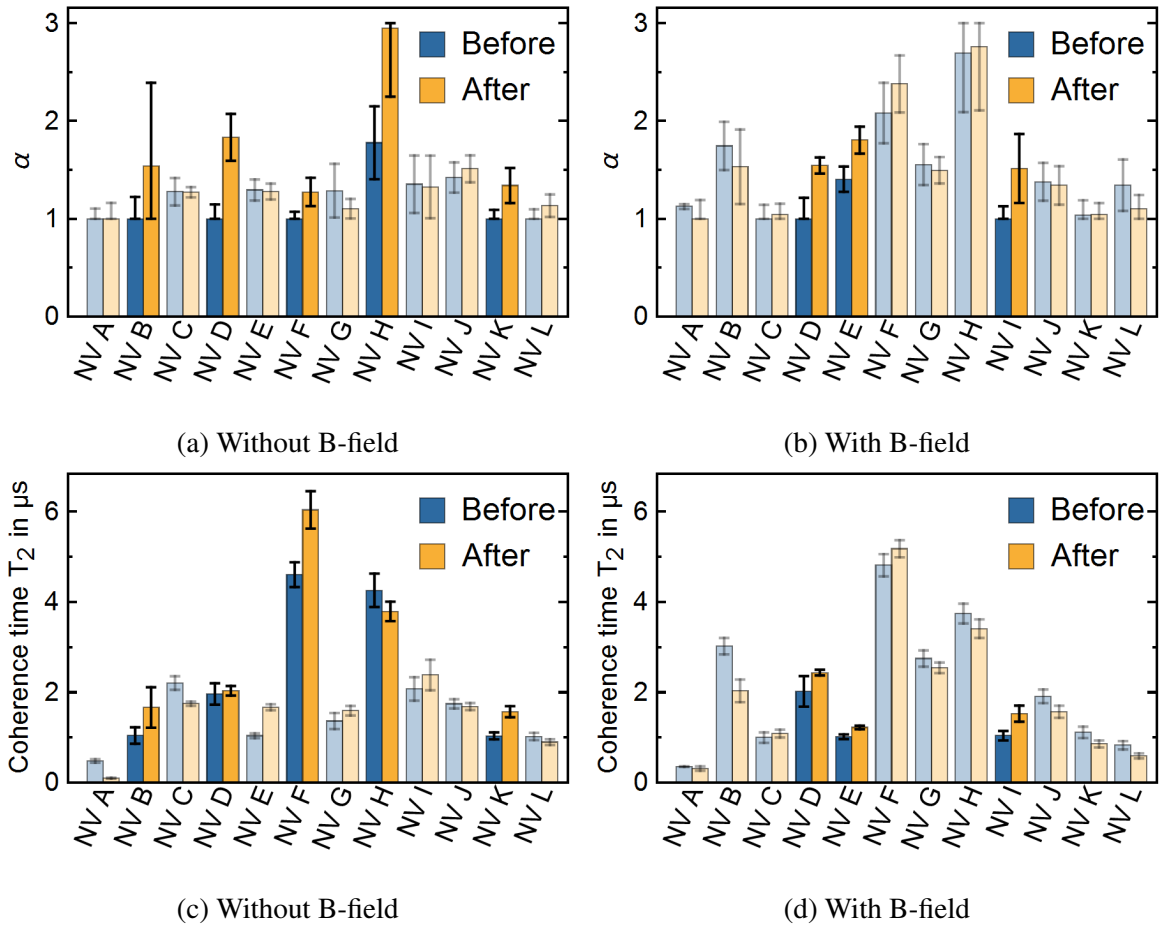

(a) Without B-field

(b) With B-field

(c) Without B-field

(d) With B-field

Fig. 4.4 **Coherence time and α before and after annealing**. Every measurement - an example is displayed in Figure 4.3.a - was fit with the function described in Equation 4.6. The found parameters α and T_2 are displayed with their respective errors. The error bars represent one standard deviation. For every NV centre exist four measurements corresponding to before (blue bar) and after (orange bars) sample treatment, and (a, c) with and (b, d) without external magnetic field bias. Measurements that have lead to an improvement above one standard deviation in α are highlighted. On the x-axis are the emitter names.

decrease in b leads to an increase in T_2 without much effect on α while an increase in τ_C causes α to increase and T_2 to slightly decrease until $\alpha > 2$ when further increases in τ_C also benefit T_2.

By applying an external magnetic field two effects occur. First, decoherence due to electric field noise is decreased while the NV centre becomes more susceptible to magnetic

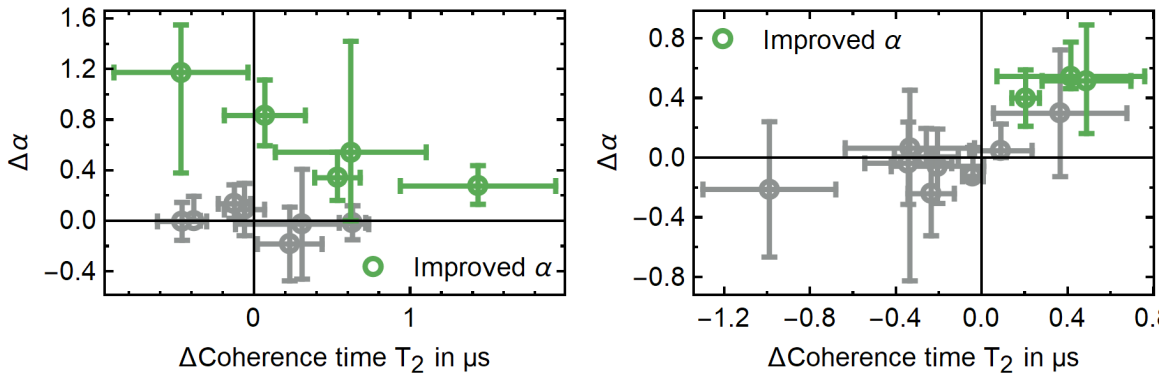

(a) Without B-field

(b) With B-field

Fig. 4.5 $\Delta\alpha - \Delta$ **coherence time scatter plots**. Here the change in α is shown compared to the change in coherence time T_2 before and after sample treatment. The data is the same as shown in Figure 4.4. Emitters which showed significant improvement of α are highlighted in green.

field noise and second, the Zeeman effect increases the energy required to flip bath spins, i.e. the inter-bath correlation time τ_C increases [72]. The former explains why the treated nanodiamonds do not necessarily show improved coherence times of NV centres. The later introduces a decrease in T_2 which is present in the data presented in Figure 4.5.

For measurements where a bias with an external magnetic field was present we also observe a very strong correlation of $\Delta\alpha$ and ΔT_2 while for the measurements without an external field the correlation is weaker. This indicates that primarily the correlation time τ_C of the electric bath is decreased after annealing while for magnetic spin noise the inter-bath coupling strength is also strongly affected. This is in line with the fact that we expect the electric bath to exhibit very short τ_C before annealing whose reduction can cause decrease in T_2.

In addition, we analyse correlations between the fitted values in Figure 4.6 and find that particularly emitters with small α have improved. This is consistent with the idea that especially NV centres close to the surface experience a large change in their environment when annealing the sample.

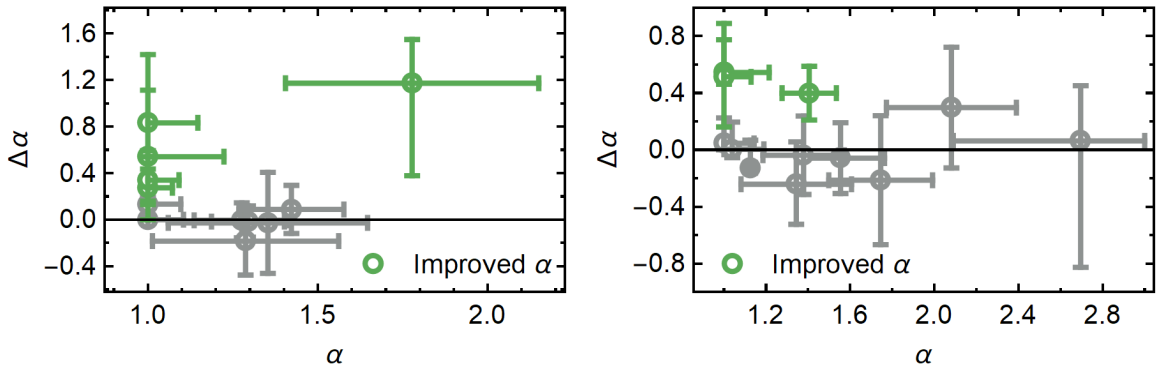

(a) Without B-field

(b) With B-field

Fig. 4.6 $\Delta\alpha - \alpha$ **scatter plots**. $\Delta\alpha$ denotes the difference between the values for α before and after annealing of the sample. On the x-axis, α before treatment is plotted. The data is the same as shown in Figure 4.4. Emitters which showed significant improvement of α are highlighted in green.

4.3.2 Spin lifetime

Tetienne et al. [189] found that the spin lifetime T_1 is also affected by surface noise. The idea is that flip-flops with the bath are due to mixing of the electron spin states of the NV centre if a transverse magnetic field is induced by nearby spins. This is further discussed in Chapter 6. Tetienne et al. [189] suggest a model given by

$$\frac{1}{T_1} = \frac{1}{T_1^{\text{bulk}}} + 3\gamma_S^2 \mathrm{B}_\perp{}^2 \frac{\tau_C}{1+(2\pi D_{gs}\tau_C)^2}, \tag{4.7}$$

where τ_C is again the correlation time of the bath consisting of spins on the surface and in the diamond, $\gamma_S \approx 2\pi \times 2.80\,\text{MHz/G}$ is the gyromagnetic ratio of the electron spin, $D_{gs} \approx 2.87\,\text{GHz}$ is the ground state spin-splitting and T_1^{bulk} is the lifetime of the NV centre electron spin limited by phonon noise. $\mathrm{B}_\perp$ is the average transverse magnetic field at the site of the NV centre induced by the paramagnetic spins. If many of these spins are on the surface of the nanodiamond and the magnetic field depends on the distance from these spins, the removal of these spins should improve the NV centre lifetime T_1. However, if the nitrogen

impurities within the diamond are more abundant than surface spins, the lifetime does not improve upon removal of the surface defects.

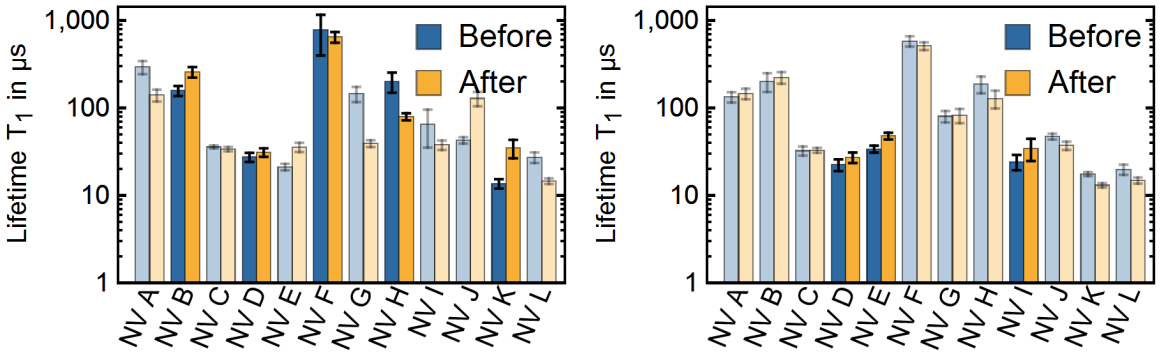

(a) Without B-field

(b) With B-field

Fig. 4.7 **Lifetime before and after annealing**. We polarise the NV centre into the $m_s = 0$ state and probe its population after time τ. The lifetime is the characteristic decay time extracted from the measurements by fitting a simple exponential. The colours and x-axis are equivalent to Figure 4.4 and the error bars denote one standard deviation. An example for a lifetime measurement is displayed in Figure 4.3.b.

The lifetimes before and after annealing are displayed in Figure 4.7. Note that the y-axis in Figure 4.7 is logarithmic. The surprisingly small improvement can be explained by primarily nitrogen bath limited lifetimes, a lack of statistics or a possible pre-selection of emitters by choosing defects showing saturation and stable count rates.

In addition, Tetienne et al. [189] measure a large spread in values due to the individual orientations and positions of NV centres within nanodiamonds and positions of paramagnetic spins on the surfaces. While we do not observe effects as strong as suggested by Tetienne et al. [189], the lifetimes do improve if α has increased as indicted by the scatter plots in Figure 4.8.

As before, the electric noise is suppressed and the magnetic field noise is enhanced for measurements with a magnetic field bias. Therefore, we compare the lifetime and coherence time measurements grouped by magnetic field bias.

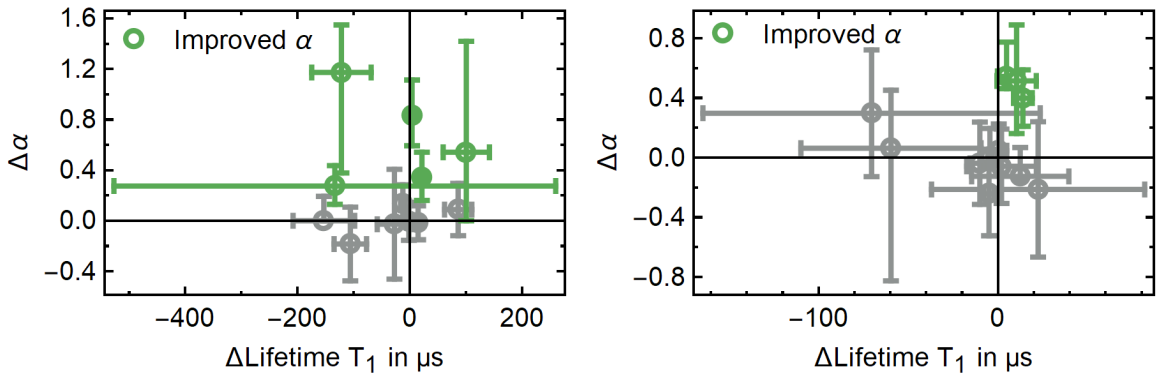

(a) Without B-field

(b) With B-field

Fig. 4.8 $\Delta\alpha - \Delta$ **lifetime scatter plots**. scatter plots of the change in α on the y-axis and a change in lifetime on the x-axis are displayed for all twelve emitters with and without external magnetic field. The change relates to the difference of values before and after annealing. The data is the same as shown in Figures 4.4 and 4.7. Emitters which showed significant improvement of α are highlighted in green.

4.3.3 Crystal size and lattice strain

In this Section, we investigate the effect of the annealing on the crystal size. Woodhams et al. [208] have measured a reduction of 0.2 ± 0.1 %nm in radius with the same surface treatment technique using an AFM. Our results using an AFM to infer the size from the nanodiamond height indicate a far more significant decrease by 6.5 ± 4.6 nm displayed in Figure 4.9.a. The error was obtained by analysing subsequent AFM images of the same crystals. The difference can be explained by insufficient statistics, measurement errors or a faster combustion rate and mass loss for larger crystals.

We further note that NV centres in smaller diamonds have a higher probability to improve their α upon annealing as demonstrated by the scatter plots in Figure 4.10. This is in line with the idea that NV centres closer to the surface experience larger changes. As expected there is no particular difference between the changes observed in the presence or absence of an external magnetic field.

We also extract another parameter of the crystal which is strain. Strain is discussed in Section 2.1.3 and we measure it here by determining the splitting of the two ODMR

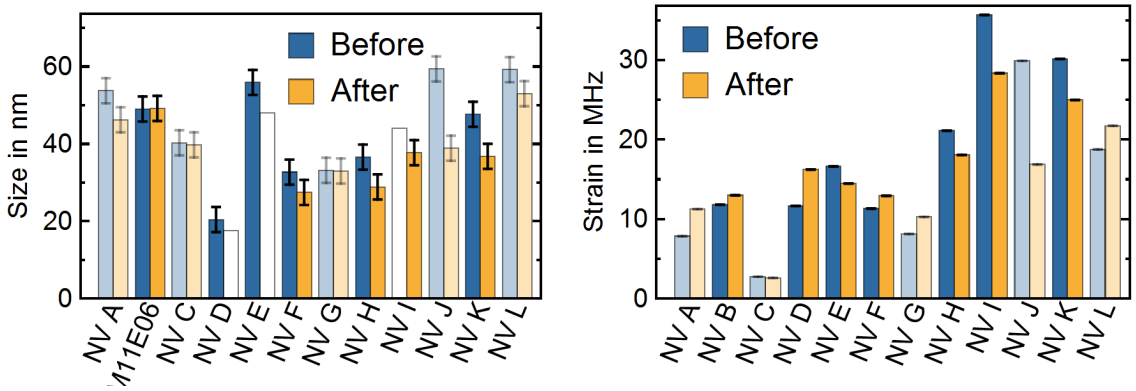

(a) Size (b) Strain

Fig. 4.9 **Nanodiamond size and strain before and after annealing scatter plots**. (a) nanodiamond sizes which were obtained by extracting the particle heights with an AFM. White bars represent extrapolated sizes based on the average change as the data is missing. (b) the strain splitting extracted from ODMR measurements at no external magnetic field. The colours and x-axis are equivalent to Figure 4.4. The error bars denote one standard deviation.

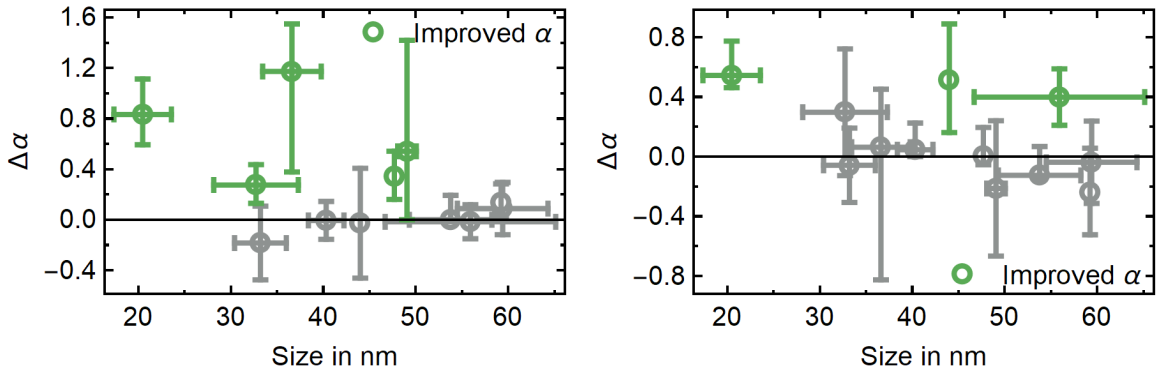

(a) Without B-field (b) With B-field

Fig. 4.10 **Change in α depending on nanodiamond size**. (a, b) scatter plots of the change in α against the nanodiamond size with and without external magnetic field, respectively. The data is the same as shown in Figures 4.4 and 4.9. Emitters which showed significant improvement of α are highlighted in green.

transitions $|m_s = 0\rangle \leftrightarrow |-1\rangle$ and $|m_s = 0\rangle \leftrightarrow |+1\rangle$ with no external electric or magnetic field applied. In Figure 4.9 we show measurements before and after annealing. In some cases

strain increases and in others it decreases with a mean of 17 MHz before and 16 MHz after surface treatment. There is a tendency of highly strained nanodiamonds to experience a reduction in strain and for weakly strained crystals to exhibit larger amounts of strain. This is reflected in a reduction of the standard deviation of the strain parameter by 32 % when comparing measurements before and after annealing. The increased temperature fosters the mobility of vacancies. A hypothesis to explain the reduction of the standard deviation which needs confirmation is that a state with an even distribution of vacancies is favoured leading to a strain value related to the global and not local properties of the diamond.

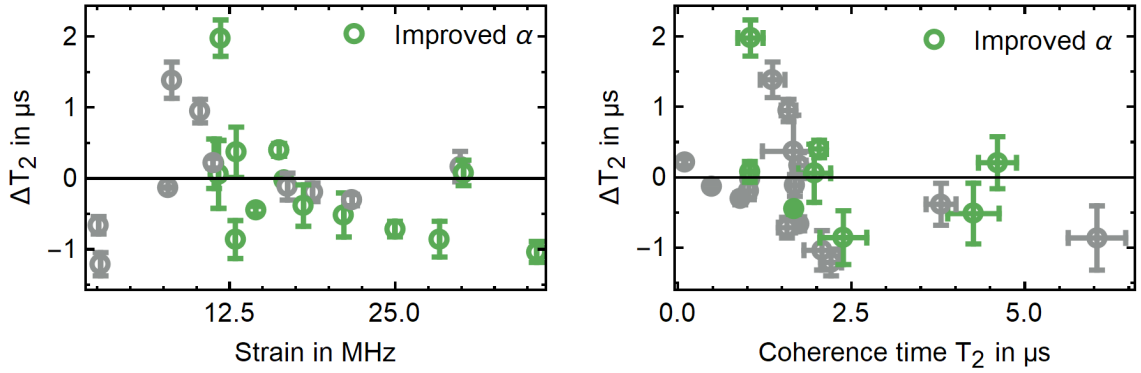

(a) ΔT_2 depending on strain

(b) ΔT_2 depending on T_2

Fig. 4.11 **Change in coherence time between presence and absence of an external magnetic field compared to strain**. (a) the change in coherence time on the y-axis and the strain splitting before sample treatment on the x-axis. (b) the change in coherence time T_2 with and without magnetic field. The x-axis shows the coherence time T_2 without B-field. The data is the same as shown in Figures 4.4 and 4.9. Emitters which showed significant improvement of α due to annealing are highlighted in green.

Strain changes the sensing capabilities of NV centres. In Section 5.3 we state that the strain parameter δ is given by

$$\delta = 2\sqrt{\left(\frac{\gamma_S}{2\pi}\mathrm{B}_z\right)^2 + \left(\frac{\Pi}{2}\right)^2}, \tag{4.8}$$

where $\gamma_S/(2\pi) = 2.8034\,\mathrm{MHz/G}$ is the electron spin gyromagnetic ratio and Π is the strain splitting. Strain acts as an external electric field as the local charge density is modified by the dislocation of the crystal lattice. Therefore, NV centres in highly strained diamond are more sensitive to electric fields if no magnetic field is applied while NV centres in weakly strained nanodiamonds react to magnetic and electric noise. If a sufficiently large external magnetic field is applied, i.e. causing a Zeeman splitting far larger than the strain splitting, the NV centre becomes more susceptible to magnetic field noise.

In Figure 4.11 we show the change in the coherence time T_2 between presence and absence of an externally applied magnetic field of approximately 100 G against the measured strain and the coherence time without external magnetic field. Nanodiamonds with high strain experience a drop whereas nanodiamonds with little strain experience an increase in coherence. The increase is explained by the suppression of electric field noise if a bias magnetic field is applied. Application of an external magnetic field to a highly strained NV centre, however, induces a change in the sensing regime. In a first order approximation at low B-fields bias the NV centre is an electric field sensor while at high B-field bias the NV centre becomes a magnetic field sensor. Therefore, the decreased coherence time upon the application of a B-field bias is an indication for stronger decoherence due to magnetic than to electric field noise. However, decoherence due to electric field noise is of the same order of magnitude.

Further, as shown in Figure 4.11.b short coherence times increase and long decrease upon the application of an external magnetic field. This behaviour is expected as NV centre spins whose coherence is short in the absence of a magnetic field bias are limited by electric noise and benefit from its suppression. Those, whose coherence is long and therefore already dominated by magnetic noise, will suffer from a magnetic field bias which increases their susceptibility to it.

4.3.4 Charge state ratio

Previous studies have found that proximity to the surface is an indicator for enhanced charge state conversion using electron tunnelling between the site of the NV centre and charge traps

on the surface as a toy model [169, 55]. We expect NV centres to exhibit a more stable NV^- charge state under laser illumination after surface treatment when the charge traps have been removed [55]. In order to quantify the change we acquire optical emission spectra and fit empirical pure NV^- and NV^0 spectra [94] to extract the NV^0 fraction. However, as the NV^- spectrum acquired by Karaveli et al. [94] contains some residual NV^0 content this method introduces an error which is estimated to be on the order of 2 %.

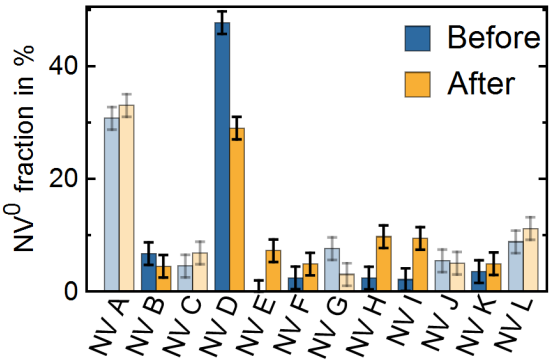

Fig. 4.12 **NV^0 fraction**. The NV centre spectra are fit using empirical spectra of pure NV^0 and NV^- [94] and the fraction of NV^0 is extracted. The colours and x-axis are equivalent to Figure 4.4.

The results presented in Figure 4.12 indicate no clear trend. This could be due to the low prevalence of NV^0 even before annealing possibly caused by pre-selecting stable emitters. Only emitter "NV D" shows a NV^0 content of almost 50 % before annealing. This emitter also displays the most dramatic changes in α and T_2 and is the only emitter where these values improve in the presence and absence of an external magnetic field. Given the small fraction of NV^0 we also do not expect large changes in the emitter fluorescence brightness. Indeed, the saturation data does not show a significant increase or decrease in the maximum number of counts that can be extracted from the emitters. We do observe a statistically significant 30 % decrease in the half saturation excitation power which might mean that the removal of the graphite allows excitation with lower power and better extraction of photons as quenching is suppressed. However, as the optical setup had to be re-aligned before data after annealing could be taken, the findings from the saturation data must be taken with care.

4.4 Conclusions

We study the effect of annealing nanodiamonds at 445 °C for 5 h on the optical and spin properties of the hosted NV centres. We find a statistically significant reduction of the electromagnetic noise in seven out of twelve characterised emitters. Five showed no changes.

In particular, we find that the crystal size is reduced and on average the coherence time and lifetime of emitters are improved. The shape of the acquired spin-echo signals changes, indicating weaker bath-NV centre spin interactions and longer inter-bath correlation times. This means that dynamical decoupling techniques can increase the coherence time more effectively after the treatment. Additionally, comparing measurements with and without magnetic field indicates that magnetic field noise is larger than electric field noise. Nevertheless, the difference is smaller than one order of magnitude.

Measurements of the different optical and spin properties are consistent with each other increasing the confidence into the very promising results. However, verification of the findings by acquiring additional statistics is desirable. Also, acid cleaning is an additional method to reduce surface noise and should be investigated in the future. Yet, as diamonds cannot be tracked individually if wet chemical treatments are applied, such a study would require the acquisition of a larger amount of data to yield statistically significant results.

CHAPTER 5

Sensing magnetism in PCMO thin films

In this Chapter we present macroscopic measurements and the first microscopic study of the magnetisation of a $Pr_{0.8}Ca_{0.2}MnO_3$ (PCMO) thin film including an investigation into the time dynamics of the domains. This study aims to provide a proof of principle and demonstrate the capabilities of NV centres in nanodiamond under relatistic conditions. In particular, we want to show that NV centres can be used to reveal the local magnetic structure of thin films and observe the formation of domains. The material was chosen for three reasons: First, below 150 K the bulk crystal has a robust ferromagnetic phase [49, 190]. Second, strain in thin films can shift the Curie temperature to lower temperatures as the distance between coupling spins is increased [185] and third, previous studies suggest the coexistence of ferromagnetic clusters in an otherwise anitferromagnetic matrix. This coexistence is a feature exhibited by many manganites and leads to a spin cluster glass or a superparamagnet [33, 34]. This study was undertaken to better understand the domain formation in PCMO thin films strained due to a lattice mismatch with its substrate.

Probing magnetic fields and their evolution on the nanoscale over a temperature range spanning from 0 K to 700 K [195] is a main advantage of the NV centre in diamond. In addition, unlike other magnetic probes such as SQUIDs, hall sensors or magnetic force microscopy, the NV centre can resolve the dynamics of domain formation. Recently, Dussaux et al. [47] carried out a study with NV centres in nanodiamond to investigate the paramagnetic-to-helimagnetic transition of FeGe. NV centres in nanodiamond are particularly well suited

for the task as the defects are close to the surface of the material which exhibits predominantly in-plane magnetisation and therefore weak stray fields as most field lines are then within the material [99]. The nanodiamonds are dispersed on the surface, as described in Section 3.3, in order to sense domains at different, albeit nearby locations. We find that the domains are smaller than 30 µm and that noise from domain dynamics exist on the minute timescale and faster. In addition, we show that the laser has a demagnetising effect on the material.

The macroscopic study is carried out using a superconducting interference device (SQUID) which averages the magnetic field over the entire sample. By sensing magnetisation, i.e. measuring the magnetic stray field using ODMR, between 7 K and 150 K under different magnetic field biases we detect strain related decrease of the Curie temperature, a second transition which we attribute to the formation of a spin-cluster glass and reveal the coerce field in-plane and out-of-plane of the sample.

In Section 5.1 we introduce the material PCMO before macroscopic measurements are presented in Section 5.2. Section 5.3 shows how the macroscopic experiments compare with the results from local probes and Section 5.4 gives insight into the dynamics of the magnetic domains.

Most measurements in this Chapter were carried out by or together with David-Dominik Jarausch who was a PhD student in the Atomic, Mesoscopic and Optical Physics Group at the Cavendish Laboratory under the supervision of Professor Mete Atatüre. In addition to his work [89] we present here further data and analysis. In particular, additional SQUID data is shown and analysed and further work is carried out on the ODMR measurements in order to reveal the typical domain size and the time dynamics underlying domain formation.

5.1 Magnetism in PCMO

PCMO belongs to the family of manganites which are described by the chemical formula $RE_{1-x}AE_xMnO_3$. RE is a trivalent rare earth and AE a bivalent alkaline ion. The specific type of PCMO we use is single crystalline $Pr_{0.8}Ca_{0.2}MnO_3$, i.e. with a rare earth fraction of $1-x=0.8$. The PCMO film is grown on top of a bulk strontium titanate ($SrTiO_3$ or STO)

substrate and is 150 nm thin. The method of growth is pulsed laser deposition (PLD) and was carried out by Angelo Di-Bernardo in the Device Materials Group at the Department of Materials Science & Metallurgy in Cambridge.

As shown in Figure 5.1 the crystal symmetry of PCMO is face centred cubic (FCC) with an additional manganese (Mn) ion in the centre of the unit cell. The primitive cubic parts of the unit cell, i.e. the corners, are populated by the rare earth praseodymium and metal calcium ions. The centres of the unit cell's faces are occupied by oxygen atoms which form an octahedron.

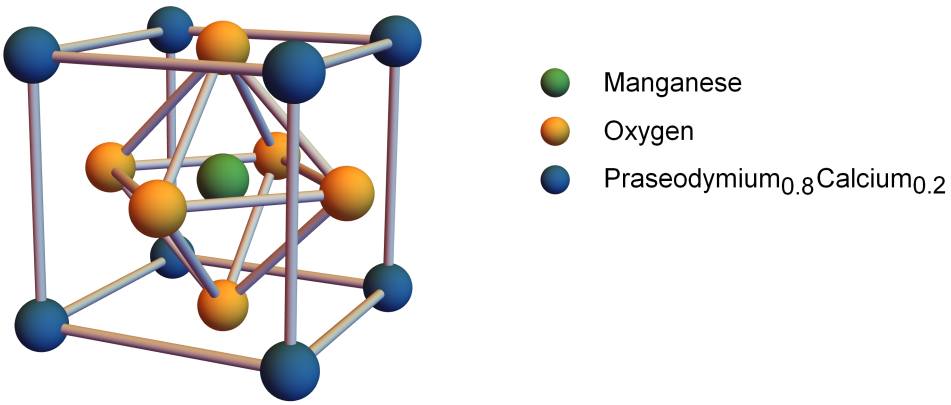

Fig. 5.1 **Unit cell of PCMO**. The symmetry is face centred cubic with an additional manganese atom at the centre. The blue spheres represent the primitive part of the lattice and can either be rare earth praseodymium or metal calcium ions depending on the stoichiometry of the material. The orange spheres make the difference between a primitive cubic and a face centred cubic structure, sit at the centres of the six unit cell faces, and are occupied by oxygen atoms. In the centre resides a single manganese atom which is here denoted by a green sphere. $SrTiO_3$ has an identical lattice structure with the strontium atoms at the edges, oxygen at the faces and a titanium atom in the centre.

Magnetism arises due to the Mn ions. For $x = 1$, i.e. $CaMnO_3$, all Mn ions have four positive charges (Mn^{+4}). For $x < 1$, $1 - x$ Mn^{3+} ions exist per unit cell as the alkaline ion is bivalent as opposed to the trivalent rare earth ion. The spin interaction is mediated by

the oxygen atoms and is of the superexchange type following the Goodenough-Kanamori rules. The $Mn^{4+} - O - Mn^{4+}$ interaction is anti-ferromagnetic, while the $Mn^{3+} - O - Mn^{3+}$ interaction can be both ferromagnetic or anti-ferromagnetic [65]. Their strengths depend on the distance between ions and, therefore, are strongly affected by lattice distortions which can be caused by a strain due to a lattice mismatch with the substrate, doping, the Jahn-Teller effect and hydrostatic pressure [81].

The magnetic properties of PCMO vary strongly as x is varied. Recent measurements on PCMO suggest that for $x = 0.2$ ferromagnetic clusters exist in an otherwise antiferromagnetic material [79]. Therefore, these clusters require local probes in order to be observed. Further, Tokura et al. [194] found the material is a ferromagnetic insulator at low cryogenic temperatures for $0.15 < x < 0.3$.

STO exhibits the same lattice structure as PCMO. However, there is a lattice mismatch with PCMO, which leads to strain and alters the physical properties of the material if PCMO is grown on top of a STO substrate [70]. Strain in general has two effects. First, the Curie temperature for the metal-insulator transition changes, and second, the easy axis of the magnetic field varies with temperature. The lattice mismatch is defined as

$$\delta = \frac{a_{\text{substrate}} - a_{\text{PCMO}}}{a_{\text{substrate}}}, \tag{5.1}$$

where $a_{\text{substrate}}$ is the lattice constant for the substrate, i.e. STO in our case, and a_{PCMO} is the lattice constant for PCMO. Positive values denote elongation in-plane, i.e. tensile strain, and negative values indicate compression in-plane. For PCMO on STO, which both have a cubic structure, the lattice constants are $a_{\text{PCMO}} \approx 0.38\,\text{nm}$ and $a_{\text{STO}} = 0.3905\,\text{nm}$, respectively. This leads to a mismatch of $\delta = 2.2\,\%$ [159]. If the PCMO is grown on LAO (Lanthanum aluminate, $LaAlO_3$) instead of STO, the lattice mismatch δ can be as low as $-0.4\,\%$. The specific lattice constant for PCMO depends on the thickness of the thin film. The thinner the PCMO, the closer is its in-plane average lattice constant to the lattice constant of STO. In the case of the film used in this work, which is approximately 150 nm thick, the in-plane lattice constant of PCMO is 0.381 nm and the out-of-plane constant is 0.379 nm as measured by

Prellier et al. [159]. Strain in the material is not necessarily evenly spread [124, 27] as cases have been observed where the material was separated into low and high strain regions [209].

Lattice distortions affect magnetism directly as the Mn ion spin interaction is modified and the distance and angle between the Mn ions change. Compressive strain fosters the double exchange mechanism between Mn spins leading to ferromagnetism by delocalisation of electrons while tensile strain causes localisation of electrons and, hence, the Curie transition temperature T_c of PCMO decreases [133, 64, 93]. Millis et al. [133] observe a decrease in the Curie temperature of 10 % per 1 % increase in the lattice mismatch δ.

Tsui et al. [197] study the effect of strain on the easy axis of the magnetic field in bulk and thin film manganese oxides. In bulk tensile strain leads to a magnetic field out-of-plane while compressive strain rotates the magnetisation into in-plane [108, 138]. However, for thin films the dominating effect is the minimisation of stray magnetic fields outside the material leading to an alignment of the magnetisation along the in-plane component [99]. In addition, temperature can induce changes of the easy axis [197, 71].

5.2 MACROSCOPIC MEASUREMENTS

A SQUID senses a magnetic field by measuring the voltage over a Josephson junction which consists of a weak link between two superconductors and is typically a layer of insulating material. If the junction is incorporated into a loop, an external magnetic field generates a screening current into the loop. The voltage over the junction induced by the current is governed by the Josephson effect. By measuring the voltage, the number of magnetic flux quanta through the loop can be inferred.

The Josephson effect was predicted by Brian Josephson in 1962 [92] and shown experimentally only one year later by Anderson and Rowell [7]. Josephson was awarded the Nobel Prize in 1973 for its discovery. The first SQUID was built by Jaklevic et al. [87] in 1964 at the Ford Research Labs. Two fundamental designs exist. One is the DC SQUID which consists of two Josephson junctions and the other is the RF SQUID which only has one Josephson junction and is cheaper and easier to build. However, the later offers a lower sensitivity.

While most implementations of SQUIDs are macroscopic devices with loops diameters in the range of milli- and centimetres, there also exist nano-SQUIDS with loops as small as 40 nm [200]. These SQUIDS can be scanned over a sample to detect the size and shape of single domains. While the design of a SQUID for out-of-plane sensing is trivial and is simply a loop parallel to the surface of the material, there are nano-SQUIDs which are also capable of measuring in-plane fields [6]. Sub-micron sized SQUIDs are relatively new and highly challenging to fabricate. Therefore, the most common diameter of a scanning probe SQUIDs is still around 1 µm.

Sensitivities of SQUIDs have reached $0.38\,\mu_B \mathrm{Hz}^{-1/2}$. Even at magnetic fields of 1 T a sensitivity of $0.6\,\mu_B \mathrm{Hz}^{-1/2}$ was observed. Nano-SQUIDs have reached single electron spin sensitivity due to their very low flux noise of $50\mathrm{n}\phi_0 \mathrm{Hz}^{-1/2}$, where ϕ_0 is one flux quantum [200]. The disadvantage of scanning squid systems is that they can only operate at low temperatures typically in the 4 K or even millikelvin range.

SETUP

The SQUID that we use is a Quantum Design MPMS SQUID and is a macroscopic device which measures the magnetic moment of the entire sample. At its heart is a RF SQUID which is inductively coupled to the pick-up loops as displayed in Figure 5.2. The voltage over the Josephson junction is measured by monitoring the resonance frequency of a LC-circuit whose inductance is modified by the SQUID.

In order to reduce the noise from fluctuating background fields which disturb the measurement, the SQUID measures gradients. As a gradiometer the sample is subsequently moved through the four superconducting pick up coils. This movement induces a changing flux in the pick-up coils which itself induces a current and thus also a voltage in the SQUID circuit. We can deduce the magnetic moment of the sample by integrating this voltage signal [130]. This method is based on the model of a magnetic dipole which is moved through the coils. By using four instead of only one pick-up coil external background flux noise is cancelled when moving the sample through the coils. A homogeneous, external field creates an equal flux in all coils but because the current direction in the lower and upper coil is opposite to

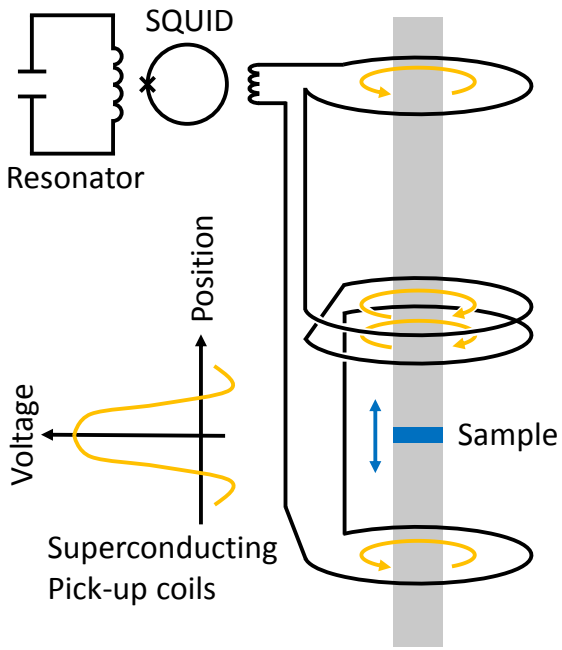

Fig. 5.2 **Schematic representation of the SQUID setup**. In order to determine the magnetic moment of a sample, it is moved through superconducting pick-up coils into which it induces a current due to the changing flux through the loops. By biasing the current until it exceeds the critical voltage over the Josephson junction it can be converted into a voltage signal. The voltage over the Josephson junction modifies the inductance of a resonator. Therefore, the shift of the resonance frequency of the LC-circuit in the upper left corner is a direct measure of the magnetic field strength in the sample. The sample is contained in a 9 mm non-magnetic plastic straw. Not depicted are the superconducting coils which can be used to generate a bias and polarising field. Also, a superconducting shield around the SQUID is not shown which protects the SQUID from background magnetic flux fluctuations.

the direction in the two middle coils no net current is induced. Only the locally varying, and therefore inhomogeneous field of the sample can generate a current and thus a voltage signal.

SQUIDs are vector sensors. In this specific setup only measurements in the z-direction are feasible, but different directions can be explored by physically rotating the sample. An external magnetic bias field up to $\pm 5\,\mathrm{T}$ along the z-direction, which we define as the measurement direction, can be applied to the sample with additional superconducting coils. There is always a remanent field left in the magnet which leads to inaccuracies of the exact

applied field of up to ± 10 Oe. This remanent field must be compensated for if measurements must be carried out in a field-free environment.

ZERO FIELD COOLING MEASUREMENTS

The type of measurement sequence we use is called zero field cooling and consists of three distinctive steps. First, the sample is cooled from room temperature to 4 K. Then, a field of 4 T is applied to polarise the spins in the entire sample along a common axis. Last, a bias field is applied and the magnetic moment is recorded with the SQUID for each temperature data point up to 150 K in steps of $5-10$ K. Step two is necessary to increase the signal to a measurable magnitude. Otherwise, the spontaneous net magnetisation of the bulk sample is solely statistical and therefore very small. This polarisation step is the fundamental difference to the measurements carried out with NV centres as the defects in nanodiamond act as a local probe to a single domain as opposed to the macroscopic nature of the SQUID measurement and therefore no alignment of all domains along a common axis is required.

First, we carried out magnetic field measurements at a number of different bias fields from -60 Oe to 60 Oe. They are presented in Figure 5.3. An applied magnetic field of 10 Oe corresponds to an effective bias field of 0 Oe as the remanent field is ≈ -10 Oe as determined by measuring the paramagnetic background at high temperatures.

We observe a ferromagnetic transition at $T_c = 80$ K which is 50 K or $\approx 40\,\%$ lower than the Curie temperature measured in bulk PCMO with the same stoichiometry, i.e. $x = 0.2$ [185]. We attribute this discrepancy to tensile strain. Given that Millis et al. [133] measure 10 % change in T_c for 1 % change in lattice mismatch, $\approx 40\,\%$ change implies a lattice mismatch of $\delta = 4\,\%$. This is not consistent with measurements by Prellier et al. [159] for a 150 nm PCMO thin film with stoichiometry with $x = 0.5$ which yield an expected mismatch of $\delta = 2.2\,\%$. A possible explanation for the discrepancy are the different stoichiometries of $x = 0.5$ and $x = 0.2$ which we known alters the properties of PCMO dramatically.

Another observation from the SQUID measurements presented in Figure 5.3 is the confirmation that most magnetisation is in-plane because the stray field outside the sample is minimised. Furthermore, in the data a second transition appears at approximately 40 K which

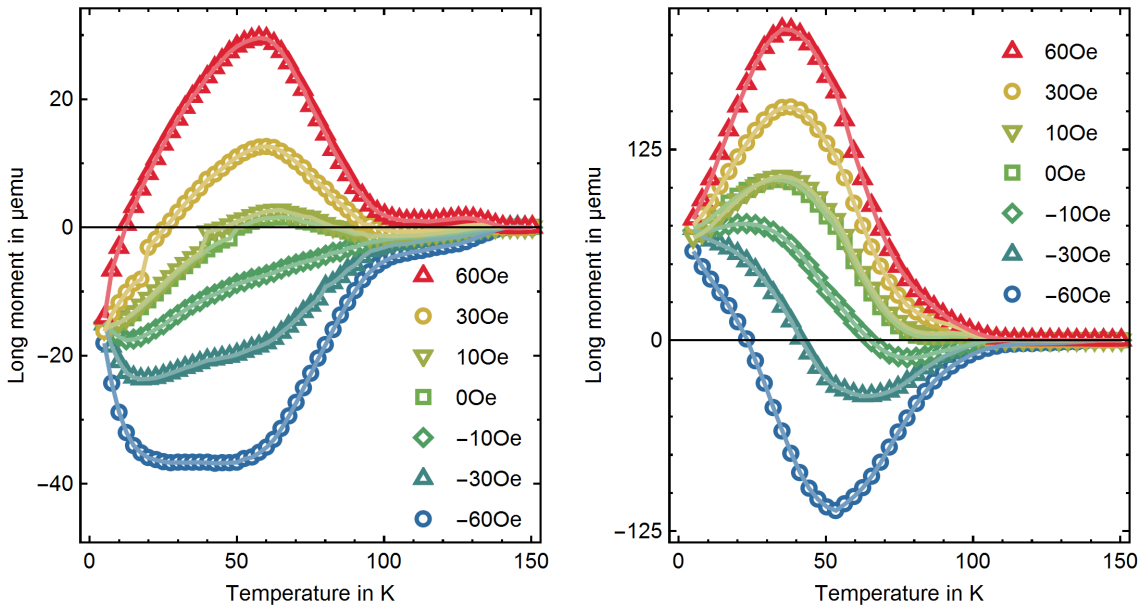

(a) Out-of-plane

(b) In-plane

Fig. 5.3 **SQUID measurements in and out-of-plane**. (a) measurements out out-of-plane. (b) measurements in-plane. The magnetic moment proportional to the magnetisation was recorded for different bias fields along the measurement direction.

is not present in bulk samples. The in-plane magnetisation decreases below this temperature but the out-of-plane component's absolute value increases. Measurements with similar results were carried out in bulk [49, 190] and thin film samples [185] with stoichiometry $x = 0.1$. The authors suggest this behaviour arises due coexistence of ferromagnetic clusters in an antiferromagnetic matrix leading to a spin cluster glass. Such a spin cluster glass can form because we cool the material in zero field. When we start to increase temperature and apply a magnetic field bias domains can align. A second explanation is that ferromagnetic and antiferromagnetic regions form due to inhomogeneous strain which creates different magnetic anisotropies and therefore regions of different spin interaction strengths. This corresponds to a superparamagnet. Third, a rotation of the anisotropy axis out-of-plane due to an elongation of the lattice in-plane might be part of the explanation [108, 138].

By sweeping the bias field over a large range as displayed in Figure 5.4 we find the coercive field which is between 300 Oe and 1000 Oe. At 1000 Oe the material starts to and

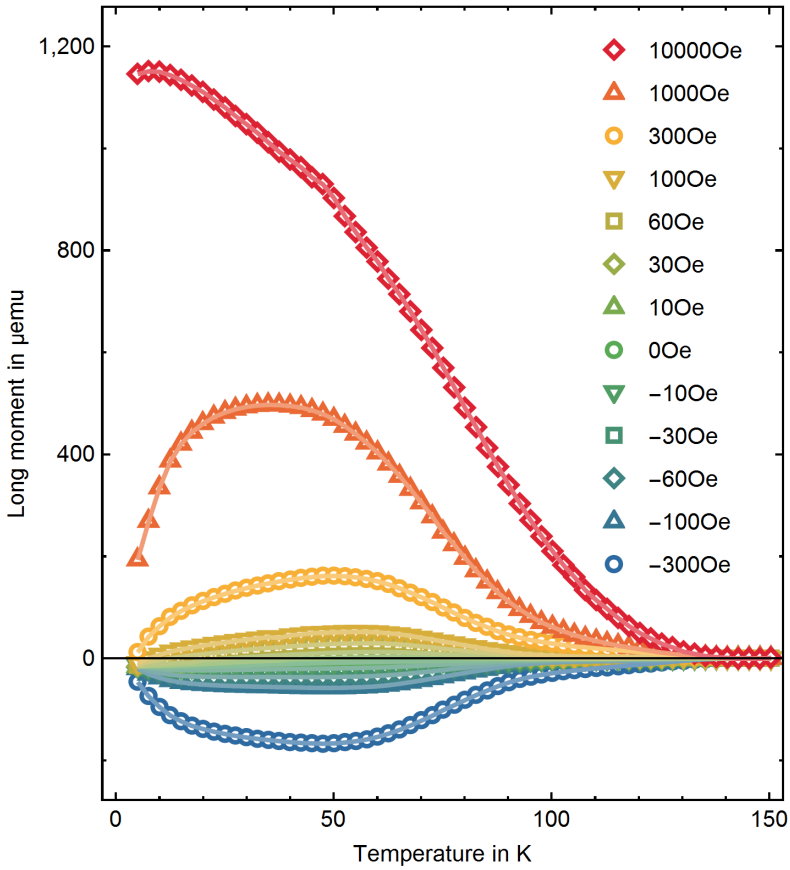

Fig. 5.4 **Magnetic moment measurements with a SQUID for the out-of-plane component of the sample**. We obtain data using a zero field cooling sequence with different bias field at warm-up ranging from −300 Oe to 10 000 Oe.

especially at 10 000 Oe the material fully exhibits the expected behaviour of a paramagnet. This is primarily a control experiment but it also provides valuable information because it means that we should not apply an external magnetic field of more than 300 Oe along the out-of-plane direction, where no coercion of magnetisation is visible, when carrying out measurements with NV centres. NV centres in nanodiamond are typically split by strain and therefore a magnetic field of about 30 G must be applied in order for the Zeeman effect to dominate the spin transition frequency which we use to sense magnetic fields.

We also record measurements along 45° in-plane, i.e. if out-of-plane is the $< 001 >$ direction and in-plane is the $< 100 >$ and the $< 010 >$ direction, then 45° in-plane corresponds to the $< 110 >$ direction. Two observations can be made.

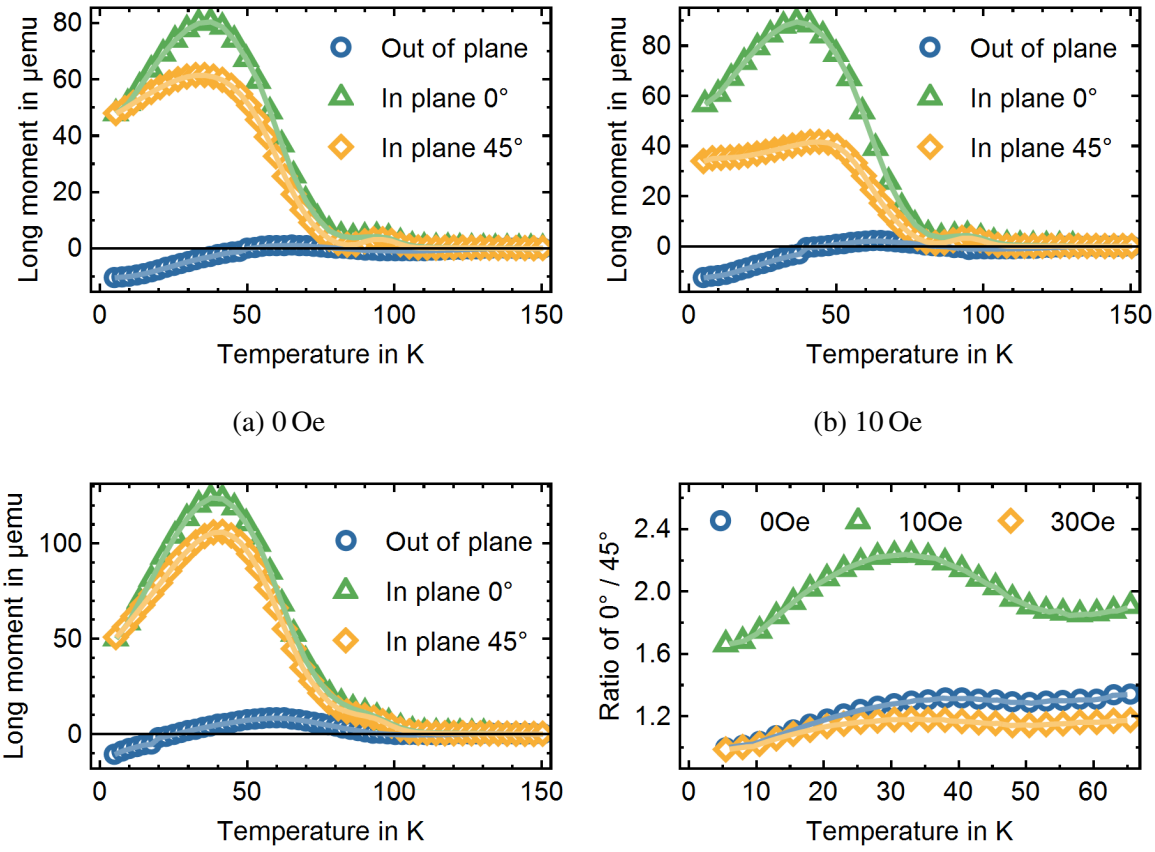

(a) 0 Oe

(b) 10 Oe

(c) 30 Oe

(d) Ratio of in-plane moments at 0° and 45°

Fig. 5.5 **SQUID measurements at 45 ° in-plane.** (a-c) measurements out-of-plane, 0° and at 45° in-plane, i.e. along the $< 001 >$, the $< 100 >$ and the $< 110 >$ direction. Traces along the $< 010 >$ direction were recorded but exactly match the measurements along $< 100 >$. Each panel shows data at a different bias field applied along the respective measurement axes. A bias of 10 Oe corresponds to an effective zero field. (d) the ratios of the values in-plane at 0° and at 45° for different bias fields. The solid lines serve as a guide to the eye.

First, Figure 5.5.b shows the field free measurements. We notice the values of the in-plane magnetisation at 0° and 45° at a temperature of 4 K from Figure 5.5.a and Figure 5.5.c that deviations of only a few Oersted is sufficient to coerce the magnetic axis. Given that the

magnetisation axis is dominated by the effort to minimise the magnetic stray field outside the sample it is not surprising that the coercive field in-plane is three order of magnitudes smaller than out-of-plane.

Second, the ratio of in-plane at 0° and at 45° as displayed in Figure 5.5.d is larger than $\sqrt{2} \approx 1.41$. In a field free environment this is surprising as the magnetisation should be aligned along the $< 100 >$ and the $< 010 >$ direction and therefore, we should measure not less than a factor $\sqrt{2}$ along the $< 110 >$ direction. However, relaxation of spins aligned along $< 100 >$ into the $< 010 >$ direction causes a change twice as high in measured magnetisation along the $< 110 >$ direction than the $< 010 >$ direction. We therefore conclude that spins typically do not reverse direction but rather slowly change direction.

5.3 DC MAGNETOMETRY WITH NV CENTRES

SQUID measurements come with two downsides. First, their spacial resolution is typically limited to many micrometres, i.e. we cannot determine local variations in the magnetic field directly or even determine the magnetic domain sizes. The net field over a sample is generally zero because domains are have random orientations along the *x*- and *y*-axes. Therefore, in order to measure a signal, the sample has to be pre-polarised before a meaningful SQUID measurement can be carried out. This polarisation, however, represents a strong deviation from the conditions under which the measured materials would be normally used. If nano-SQUIDs are used, these problems can be overcome but the temperature range, over which measurements can be conducted, is very limited as nano-SQUIDs have to be operated at a few kelvin [200]. The second issue with SQUIDs is their lacking ability to probe fast time dynamics of the magnetic field which could provide insight into the process of domain formation.

The two disadvantages do not exist if we employ NV centres as magnetometres. They can operate over a large temperature range from essentially 0 K to more than 600 K [195]. Furthermore, as NV centres are point defects, their measurement volume is limited to only a few tens of nanometres. This allows probing the local magnetic field and single domains

without the need for pre-polarisation. In addition, similar to SQUIDs, NV centres are vector field probes. In contrast to SQUIDs, NV centres can also detect AC magnetic fields and, thus, reveal time dynamics of magnetic domains. This is discussed further in Section 5.4.

SETUP

Nanodiamonds with 17 nm mean diameter hosting NV centres are dispersed over the PCMO thin film sample. The small size of nanodiamonds allows probing magnetic fields directly on the surface of the sample. The NV centres in the nanodiamond have a random position and orientation. While the later can be determined by applying a number of external magnetic fields, the position can be revealed by confocal microscopy with sub-micron resolution as described in Section 2.2.

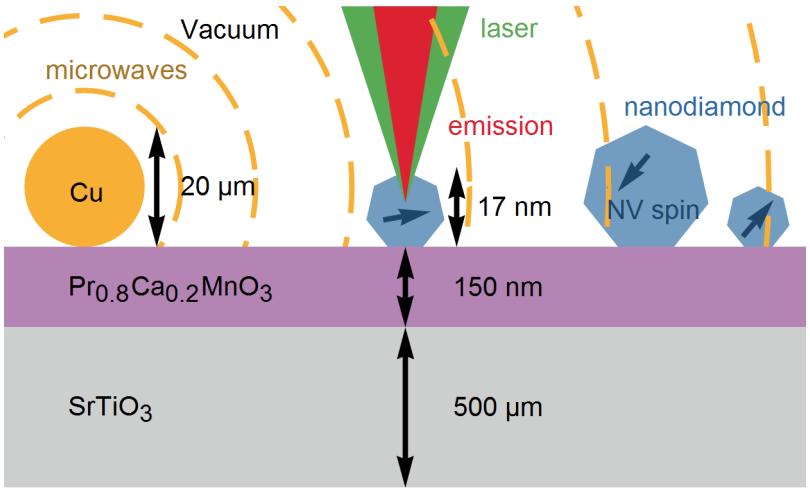

Fig. 5.6 **Schematic representation of the measurement of the magnetic field on the surface of PCMO with NV centres**. The nanodiamonds (blue) are dispersed directly on top of the thin film. They host NV centres whose spin (dark blue) senses the magnetic field environment. In order to prepare and readout the NV centre spin a confocal microscope (not shown) is used. It consists of a 532 nm excitation arm (green) and a collection arm in the red part of the visible spectrum to collect the fluorescence from the NV centre. The NV centre electron spin can be manipulated by microwaves which are generated by a current through a copper wire only a few micrometres away from the investigated NV centres. The laser and the microwaves can be pulsed and the collection of photons can be gated in order to enable controlled coherent manipulation of the NV centre spin.

In Figure 5.6, a cross-Section of the sample is shown. In particular, nanodiamonds on its surface and a copper wire for generating microwaves, which in turn control the NV centre spins, are shown. The sample is contained in a vacuum chamber and can be cooled to 4 K by a Montana dry cryogenic system. Temperatures up to room temperature are in principle feasible. However, at room temperature under vacuum the excitation laser damages the PCMO thin film through local heating.

Not depicted in Figure 5.6 are the radiation shields to prevent heating from thermal radiation and the external objective through which the photons for excitation and collection of fluorescence pass. Apart from minor changes such as the use of different filters, the setup follows the confocal presented in Section 2.2.

ODMR MEASUREMENTS

In order to measure the magnetic field of PCMO we perform ODMR as described in Section 2.5.1 on a number of single emitters. The ODMR splitting between the $|m_s = 0 \leftrightarrow -1\rangle$ and the $|m_s = 0 \leftrightarrow +1\rangle$ transitions directly depends on the magnetic field $\mathrm{B_z}$ at the site of the NV centre along the NV axis and the electric field induced by the strain Π. For small magnetic fields, which lead to shifts much smaller than the ground state splitting $\mathrm{D}_{gs} = 2.87\,\mathrm{GHz}$, the spin splitting follows the equation

$$\delta = 2\sqrt{\left(\frac{\gamma_S}{2\pi}\mathrm{B_z}\right)^2 + \left(\frac{\Pi}{2}\right)^2}, \tag{5.2}$$

where $\gamma_S/(2\pi) = 2.8034\,\mathrm{MHz/G}$ is the electron spin gyromagnetic ratio. The strain splitting Π is typically between 5 and 40 MHz.

The NV centres are dispersed over an area of approximately $500\,\mu\mathrm{m}^2$ and their orientation is unknown. Because NV centres in nanodiamond are typically strained, a small external magnetic field below 10 G is applied. It ensures that the NV centre spins are sensitive to changes in the magnetic field from the PCMO but has potentially a partial coercive effect on the domain formation in the material.

A single run, i.e. sequence of measurements, consists of a cool down to approximately 6 K from which on an ODMR trace is recorded for every emitter every 1.5 K until 130 K are reached. The absolute temperature stability is typically well below 0.1 K. Two such runs have been successfully carried out with the five emitters at four locations. The resulting ODMR measurements are displayed in Figure 5.7 and 5.8.

We observe rich behaviour of the NV centre spin splitting as temperature is increased due to the interplay of the external magnetic field and the field generated by the thin film. At site 12, four distinct peaks can be observed which is a strong indication for two NV centres in a crystal or two crystals hosting NV centres closer than 0.5 µm to each other.

Every ODMR scan can be fit and the frequency of the ODMR resonance can be extracted. The frequencies directly relate to the magnetic field from the sample. At high temperatures, i.e. above 110 K, the SQUID measurements provide strong evidence that the magnetic field from the PCMO is zero. This is consistent with the Curie temperature between 110 K and 115 K measured in $Pr_{0.7}Ca_{0.3}MnO_3$, which has a slightly different chemical composition from the used material [216]. The remaining splitting between the $|m_s = 0 \rightarrow +1\rangle$ and $|m_s = 0 \rightarrow -1\rangle$ transitions is due to the applied external magnetic field and natural strain present in the nanodiamonds.

By comparing the ODMR with the SQUID measurements we can obtain information about the domain sizes. We find that it is highly unlikely that the NV centres, which are dispersed over an area of approximately $30^2\,\mu m^2$, sense the same domain, i.e. show a uniform response, indicating a domain size of 30 µm in diameter or less. For this conclusion we first make the assumption that the magnetic field experienced by all NV centres is proportional to the magnetic moment measured by the SQUID. The ODMR data is then fitted using the SQUID data. The free parameters include two angles for the external magnetic field and ten angles for the five NV centre axes to the domain magnetisation. In addition, a proportionality constant for mapping the moment measured by the SQUID to the actually magnetic field on the surface and the strain splittings of all five emitters are included. If this fit converges with an error comparable to the error on the ODMR data, it is very probable that the NV centres all see the same domain.

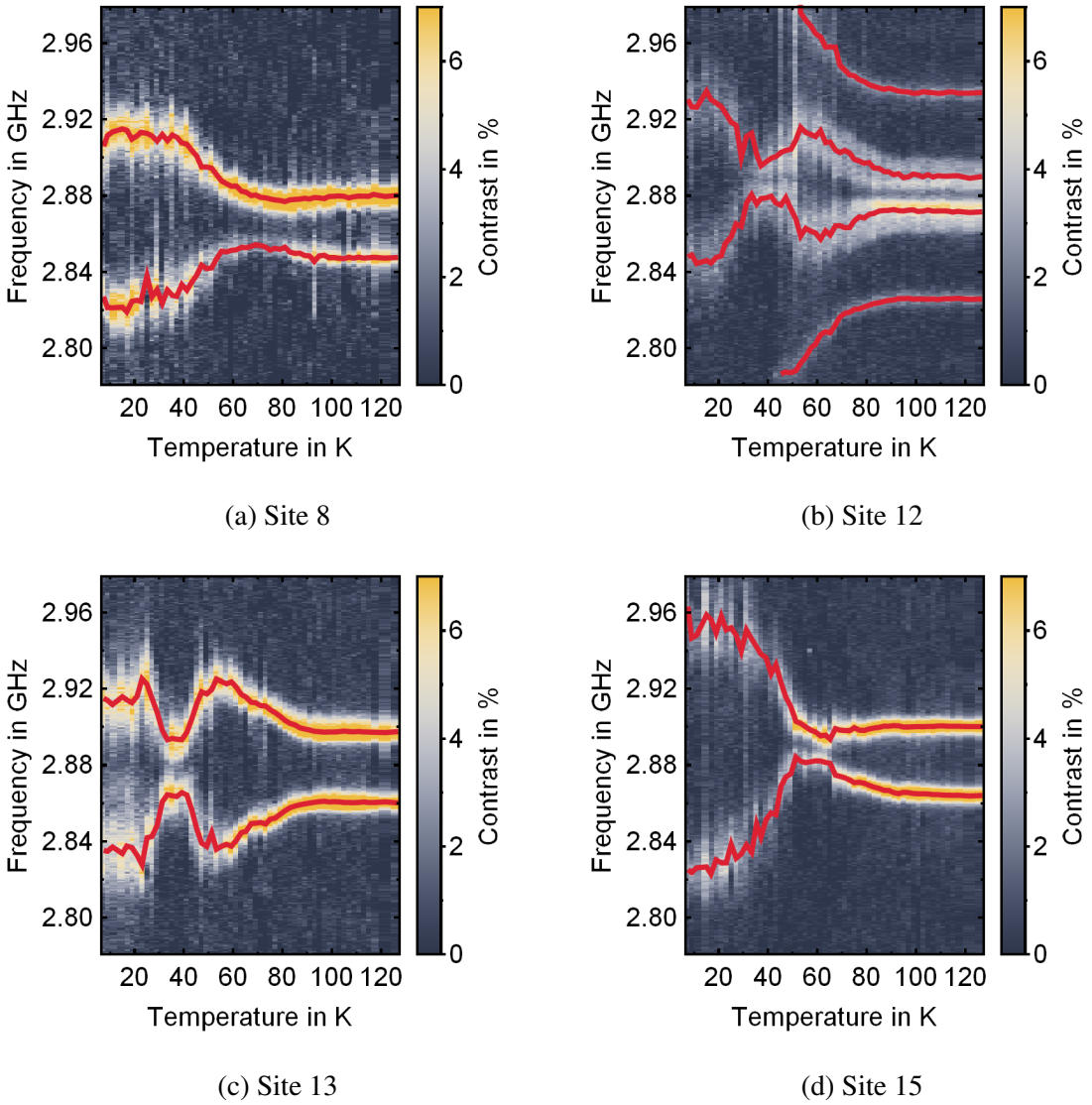

(a) Site 8

(b) Site 12

(c) Site 13

(d) Site 15

Fig. 5.7 **ODMR scans from run number four**. The sample is first cooled down and then, for each emitter an ODMR scan is taken before the temperature is increased for the next set of scans. Typically, one scan takes three hours with each single scan taking two minutes. Bright areas denote dips in the ODMR spectra. The red curves indicate the position of the ODMR resonances extracted from fits to every ODMR scan. The photon counts from each measurement, i.e. every line, has been normalised to ensure comparability of the measurements.

The two runs (see Figure 5.7 and 5.8) on their own can be fit with the single domain assumption. However, the parameters for the fits are highly unstable indicating overfitting.

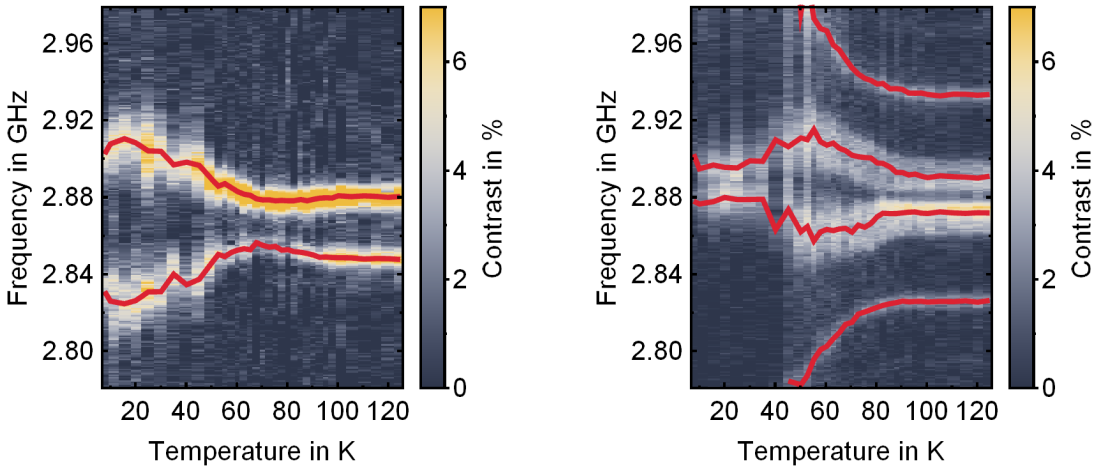

(a) Site 8

(b) Site 12

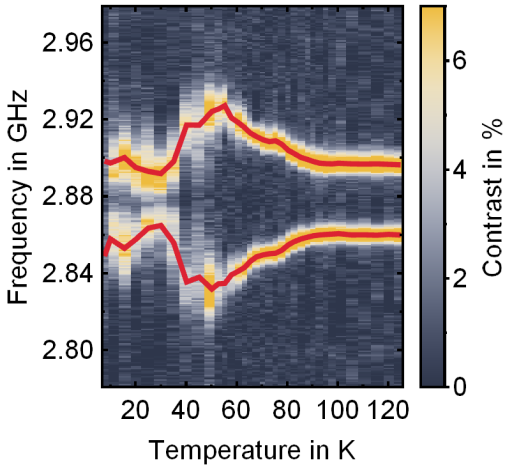

(c) Site 13

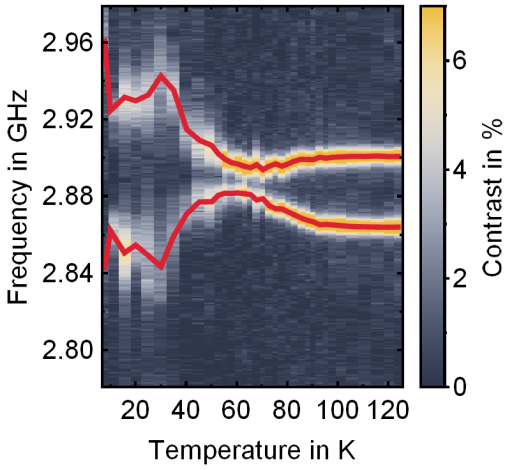

(d) Site 15

Fig. 5.8 **ODMR scans from run number five**. The sample is first cooled down and then, for each emitter an ODMR scan is taken before the temperature is increased for the next set of scans. Typically, one scan takes three hours with each single scan taking two minutes. Bright areas denote dips in the ODMR spectra. The red curves indicate the position of the ODMR resonances extracted from fits to the every ODMR scan. Every line in the displayed data has been rescaled to ensure comparability.

Having measured the NV directions beforehand by applying external magnetic fields from different directions would have very much helped reducing the number of free parameters in the fit and increased the confidence in its results. This approach should be taken in the

future. The best fit was obtained for a SQUID warming field of 6 Oe. This is consistent with a measured remanent field between -10 Oe and 0 Oe, i.e. the net external field at the site of the sample is likely to be 0 Oe at a warming field of 6 Oe.

However, if we try to fit the two runs together with the only distinction between them being a different magnetisation axis of the domain in PCMO (the external field and the axes of the NV centres remain unchanged), no good fit can be found. This is a strong indication that at least in one of the two runs not all NV centres sensed the same domain and, therefore, the response is non-uniform. Fitting the two runs on their own is likely only feasible because of over-fitting with a high number of free parameters. This notion is supported by the high instability of the fits.

By investigating the change in the linewidth of the ODMR scans we can make conclusions on the time dynamics of the magnetic field generated by the PCMO thin film. These are the topic of the next Section.

5.4 Probing time dynamics with NV centres

Until now, it has been very difficult to sense fast time dynamics of magnetic field domains. NV centres provide a unique opportunity to investigate these dynamics. In order to quantify the magnitude of the magnetic field noise, ODMR measurements can be carried out. The linewidths of the transitions gives a good indication of the noise amplitude and studies of successive ODMR scans over time also reveal how much of the noise is on the minute or a faster time scale. To further characterise the noise we conduct Rabi spectroscopy.

From the SQUID measurements we know that the easy axis is (close to) in-plane and that a spin cluster glass is likely to form at non-coercive external magnetic field biases, i.e. B-fields smaller than 30 Oe. The magnetic field to expect from such a sample is concentrated at the domain boundaries as most field lines are in the material. The magnetic noise amplitude should also increase close to the boundaries, as it is only there, where spin flips occur. A non-uniform response of the NV centers would indicate the proximity of different domains.

We find that additional magnetic field noise sets in between 60 K and 80 K which is consistent with the ferromagnetic transition observed in the SQUID measurements in Section 5.2. The maximal observed magnetic noise amplitude reaches between 1.5 G and 6 G depending on the NV centre indicating different distances to domain boundaries or orientations of the NV centre axis with respect to the noise. Slow noise on the minute time scales makes up between 25 % and 50 % of the total noise. This ratio remains relatively constant over different temperatures.

5.4.1 Probing noise using ODMR measurements

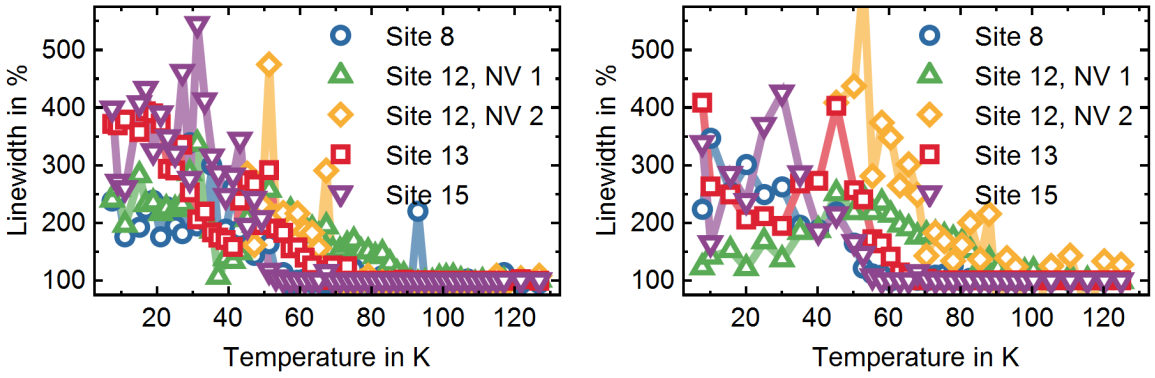

(a) Run 4

(b) Run 5

Fig. 5.9 **Linewidths extracted from the ODMR data in Figure 5.7 and 5.8**. The linewidths are plotted as percentage of the linewidth at high temperature. Qualitatively, the linewidths increase with the amplitude of the magnetic field generated by the PCMO. However, the exact temperature from which the linewidths do increase is different for every NV centre. The increase in linewidth with decreasing temperature is between 100 % and 300 %.

In Figure 5.9 the linewidths for each NV centre and run are plotted vs. temperature. The linewidths roughly follow the magnitude of the spin splitting due to the stray magnetic field from the sample. This is surprising as one would expect the noise to be related to the formation of new domains. Therefore, the noise should first increase when lowering the temperature below the Curie temperature but once the domains are formed the noise is expected to drop to its previous level. There are two explanations for this behaviour. First,

one can imagine the green excitation laser to cause demagnetisation through local heating or direct excitation of the manganese ions which causes domains to become unstable. This is further investigated in Section 5.4.3. And second, domain boundaries move which causes magnetic field noise determined by the distance of the NV centre to the domain boundary. This noise is similar to Backhausen noise which describes the phenomenon of step-like movement of domain boundaries despite a continuously changing external magnetic field.

For run 5 the onset of the magnetic field noise divides the NV centres into two groups. On site 12, both NV centres exhibit a significantly increased linewidth below 100 K while all other NV centres show an increase only below 60 K. For run 4, a similar pattern can be observed with the only difference being that the NV centre at site 13 forms a group on its own. The groups defined by the onset of the magnetic field noise are different from groups defined by the noise magnitude at high magnetic field.

The different behaviour of the NV centres can be explained by their relative distances to domain boundaries. Assuming that magnetic field noise is caused by the formation and movement of domain boundaries, the different onsets of magnetic field noise relate to the temperature at which a spreading domain becomes proximal to the NV centre while the final noise amplitude or linewidth, respectively, can be explained by the distance to the final domain boundary position.

By comparing the ODMR linewidths in Figure 5.9 with the splittings in Figure 5.7 and 5.8 we find that both are highly correlated to each other. This finding supports the idea that the noise is induced by a demagnetising laser and the idea that most noise is generated when domain boundaries move. Such boundaries would create the most magnetic field noise if direct spin flips between them can occur.

5.4.2 Probing noise by Rabi spectroscopy and decomposition of ODMR measurements

We can further characterise the magnetic field noise by investigating its spectrum. Typically, one would use techniques such as dynamical decoupling for this purpose but there are two issues in this concrete case which prevent its application. First, a significant part of the noise

is caused by slow drifts on the minute timescale. NV centres with a homogeneous coherence time T_2 on that order are yet to be discovered. Second, the amplitude of this slow noise is so high that it renders the attempt to apply a π-pulse impossible. For these reasons, we characterise the noise on the minute timescale by investigating the ODMR measurements further but also acquire Rabi curves for each temperature point and emitter to determine the temperature at which the noise starts.

Each ODMR scan consists of 75 single scans which each take two minutes. We can fit an ODMR spectrum to each of these curves. These 75 fits are constrained to have the same amplitude, linewidth and baseline in order to avoid overfitting the data. This linewidth captures only the noise faster than the time it takes for a single scan, i.e. approximately two minutes, while the linewidth obtained from the average of all 75 scans contains information about the slow and fast part of the noise spectrum. For Lorentzian lineshapes linewidths corresponding to different noise sources add up. Therefore the slow noise amplitude can be extracted by subtracting the linewidth for the average fit from the linewidth of the fit to all the single scans.

In Figure 5.10 the total noise or linewidth, respectively, is shown and decomposed into its fast and slow components, where slow means noise on the minute timescale. Clearly, there is no slow noise present until the magnetic field is building up in the PCMO. If there is slow noise present, its fraction of total noise remains relatively stable around 30 % of the total noise or linewidth and approximately 50 % of additional noise due to the formation of magnetic domains. This means the magnetic domains contribute approximately equally to fast and slow noise in the system indicating a broad noise spectrum.

In order to better understand at what temperature the noise starts, i.e. at what temperature the first domains form, we resort to Rabi spectroscopy. This is a technique that has been employed to gain insight into the environment of superconducting qubits [83, 23]. By monitoring the dephasing rate of the Rabi oscillations we can infer the noise amplitude. Geva et al. [63] provide a review on the subject. In essence, the Rabi dephasing rate Γ_2 consists of the longitudinal decay rate Γ_1 which is the inverse of the spin lifetime T_1. In the absence of noise $\Gamma_2 = \frac{1}{2}\Gamma_1$ which corresponds to the well-known statement that the homogeneous

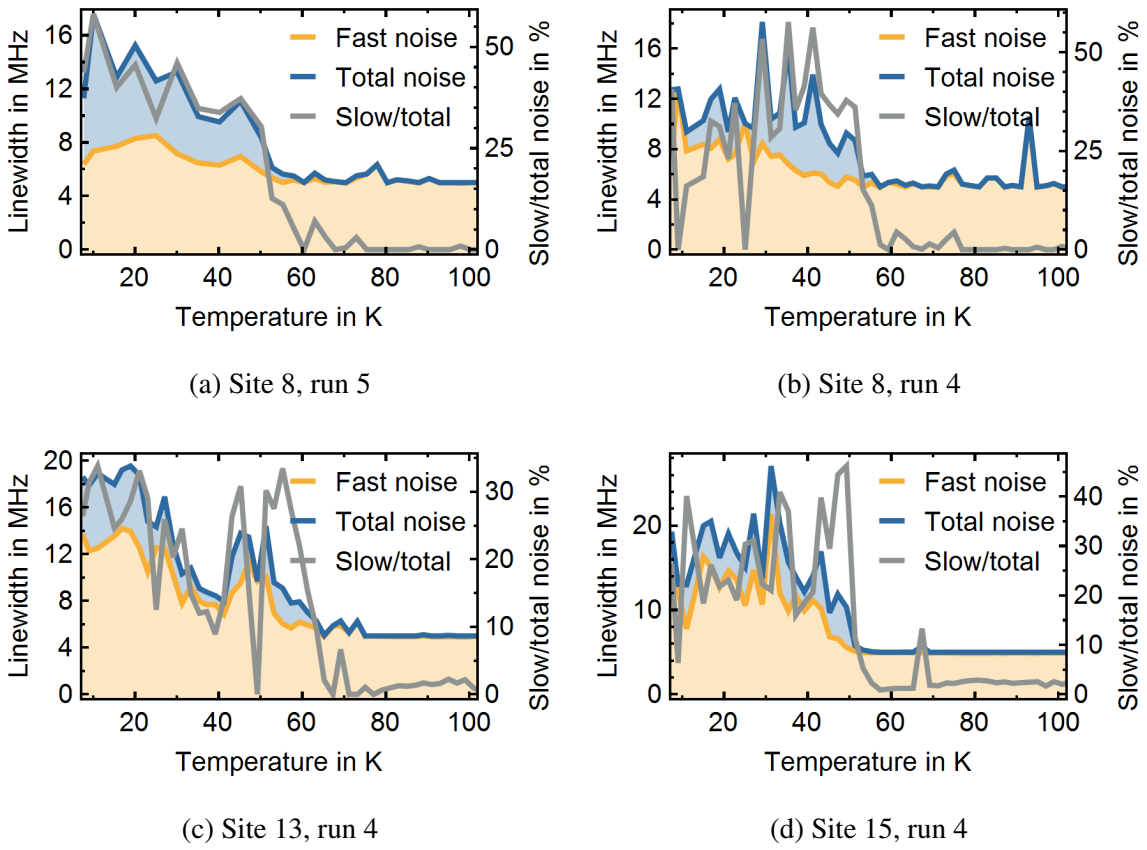

(a) Site 8, run 5

(b) Site 8, run 4

(c) Site 13, run 4

(d) Site 15, run 4

Fig. 5.10 **Noise amplitude decomposed into its fast and slow components**. Slow means here on the minute time scale; to be precise slow is between two minutes and two and a half hours. The orange area denotes fast noise and the blue corresponds to slow noise. The gray line shows the fraction of slow noise in percent. Note that this percentage is displayed on the right vertical axis.

coherence time is limited by half the lifetime. If noise is added to the model, the Rabi decay rate becomes $\Gamma_2 = \frac{1}{2}\Gamma_1 + \Gamma_\nu$, where Γ_ν is the dephasing rate due to the additional noise. In other words we can view a Rabi experiment as a dynamical decoupling experiment, where Γ_ν describes how efficient the decoupling sequence is or how much noise is left over. Therefore, Γ_ν is a measure of the noise in the system.

In Figure 5.11 Rabi curves for different temperatures and NV centres are displayed. Clearly, the Rabi amplitude decays quickly between 50 K and 80 K which can be explained by either a fast decoherence process or slow noise on the resonance transitions. In order to

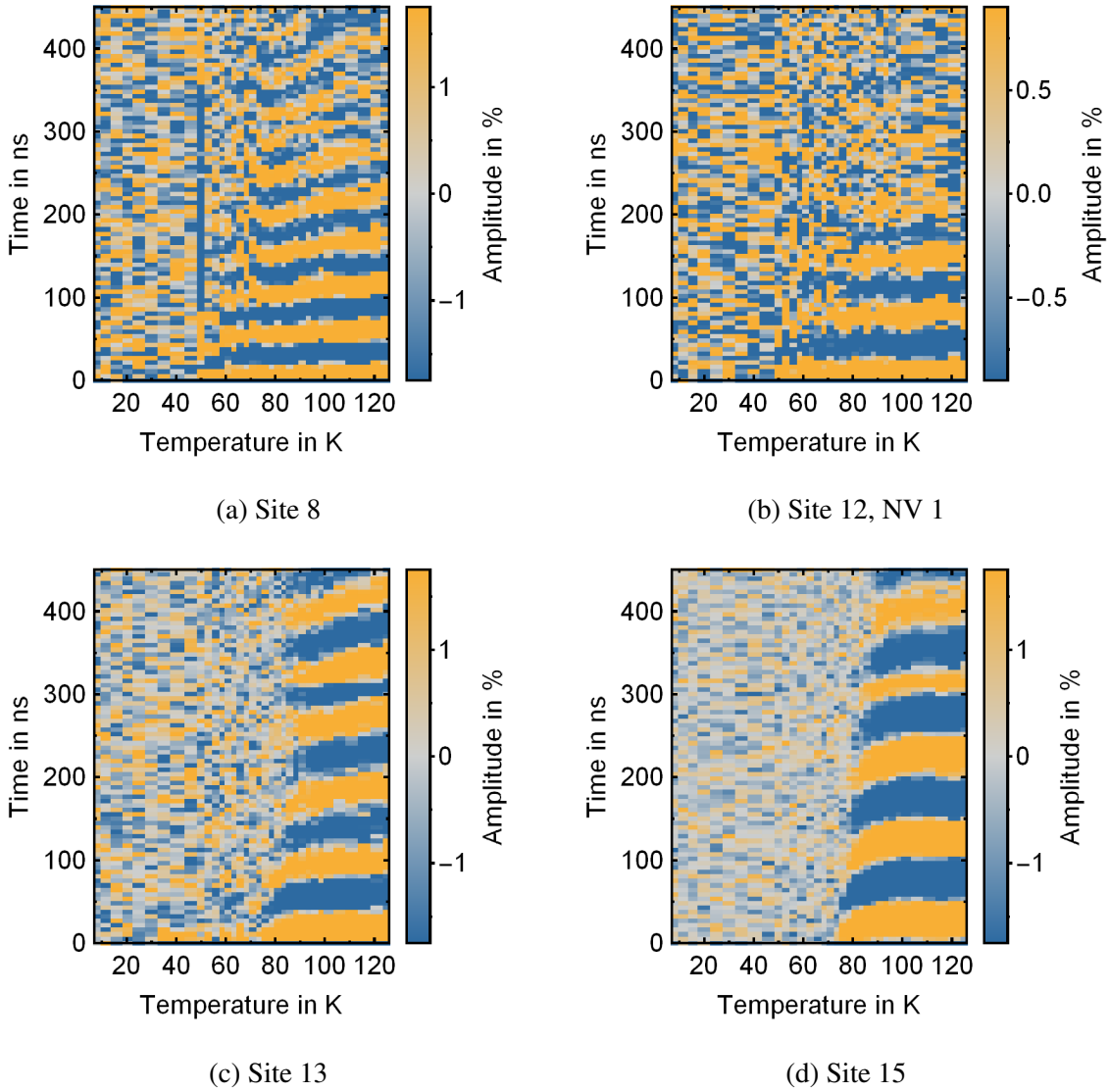

(a) Site 8

(b) Site 12, NV 1

(c) Site 13

(d) Site 15

Fig. 5.11 **Rabi curves of different NV centres at temperatures from 6 K to 130 K**. These measurements were taken at the same time as the ODMR measurements in Figure 5.8, i.e. during run 5. Every (vertical) line in the displayed data has been rescaled to ensure comparability of the measurements.

further investigate this decoherence process, the characteristic parameters of the Rabi curves are plotted in Figure 5.12.

The data in Figure 5.12.a and 5.12.b indicate that magnetic field noise appears or disappears, respectively, at different samples locations at different temperatures. This finding is in line with the ODMR linewidth change in Figure 5.9. However, as the Rabi measurements

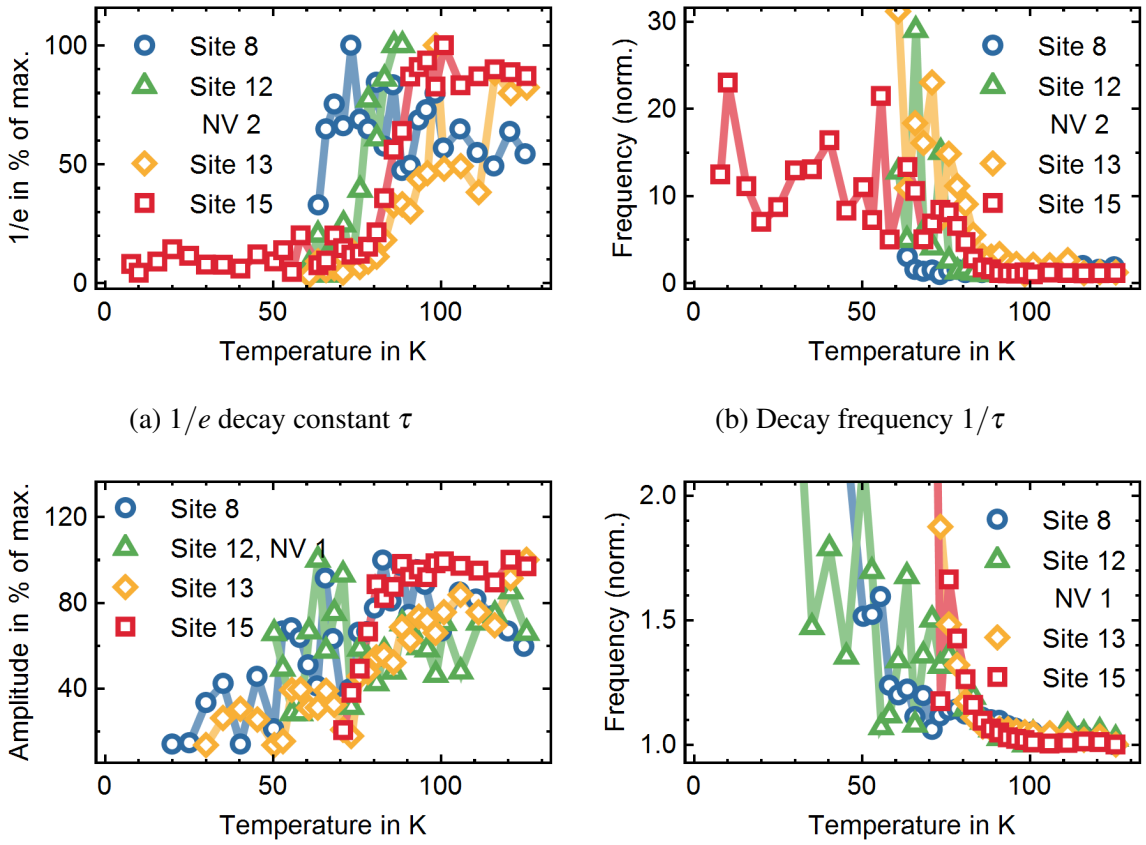

(a) $1/e$ decay constant τ

(b) Decay frequency $1/\tau$

(c) Rabi amplitude

(d) Rabi frequency

Fig. 5.12 **Parameters describing the Rabi curves in Figure 5.11 from run 5**. The parameters have been obtained by fitting each individual curve and are shown if sensible parameters could be extracted which is often not the case for curves with low signal below 50 K. The upper two figures show the decay constant τ and its inverse, the decay frequency $1/\tau$. In the lower two figures the amplitude of the Rabi measurements and the Rabi nutation frequency are displayed.

are more sensitive than ODMR experiments, they allow us to determine the temperature at which domain formation occurs at the site of the NV centres with higher precision.

In Figure 5.12.c and Figure 5.12.d the amplitude and the Rabi nutation frequency are plotted. The amplitude of the oscillations does not increase as rapidly with temperature as the decay parameter τ. This is potentially an artefact due to the low signal in the data. The data for the nutation frequencies which shows faster oscillations at the temperature, where the magnetic field noise arises, indicates that the dephasing is at least significantly due to slow

drifts of the spin transition resonance frequency. These drifts cause the driving microwaves to be slightly detuned which leads to an increased Rabi frequency as described in Section 2.5.2.

The temperature at which the linewidth broadens and the Rabi nutations dephase is surprising as it is not directly related to the magnitude in magnetic field. However, as discussed in Section 5.1 a second transition at 40 K occurs in the material. This noise might be related to the formation of a spin cluster glass and indicate spin flips at the boundaries of ferromagnetic and antiferromagnetic regions.

5.4.3 Local laser induced demagnetisation

One potential source of noise is laser induced demagnetisation. We therefore acquire the ODMR traces for different excitation laser powers of an NV centre in nanodiamond on PCMO at 7 K and extract the ODMR frequency and linewidth as displayed in Figure 5.13.

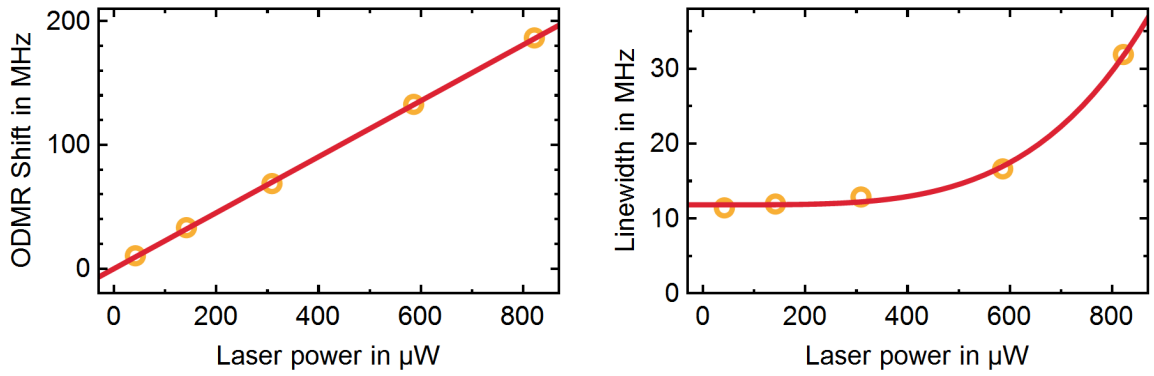

(a) ODMR shift

(b) Linewidth

Fig. 5.13 **Laser induced demagnetisation**. ODMR curves were recorded for different laser powers and the OMDR linewidth and frequency were extracted. The sample is at 7 K and the extracted slope is $0.23\,\mathrm{MHz}(\mu\mathrm{W})^{-1}$. The laser power for all experiments is below 500 µW.

We observe a strong linear relationship between laser power and the Zeeman shift with a slope of $-0.23\,\mathrm{MHz}(\mu\mathrm{W})^{-1}$ which indicates demagnetisation of the sample. In addition, the linewidth increases dramatically at powers above 600 µW, i.e. at powers which are not reached in the presented experiments. The fit in Figure 5.13.b is of the form $a + bs^4$, where a and b are fitting constants and s is the laser power. This function has no physical

interpretation but demonstrates that the relation between linewidth and laser power is highly non-linear.

The demagnetisation mechanism is not known but could stem from two different effects or a combination thereof. First, the laser causes local heating leading the temperature to rise above the Curie temperature. Second, the direct excitation of the manganese ions fundamentally changes the spin interaction in the material. Indeed, two sharp fluorescent peaks were observed at 793.7 nm and 793.9 nm under excitation of the PCMO thin film with a green 532 nm laser whose intensity related linearly to the excitation power. The existence of two transitions split only by a few nanometres might be explained the presence of strain. In addition, double-photon induced ionisation of the NV c3xentre can cause charge noise and explain the rise of the linewidth at very high laser powers as shown in Figure 5.13.b above 600 µW.

As the effect is linear, the data is only compromised if the laser power fluctuations induce noise with an amplitude higher than other noise sources. Given the measured dependence of the ODMR frequency and laser power, power fluctuations of at least 20 µW are necessary to cause broadening of the ODMR frequency by 5 MHz. The typical excitation power is 200 µW. Therefore, a 10 % change in laser power is required to cause fluctuations on the order of the observed noise. In the first order approximation the observed photon count rates are linear in the laser power fluctuations. They vary by less than 5 %. An upper bound for the fluctuations caused by the laser is 50 % of the observed signal. We therefore conclude that, although laser induced demagnetisation is a problem to keep in mind, it is unlikely to compromise the presented data to an extent that it the results are rendered statistically insignificant.

5.5 Conclusions

We have investigated the magnetisation of a 150 nm thick $Pr_{0.8}Ca_{0.2}MnO_3$ thin film on a $SrTiO_3$ substrate by macroscopic and microscopic measurements between 6 K and 150 K.

Macroscopic measurements were carried out with a SQUID. We find two transitions. The first transition is ferromagnetic and occurs at 80 K which is 50 K lower in temperature than measured in bulk diamond. This can be explained by strain in the thin film resulting from a lattice mismatch with its host substrate. We attribute the second transition at 40 K to the formation of a spin cluster glass and the rotation of the easy axis of the magnetisation. In addition, we identify the coercive field strength in- and out-of-plane. They are between 10 G and 30 G, and 300 G and 1000 G, respectively. This difference and the fact that the magnetisation is predominantly in-plane is consistent with minimisation of stray field outside a magnetic material [99].

NV centres in nanodiamond dispersed over the surface of PCMO allow probing single domains and their time dynamics without pre-polarisation of the entire sample as required for macroscopic SQUID measurements. By employing ODMR spectroscopy we can limit the domain size to less than 30 µm and identify magnetic field noise from 0 K to 80 K. The noise amplitude is between 1.5 G and 6 G and approximately 50 % of the noise can be attributed to time dynamics on the minute scale while the remaining noise is faster. We further establish Rabi spectroscopy with NV centres as a very sensitive tool to measure the Curie temperature. In addition, we observe laser induced demagnetisation potentially caused by local heating or direct excitation of the manganese ions. This last finding motivates the selection of materials which are optically transparent at 532 nm for future research.

An improved approach to sense single domains with NV centres is to mount nanodiamonds on the tip of an AFM. Albeit the technical difficulties of this approach, some progress has been made towards the realisation of such a scanning probe NV centre magnetometer [122, 69].

CHAPTER 6

Improving sensitivity and resolution with the nuclear host spin

The host nuclear spin is an intrinsic part of the nitrogen-vacancy centre. In particular, compared to using other proximal spins such as ^{13}C spins, it has the advantage to always be present and couple with the same strength to the NV centre electron spin which can be addressed and initialised optically.

Nuclear spins, due to their lower gyromagnetic moment and reduced sensing volume, are far less sensitive to external noise and, hence, exhibit far longer coherence and lifetimes. Here, we focus on working with the ^{14}N spin ($I = 1$) which occurs far more often than the ^{15}N ($I = 1/2$) spin due its natural abundance of 99.6 %. Obtaining an isotopically pure ^{15}N sample is possible by implanting only ^{15}N into a high grade diamond or delta doping; these techniques are both discussed in Section 3.2. The ^{14}N spin is slightly more complicated to work with as it is a spin $I = 1$ system but offers other advantages as we will discuss in Section 6.5.

Recently, the host nuclear spin has received a lot of attention because it can be used to increase the sensitivity [91, 141, 121, 171], dynamic range [201] and resolution [109, 136, 213, 184, 171, 118, 153, 125] of the NV centre as a magnetometer and can be also employed to create a highly sensitive gyroscope [114, 4, 105]. In this Chapter we discuss how the nuclear spin state can be prepared and how it can be employed to improve the sensing

properties of the NV centre electron spin. In particular, we show that the ^{14}N nuclear spin as a $I = 1$ system can be used to further increase the readout fidelity of the NV centre electron spin. In addition, we present a study on its lifetime and its inhomogeneous coherence time in nanodiamond and show measurements of the electron spin properties at different magnetic fields.

6.1 Polarisation of the host nuclear spin

In order to use the host nuclear spin, we first must be able to prepare its state. There are three pathways to preparation or polarisation, respectively. First, measurement induced polarisation relies on long lifetimes. This method simply works by projecting the spin state of the nucleus into one of its eigenstates by measurement which consists of entanglement with the electron spin using a CNOT gate and subsequent readout of the NV centre electron spin state. After initialisation the spin is transferred to the desired spin state coherently using radio frequency (RF) π-pulses. The main caveat here is that the readout fidelity sets an upper limit for the polarisation fidelity which can lower the achievable sensitivities significantly.

The second and third methods are both based on polarisation transfer of the electron spin state to the nuclear spin. The second method is called dynamic nuclear polarisation and relies on the interaction of the electron with the nuclear spin in the excited state. If a magnetic field is tuned to a value so that this spin exchange requires no energy, the electron spin polarisation is transferred to the nuclear spin. Therefore, long periods, i.e. typically 5 µs, of optically polarising excitation of the electron spin with a green laser lead to initialisation of the nuclear spin. While this method only works at certain magnetic field range, it is remarkably simple to apply. Third and last, the electron spin polarisation can be transferred by applying a SWAP gate consisting of CNOT gates to the electron and nuclear spin. The CNOT gates are made of nuclear (electron) spin selecting microwave (radio frequency) π-pulses on the electron (nuclear) spin.

In the following, we explore the second and third method because of the simplicity of the second and the universality and high fidelities at high magnetic fields of the third.

6.1.1 DYNAMIC NUCLEAR POLARISATION

Dynamic nuclear polarisation (DNP) of the nuclear spin was first observed by Gaebel et al. [59] and further explored by Fuchs et al. [56] and Jacques et al. [86]. In the following we employ a model by Gali [60] which explains the polarisation mechanism for a NV centre with a host ^{15}N spin. Its extension to a host ^{14}N spin is straight forward and requires the consideration of only two additional states. For a detailed review, theoretical description and calculations of how dynamic nuclear polarisation works and is affected by limited coherence refer to Ivády et al. [84]. Other authors who discuss limitations particular in nanodiamonds are Casabianca et al. [24]. A large number of articles also investigate the polarisation transfer to ^{13}C which has lifetimes of the order of minutes even at low external magnetic fields [180, 97, 117, 53, 127, 98, 5, 204, 161].

In order to find the polarisation depending on the magnetic field amplitude, we need to define the polarisation, find the rate of polarisation transfer from the $m_s = 0$ electron spin state to the nuclear spin and then solve the rate equations of the NV centre spin dynamics under non-resonant laser excitation.

We first start by determining the rate of polarisation transfer from the electron spin state to the nuclear spin state in the NV excited state. As the polarisation mechanism only includes a subset of the excited states we can reduce our considerations to the excited state Hamiltonian

$$\hat{\mathrm{H}}_{es} = \mathrm{D}_{es}\hat{\mathrm{S}}_{\mathrm{z}}^2 + \frac{\gamma_S}{2\pi}\mathrm{B}_{\mathrm{z}}\hat{\mathrm{S}}_{\mathrm{z}} + \mathrm{A}_{es}\hat{\mathbf{S}}\cdot\hat{\mathbf{I}}, \tag{6.1}$$

where we have neglected the quadrupole and the Zeeman effect on the nuclear spin as their influence on the energy levels is far smaller than all other energies in the system. A_{es} is the hyperfine interaction in the excited state which has parallel and perpendicular components $\mathrm{A}_{es}^{\parallel}$ and $\mathrm{A}_{es}^{\perp}$, respectively. We solve the time-dependent Schrödinger equation

$$\hat{\mathrm{H}}_{es}\Psi(t) = i\frac{\partial}{\partial t}\Psi(t), \tag{6.2}$$

where $\hbar = 1$ with

$$\hat{\mathrm{H}}_{es} = \begin{pmatrix} \mathrm{D}_{es} + \mathrm{A}_{es}^{\parallel} - \frac{\gamma_s}{2\pi}\mathrm{B_z} & 0 & 0 & 0 & 0 & 0 \\ 0 & \mathrm{D}_{es} - \frac{\gamma_s}{2\pi}\mathrm{B_z} & 0 & \mathrm{A}_{es}^{\perp} & 0 & 0 \\ 0 & 0 & \mathrm{D}_{es} - \mathrm{A}_{es}^{\parallel} - \frac{\gamma_s}{2\pi}\mathrm{B_z} & 0 & \mathrm{A}_{es}^{\perp} & 0 \\ 0 & \mathrm{A}_{es}^{\perp} & 0 & 0 & 0 & 0 \\ 0 & 0 & \mathrm{A}_{es}^{\perp} & 0 & 0 & 0 \\ 0 & 0 & 0 & 0 & 0 & 0 \end{pmatrix} \tag{6.3}$$

and

$$\Psi = \begin{pmatrix} \psi(|-,-\rangle) & \psi(|-,0\rangle) & \psi(|-,+\rangle) & \psi(|0,-\rangle) & \psi(|0,0\rangle) & \psi(|0,+\rangle) \end{pmatrix}^{\mathrm{T}}. \tag{6.4}$$

Here, the convention is that the first number in the kets denotes the electron and the second the host nuclear spin state. The $m_s = +1$ states are not included but their properties can be computed easily from the $m_s = -1$ states by reversing the sign of the magnetic field, i.e. $\mathrm{E}(|+,+\rangle, \mathrm{B_z}) = \mathrm{E}(|-,+\rangle, -\mathrm{B_z})$. By solving the time-independent Schrödinger equation we find the energies of the eigenstates as displayed in Figure 6.1. There is a level anti-crossing in the excited state (ESLAC) because flips between the electron and nuclear spin are allowed if they conserve the total spin number $m_s + m_I$. It should be noted that the applied magnetic field must be along the axis of the NV centre to avoid mixing of the $m_s = 0$ and $m_s = \pm 1$ spin states. Such mixing prevents polarisation of the electron spin and hence polarisation transfer from the electron to the nuclear spin.

In order to determine the flip probabilities, we first examine the eigenstates of the Hamiltonian and then determine the flip rates. In principle four different flips are possible as shown in Figure 6.2: $|0,-\rangle \leftrightarrow |-1,0\rangle$, $|0,0\rangle \leftrightarrow |-1,+\rangle$, $|0,0\rangle \leftrightarrow |+1,-\rangle$, $|0,+\rangle \leftrightarrow |+1,0\rangle$. Therefore, the eigenstates are linear superpositions of the two states in each flip-pair. We define a convention such that the eigenstates can be identified with $|(m_s, m_I) \leftrightarrow (m_s \pm 1, m_I \mp 1)^+\rangle$ and $|(m_s, m_I) \leftrightarrow (m_s \pm 1, m_I \mp 1)^-\rangle$, where $|(m_s, m_I) \leftrightarrow (m_s \pm 1, m_I \mp 1)^+\rangle$ is higher in energy.

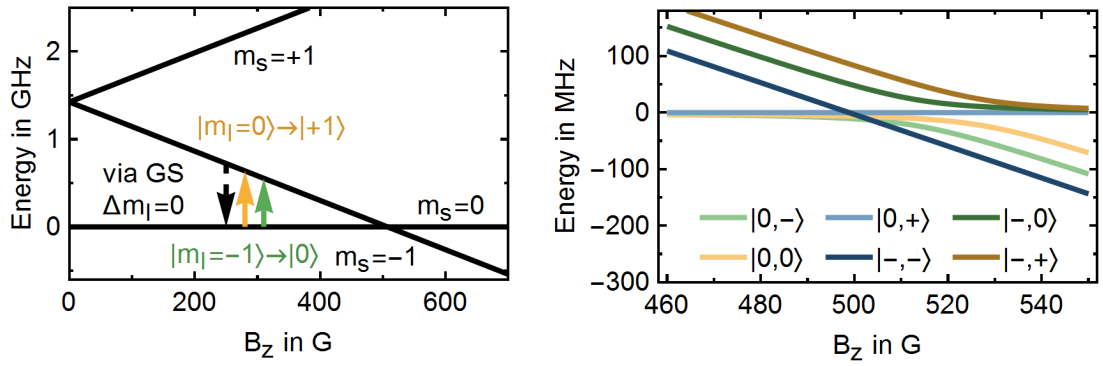

(a) Excited state levels

(b) Zoom in on level anti-crossing

Fig. 6.1 **Excited state level anti-crossing**. (a) the electron spin levels of the excited state depending on the applied magnetic field. The yellow and green arrows represent spin flips of the electron ($m_s = 0$ to $m_s = -1$) with the nuclear spin ($m_I = 0$ to $m_I = +1$ and $m_I = -1$ to $m_I = 0$). The black, dashed arrow denotes polarisation of the electron spin via the ground state into $m_s = 0$. (b) zoom-in on the crossing of the electron spin levels $m_s = -1$ and $m_s = 0$. The legend shows the pure state of the eigenstates at $B_z = 0$ and follows the convention $|m_s, m_I\rangle$. The light and dark blue states do not couple to any other but the light and dark green interact and the light and dark orange can exchange spins.

Given a flip-pair of states $|1\rangle$ and $|2\rangle$ with eigenstates $|+\rangle$ and $|-\rangle$, the eigenstates are

$$|+\rangle = \alpha\,|1\rangle + \beta\,|2\rangle \tag{6.5}$$

$$|-\rangle = \beta\,|1\rangle - \alpha\,|2\rangle\,. \tag{6.6}$$

α and β depend on the magnetic field B_z and $\alpha^2 + \beta^2 = 1$. In the excited state the NV centre spin state precesses between $\alpha\,|+\rangle + \beta\,|-\rangle = |1\rangle$ and $\alpha\,|+\rangle - \beta\,|-\rangle = \left(\alpha^2 - \beta^2\right)|1\rangle + 2\alpha\beta\,|2\rangle$. Therefore, the maximum probability for a flip between $|1\rangle$ and $|2\rangle$ is $P_{\max} = 4\alpha^2\beta^2$.

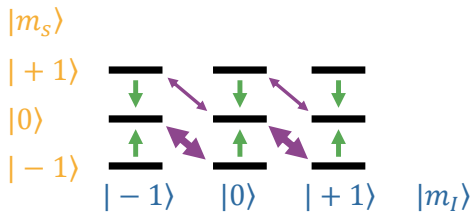

Fig. 6.2 **Flip-flops between electron and nuclear spins**. Shown are all spin levels. Green arrows denote polarisation of the electron spin via optical pumping and purple arrows indicate flip-flops between the spin states. The flip-flop rate is indicated by the size of the arrows. The imbalance in flip-flop rates leads to nuclear polarisation under optical pumping.

We find the eigenstates and eigenenergies by solving the time-dependent Schrödinger equation. The maximum flip probabilities, given $h = 1$, are

$$P_{\max,|(0,0)\leftrightarrow(-,+)\rangle}(\mathrm{B_z}) = \frac{4{\mathrm{A}_{es}^{\perp}}^2}{4{\mathrm{A}_{es}^{\perp}}^2 + \left(\mathrm{D}_{es} - \mathrm{A}_{es}^{\parallel} - \frac{\gamma_S}{2\pi}\mathrm{B_z}\right)^2} \tag{6.7}$$

$$P_{\max,|(0,-)\leftrightarrow(-,0)\rangle}(\mathrm{B_z}) = \frac{4{\mathrm{A}_{es}^{\perp}}^2}{4{\mathrm{A}_{es}^{\perp}}^2 + \left(\mathrm{D}_{es} - \frac{\gamma_S}{2\pi}\mathrm{B_z}\right)^2} \tag{6.8}$$

$$P_{\max,|(0,0)\leftrightarrow(+,-)\rangle}(\mathrm{B_z}) = P_{|0,0\rangle\leftrightarrow|-,+\rangle}(-\mathrm{B_z}) \tag{6.9}$$

$$P_{\max,|(0,+)\leftrightarrow(+,0)\rangle}(\mathrm{B_z}) = P_{|0,+\rangle\leftrightarrow|-,0\rangle}(-\mathrm{B_z}). \tag{6.10}$$

In Figure 6.3 the maximum flip probabilities for $|m_s = 0\rangle \leftrightarrow |m_s = -1\rangle$ are depicted. The flip rates between the states are governed by their energy differences which are

$$\Delta\mathrm{E}_{|(0,0)\leftrightarrow(-,+)\rangle}(\mathrm{B_z}) = \sqrt{4{\mathrm{A}_{es}^{\perp}}^2 + (\mathrm{D}_{es} - \mathrm{A}_{es}^{\parallel} - \frac{\gamma_S}{2\pi}\mathrm{B_z})^2} \tag{6.11}$$

$$\Delta\mathrm{E}_{|(0,-)\leftrightarrow(-,0)\rangle}(\mathrm{B_z}) = \sqrt{4{\mathrm{A}_{es}^{\perp}}^2 + (\mathrm{D}_{es} - \frac{\gamma_S}{2\pi}\mathrm{B_z})^2} \tag{6.12}$$

$$\Delta\mathrm{E}_{|(0,0)\leftrightarrow(+,-)\rangle}(\mathrm{B_z}) = \Delta\mathrm{E}_{|0,0\rangle\leftrightarrow|-,+\rangle}(-\mathrm{B_z}) \tag{6.13}$$

$$\Delta\mathrm{E}_{|(0,+)\leftrightarrow(+,0)\rangle}(\mathrm{B_z}) = \Delta\mathrm{E}_{|0,+\rangle\leftrightarrow|-,0\rangle}(-\mathrm{B_z}). \tag{6.14}$$

The flip rates from state i to j are $\Delta\mathrm{E}_{i\leftrightarrow j}/2$ and therefore the rates are at least of the order of $\mathrm{A}_{es}^{\perp}$ or faster. As $\mathrm{A}_{es}^{\perp} = -23\,\mathrm{MHz}$ [158] and the lifetime of the excited state is 23 ns [82], the

flip rate is higher or of the same order as the lifetime of the state. Therefore, the probability of flipping the two spins can be approximated to be half the maximum probability of a flip.

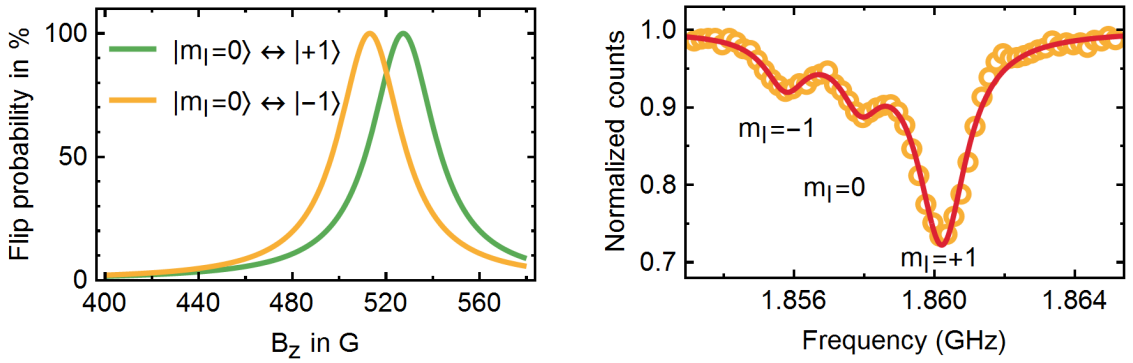

(a) Flip probabilities

(b) Polarised ODMR at 360 G

Fig. 6.3 **Dynamic nuclear polarisation**. (a) flip probabilities for the different nuclear spin states for $|m_s = 0\rangle \leftrightarrow |m_s = -1\rangle$. (b) polarised ODMR at 360 G, i.e. a magnetic field not leading to full polarisation, which has been recorded with sufficiently low microwave power to resolve the hyperfine interaction with the host nuclear spin.

By solving the rate equations for the nuclear spin dynamics we can determine the polarisation at a given magnetic field. They are

$$\Gamma\left(p_0 P_{0\leftrightarrow+1} - p_{+1} P_{+1\leftrightarrow0}\right) + k_{eq}\left(\frac{p_{-1}+p_0}{2} - p_{+1}\right) = 0 \quad (6.15)$$

$$\Gamma\left(p_{+1} P_{+1\leftrightarrow0} + p_{-1} P_{-1\leftrightarrow0} - p_0\left[P_{0\leftrightarrow+1} + P_{0\leftrightarrow-1}\right]\right) + k_{eq}\left(\frac{p_{-1}+p_{+1}}{2} - p_0\right) = 0 \quad (6.16)$$

$$\Gamma\left(p_0 P_{0\leftrightarrow-1} - p_{-1} P_{-1\leftrightarrow0}\right) + k_{eq}\left(\frac{p_0+p_{+1}}{2} - p_{-1}\right) = 0 \quad (6.17)$$

where p_{-1}, p_0 and p_{+1} are populations of the nuclear spin states $m_I \in \{-1, 0, +1\}$. The flip probabilities between states i and j are denoted by $P_{i\leftrightarrow j}$. Γ is the rate of the electron spin polarisation due to optical pumping of the NV centre and k_{eq} is the relaxation rate of the nuclear spin which we assume to be phonon-dominated, i.e. flips between the $m_I = \pm1$ states happen with the same probability as flips between the $m_I = 0$ and $m_I = \pm1$ states.

We define the polarisation (into the $m_I = +1$ state) as

$$P = \frac{p_{+1} - \frac{p_0+p_{-1}}{2}}{p_{+1} + \frac{p_0+p_{-1}}{2}} \tag{6.18}$$

and solve the rate equations. We acquire pulsed ODMR curves as discussed in Section 2.5.3 to confirm the polarisation. In Figure 6.3.b such a polarised ODMR is shown. In Figure 6.4.a a fit to data at different magnetic fields is displayed. As expected, it peaks at the ESLAC at approximately 500 G. We also observe that the polarisation mechanism works in a large range of magnetic fields due to the strong hyperfine interaction in the excited state. The total polarisation reaches almost 100 %. While this might appear to be counter-intuitive on first sight because the maximum electron polarisation in the ground state is smaller, it can be explained by higher electron polarisation in the excited state. This higher polarisation is caused by the different lifetimes of the spin $m_s = 0$ and $m_s = \pm 1$ states. As there is an additional decay path via the singlet states to the ground state available for the $m_s = \pm 1$ states, the $m_s = \pm 1$ states exhibit shorter lifetimes than the $m_s = 0$ state. This increases the average total electron polarisation in the excited state.

An equivalent polarisation mechanism exists in the NV ground state. However, since the hyperfine interaction with the host nuclear spin in the ground state is a factor of 20 smaller compared to the excited state, the polarisation in the excited state dominates even for Zeeman shifts larger than the ground state splitting.

From the fit in Figure 6.4.a, the lifetime of the nuclear spin is estimated to $1/k_{eq} \approx 7\,\mu s$. This value is so small because the nuclear spin performs rapid flip-flops with the electron spin close to the ESLAC. The details of this relaxation mechanism are discussed in Section 6.2.

An important consideration is the time it takes to polarise the nuclear spin. We model the entire Hamiltonian of the NV centre and include Lindblad operators for relaxation and dephasing. Then, we plot the average polarisation of the nuclear and electron spin under optical pumping at half saturation power over time for different magnetic fields in Figure 6.4.b. The electron spin is mostly polarised quicker than the nuclear spin. An exception are magnetic fields close to the ESLAC at 500 G (not shown in Figure 6.4.b). The nuclear spin reaches not

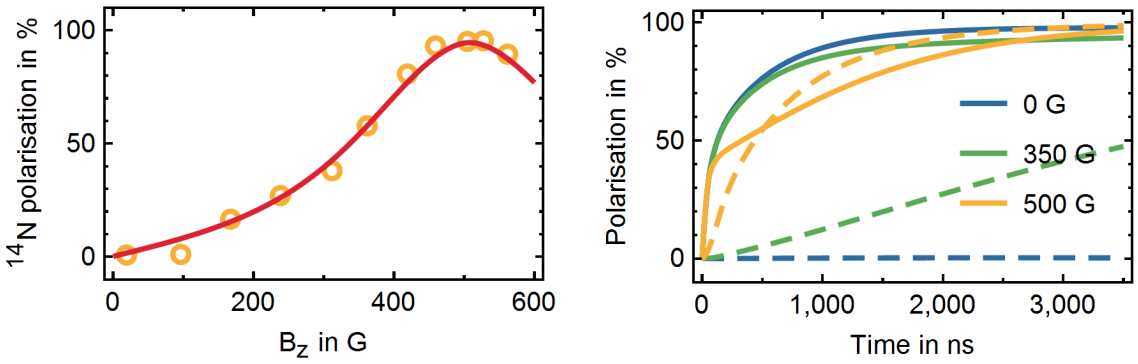

(a) Dependence on magnetic field amplitude

(b) Dependence polarisation time

Fig. 6.4 **Polarisation dependence on magnetic field amplitude and polarisation time**. (a) the polarisation at various magnetic fields along the NV centre axis has been extracted from hyperfine resolving ODMR measurements (orange circles). The red curve is a fit to these data points with the only free fit parameters being the natural depolarisation rate of the nuclear spin and the excitation rate of the NV centre. (b) the polarisations of the electron (solid line) and the nuclear spin (dashed line) for different magnetic field amplitudes along the NV axis. The curves were obtained by using a simplified model of the NV centre spin dynamics.

only higher values of polarisation but is also faster polarised at fields closer to the ESLAC. To ensure reliable polarisation of the nuclear spin, we typically excite the NV centre for 10 µs at half saturation laser power.

6.1.2 Gate induced polarisation

Dynamic nuclear polarisation relies on the applied magnetic field along the NV axis. In particular, it works best at 500 G. However, higher fields are desirable for NMR to increase the precession rate of nuclear spins which as to be on the order of the decoherence rate of the NV centre spin or faster in order to be detectable. Therefore, a universal polarisation mechanism working at arbitrary magnetic fields is an important step towards NMR measurements with NV centres.

There are in principle two alternative routes to polarisation. As mentioned, there is measurement based polarisation which relies on detecting the nuclear spin state by projection through observation. The fidelity of this measurement-based polarisation mechanism depends

on the readout fidelity of the nuclear spin which can be low. In Section 6.5.1 we discuss which fidelities can be reached and on which parameters they depend. A more deterministic approach is gate induced polarisation. In the following, we will explore the mechanism in more detail.

The basic idea is to swap the nuclear and electron spin states by a sequence of CNOT gates consisting of nuclear spin selecting microwave pulses on the electron spin and electron spin selecting RF pulses on the nuclear spin state. The swap operation transfers the polarisation from the electron spin state to the nuclear spin state. Thereafter, the electron spin can be re-polarised by applying a short laser pulse sufficient to polarise the electron but too short to significantly depolarise the nuclear spin. As shown in Section 6.1.1 this requirement prevents operation close or at the ESLAC as the electron spin cannot be polarised at such magnetic fields without affecting the nuclear spin. Nevertheless, gate induced polarisation is the method of choice at magnetic fields above 2000 G and in particular for fields traditionally used for MRI, i.e. 4 T.

In the following, we show how CNOT gates can be used to swap polarisations, introduce a protocol for polarisation which requires less pulses and achieves higher fidelities than a SWAP operation, demonstrate the implementation of CNOT gates and coherent control of the nuclear spin. Eventually, we demonstrate gate induced polarisation at magnetic fields below 10 G and above 2000 G.

SWAP GATE FOR NV CENTRE ELECTRON WITH HOST NUCLEAR ^{14}N SPIN

Up to today, most implementations of gate induced polarisation of NV centre spins were carried out with ^{15}N nuclei. As the ^{15}N is a spin $I = 1/2$ system, only two gates are required for a swap of state populations. However, the lifetime of the nuclear spin is shorter for a NV centre with a ^{15}N host nuclear spin as the hyperfine interaction is stronger. $A_{gs}^{\parallel} = 3.03\,\mathrm{MHz}$ ($A_{gs}^{\perp} = 3.65\,\mathrm{MHz}$ [52]) and $A_{es}^{\parallel} = 61\,\mathrm{MHz}$ ($A_{es}^{\perp}$ has not been measured yet) in the ground and excited state, respectively [56, 58]. This is around 50 % larger than for the ^{14}N spin with $A_{gs}^{\parallel} = -2.162\,\mathrm{MHz}$ [180] ($A_{gs}^{\perp} = -2.65\,\mathrm{MHz}$ [28]) and $A_{es}^{\parallel} = -40\,\mathrm{MHz}$ ($A_{es}^{\perp} = -23\,\mathrm{MHz}$) [158].

We start with the state after optical initialisation of the electron spin and use the $|m_s, m_I\rangle$ convention. The initial state is

$$\Psi = \frac{1}{3}\left(|0,-1\rangle + |0,0\rangle + |0,+1\rangle\right). \tag{6.19}$$

We apply a microwave pulse resonant with the $|0,+1\rangle \leftrightarrow |+1,+1\rangle$ transition. Subsequently, a RF pulse addressing the nuclear spin transition $|+1,0\rangle \leftrightarrow |+1,+1\rangle$ is administered. After this first step the state is

$$\Psi = \frac{1}{3}\left(|0,-1\rangle + |0,0\rangle + |1,0\rangle\right). \tag{6.20}$$

In order to fully swap the populations, a similar set of CNOT gates is used to swap the spin states of state $|0,-1\rangle$. These gates are a microwave pulse resonant with the $|0,-1\rangle \leftrightarrow |-1,-1\rangle$ transition and a RF pulse resonant with the $|-1,0\rangle \leftrightarrow |-1,1\rangle$ transition. The final state is

$$\Psi = \frac{1}{3}\left(|-1,0\rangle + |0,0\rangle + |1,0\rangle\right), \tag{6.21}$$

i.e. the spin states are swapped.

Repetitive transfer of polarisation

We typically reset the electron spin after swapping the state populations of the electron with the nuclear spin because the nuclear spin is randomly polarised and, hence, carries no information. In addition, incoherent state transfer is sufficient as we only aim to polarise the nuclear spin. Coherent state transfer requires us to carry out the nuclear spin manipulations on the timescale of the electron inhomogeneous coherence time T_2^*, which is typically between 0.5-2 µs. So far, this has been only achieved by exploiting adiabatic transfer at the ESLAC [57], i.e. a technique that is tied to magnetic fields very close to 500 G. Resonant RF pulses to swap spin states are on the order of microseconds and are therefore not suitable for coherent transfer.

We can use a sequence of gates that takes advantage of the fact that the nuclear spin carries no information. In particular, we can develop a sequence of gates that can be repeated to transfer more polarisation to the nuclear spin. Repetitive transfer of polarisation is beneficial as the gates operate below unit fidelity which is, as we will see, primarily due to only partial polarisation of the NV centre electron. The main idea is to reset the electron spin after every polarisation step. Therefore, we insert a laser pulse after the first and the final step to reinitialise the electron spin yielding a fully polarised state $\Psi = |0,0\rangle$. By administering a final RF π-pulse any nuclear spin state can be prepared.

CNOT GATES AND COHERENT CONTROL OF THE NUCLEAR SPIN

In order to polarise the nuclear spin and employ it for sensing we need to establish coherent control over the electron and nuclear spins. In Section 2.5.2 we demonstrate control over the electron spin. The two spins are coupled via the hyperfine interaction and the application of a magnetic field can lift the remaining degeneracy of the energy levels. CNOT gates depending on the nuclear spin can therefore be realised by selectively addressing the resonance of only one nuclear or electron spin species. To ensure selective addressing, the Rabi frequency must be smaller than the Zeeman splitting and the hyperfine interaction. Alternatively, the Rabi frequency must be chosen such that a multiple of a 2π-flip is performed on close-by transitions.

Similar to the six addressable transitions of the electron spin, there are six transitions of the nuclear spin determined by the NV centre Hamiltonian which is discussed in Section 2.1.3. We write its nuclear part in the NV ground state as

$$\hat{H} = \hat{H}_I + \hat{H}_{SI}^{\parallel} + \hat{H}_{B,I} \tag{6.22}$$

with

$$\hat{H}_I = P\left[I_z^2 - I(I+1)/3\right] \tag{6.23}$$

$$\hat{H}_{SI}^{\parallel} = A_{gs}^{\parallel}\hat{S}_z\hat{I}_z \tag{6.24}$$

$$\hat{H}_{B,I} = \frac{\gamma_I}{2\pi}B_z I_z. \tag{6.25}$$

where $P = -4.95\,\text{MHz}$ is the quadrupole constant [180], $\frac{\gamma_I}{2\pi} = 307.7\,\text{HzG}^{-1}$ is the gyromagnetic ratio of the ^{14}N nucleus [9] and $A_{gs}^{\parallel} = -2.162\,\text{MHz}$ is longitudinal hyperfine interaction [180]. In Figure 6.5 the energy levels of the nuclear spin are displayed.

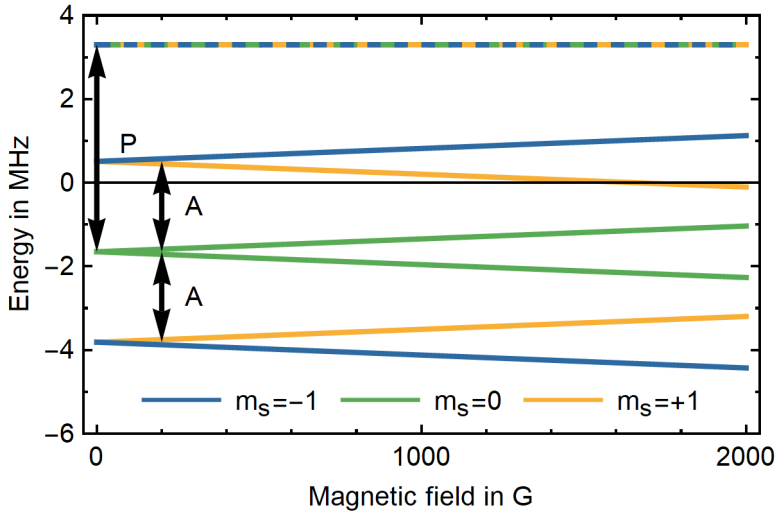

Fig. 6.5 **Nuclear spin energy levels**. The energy levels of the ^{14}N spin are determined by the Hamiltonian in Equation 6.25. The horizontal lines denote states with $m_I = 0$, the upward lines states with $m_I = +1$ and the downward lines states with $m_I = -1$. Only transitions conserving the electron spin number m_s and changing the nuclear spin number by one, i.e. $\Delta m_I = 1$, can be addressed with RF pulses.

We sweep the frequency of an RF pulse to identify the nuclear spin transitions. An example is shown in Figure 6.6. Once the spectrum has been confirmed, we use resonant pulses to coherently drive spin-flips. Despite similar RF driving powers the obtained Rabi measurements at external magnetic fields close to the ESLAC and at 2445 G have different Rabi frequencies. This is due to the pseudo nuclear Zeemann effect which describes an

increase in the nuclear spin gyromagnetic ratio by mixing of the electron spin with the nuclear spin due to the transverse hyperfine interaction [163]. This mixing is reduced at high magnetic fields along the NV centre axis as the transverse magnetic field magnitude becomes negligible compared to the total magnetic field and spin flips are reduced because of the greater energy gap between spin levels induced by the Zeeman effect.

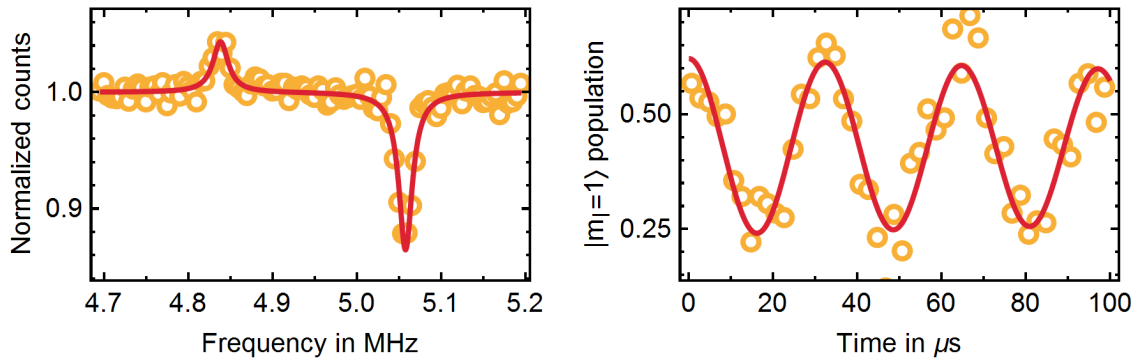

(a) Spectrum of nuclear spin transitions for $m_s = 0$ (b) Rabi of $|0,0\rangle \leftrightarrow |0,+1\rangle$ transition

Fig. 6.6 **Spectrum and Rabi measurements of nuclear spin close to the ESLAC**. (a) spectrum of the nuclear spin which was acquired by sweeping a fixed length RF pulse and probing the population in the $m_I = 0$ state with a nuclear spin selecting microwave pulse. (b) data of a Rabi measurement. Note that the Rabi frequency is one order of magnitude smaller than for the electron spin due to the lower gyromagnetic ratio of the nuclear spin. The nuclear spin needs to be polarised for both experiments before a measurement can be carried out. Here, we used DNP for initialisation of the nuclear spin.

Examples of gate induced polarisation

In order to demonstrate the capabilities of gate induced polarisation, we employ the technique at magnetic fields as low as 11 G and as high as 2445 G. In Figure 6.7 the results are shown and compared to the DNP which cannot be avoided under optical pumping. The achieved gate induced polarisation is limited, first, by the polarisation of the electron which is transferred to the nucleus. It is smaller in the ground state than in the excited state. Second, when re-initialising the electron spin, the NV centre is elevated to its excited state where the spin-flips are caused by mixing of the nuclear and electron spin. The probability of spin-flips

in the ground state can be neglected since it is small compared to the spin-flip probability in the excited state where the transverse hyperfine interaction is approximately 8.7 times stronger.

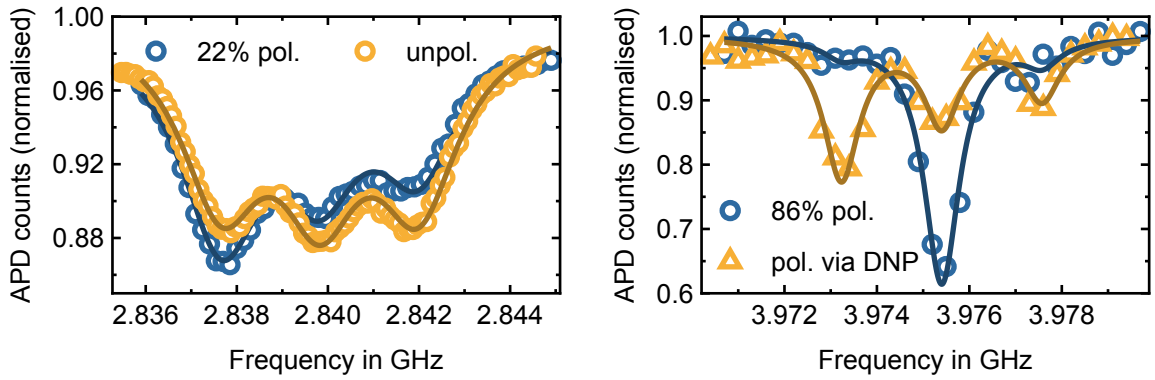

(a) $B_z = 11\,G$ (b) $B_z = 2445\,G$

Fig. 6.7 **Pulsed ODMR after polarisation of the nuclear spin with gates at low and high magnetic field**. Both figures display a pulsed ODMR measurement with (blue) and without (yellow) gate induced polarisation. For gate induced polarisation, the nuclear spin is polarised into the $m_I = -1$ state at low magnetic field and into the $m_I = 0$ state at high magnetic fields.

As shown in Figure 6.7.a at low magnetic fields the strong interaction in the excited state prevents effective polarisation of the nuclear spin. As the energy difference between the $m_s = \pm 1$ states is small, optical pumping does not result in strong polarisation. As demonstrated by the data in Figure 6.7.b the achieved polarisation at high magnetic field is comparable to the electron polarisation as the spin-exchange mechanism in the excited state is slow. However, under continued excitation of the NV centre, the nuclear spin can still become significantly polarised via DNP in the ESLAC.

6.2 Lifetime

Lifetimes of nuclear spins are often on the minute or even hour timescale. However, this is not true for the host nuclear spin of the NV centre. There are a number of relaxation

mechanisms to be considered according to Neumann et al. [141] which are presented in the following.

The ^{14}N nuclear spin is a spin $S_{^{14}\mathrm{N}} = 1$ system and therefore has a quadrupole moment. This quadrupole moment provides a mechanism for decoherence due to electric field noise. Since ^{15}N has spin $S_{^{15}\mathrm{N}} = 1/2$, this relaxation mechanism does not exist. However, for both isotopes, magnetic field noise is relevant as it induces changes in the Zeeman splitting.

The measured electron spin lifetimes of the NV centres used in this thesis vary between 30 µs and 800 µs. The specific NV centre employed for repetitive readout in Section 6.5.1 has a lifetime of approximately 500 µs. Given that the gyromagnetic ratio of the electron spin is 10,000 times higher than of the nuclear spin for NV centres with ^{14}N host spin electric noise from charge traps, magnetic noise from P1 or surface spins would lead to a lifetime of approximately $10,000 \times 500\,\mu\mathrm{s} = 5\,\mathrm{s}$. We will see that other relaxation mechanisms are more important in the excited state. However, in the ground state these noise sources might limit the lifetime.

Phonon induced relaxation via spin orbit coupling is an additional mechanism for relaxation. However, in the NV centre ground state no spin orbit coupling exists and in the excited state it has been shown to average out at ambient conditions [14, 56, 143]. We can therefore consider relaxation due to phonons negligible.

Charge state conversion can be another source of relaxation as there is evidence that the nuclear spin has a shorter lifetime in the NV^0 state [202]. However, an optical spectrum indicates that the NV centre spends close to 100 % of the time in the NV^- state. Additionally, in the ground state the charge state conversion rate is expected to be very small because the NV centre is not constantly ionised by optical pumping.

Differences in the quadrupole moment and the hyperfine interaction in the ground and excited state can in principle lead to spin-flips. However, due to symmetry reasons all tensors are collinear and only a phase is acquired in the excited state [182].

The transverse hyperfine coupling provides a further flip-flop mechanism which can be exploited to polarise the nuclear spin as discussed in Section 6.1.1. This flip-flop mechanism is the dominating cause of nuclear spin relaxation [141]. Anisotropic components of the

hyperfine tensor are zero but would otherwise cause relaxation rates exceeding those caused by transverse coupling. Such is the case for the hyperfine interaction with ^{13}C [45].

In Section 6.1.1 we state the probability for a spin flip in Equations 6.10. We hypothesize that these spin-flips are the dominating source of state population decay and, therefore, the relaxation rate must be proportional to these probabilities. Hence, the lifetime of the nuclear spin goes quadratically with the external magnetic field. The proportionality constant describes how often the nuclear spin is given the opportunity to flip. It depends therefore, first, on how much time the NV centre is in its ground or excited state, second, on the lifetime of the electron spin state and, third, of the magnetic field applied perpendicular to the NV centre axis.

In order to quantify the last effect we solve the Hamiltonian in Equation 6.2 including an external magnetic field perpendicular to the NV axis. The energy differences do not change significantly which means that the steady state polarisation due to DNP remains the same. However, we find that the flip-flop probability in the excited state does increase significantly when applying a perpendicular field. This leads to increased flip-rates in the excited state which we show in Figure 6.8. The increase is of increasing exponential nature but for low magnetic fields below the transverse hyperfine coupling of $-23\,\mathrm{MHz}$ we find decreasing flipping probabilities indicating that a small misalignment of the external magnetic field is beneficial to the nuclear spin lifetimes.

We distinguish six different lifetimes: Three for each nuclear spin state under (no) illumination. Under illumination, the flipping probabilities in the excited state are dominating as the transverse hyperfine interaction is 8.7 times stronger than in the ground state translating to a factor of approximately 123 times higher flipping probability in the excited state at $\mathrm{B_z} = 2445\,\mathrm{G}$. However, most of the time, the NV centre spends in the singlet $^1\mathrm{A}_1$ state which has an approximately eleven times longer lifetime than the excited state. Under strong laser excitation such that the lifetime of the ground state is effectively zero, the NV centre spends 2/3 of its time in the singlet state as it has to be optically cycled a number of times before it decays to the singlet state if it is in the $m_s = 0$ state. This reduces the ratio of the flipping rates with and without laser excitation to $123/3 \approx 40$. The electron spin under

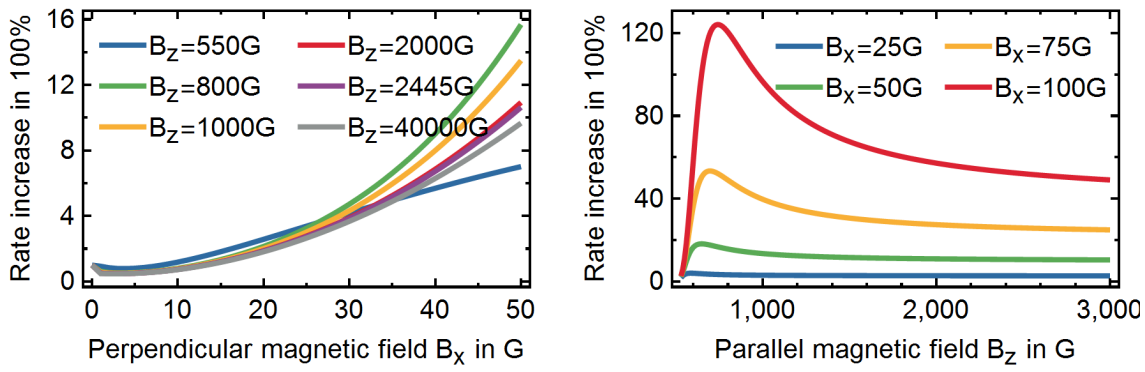

(a) Rate increase by B_x

(b) Rate increase by B_z

Fig. 6.8 **Flip-flop probability in excited state depending on perpendicular external magnetic field**. We solve the excited state Hamiltonian including a perpendicular field and plot the increase in the flip-flop probability between the electron and nuclear spin compared to no perpendicular field. (a) the effect of a perpendicular field on the flip-flop probability. (b) the increase depending on the applied field along the NV axis.

illumination has a lifetime on the order of the time spent in the excited state, i.e. $3 \times 23\,\text{ns}$. Under no illumination the measured lifetime was $\approx 500\,\mu\text{s}$, leading to a ratio of the nuclear spin lifetime in the ground to the excited state of about 283,000.

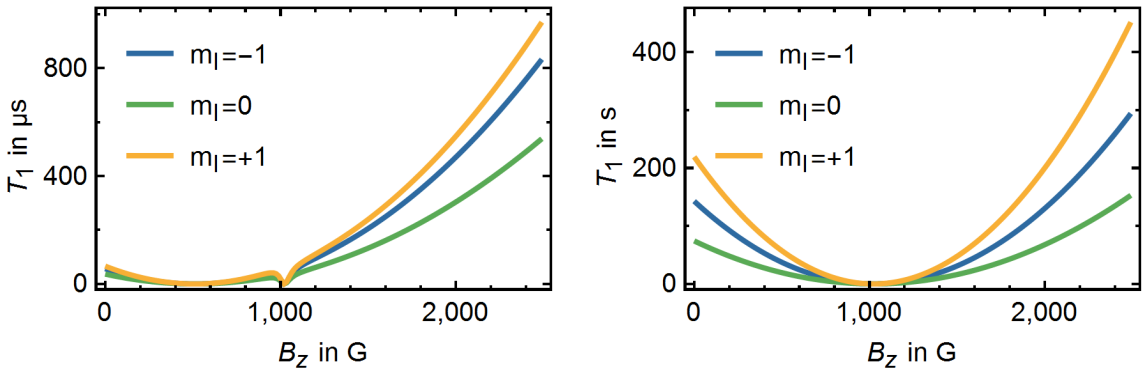

(a) Under illumination

(b) Without laser excitation

Fig. 6.9 **Nuclear spin lifetimes**. The values were obtained by the rate equations under excitation of a strong laser leading to the depletion of the NV centre ground state. Under excitation, the behaviour of the lifetime curve is dominated by spin-flips in the ESLAC but under no optical pumping the spin is only subject to flips in the ground state.

We simulate all rates between the energy levels of the NV centre under (no) illumination and obtain the numbers shown in Figure 6.9. Table 6.1 shows the lifetimes at the magnetic field at which we work to employ repetitive readout. The values were obtained by modelling the excited and ground state with 9 spin levels each, i.e. one for every combination of m_s and m_I states, and three nuclear spin levels in the singlet state.

These lifetimes were calculated under the assumption that the external magnetic field is perfectly aligned with the NV centre axis. Any misalignment would cause mixing of the spin states and reduce the nuclear spin lifetimes. The angles of the external magnet with the sample was found by maximising the photon count rates from the defect which suffer under misalignment due to mixing of the electron spin states. More careful alignment of the external magnetic field with the NV axis could be achieved by monitoring the transition frequencies of the $|m_s = 0\rangle \leftrightarrow |-1\rangle$ and $|m_s = 0\rangle \leftrightarrow |+1\rangle$ transitions. For perfect alignment the ratio of their sum to their difference has a minimum. In addition, we observe long term drifts of $\approx 0.3\,\mathrm{G}$ in the magnetic field along the NV axis which implies that the permanent magnet which generates these fields does move and causes some mixing of the spin states. Due to misalignments in the magnetic field we expect the measured T_1 times presented in Table 6.10 to deviate from the simulated data by a proportionality constant whose dependence on misalignment is shown in Figure 6.8.

m_I	T_1 under illumination (ms)	T_1 under no illumination (s)
+1	1.44 (0.39 or 27 %)	605
0	0.78 (0.17 or 22 %),	243
-1	1.06 (0.37 or 35 %)	536

Table 6.1 **Lifetimes of the NV host nuclear spin**. The values were obtained by solving rate equations for the NV centre at 2445 G. In brackets we denote measured values.

From Table 6.1 we can see that the ratio of $T_{1,gs}/T_{1,es} \approx 500,000$. The measured lifetimes of the nuclear T_1 under no illumination are indeed shorter than the theoretically calculated which indicates a misalignment of the external magnetic field caused by a factor 4 increased flip-rates. This corresponds to approximately 30 G or 100 MHz Zeeman shift according to our

model. Another observation from the simulated lifetimes is that the lifetimes differ by nuclear spin state. We assume only flips with $\Delta m_I = 1$, i.e. the $m_I = 0$ state has the shortest lifetime. The lifetimes of the $m_I = \pm 1$ spin states deviate because, first, the values at $B_z = 2445\,G$ are depending on the time spent in the excited state, i.e. the exact excitation power and, second, the flip-flop probabilities are lower for flip-flops with the $m_s = +1$ state as indicated by Figure 6.2 and Equations 6.10 because the energy difference between the $m_s = +1$ and the $m_s = 0$ states is larger. The simulated figures and ratios are in good agreement with previous experimental work by Neumann et al. [141].

In Figure 6.10.c and 6.10.d we present data showing that the lifetime does not reduce over at least 30 ms under no illumination. An additional data point at 70 ms, which is not shown here, was taken to confirm that no decay is observed even for long delays as expected from the results of the rate equation model in Table 6.1. We present data for two different nuclear spin states to ensure that the observed states do not represent the steady state of the ground spin polarisation. The decay of a small fraction of the polarisation has a time constant of approximately 7 ms and appears to increase the population in the $m_I = \pm 1$ states at the expense of the $m_I = 0$ state. We attribute this decay to the relaxation of the nuclear spin state in the NV^0 charge state which is expected to be far faster than in the NV^- state [202]. The NV centre is last excited after polarisation into the $m_I = 0$ state after which a conditional RF π-pulse is applied to prepare the desired nuclear spin state. Therefore, the nuclear spin of a NV centre which is ionised to a NV^0 has a spin polarised into the $m_I = 0$ explaining why the population in the $m_I = 0$ state is reduced.

6.3 INHOMOGENEOUS COHERENCE TIME

In isotopically pure diamond coherence times of 7 ms for ^{14}N [201] were observed which is short given that the nuclear gyromagnetic ratio is 10,000 times larger for the electron spin [9]. There are four mechanisms that can lead to dephasing of the nuclear spin. First, electric field fluctuations change the quadrupole moment of the nuclear spin. Second, magnetic field fluctuations cause noise via the Zeeman effect. As the gyromagnetic ration is small such

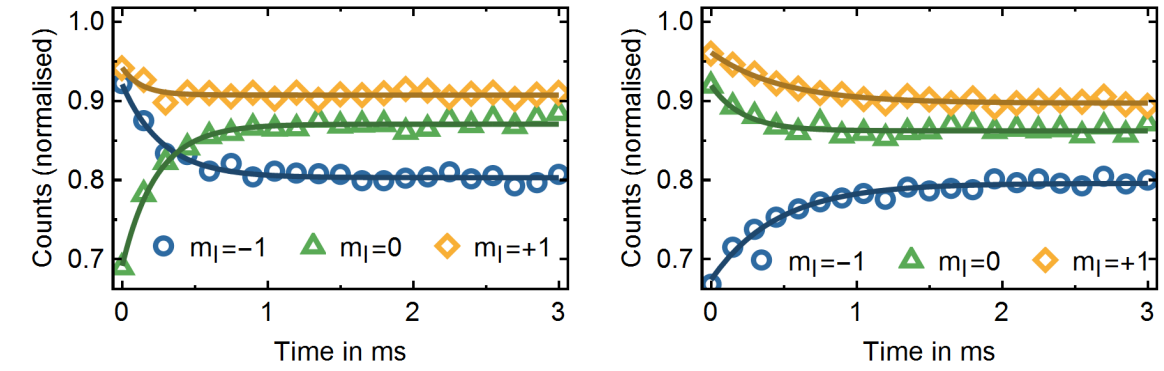

(a) Polarisation into $m_I = 0$ under illumination

(b) Polarisation into $m_I = -1$ under illumination

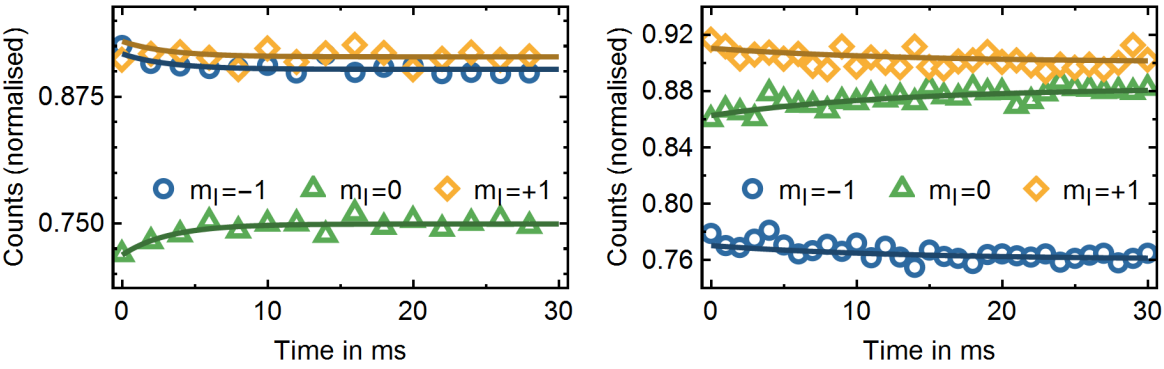

(c) Polarisation into $m_I = 0$

(d) Polarisation into $m_I = -1$

Fig. 6.10 **Nuclear spin lifetimes**. First, the nuclear spin is polarised. Then, (a, b) we excite the NV centre or (c, d) wait for time τ and probe all three nuclear spin states by applying selective microwave pulses on the $m_s = 0 \leftrightarrow m_s = -1$ transitions repetitively as discussed in Section 6.5.1. The resulting counts are plotted, i.e. lower counts denote higher population in the spin state. (a, c) the lifetime of the $m_I = 0$ nuclear spin state. (b, d) the T_1 of the $m_I = -1$ state. Data for the $m_I = +1$ state was taken, shows similar behaviour, but is not shown here.

fluctuations are typically negligible. Third, as the nuclear spin is coupled to the NV centre electron spin, electron spin flips cause a change in the hyperfine coupling. Hence, the nuclear spin free induction decay is limited by the electron spin lifetime. This is particularly true for emitters in nanodiamond where the electron spin lifetime does not reach milliseconds. Fourth, by excitation of the NV centre the hyperfine and quadrupole coupling strengths change causing stochastic phase acquisition as the electron decays spontaneously to the ground state.

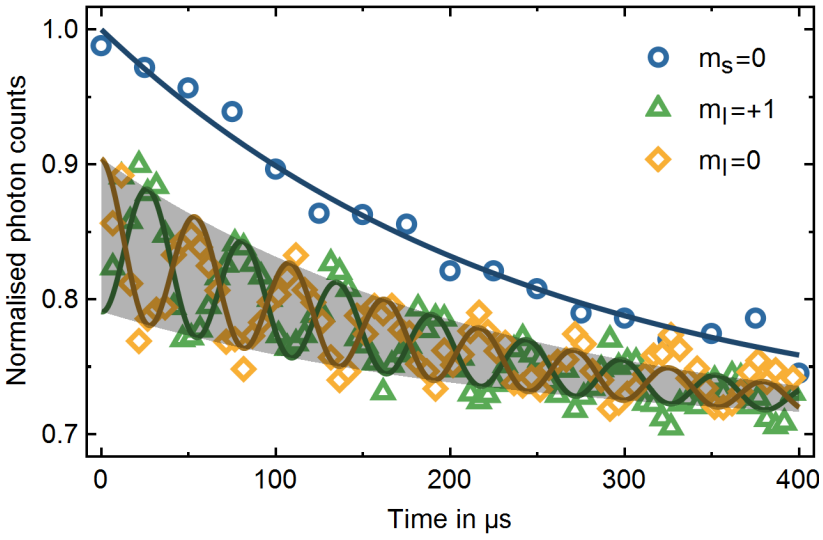

Fig. 6.11 **Inhomogeneous nuclear coherence time and electron lifetime close to the ESLAC**. The blue curve is obtained by first initialising the electron spin and subsequent probing of the NV brightness after a given time. It therefore is a $T_{1,e}$ measurement of the electron spin $m_s = 0$ state. We fit a decay constant of $225 \pm 25\,\mu s$. The green and yellow curves probe the fluorescence of the $|m_s = -1, m_I = +1\rangle$ and the $|m_s = -1, m_I = 0\rangle$ states after dynamic nuclear polarisation into the $m_I = +1$ state and a Ramsey sequence on the $|m_I = 0\rangle \leftrightarrow |+1\rangle$ transition. We obtain a decay constant of $241 \pm 41\,\mu s$.

In Figure 6.11 we show a Ramsey measurement of the nuclear spin and a measurement of the electron spin lifetime at an external magnetic field close to the ESLAC. The downward trend of the Ramsey signal can be attributed to the relaxing electron spin. We find that the electron lifetime $T_{1,e} = 225 \pm 25\,\mu s$ while the nuclear free induction decay $T^*_{2,n} = 241 \pm 41\,\mu s$ which indicates as expected that the nuclear spin inhomogeneous coherence time is limited by the electron spin lifetime. Note that the displayed measurements were carried out using a different NV centre than in Section 6.5 and 6.2. However, we also confirmed for the emitter used in these Sections that the $T^*_{2,n}$ is limited by the electron spin lifetime $T_{1,e} = 454\,\mu s$ at an external magnetic field of 2445 G.

One should be able to decouple from electron spin flip-flops by driving the electron spin into a motional narrowing regime, i.e. decoupling the m_s spin levels faster than the hyperfine coupling which is -2.162 MHz [180]. However, both the $|m_s = 0\rangle \leftrightarrow |-1\rangle$ and

the $|m_s = 0\rangle \leftrightarrow |+1\rangle$ transitions have to be decoupled simultaneously to achieve significant improvements. A similar problem arises in sensing as the magnetic field noise from the electron spin can cause broadening of the NMR signal from nuclear spins. However, the far smaller hyperfine interaction with these nuclear spins requires a far smaller number of decoupling pulses [171]. In addition, another path of decoupling opens with proximal ^{13}C nuclear spins. The electron spin can be re-polarised optically into the $m_s = 0$ state at timescales faster than the hyperfine coupling. However, this is not possible if the hyperfine interaction is as strong as for the host nuclear nitrogen spin.

6.4 Electron spin properties

In Table 6.2 we display the spin properties of the NV centre which we use for the lifetime measurements of the nuclear spin states. The free induction decay of 1.1 µs approaches the 1.7 µs measured in bulk diamond [30] and corresponds to an impurity concentration of only ≈ 7 ppm [206]. According to Klauder and Anderson [100] the inhomogeneous coherence time $T_2^* = \sqrt{2}/b$, where b is the coupling strength of the NV centre with the bath. We observe a decrease in the free induction decay at high magnetic fields which indicates a stronger coupled bath. The free induction decay of Gaussian shape lets us extract T_2^* of 1.1 µs and 0.83 µs which correspond to coupling strengths of 1.3 μs^{-1} and 1.7 $\mu s^{-}1$, respectively. The increase in the coupling strength is due to a misaligned magnetic field causing mixing of the NV electron spin with the bath [30].

From Hahn-echos we extract the shape parameter $\alpha \approx 3.0$ at low magnetic fields which indicates very slow bath dynamics [100]. At high magnetic fields α decreases to 1.6 and the coherence time increases to 14.4 µs. Fits to the respective curves indicate that the inter-bath correlation time τ_C increases from at 34 µs to 677 µs. A number of relaxation and dephasing mechanisms or a combination of them could constitute the reason for the observed changes. Sources for decoherence and relaxation are magnetic or electric. Magnetic noise is due to nearby nuclear spins such as nitrogen or ^{13}C nuclei and electron spins such as surface spins or P1 centres, which consist of the electrons belonging to nitrogen impurities. Electric noise

Property	T_2^* in µs	T_2 in µs, α	T_1 in µs
≈ 100 G (small)	1.1	6.5, 3.0	181
510 G (ESLAC)	-	-	81
2445 G (high)	0.83	14.4, 1.6	454

Table 6.2 **Properties of the NV centre electron spin at selected external magnetic fields**. The inhomogeneous coherence time T_2^* was obtained using a Ramsey measurement, the homogeneous coherence time T_2 and α are the optimized fit parameters to a curve acquired using a Hahn-echo sequence and the lifetime T_1 relates to the lifetime of the $m_s = 0$ spin state.

is caused by charges on the surface or inhomogeneous strain and is suppressed as $\propto 1/\mathrm{B_z}$ for $\gamma_S \mathrm{B_z} \gg d_{gs}\mathrm{E}$, where d_{gs} is the dipole strength in the NV centre ground state. Given an increase in the bath-to-spin coupling we can assume that this NV centre is not dominated by electric noise which would lead to a decrease. The defect is likely far away from the surface and, thus, hosted by a large nanodiamond. The increased inter-bath correlation time can be explained by an increased energy splitting required for a spin flip and therefore leading to reduced bath dynamics [72]. The splitting is caused by the Zeeman effect which is proportional to the external magnetic field.

The lifetime also benefits from such slowed spin dynamics. The reduced lifetime close to 510 G, however, cannot be explained by increasingly frozen spins. Assuming that the bath spins are $S = 1/2$ systems, their Zeeman energy splitting at 0 G is 0 MHz while the energy difference between the NV centre $m_s = 0$ and $m_s = -1$ states is the ground state splitting $D_{gs} = 2.87$ GHz. However, at an external magnetic field of 510 G these energy differences are 1.429 GHz and 1.440 GHz which means there is only an energy difference of 11.6 MHz to prevent flip-flops between the bath and the NV centre ground state spin. Given this small difference flip-flops between the NV centre and bath spins are directly possible explaining the reduction in lifetime close to the ESLAC.

6.5 Applications of the host nuclear spin

The host nuclear spin can be employed as a quantum memory for the electron spin state. However, as coherent transfer would require a CNOT gate on the timescale of the electron T_2^* which is below 2 µs only the population or phase (by mapping to poplation) can be stored. Therefore, the lifetime of the nuclear spin state determines the storage time. Based on this memory hybrid systems of the NV centre electron and nuclear spin have been developed. Efforts have focused on increasing the electron spin readout fidelity to single-shot [91, 141, 121, 171] and on increasing the resolution of NMR techniques to almost 10 kHz [109, 136, 213, 184, 171, 118, 153, 125].

The coherence time of the nuclear spin is of lesser interest for sensing than the lifetime because the gyromagnetic ratio of the ^{14}N nuclear spin is a factor 10,000 smaller than of the electron spin. The acquisition of a geometric phase is an exception because it does not rely on the external field to spin coupling strength and therefore the host nuclear spin's inhomogeous coherence time or the free induction decay, respectively, limits some proposals of gyroscopes with ensembles of NV centres [114, 4]. However, most recently, a technique based on non-Abelian geometric phase has been presented which is predicted to increase the sensitivity by an order of magnitude. The sensitivity stated in the proposal is limited by the lifetime of the electron spin but the method should equally apply to the nuclear spin [105]. Hence, a more important application limited by the coherence time of the nuclear spin is sensing magnetic fields with a large dynamic range. By performing Ramsey interferometry with the nuclear spin the dynamic range of the NV centre can be increased by more than two orders of magnitude to up to 160 G [201].

In this Section, we will first explore ways to increase the readout fidelity of the electron spin in detail and then discuss how the nuclear spin can be employed to increase the resolution of NMR techniques.

6.5.1 Increasing sensitivity by repetitive readout of the electron spin state

Optical readout of the NV centre electron is traditionally performed in two different ways: First, at low temperature, resonant excitation can select for spin levels and therefore has fidelities well above 90 % [182]. Second, non-resonant readout relies on different decay rates of the $m_s = \pm 1$ states compared to the $m_s = 0$ state into the dark singlet state via the ISC. This leads to different fluorescence strengths of the NV centre depending on its spin state. While the former readout mechanism is not available at room temperature due to phonon broadening of the transitions, the later shows fidelities far below the single shot threshold which is defined as a signal-to-noise ratio of one. Alternative readout mechanisms based on selective charge-state conversion have been explored [78] but are not practical for NV centres in nanodiamond because electrical contacts cannot be patterned on nanocrystals.

This leaves us with optical non-resonant readout of the spin state. Polarisation and readout rely on the same spin dynamics. Hence, the readout is destructive, i.e. the lifetime of the electron spin under green laser illumination is on the timescale of the readout. The idea of repetitive readout, which has been first investigated by Jiang et al. [91] and since then applied with great success [121, 171], is to store the spin state in a memory with a long lifetime under illumination. The stored state can be re-transferred to the electron spin state after every optical readout cycle. Therefore, the electron spin can be effectively read multiple times; the exact number depends on the lifetime of the memory. A natural choice for the memory is a proximal nuclear spin. As the host nuclear nitrogen spin is an intrinsic part of the defect it does not have to be engineered separately and thus is always available. In addition, at magnetic fields above 2000 G aligned with the NV centre axis, its lifetime under illumination is many orders of magnitude greater than the NV centre electron spin T_1. As the lifetime is dominated by interactions with the electron spin no differences exist between bulk and nanodiamond. The aspects of the nuclear spin lifetime are discussed in Section 6.2.

SIMPLE REPETITIVE READOUT

Repetitive readout requires preparation of the memory plus storage and retrieval of a state. Preparation is implemented by gate induced polarisation of the nuclear spin as presented in Section 6.1.2. We typically apply the nuclear spin polarisation sequence $N_p = 4$ times to increase the state initialisation fidelities. Storage is achieved by a CNOT gate, i.e. in this case a RF π-pulse on the nuclear spin conditional on the electron spin state. We similarly use a microwave π-pulse on the electron spin for repetitive retrieval for N_r times. In Figure 6.12 the pulse sequence required is displayed and in Figure 6.13 an example of repetitive readout is shown.

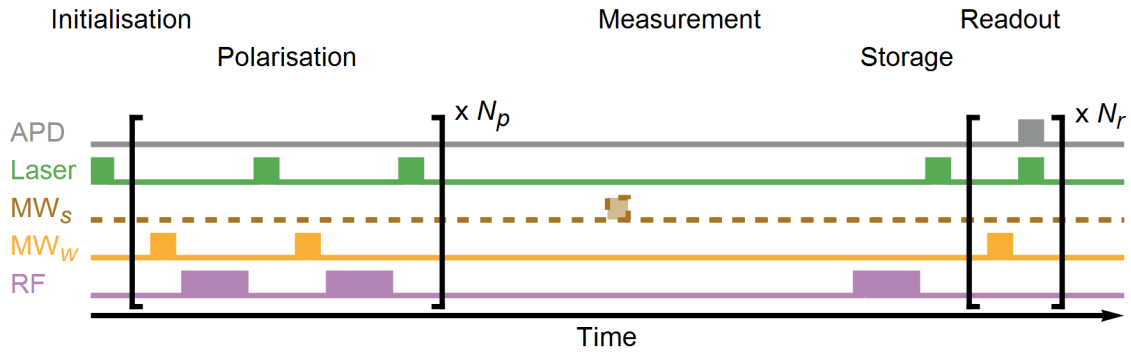

Fig. 6.12 **Repetitive readout pulses**. Five different channels are shown. MW$_s$ stands for 'strong' microwaves with a high amplitude, i.e. the power broadening exceeds the hyperfine coupling so that all nuclear spin sub-levels are addressed equally. MW$_w$ indicates 'weak' microwaves that do resolve the hyperfine coupling and select for a nuclear spin state. The microwave and radio frequency pulses are all π-pulses. They are not all of the same frequency in order to avoid displaying a large number of channels. The polarisation sequence is slightly modified from the sequence discussed in Section 6.1.2 to account for the finite lifetime of the electron spin. It is repeated N_p times after which a measurement such as a AC magnetic field sensing sequence can be performed. The state of the nuclear spin is transferred to the nuclear spin before it is read N_r times.

We can choose two out of three nuclear spin states into which the electron spin state is mapped. In addition, we can either read out on the $|m_s = 0\rangle \leftrightarrow |+1\rangle$ or $|m_s = 0\rangle \leftrightarrow |-1\rangle$ transition. Our microwave equipment is mostly designed for frequencies up to 4 GHz which would restrict us to the $|m_s = 0\rangle \leftrightarrow |-1\rangle$ transition. However, addressing the $|m_s = 0\rangle \leftrightarrow$

$|+1\rangle$ at $\approx 9.2\,\text{GHz}$ is possible albeit four times higher power at the output of the AWG is required to achieve the same Rabi frequency. We test combinations of storage and readout transitions to confirm that there are differences as indicated by the coupling strength displayed in Figure 6.2.

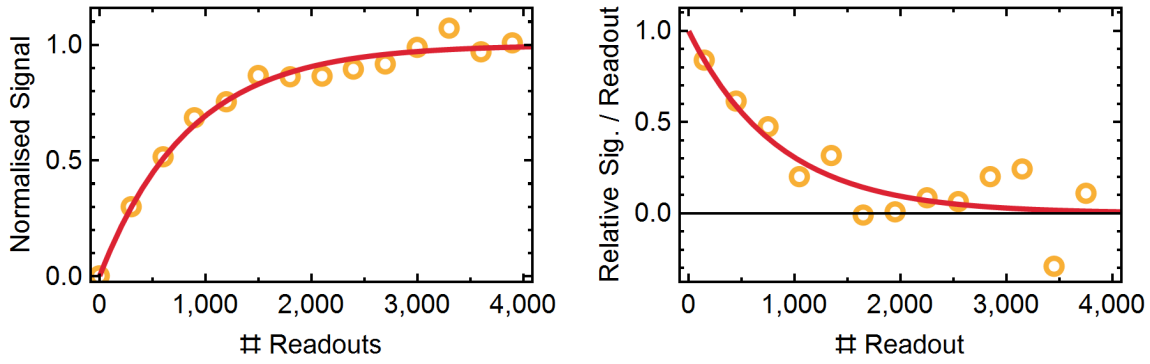

(a) Signal

(b) Signal per additional readout

Fig. 6.13 **Repetitive readout signal**. The repetitive readout sequence in Figure 6.12 was run once with a blank measurement and once with a π-pulse on the electron spin as measurement.(a) their difference in photon count for different numbers of readout cycles N_r. An exponential curve was fit which has a decay constant of $N_r|_{S=1/e} = 844$. (b) no new data or fit, but the (discrete) derivative of data in (a) was taken. Hence, (b) shows the signal amplitude per single readout.

According to these coupling strengths between the different spin sub-levels the best combination is storage in $m_I = \pm 1$ and readout on $|m_s = 0, m_I = +1\rangle \leftrightarrow |+1,+1\rangle$ because this scheme provides the least coupling of the nuclear with the electron spin and leads to the highest lifetime of a state stored in the $m_I = +1$ and $m_I \in \{-1,0\}$ manifolds. As we can see from measurements presented in Table 6.3 this is indeed the case. The displayed relative improvement factors are the numbers of readouts at which the signal per readout has fallen to $1/e$ compared to the first readout. These relative improvement factors can be converted to absolute improvement factors by multiplication with a constant $\alpha < 1$, which accounts for lower state preparation fidelities and is the same for all measurements.

Nuclear spin storage states m_I	Readout transition $\|m_s, m_I\rangle$	$N_r\|_{S=1/e}$
-1,0	$\|0,-1\rangle \leftrightarrow \|-1,-1\rangle$	1494
0,+1	$\|0,+1\rangle \leftrightarrow \|+1,+1\rangle$	1525
-1,+1	$\|0,-1\rangle \leftrightarrow \|-1,-1\rangle$	1507
-1,+1	$\|0,+1\rangle \leftrightarrow \|+1,+1\rangle$	1803

Table 6.3 **Relative improvement factors for repetitive readout by storage and readout states**. $N_r|_{S=1/e}$ denotes the number of readouts after which the normalised signal has decreased from $S(1) = 1$ to $S(N_r) = 1/e$.

REPETITIVE READOUT WITH PARTIAL ERROR CORRECTION

The ^{14}N nuclei has three spin states while the ^{15}N nuclei only has two. Typically only two spin states are used for storage. Therefore, we can use the remaining state for correcting undesired flips with one of the memory states.

The lifetime of the spin is dominated by spin-flips with $\Delta m_I = 1$. Therefore, no direct flips occur between the $m_I = \pm 1$ states as both states first relax into the $m_I = 0$ state. By re-pumping the population of $m_I = 0$ into either the $m_I = -1$ or the $m_I = +1$ state, the lifetime of the stored state can be prolonged and, hence, the signal drops less with every consecutive readout cycle. Figure 6.14 shows the pulse sequence required for repetitive readout with error correction.

Since the relaxation rates are not equal but dependent on the electron spin polarisation and the coupling strengths between the different electron and nuclear states indicated in Figure 6.2, there is a case for re-pumping into the $m_I = -1$ state which decays faster than the $m_I = +1$ state.

The data in Table 6.4, which is based on re-pumping every 100 repetitions, confirms that this is indeed the best available option. The signal increases by 66 % for re-pumping into the $m_s = -1$ state. The measured relative improvement factors are well in-line with the predicted factors which we obtain by simulating repetitive readout (with partial error correction) by using the lifetimes measured in Section 6.2.

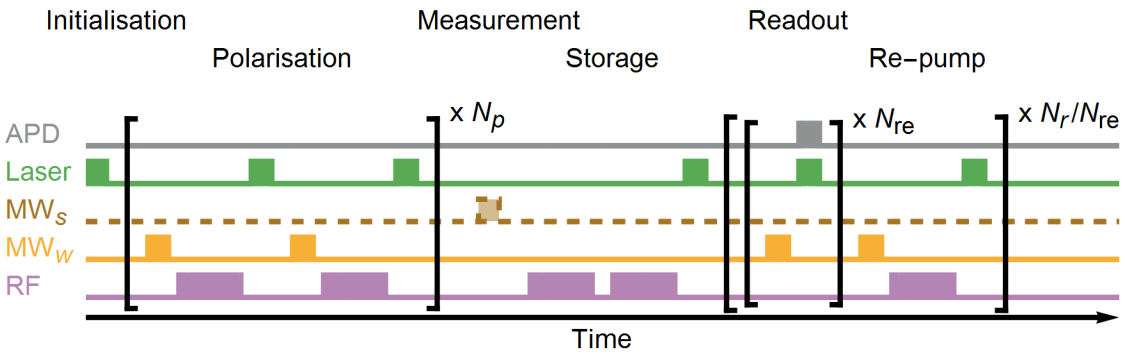

Fig. 6.14 **Repetitive readout with error correction**. The pulse sequence describing repetitive readout in Figure 6.12 is modified by adding a RF pulse to store the electron state in either $m_I = -1$ or $m_I = +1$ and by adding a re-pumping sequence every N_{re} readout pulses. This re-pumping sequence consists of one microwave and one RF π-pulse to selectively transfer polarisation from the $m_I = 0$ state into the $m_I = -1$ state.

Readout transition $\|m_s, m_I\rangle$	Re-pumping transition $\|m_s, m_I\rangle$	$N_r\|_{S=1/e}$
$\|0,-1\rangle \leftrightarrow \|-1,-1\rangle$	$\|0,0\rangle \leftrightarrow \|0,+1\rangle$	1641
$\|0,+1\rangle \leftrightarrow \|+1,+1\rangle$	$\|0,0\rangle \leftrightarrow \|0,-1\rangle$	2509

Table 6.4 **Relative improvement factors for repetitive readout with partial error correction by storage and readout states**. The nuclear spin is prepared either in the $m_I = -1$ or $m_I = +1$ state. $N_r|_{S=1/e}$ denotes the number of readouts after which the normalised signal has decreased from $S(1) = 1$ to $S(N_r) = 1/e$.

These results constitute a strong case for favouring the ^{14}N nuclear spin over the ^{15}N nuclear spin. Error correction can only be implemented with the ^{14}N nuclear spin as it exhibits an unused spin state. In addition, the ^{14}N nuclear spin's hyperfine coupling is 27 % lower than the ^{15}N nuclear spin's hyperfine coupling with the NV centre electron spin [28, 52]. Only very short measurement sequences that benefit from the smaller number of RF pulses required for polarising of the ^{15}N spin might benefit from employing the ^{15}N nuclei.

ABSOLUTE SIGNAL AMPLITUDE

One important question to answer is when repetitive readout is the better choice compared to traditional, direct readout of the electron spin. We therefore compare the signal amplitudes of direct readout, repetitive readout and repetitive readout with partial error correction. For each scenario, given the current experimental parameters for the pulse lengths we can calculate the overhead T_{Overhead} required to prepare and readout the states. We define the measurement time $T_{\text{Meas.}}$ which, e.g. are for a Ramsey sequence two $\pi/2$-pulses and a period for phase acquisition. The signal amplitude is given by

$$A = \frac{S}{T_{\text{Overhead}} + T_{\text{Meas.}}}, \tag{6.26}$$

where S and T_{Overhead} differ for each scenario. The signal for a single readout is S_1 and the signal from the repetitive readout with decay constant $N_{\text{rep.}}$ is $S_{rep.} = \alpha N_{\text{rep.}} S_1$, where α is the ratio of the signal per readout of repetitive and traditional readout. $\alpha < 1$ because we do not fully initialise the electron spin in order to avoid additional depolarisation of the nuclear spin, i.e. in order to maximise $N_{\text{rep.}}\alpha$. Further, the additional pulses required to enable repetitive readout introduce pulse errors which reduces α.

In Figure 6.15 we plot the repetitions $N_{\text{rep.}}$ required to improve the signal amplitude compared to direct readout and we also consider below which α repetitive readout cannot enhance the signal. In Figure 6.15.a we use currently achievable experimental parameters and assume a conservative $\alpha = 0.2$. We conclude that even rather short measurement sequences such as Hahn-echo in the nanodiamonds benefit from employing repetitive readout and that repetitive readout with partial error correction is almost always increasing the signal amplitude.

DIRECT MEASUREMENT OF NV ELECTRON POLARISATION

Traditional readout only probes the amount of population in the $m_s = 0$ state. However, by swapping the nuclear and electron spin states we can also probe the $m_s = \pm 1$ states directly. A simple experiment is to drive Rabi oscillations between two nuclear spin levels and monitor

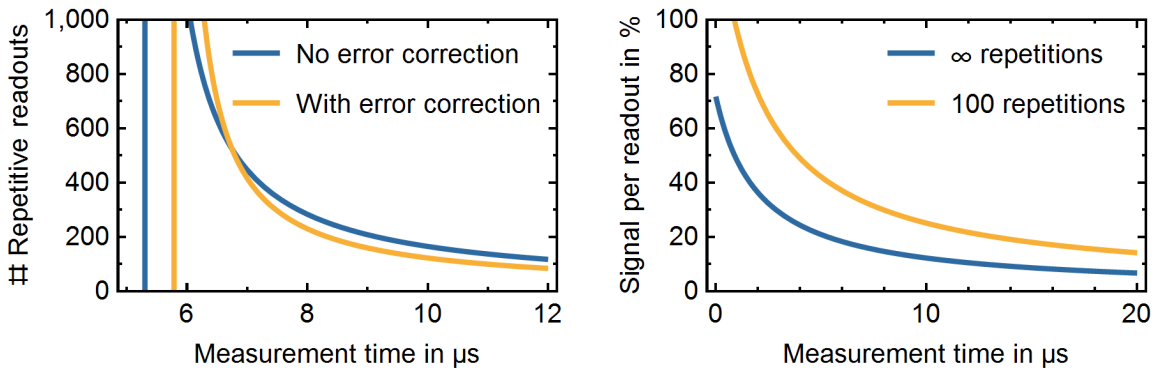

(a) Required repetitions

(b) Required readout signal

Fig. 6.15 **Signal from repetitive and normal readout compared**. (a) the number of repetitions required to exceed the signal amplitude of a sequence without repetitive readout depending on the measurement time, e.g. the duration of a sensing / decoupling sequence. Below the vertical bars at approximately 5.4 µs and 5.8 µs direct readout is always preferable, i.e. without repetitions. Compared are repetitive readout with partial error correction and simple repetitive readout with traditional, direct readout. Assumed is a 80 % lower signal amplitude per repetitive readout compared with direct readout, i.e. $\alpha = 0.2$ and a 66 % higher signal from repetitive readout with partial error correction. (b) the α required in order for the experimentalist to prefer repetitive readout to direct readout. Two examples are considered: First, an infinite number of repetitions are possible or, second, the signal decays to $1/e$ after 100 repetitions.

the nuclear spin state populations. Repetitive readout is not a requirement but is used here for convenience.

Figure 6.16 displays the nuclear spin populations of the described experiment. By comparing the populations in the $m_I = 0$ and $m_I = -1$ spin states, we can deduce that even though the oscillations do not suffer from decoherence on the chosen timescale, the nuclear spin is not flipped approximately 25 % of the time despite the application of a π-pulse. This indicates that the RF pulse is not on resonance in 25 % of the measurements which, can be explained by insufficient polarisation of the NV centre electron spin by non-resonant excitation. As the electron spin couples to the nuclear spin via hyperfine interaction the RF driving field is not on resonance and cannot flip the nuclear spin if the electron spin is in the $m_s = \pm 1$ states. This is therefore a direct measurement of the electron polarisation

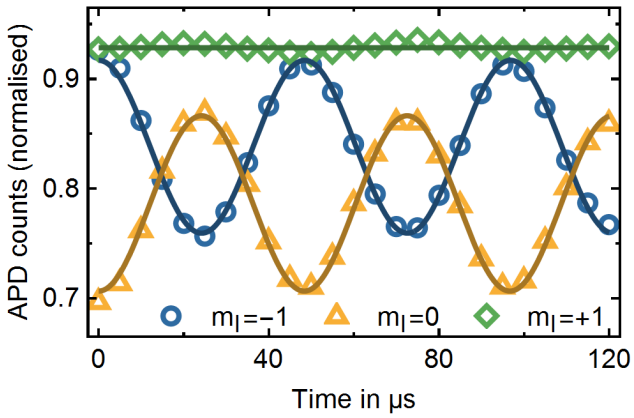

Fig. 6.16 **Rabi of nuclear spin using electron spin for readout**. The pulse sequence consists of polarisation of the nuclear spin, subsequent re-initialisation of the electron spin, driving the $|m_I = 0\rangle \leftrightarrow |-1\rangle$ transition for time τ and repetitive readout of the nuclear spin state. Three curves are recorded for each nuclear spin state.

fidelity by nonresonant excitation. A fidelity of 75 % is in good agreement with previous measurements [41]. The non-unit initialisation fidelity is the reason why repetitive application of the nuclear spin polarisation sequence is beneficial.

Waldherr et al. [202] suggest that such a reduction in contrast stems from charge conversion and the spin cannot be flipped as the NV centre is in the NV^0 state. However, the NV^0 ZPL is barely visible in the spectrum taken for this NV centre and we can thus exclude charge conversion as the reason for a 25 % reduced contrast.

6.5.2 Increasing the sensing resolution to the nuclear spin lifetime

Fine spectral features below 100 Hz have to be discriminated with NV centres for a range of measurements. Examples are protocols and first demonstrations to determine the location and species of nuclei in single molecules [3, 113, 19, 104]. The development of such high resolution sensors ultimately leads to microscopy of arbitrary single molecules which enables the study of new areas for researchers in chemistry, material science and biology.

Resolving a certain frequency of an external magnetic field as produced by a precessing nuclear spin is vastly different from enhanced sensitivities albeit the two often go hand in hand. High resolution is determined by the interrogation time while sensitivity is set by the signal amplitude, the speed and total time of phase acquisition. Typically, such as for a Hahn sequence, the interrogation and phase acquisition times are equal and limited by the homogeneous coherence time T_2. Resolution should not be confused with bandwidth albeit both are linked to the interrogation time, as the former determines the accuracy of the to-be-sensed frequency and the later decides if a frequency can be sensed or not with a given sensor.

In 2011, Laraoui et al. [111] realised that a correlation type measurement can be used to prolong the interrogation time and therefore the resolution to the lifetime T_1 without compromising absolute sensitivity. The idea is to add two phases acquired during two measurements separated by time τ. This approach does not sound profoundly different from other sensing protocols where well-designed decoupling sequences determine the phase acquisition but its main advantage is that the phase acquired in the first measurement can be mapped to population during time τ and re-mapped to phase before the second measurement. Since the lifetime of spins, in particular in the case of NV centres, is far longer than the coherence time, the resolution is increased. Even though this approach decreases the time available for phase acquisition as most time is spent waiting for time τ, the resolution can be enhanced.

Instead of using the lifetime of the electron spin, the acquired phase can be also mapped to a nuclear spin to allow for even longer interrogation times τ as first described by Laraoui et al. [109] in 2013. In particular, the host nuclear spin is an interesting candidate for the phase memory because it is intrinsic to the NV centre. Figure 6.17 presents a pulse sequence which implements the correlation measurement approach with storage of the phase in the nuclear spin population. Utilising the host nuclear or a proximal ^{13}C spin as a memory to for high resolution spectroscopy has recently become popular [136, 213, 184, 171, 118, 153, 125]. Signals with a linewidth of only 13 Hz were resolved corresponding to a 100-fold improvement compared to measurements not employing the nuclear spin [153].

The improvement would be even more dramatic if the measurement was carried out using nanodiamonds because the nuclear spin properties are not limited by electro-magnetic noise from surface states. The 13 Hz linewidth is linked to pulse sequences with 43 ms storage times in the nuclear spin. Given that the T_1 of the host nuclear spin is expected to be many seconds under no illumination as discussed in Section 6.2 experiments are typically limited not by the attainable resolution but the intrinsic linewidth of the measured signal.

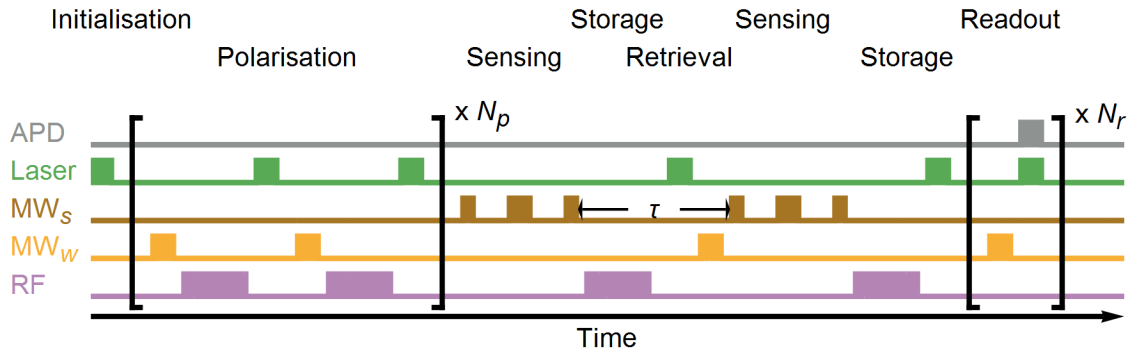

Fig. 6.17 **Interferometer using the nuclear spin to increase resolution**. The spin system is first prepared in a single nuclear spin state by applying a polarisation sequence N_p times. A traditional Hahn echo sequence is used to acquire the first phase that is subsequently mapped to the nuclear spin using a electron spin selecting RF π-pulse on the nuclear spin. Before the second phase is added after the interrogation time τ, the phase is re-mapped onto the electron spin by a nuclear spin selecting microwave pulse. In order to increase the readout fidelity, the electron spin state is again stored in the nuclear spin population so that repetitive readout can be employed N_r times. Repetitive readout is discussed in Section 6.5.1. The Hahn echo sequences can also be replaced by more sophisticated decoupling sequences such as the XY8 sequence presented in Chapter 3.

Employing a host nuclear spin is especially beneficial to sensing with NV centre in nanodiamond. The NV centre electron spin coherence is limited by noise in the environment to values orders of magnitude below the coherence times in bulk diamond. However, the nuclear spin lifetime in bulk and in nanodiamond at magnetic fields above 2000 G is limited in both cases by a flip-flop process in the excited state close to the ESLAC as discussed in Section 6.2. Hence, the achievable resolution of such sensing schemes is similar for NV centres in bulk and nanodiamond though the sensitivity is lower with nanodiamonds.

6.6 CONCLUSIONS

We have shown the merits of employing the nuclear host spin of the NV centre for enhancing sensing capabilities of the NV centre. We demonstrated initialisation, coherent control and repetitive readout of the nuclear spin and suggest an improvement to current repetitive readout protocols. In addition we investigated the spin bath by measuring the spin properties of the electron spin.

The lifetime $T_{1,n}$ of the nitrogen host spin determines the resolution of many sensing protocols and limits the increases in sensitivity achievable using the nuclear spin. Our model predicts lifetimes of many minutes in the ground state and suggests a excited to ground state lifetime ratio of $1/500,000$. Data confirms that no relaxation is observed within 70 ms. In addition, we highlight the necessity to align the external magnetic field precisely with the NV axis as deviations larger than the hyperfine can decrease the nuclear spin lifetime by more than an order of magnitude. The nuclear spin's inhomogeneous coherence time $T^*_{2,n}$ is limited by the electron lifetime $T_{1,e}$ in the ground state. Decoupling the electron and the nuclear spin is only effective if a decoupling sequence is applied which filters for noise on frequencies at least as large as the hyperfine coupling of -2.162 MHz and decouples all three electron spin states. This experiment is within the capabilities of our setup but has not been implemented, yet.

Based on the lifetime of the nuclear spin we examine repetitive readout of the electron spin by experiments and modelling. We find that the possibility to perform repetitive readout with error correction gives the ^{14}N spin a significant advantage over the ^{15}N spin. In fact, we observe a 66 % increase of the readout signal by employing repetitive readout compared to current protocols. This improvement is likely to be even more pronounced if the numbers are compared to repetitive readout with a ^{15}N nuclei because of the higher transverse hyperfine coupling of the ^{15}N spin which leads to faster relaxation of the host nuclear spin. Last, we consider when repetitive readout is beneficial to the readout signal and find that it can be enhanced by using the nuclear spin for measurement sequences exceeding 6 µs.

CHAPTER 7

Conclusions and Outlook

This thesis aims at readying the NV centre in nanodiamond for future research especially in biological systems. We therefore demonstrate its current sensing capabilities, show that techniques used for NV centres in bulk diamond can be transferred to NV centres in nanodiamond and propose new approaches to enhance its prospects in magnetometry.

The relative sensitivity of the detection of electro-magnetic fields is limited by the available integration time and hence by the collection efficiency. In Section 2.7 we recognize that current readout methods do not extract all information about the spin state that is contained in the collected photons. By time-tagging and weighting every single photon with its individual signal-to-noise ratio, we show that the total measurement time can be decreased by 15 %. This improvement is very modest and requires extensive calibration for every single NV centre and, therefore, the implementation of this approach is only recommended for NV centres which are used for a long time period. As discussed other methods to enhance the collection efficiency provide far higher prospective gains and should be pursued first.

In Chapter 3 we introduce techniques for sensing electro-magnetic fields and temperature with NV centres. The Chapter aims at providing a base for the measurements conducted in the remaining text.

A limiting factor for the sensitivity of the NV centre is the coherence time of the electron spin which primarily suffers due to the emitter's proximity to the nanodiamond surface. Charge traps and surface spins exhibit particularly fast dynamics and therefore dominate

dephasing. For bulk diamond methods have been established to remove these surface defects. This has given shallow implanted NV centres a significant advantage over NV centres in nanodiamond. One of these methods is annealing. We show in Chapter 4 that it is directly transferable to NV centres in nanodiamond. A side effect from the treatment is the removal of graphite from the surface which is then exposed for functionalisation. Functionalisation is a major requirement for many applications in biology and, hence, opens doors to research with NV centres in nanodiamond. While the demonstrated improvements are larger for shallow implanted NV centres, this work is an important step as it suggests that other chemical treatments such as acid cleaning could as well be beneficial to the coherence of spins in nanodiamonds. However, the nanodiamond surface is not flat and therefore more complex than the surface of a bulk diamond. It is therefore to be questioned if NV centres in nanodiamond can reach the coherence of shallow NV centres which are created by implantation or delta doping in bulk diamond.

In Chapter 5 we show as a proof of concept how NV centres in nanodiamond can be used to probe magnetisation of the material and reveal time dynamics of the domain formation in a large temperature range from 4 K to 130 K. This experiment is a pre-cursor for a technically more challenging undertaking: A AFM type magnetic scanning probe device where the probe consists of either a NV centre hosted in nanodiamond or at the tip of a diamond pillar. Such a device would leverage the current sensing capabilities of NV centres considerably and has the potential to become a standard research tool in material science and chemistry because other techniques such as nano-SQUIDS cannot be used over the temperature range of 0 K to more than 600 K and lack single nuclear spin sensitivity.

However, one unsolved problem is the demagnetisation effect of the green laser excitation which currently limits future studies to optically transparent samples. Further, the collection efficiency of the NV centre emission must be improved to reduce current required signal integration times of many hours. Potential remedies are to use an entire array of sensors or an ensemble of NV centres instead of single defects. The later approach, while impeding single molecule NMR, might present a good compromise until a better solution has been developed because the pillar solution requires very careful sample to sensor alignment.

A method which has been used in bulk diamond to increase the sensing capabilities of the NV centre is employing its host nuclear spin as a quantum memory. We show in Chapter 6 that the same techniques apply to the NV centre in nanodiamond and that other than the electron spin the host nuclear spin properties do not suffer from its proximity to the surface. Further, we build a convincing case for using NV centres with a ^{14}N nuclei as opposed to a ^{15}N host because partial error correction is enabled by the ^{14}N nuclear spin leading to shorter signal integration times for a given absolute sensitivity. The developed technique is also applicable in bulk diamond, requires only minor changes in the currently used pulse protocols and leads to a 66 % higher signal.

The future of the NV centre in nanodiamond depends on, first, how similar its spin properties can get to shallow NV centres in bulk diamond and, second, with how much success it can be employed in biological systems such as cells. The former task is largely set by the available techniques for bulk diamond. In order to create the best NV centres in nanodiamond available we suggest to create impurity free nanodiamonds, irradiate them with nitrogen ions for implantation and subsequently anneal and acid clean their surfaces. The later challenge is open-ended and more difficult to define. In the next Section we try to lay out a path to sensing in cells and concretise the first experiment by evaluating its current feasibility.

OUTLOOK: NMR IN CELLS

The major advantage of NV centres in nanodiamond compared to their shallow implanted counterparts in bulk is that nanodiamonds can be employed in-vivo. First steps have been taken towards this goal. For example, ingestion of nanodiamonds by cells has been observed [208]. We envision the following roadmap towards sensing in cells:

1. Sensing proton concentrations in immersion oil
2. Sensing ion concentrations (i.e. fluorine) in water
3. Sensing ion concentrations in cells

This Section discusses step one and its feasibility by extending a model by Pham et al. [154] which aims at predicting the echo signal from a shallow implanted NV centre in bulk diamond due to protons in immersion oil on its surface. By slight modifications, we can obtain the signal from a NV centre at the centre of a nanodiamond in immersion oil. Given the coherence times measured in Chapters 6 and 4 and by Knowles et al. [101] we find that the signal from the immersion oil should be easily detectable. In the following, the modified model and its results are presented.

First, Pham et al. [154] describe the normalised echo signal $C(\tau)$ from a echo sequence, where τ is the length of a single measurement pulse sequence as defined in Chapter 3. It is given by

$$C(\tau) = \frac{S(\tau)}{E(\tau)} = \langle \cos[\Delta\phi(\tau)] \rangle \approx \exp\left[-\frac{2}{\pi^2} \gamma_S^2 \mathrm{B}_{\mathrm{RMS}}^2 K(N\tau) \right], \tag{7.1}$$

where $S(\tau)$ is the signal with immersion oil and $E(\tau)$ is the signal without immersion oil. $\gamma_S \approx 2\pi \times 2.8024\,\mathrm{MHz/G}$ is the gyromagnetic ratio of the electron, $\mathrm{B}_{\mathrm{RMS}}$ is the root mean squared of the magnetic field fluctuations and $K(N\tau)$ is a functional depending on the used pulse sequence. Hence, $N\tau$ is the length of the total measurement sequence. The signal depends on the average accumulated phase $\Delta\phi(\tau)$ which is normal distributed for a statistically polarised sample with mean zero and variance $\langle \Delta\phi(\tau)^2 \rangle$ and, thus, the signal can be approximated by an exponential function.

The strength of the magnetic field fluctuations can be calculated by

$$\mathrm{B}_{\mathrm{RMS}}^2 = \langle \mathrm{B_z}(0)\mathrm{B_z}(t) \rangle = \rho \left(\frac{\mu_0 \hbar \gamma_N}{4\pi} \right)^2 \tilde{\Gamma} \tag{7.2}$$

with the proton density ρ which is $68\,\mathrm{nm}^{-3}$ for the Nikon Type NF immersion oil [154], the magnetic constant $\mu_0 = 4\pi \times 10^{-7}\,\mathrm{N/A}^2$, the reduced Planck constant $\hbar$, the proton gyromagnetic ratio of $7.62\,\mathrm{MHz/T}$ and a geometric factor for the spacial distribution of the proton spins. This factor is different for a NV centre in nanodiamond and for a shallow implanted NV centre. For a NV centre at the centre of a nanodiamond it can be calculated by

evaluating the an integral not only over a surface but a sphere, i.e.

$$\tilde{\Gamma} = \int_0^{2\pi} \mathrm{d}\varphi \int_0^{\pi} \mathrm{d}\theta \int_R^{\infty} \mathrm{d}r \frac{u_z^2(1-u_z^2)}{r^6} r^2 \sin(\theta) = \frac{8\pi}{45R^3}, \tag{7.3}$$

where R is the radius of the nanodiamond and u_z is the projection of the unit vector $\mathbf{u}_r(\theta,\varphi)$ on the NV centre axis $\mathbf{z}(\alpha,\beta)$, i.e.

$$u_z = \mathbf{z} \cdot \mathbf{u}_r \tag{7.4}$$

with

$$\mathbf{u}_r = [\sin(\theta)\cos(\varphi), \sin(\theta)\sin(\varphi), \cos(\theta)], \tag{7.5}$$

$$\mathbf{z} = [\sin(\alpha)\cos(\beta), \sin(\alpha)\sin(\beta), \cos(\alpha)]. \tag{7.6}$$

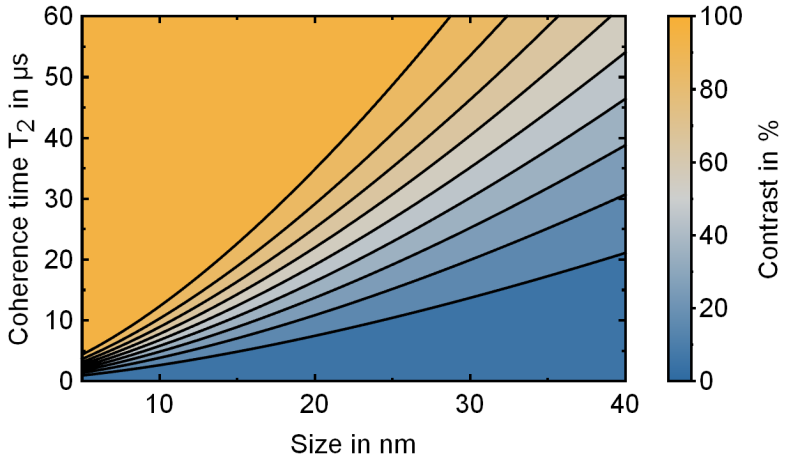

Fig. 7.1 **Signal contrast of a XY8 spin echo from a NV centre in nanodiamond detecting protons in immersion oil**. The signal contrast $1-C(T_2)$ is displayed in dependence of the coherence time T_2 of the NV centre which is in the centre of a nanodiamond with diameter or size $2R$. Contour lines are plotted every 10 %.

Finally, we need the filter function $K(N\tau)$ of the XY8 sequence as displayed in Figure 3.9 in Chapter 3. It can be obtained by squaring the pulse sequence's Fourier transform and is

given by

$$K(N\tau) \approx (N\tau)^2 \mathrm{sinc}^2 \left[\frac{N\tau}{2} \left(\omega_L - \frac{\pi}{\tau} \right) \right], \tag{7.7}$$

where $\omega_L = \gamma_N \mathrm{B}$ is the Larmor frequency. The expression assumes that the proton inhomogeneous coherence time $T_{2,p}^*$ is greater than the NV centre coherence time $T_{2,e}$ which is true for protons in immersion oil and our NV centres. As $T_{2,p}^*$ is limited by spin-spin interactions and diffusion in and out of the sensing volume of the NV centre, this is not necessarily the case any more for liquids with lower viscosity. In this case Pham et al. [154] also provide an expression for a finite $T_{2,p}^*$.

The point of maximum sensitivity is at $\tau N = T_2$ as discussed in Chapter 3. In Figure 7.1 we plot the signal contrast $1 - C(T_2)$ for different coherence times T_2 and nanodiamond diameters $2R$. Given a nanodiamond with 30 nm in diameter we only need a coherence time of 15 µs to observe a signal with 10 % contrast. We conclude that given the coherence time $T_2 = 60\,\mu\mathrm{s}$ measured in nanodiamonds of the same batch using a XY8 sequence for decoupling [101], it is realistic to detect proton spins in immersion oil employing the nanodiamonds used in this thesis.

APPENDIX A

Temperature dependence of the zero-field splitting in nanodiamond

In order to measure the temperature dependence for NV centres in nanodiamond, we mount a sample on a metal block which is insulated from the piezo stages with Teflon. The temperature is controlled by a cartridge heater. A feedback loop implemented in custom software controls the heater. It is established with two thermistors of which one measures the temperature in the metal block and the other senses the temperature directly on the sample.

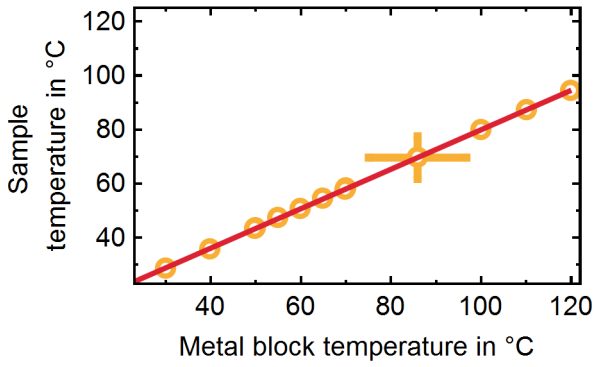

Fig. A.1 **Relation between the temperature on the quartz sample with nanodiamonds and the heated metal block**. The data fits well a line which means that the relation between temperature on the sample and close to the heater is linear. The errors on both thermistors are comparable, i.e. the temperatures are stable.

We observe a stable relationship between the two temperatures as displayed in Figure A.1 which confirms that we can reliably set a specific temperature. The temperature stability is 0.7 K. For a linear fit of the sample temperature depending on the metal block temperature $T_{\text{sample}} = a_0 + a_1 T_{\text{block}}$ we find the coefficients $a_0 = 6.9\,°\text{C}$ and $a_1 = 0.73$. In the following "temperature" refers to the sample temperature.

After taking the recording ODMR curves at temperatures from 29 °C to 94 °C, we obtain the ZFSs D_{gs} by fitting the Gaussian lineshapes. The lineshape is broadened to a Gaussian because of temperature drifts and simultaneously addressing the threefold, degenerate nuclear spin subspace with the microwave field. The extracted dip positions vs. temperature are plotted and fit with a cubic polynomial as displayed in Figure A.2 which is also displayed in Section 3.5.

The results are in line with previous measurements in bulk by Toyli et al. [195]. The gradient D_{gs} at room temperature is approximately $80\,\text{kHz/K}$ for our measurements and those of Toyli et al. [195]. At higher temperature the two models deviate slightly and we observe a gradient of $121\,\text{kHz/K}$ while Toyli et al. [195] calculate $101\,\text{kHz/K}$ at 80 °C. However, given the limited temperature range in which the measurements were conducted, we likely overfit the data. Therefore, it is unlikely that there are differences between the temperature dependence of the NV centre ZFS in bulk or nanodiamond.

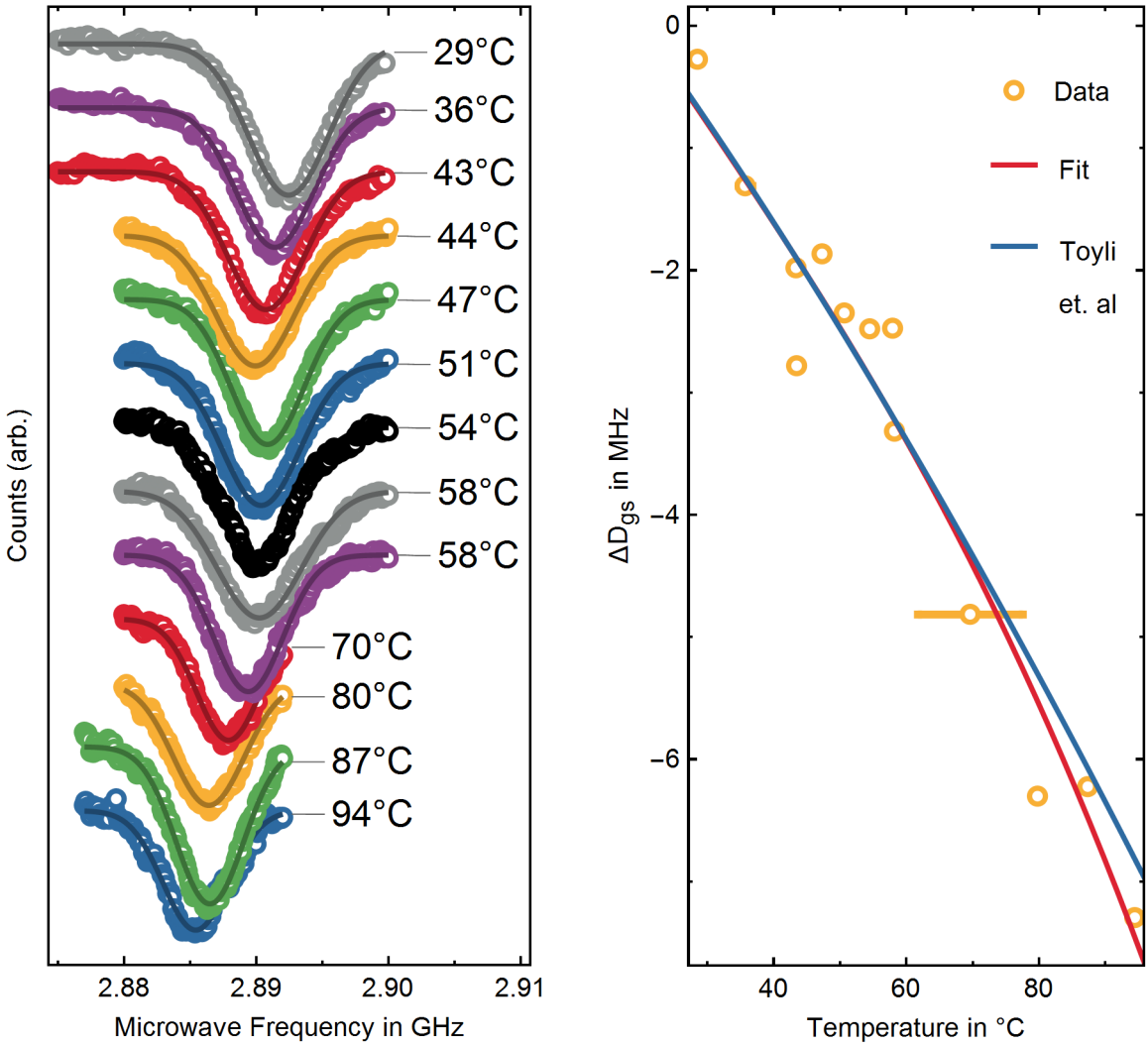

(a) ODMRs at different temperature

(b) Temperature dependence of D_{gs}

Fig. A.2 **The temperature dependence of the ground state ZFS D_{gs}.** (a) ODMR measurements at different temperature along with fits to their Gaussian lineshapes. (b) the shift of the ODMR resonances compared to 20 °C is plotted against temperature. The obtained fit is compared against the results from Toyli et al. [195] who carried out experiments in bulk diamond.

APPENDIX B

Experiment control and analysis with Python

Every experiment requires the interplay and synchronisation of various devices from simple voltage sources to time-tagged photon counting and microwave generation. Typically, a single central computer runs a software controlling the entire process of data acquisition. Often, the software is implemented in LabView. We decided to switch from LabView to Python because the following features are difficult to implement:

- Self-documenting data acquisition
- High stability of the software
- Ease of understanding and maintaining a written program
- Simplicity of creating a new experiment
- Easily configurable experiments
- Exchanging hardware in experiments (such as a microwave source)
- Integration of data analysis and automated decision making

In order to ensure maintainability, we chose to use a highly modular approach, i.e. object oriented approach. This also means that every hardware device or experiment can be used without starting the main software whose modules only administer the experiments and devices. The software is not limited to confocal microscopy and can be very easily adapted for other purposes. Care was taken so that the classes `Experiment` and `Device` implement almost all functionality and only device specific commands must be implemented or the

experimental measurement sequence must be defined after inheritance. This avoids the need to write code twice and therefore enhances stability and reduces mistakes. Typically, a new experiment is only twenty or less lines long. Devices and experiments have a `Configuration` containing all parameters such as the device address or experiment parameters. It can be modified live and can be saved and read from a CSV file.

Experiments can be categorised. This categorisation of experiments is made to simplify the task of writing a new one because one can inherit from the base experiments but is not reflected in the software architecture.

- **Idle**: Experiment that has a low priority and can help to monitor a parameter such as APD counts.
- **Plotter**: Experiment that always runs and displays data available, e.g. from the time series manager.
- **Meta-experiment**: Experiment that runs other experiments and makes decisions based on live data analysis concerning the choice of experiments and their parameters.
- **Pulsed experiment**: Experiment that requires pulsing. Often more than one set of data is recorded. Examples are pulsed ODMR, spin echoes and lifetime measurements. There exists a base experiment from which inheritance is recommended for any new experiment based on a pulsed device.
- **Other experiment**: Many experiments fall in this category. Amongst them are the Scanner to obtain fluorescence images and continuous wave ODMR.

In order to give an overview over the capabilities of the software we list all hardware devices whose interfaces have been implemented:

- **Microwave sources and attenuators:** SMF100A (Rhode & Schwarz), SG384 (Stanford Research Systems), BK4064 (B&K Precision), SynthNV (Windfreak Technologies), RCDAT-8000-30 (Thorlabs)
- **Pulse and delay generator:** AWG70002A (Tektronix), PulseBlaster-ESR Pro (SpinCore Technologies), DG645 (Stanford Research Systems)
- **NIDAQCard controlled devices:** APD Counter, Photodiode, AOM, Piezo Mirror S-334.2SL (Physik Instrumente), Shutter, Thermistor

- **Motors:** Mint motion control (ABB), APT Systems (Thorlabs), C843 (Physik Instrumente), two different custom-built Arduino controlled stepper motors
- **Piezos:** ANC150 (Attocube), ECC100 (Attocube)
- **Power sources:** 2400 (Keithley), E3631A (Keysight Technologies)
- **Other:** generic camera, quTau (quTools), Cryostation (Montana Instruments), Temperature Controller (Oxford Instruments), Oscilloscope TDS2022B (Tektronix), Power meter 1830C (Newport), Power meter PM100D (Thorlabs), PID SIM960 and Mainframe SIM900 (Stanford Research Instruments)
- **Meta devices**: Pulser (synchronises different pulse and delay generators and provides a common interface), Optimizer (can operate with an APD and a mirror to optimise the number of counts depending on position), Laser lock (PID to stabilise the laser using a Photodiode and an AOM)

Although all hardware devices can be used on their own and come with a separate user interface, they are typically managed by the software to ensure that the resources are used efficiently and are used only by one experiment at a time. Several modules are implemented to ensure this and the proper functionality of the software:

- A **data container** manages a multidimensional array and all information associated with an experiment such as its parameters, its date, etc. Import and export is possible with CSV and hdf5 files.
- The **data explorer** is a separate program which allows to quick search all experiments for values, configuration, etc. It also allows complicated queries such as “search for spin echoes which have shown coherence times longer than 5 µs”. All acquired data is indexed for this purpose.
- The **hardware manager** administers all devices and ensures that no device is initialised twice or accessed by two experiments at the same time. By using aliases in experiments such as "Microwave", devices with identical interfaces can be easily swapped so that the software can be ported to a different setup by small modifications of the hardware configuration file.

- The **job manager** runs jobs based on priority and available hardware. One or more Jobs are typically part of an experiment. They are re-runnable threads that contain information about the used hardware. Their status can be 'waiting' (waiting for execution), 'idle' (not running), 'running' and 'stopping' (stop variable, which is constantly checked by the running thread, is set to true).
- The **root window** hosts docks which contain the user interface of an experiment, a device or another module such as the job manager.
- The **experiment initialiser** allows the initialisation of experiment instances. It administers a list of open experiments and registers the user interface of an experiment with the root window and its jobs with the job manager.
- The **pulse designer** allows the quick creation of user-readable pulse sequences which can then be further processed by the respective hardware.
- The **time series manger** hosts creates time series which can be displayed in a live plot. This is useful if temperature, photon counts or laser power should be monitored.
- The **fitting toolbox** allows live analysis of acquired data.

The acquisition of data and its presentation in the user interface are strictly separated and run in different threads to ensure performance and flexibility of the software of which a typical state is displayed in Figure B.1. For reference, we further want to provide a list of libraries which are vital to the software's functionality and might proof useful for developers:

- `numpy` and `h5py` for data management.
- `traits` to ensure data validation of user input.
- `traitsui`, `chaco` and `pyqtgraph` with a `pyqt` backend to create a user interface without only a few lines of code. It is crucial to employ `pyqt`-signals for `pyqtgraph` windows instead of `traits`-notifications for stability reasons.
- `pyvisa` to access devices via standardised hardware interfaces, `pylibnidaqmx` to use National Instruments DAQCards, `ctypes` to write a python interface to DLLs controlling hardware, `cv2` for cameras and `pythoncom` and `win32com` to create an API for Microsoft Windows COM objects.
- `threading` to run every experiment in a different thread.

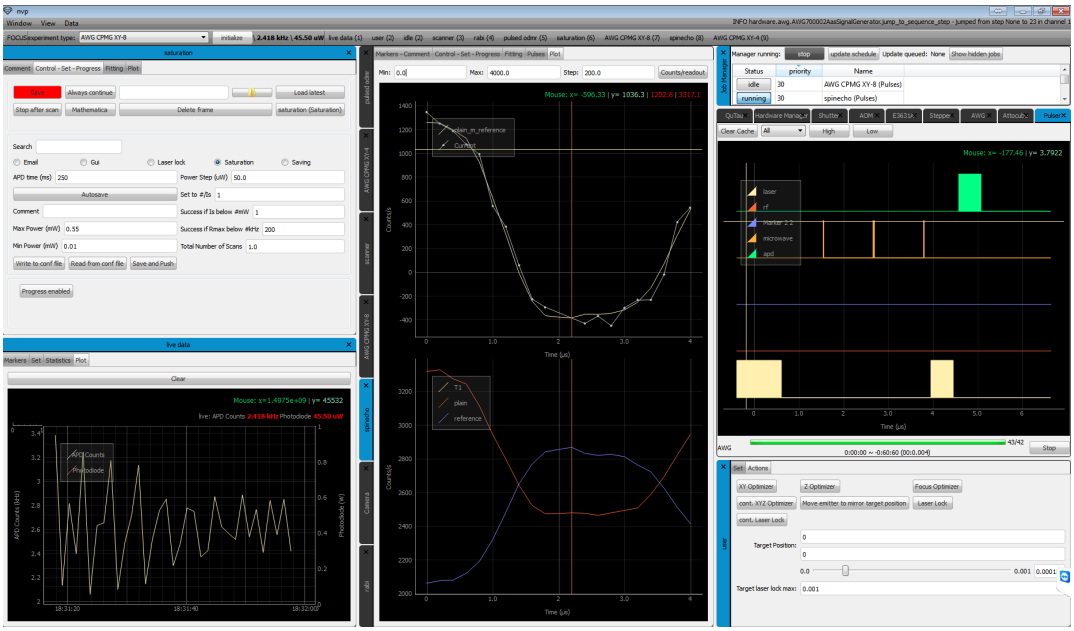

Fig. B.1 **Screenshot of the custom software**. Shown is the acquisition of a spin echo in the central dock. On the left is the saturation measurement whose configuration tab is selected and the live data plotter which uses data from the time series manager. On the right is the job manager, the pulser and a dock which provides shortcuts to run different optimizers (jobs).

- `multiprocessing` for computationally heavy tasks.
- `scipy`, `pymc` and `scikit-image` to analyse data.
- `jupyter` with `nbextensions` to analyse data in Wolfram Mathematica-like notebooks using Python. They can also serve as laboratory books.

Additional capabilities of the software, which are worth mentioning, are:

- Sending emails when certain events occur such as the end of an experiment.
- Comprehensive logging of all activities. The logs can be searched live and are tagged with date, time and origin.
- Integrated IPython console for live debugging.
- Sending crash reports.
- Initial configuration file to determine which hardware and experiments to initialise at the start of the software.

References

[1] Acosta, V. M., Bauch, E., Ledbetter, M. P., Santori, C., Fu, K.-M. C., Barclay, P. E., Beausoleil, R. G., Linget, H., Roch, J. F., Treussart, F., Chemerisov, S., Gawlik, W., and Budker, D. (2009). Diamonds with a high density of nitrogen-vacancy centers for magnetometry applications. *Physical Review B*, 80(11):115202. doi:10.1103/PhysRevB.80.115202.

[2] Acosta, V. M., Bauch, E., Ledbetter, M. P., Waxman, A., Bouchard, L.-S., and Budker, D. (2010). Temperature dependence of the nitrogen-vacancy magnetic resonance in diamond. *Physical Review Letters*, 104(7):070801. doi:10.1103/PhysRevLett.104.070801.

[3] Ajoy, A., Bissbort, U., Lukin, M. D., Walsworth, R. L., and Cappellaro, P. (2015). Atomic-Scale nuclear spin imaging using quantum-assisted sensors in diamond. *Physical Review X*, 5(1):011001. doi:10.1103/PhysRevX.5.011001.

[4] Ajoy, A. and Cappellaro, P. (2012). Stable three-axis nuclear-spin gyroscope in diamond. *Physical Review A*, 86(6):062104. doi:10.1103/PhysRevA.86.062104.

[5] Álvarez, G. A., Bretschneider, C. O., Fischer, R., London, P., Kanda, H., Onoda, S., Isoya, J., Gershoni, D., and Frydman, L. (2015). Local and bulk ^{13}C hyperpolarization in nitrogen-vacancy-centred diamonds at variable fields and orientations. *Nature Communications*, 6:8456. doi:10.1038/ncomms9456.

[6] Anahory, Y., Reiner, J., Embon, L., Halbertal, D., Yakovenko, A., Myasoedov, Y., Rappaport, M. L., Huber, M. E., and Zeldov, E. (2014). Three-junction SQUID-on-tip with tunable in-plane and out-of-plane magnetic field sensitivity. *Nano Letters*, 14(11):6481–6487. doi:10.1021/nl503022q.

[7] Anderson, P. W. and Rowell, J. M. (1963). Probable observation of the josephson superconducting tunneling effect. *Physical Review Letters*, 10(6):230–232. doi:10.1103/PhysRevLett.10.230.

[8] Arcizet, O., Jacques, V., Siria, A., Poncharal, P., Vincent, P., and Seidelin, S. (2011). A single nitrogen-vacancy defect coupled to a nanomechanical oscillator. *Nature Physics*, 7(11):879–883. doi:10.1038/nphys2070.

[9] Astle, M. J. and Weast, R. C. (1982). *CRC handbook of chemistry and physics: a ready-reference book of chemical and physical data*. CRC Press, 63 edition. ISBN:0849304636.

[10] Balasubramanian, G., Chan, I. Y., Kolesov, R., Al-Hmoud, M., Tisler, J., Shin, C., Kim, C., Wojcik, A., Hemmer, P. R., Krueger, A., Hanke, T., Leitenstorfer, A., Bratschitsch, R., Jelezko, F., and Wrachtrup, J. (2008). Nanoscale imaging magnetometry with diamond spins under ambient conditions. *Nature*, 455(7213):648–51. doi:10.1038/nature07278.

[11] Balasubramanian, G., Neumann, P., Twitchen, D., Markham, M., Kolesov, R., Mizuochi, N., Isoya, J., Achard, J., Beck, J., Tissler, J., Jacques, V., Hemmer, P. R., Jelezko, F., and Wrachtrup, J. (2009). Ultralong spin coherence time in isotopically engineered diamond. *Nature Materials*, 8(5):383–7. doi:10.1038/nmat2420.

[12] Bar-Gill, N., Pham, L. M., Jarmola, A., Budker, D., and Walsworth, R. L. (2013). Solid-state electronic spin coherence time approaching one second. *Nature Communications*, 4:1743. doi:10.1038/ncomms2771.

[13] Barends, R., Kelly, J., Megrant, A., Veitia, A., Sank, D., Jeffrey, E., White, T. C., Mutus, J., Fowler, A. G., Campbell, B., Chen, Y., Chen, Z., Chiaro, B., Dunsworth, A., Neill, C., O'Malley, P., Roushan, P., Vainsencher, A., Wenner, J., Korotkov, A. N., Cleland, A. N., and Martinis, J. M. (2014). Superconducting quantum circuits at the surface code threshold for fault tolerance. *Nature*, 508(7497):500–503. doi:10.1038/nature13171.

[14] Batalov, A., Jacques, V., Kaiser, F., Siyushev, P., Neumann, P., Rogers, L. J., McMurtrie, R. L., Manson, N. B., Jelezko, F., and Wrachtrup, J. (2009). Low temperature studies of the excited-state structure of negatively charged nitrogen-vacancy color centers in diamond. *Physical Review Letters*, 102(19):195506. doi:10.1103/PhysRevLett.102.195506.

[15] Beha, K., Batalov, A., Manson, N. B., Bratschitsch, R., and Leitenstorfer, A. (2012). Optimum photoluminescence excitation and recharging cycle of single nitrogen-vacancy centers in ultrapure diamond. *Physical Review Letters*, 109(9):097404. doi:10.1103/PhysRevLett.109.097404.

[16] Bernien, H., Childress, L., Robledo, L., Markham, M., Twitchen, D., and Hanson, R. (2012). Two-photon quantum interference from separate nitrogen vacancy centers in diamond. *Physical Review Letters*, 108(4):043604. doi:10.1103/PhysRevLett.108.043604.

[17] Bernstein, M. A., King, K. F., and Zhou, X. J. (2004). *Handbook of MRI pulse sequences*. Academic Press. ISBN:0120928612.

[18] Biercuk, M. J., Doherty, A. C., and Uys, H. (2011). Dynamical decoupling sequence construction as a filter-design problem. *Journal of Physics B*, 44(15):154002. doi:10.1088/0953-4075/44/15/154002.

[19] Boss, J. M., Chang, K., Armijo, J., Cujia, K., Rosskopf, T., Maze, J. R., and Degen, C. L. (2016). One- and two-dimensional nuclear magnetic resonance spectroscopy with a diamond quantum sensor. *Physical Review Letters*, 116(19):197601. doi:10.1103/PhysRevLett.116.197601.

[20] Bourgeois, E., Jarmola, A., Siyushev, P., Gulka, M., Hruby, J., Jelezko, F., Budker, D., and Nesladek, M. (2015). Photoelectric detection of electron spin resonance of nitrogen-vacancy centres in diamond. *Nature Communications*, 6:8577. doi:10.1038/ncomms9577.

[21] Bradac, C., Gaebel, T., Naidoo, N., Sellars, M. J., Twamley, J., Brown, L. J., Barnard, A. S., Plakhotnik, T., Zvyagin, A. V., and Rabeau, J. R. (2010). Observation and control of blinking nitrogen-vacancy centres in discrete nanodiamonds. *Nature Nanotechnology*, 5(5):345–9. doi:10.1038/nnano.2010.56.

[22] Brenneis, A., Gaudreau, L., Seifert, M., Karl, H., Brandt, M. S., Huebl, H., Garrido, J. A., Koppens, F. H. L., and Holleitner, A. W. (2014). Ultrafast electronic readout of diamond nitrogen–vacancy centres coupled to graphene. *Nature Nanotechnology*, 10(2):135–139. doi:10.1038/nnano.2014.276.

[23] Bylander, J., Gustavsson, S., Yan, F., Yoshihara, F., Harrabi, K., Fitch, G., Cory, D. G., Nakamura, Y., Tsai, J.-S., and Oliver, W. D. (2011). Noise spectroscopy through dynamical decoupling with a superconducting flux qubit. *Nature Physics*, 7(7):565–570. doi:10.1038/nphys1994.

[24] Casabianca, L. B., Shames, A. I., Panich, A. M., Shenderova, O., and Frydman, L. (2011). Factors affecting DNP NMR in polycrystalline diamond samples. *Journal of Physical Chemistry C*, 115(39):19041–19048. doi:10.1021/jp206167j.

[25] Castelletto, S., Johnson, B. C., Ivády, V., Stavrias, N., Umeda, T., Gali, A., and Ohshima, T. (2013). A silicon carbide room-temperature single-photon source. *Nature Materials*, 13(2):151–156. doi:10.1038/nmat3806.

[26] Chandran, M., Michaelson, S., Saguy, C., and Hoffman, A. (2016). Fabrication of a nanometer thick nitrogen delta doped layer at the sub-surface region of (100) diamond. *Applied Physics Letters*, 109(22):221602. doi:10.1063/1.4971312.

[27] Chen, A., Bi, Z., Hazariwala, H., Zhang, X., Su, Q., Chen, L., Jia, Q., MacManus-Driscoll, J. L., and Wang, H. (2011a). Microstructure, magnetic, and low-field magnetotransport properties of self-assembled $(La_{0.7}Sr_{0.3}MnO_3)_{0.5}$:$(CeO_2)_{0.5}$ vertically aligned nanocomposite thin films. *Nanotechnology*, 22(31):315712. doi:10.1088/0957-4484/22/31/315712.

[28] Chen, M., Hirose, M., and Cappellaro, P. (2015). Measurement of transverse hyperfine interaction by forbidden transitions. *Physical Review B*, 92(2):020101. doi:10.1103/PhysRevB.92.020101.

[29] Chen, X.-D., Dong, C.-H., Sun, F.-W., Zou, C.-L., Cui, J.-M., Han, Z.-F., and Guo, G.-C. (2011b). Temperature dependent energy level shifts of nitrogen-vacancy centers in diamond. *Applied Physics Letters*, 99(16):161903. doi:10.1063/1.3652910.

[30] Childress, L., Gurudev Dutt, M. V., Taylor, J. M., Zibrov, A. S., Jelezko, F., Wrachtrup, J., Hemmer, P. R., and Lukin, M. D. (2006). Coherent dynamics of coupled electron and nuclear spin qubits in diamond. *Science*, 314(5797):281–5. doi:10.1126/science.1131871.

[31] Cole, J. H. and Hollenberg, L. C. L. (2009). Scanning quantum decoherence microscopy. *Nanotechnology*, 20(49):495401. doi:10.1088/0957-4484/20/49/495401.

[32] Collins, A. T., Thomaz, M. F., and Jorge, M. I. B. (1983). Luminescence decay time of the 1.945 eV centre in type Ib diamond. *Journal of Physics C*, 16(11):2177–2181. doi:10.1088/0022-3719/16/11/020.

[33] Dagotto, E. (2003). *Nanoscale phase separation and colossal magnetoresistance : The physics of manganites and related compounds*. Springer. ISBN:978-3-662-05244-0.

[34] Dagotto, E., Hotta, T., and Moreo, A. (2001). Colossal magnetoresistant materials: The key role of phase separation. *Physics Reports*, 344(1-3):1–153. doi:10.1016/S0370-1573(00)00121-6.

[35] Davies, G. (1994). *Properties and growth of diamond*. INSPEC, the Institution of Electrical Engineers, emis data edition. ISBN:0852968752.

[36] Davies, G. and Hamer, M. F. (1976). Optical studies of the 1.945 eV vibronic band in diamond. *Proceedings of the Royal Society A*, 348(1653):285–298. doi:10.1098/rspa.1976.0039.

[37] Degen, C. L., Poggio, M., Mamin, H. J., Rettner, C. T., and Rugar, D. (2009). Nanoscale magnetic resonance imaging. *Proceedings of the National Academy of Sciences*, 106(5):1313–1317. doi:10.1073/pnas.0812068106.

[38] DiVincenzo, D. P. (2000). The physical implementation of quantum computation. *Fortschritte der Physik*, 48(9-11):771–783. doi:10.1002/1521-3978(200009)48:9/11<771::AID-PROP771>3.0.CO;2-E.

[39] Doherty, M. W., Dolde, F., Fedder, H., Jelezko, F., Wrachtrup, J., Manson, N. B., and Hollenberg, L. C. L. (2012). Theory of the ground-state spin of the NV center in diamond. *Physical Review B*, 85(20):205203. doi:10.1103/PhysRevB.85.205203.

[40] Doherty, M. W., Manson, N. B., Delaney, P., and Hollenberg, L. C. L. (2011). The negatively charged nitrogen-vacancy centre in diamond: The electronic solution. *New Journal of Physics*, 13(2):025019. doi:10.1088/1367-2630/13/2/025019.

[41] Doherty, M. W., Manson, N. B., Delaney, P., Jelezko, F., Wrachtrup, J., and Hollenberg, L. C. (2013). The nitrogen-vacancy colour centre in diamond. *Physics Reports*, 528(1):1–45. doi:10.1016/j.physrep.2013.02.001.

[42] Dolde, F., Fedder, H., Doherty, M. W., Nöbauer, T., Rempp, F., Balasubramanian, G., Wolf, T., Reinhard, F., Hollenberg, L. C. L., Jelezko, F., and Wrachtrup, J. (2011). Electric-field sensing using single diamond spins. *Nature Physics*, 7(6):459–463. doi:10.1038/nphys1969.

[43] Douce, T., Stern, M., Zagury, N., Bertet, P., and Milman, P. (2015). Coupling a single nitrogen-vacancy center to a superconducting flux qubit in the far-off-resonance regime. *Physical Review A*, 92(5):052335. doi:10.1103/PhysRevA.92.052335.

[44] Dréau, A., Lesik, M., Rondin, L., Spinicelli, P., Arcizet, O., Roch, J.-F., and Jacques, V. (2011). Avoiding power broadening in optically detected magnetic resonance of single NV defects for enhanced DC magnetic field sensitivity. *Physical Review B*, 84(19):195204. doi:10.1103/PhysRevB.84.195204.

[45] Dréau, A., Spinicelli, P., Maze, J. R., Roch, J.-F. F., and Jacques, V. (2013). Single-shot readout of multiple nuclear spin qubits in diamond under ambient conditions. *Physical Review Letters*, 110(6):1–5. doi:10.1103/PhysRevLett.110.060502.

[46] du Preez, L. (1965). *Electron paramagnetic resonance and optical investigations of defect centres in diamond*. PhD thesis, University of Witwatersrand.

[47] Dussaux, A., Schoenherr, P., Koumpouras, K., Chico, J., Chang, K., Lorenzelli, L., Kanazawa, N., Tokura, Y., Garst, M., Bergman, A., Degen, C. L., and Meier, D. (2016). Local dynamics of topological magnetic defects in the itinerant helimagnet FeGe. *Nature Communications*, 7:12430. doi:10.1038/ncomms12430.

[48] Dyer, H. B., Raal, F. a., Du Preez, L., and Loubser, J. H. N. (1965). Optical absorption features associated with paramagnetic nitrogen in diamond. *Philosophical Magazine*, 11(112):763–774. doi:10.1080/14786436508230081.

[49] Elovaara, T., Huhtinen, H., Majumdar, S., and Paturi, P. (2012). Irreversible metamagnetic transition and magnetic memory in small-bandwidth manganite Pr $_{1-x}$Ca$_x$MnO$_3$ (x = 0.0-0.5). *Journal of Physics: Condensed Matter*, 24(21):216002. doi:10.1088/0953-8984/24/21/216002.

[50] Englund, D., Shields, B., Rivoire, K., Hatami, F., Vučković, J., Park, H., and Lukin, M. D. (2010). Deterministic coupling of a single nitrogen vacancy center to a photonic crystal cavity. *Nano Letters*, 10(10):3922–3926. doi:10.1021/nl101662v.

[51] Felton, S., Edmonds, A. M., Newton, M. E., Martineau, P. M., Fisher, D., and Twitchen, D. J. (2008). Electron paramagnetic resonance studies of the neutral nitrogen vacancy in diamond. *Physical Review B*, 77(8):081201. doi:10.1103/PhysRevB.77.081201.

[52] Felton, S., Edmonds, A. M., Newton, M. E., Martineau, P. M., Fisher, D., Twitchen, D. J., and Baker, J. M. (2009). Hyperfine interaction in the ground state of the negatively charged nitrogen vacancy center in diamond. *Physical Review B*, 79(7):075203. doi:10.1103/PhysRevB.79.075203.

[53] Fischer, R., Bretschneider, C. O., London, P., Budker, D., Gershoni, D., and Frydman, L. (2013). Bulk nuclear polarization enhanced at room temperature by optical pumping. *Physical Review Letters*, 111(5):1–5. doi:10.1103/PhysRevLett.111.057601.

[54] Flagg, E. B., Muller, A., Robertson, J. W., Founta, S., Deppe, D. G., Xiao, M., Ma, W., Salamo, G. J., and Shih, C. K. (2009). Resonantly driven coherent oscillations in a solid-state quantum emitter. *Nature Physics*, 5(3):203–207. doi:10.1038/nphys1184.

[55] Fu, K.-M. C., Santori, C., Barclay, P. E., and Beausoleil, R. G. (2010). Conversion of neutral nitrogen-vacancy centers to negatively charged nitrogen-vacancy centers through selective oxidation. *Applied Physics Letters*, 96(12):121907. doi:10.1063/1.3364135.

[56] Fuchs, G., Dobrovitski, V., Hanson, R., Batra, A., Weis, C., Schenkel, T., and Awschalom, D. (2008). Excited-state spectroscopy using single spin manipulation in diamond. *Physical Review Letters*, 101(11):117601. doi:10.1103/PhysRevLett.101.117601.

[57] Fuchs, G. D., Burkard, G., Klimov, P. V., and Awschalom, D. D. (2011). A quantum memory intrinsic to single nitrogen–vacancy centres in diamond. *Nature Physics*, 7(10):789–793. doi:10.1038/nphys2026.

[58] Fuchs, G. D., Dobrovitski, V. V., Toyli, D. M., Heremans, F. J., Weis, C. D., Schenkel, T., and Awschalom, D. D. (2010). Excited-state spin coherence of a single nitrogen–vacancy centre in diamond. *Nature Physics*, 6(9):668–672. doi:10.1038/nphys1716.

[59] Gaebel, T., Domhan, M., Popa, I., Wittmann, C., Neumann, P., Jelezko, F., Rabeau, J. R., Stavrias, N., Greentree, A. D., Prawer, S., Meijer, J., Twamley, J., Hemmer, P. R., and Wrachtrup, J. (2006). Room-temperature coherent coupling of single spins in diamond. *Nature Physics*, 2(6):408–413. doi:10.1038/nphys318.

[60] Gali, A. (2009a). Identification of individual ^{13}C isotopes of nitrogen-vacancy center in diamond by combining the polarization studies of nuclear spins and first-principles calculations. *Physical Review B*, 80(24):1–4. doi:10.1103/PhysRevB.80.241204.

[61] Gali, A. (2009b). Theory of the neutral nitrogen-vacancy center in diamond and its application to the realization of a qubit. *Physical Review B*, 79(23):235210. doi:10.1103/PhysRevB.79.235210.

[62] Geiselmann, M., Marty, R., García de Abajo, F. J., and Quidant, R. (2013). Fast optical modulation of the fluorescence from a single nitrogen–vacancy centre. *Nature Physics*. doi:10.1038/nphys2770.

[63] Geva, E., Kosloff, R., and Skinner, J. L. (1995). On the relaxation of a two-level system driven by a strong electromagnetic field. *The Journal of Chemical Physics*, 102(21):8541–8561. doi:10.1063/1.468844.

[64] Gommert, E., Cerva, H., Wecker, J., and Samwer, K. (1999). Influence of misfit stress on the magnetoresistive properties of $La_{0.7}Ca_{0.3}MnO_3$-δ thin films. *Journal of Applied Physics*, 85(8):5417–5419. doi:10.1063/1.369961.

[65] Goodenough, J. B. (1955). Theory of the role of covalence in the perovskite-type manganites [La, M(II)]MnO_3. *Physical Review*, 100(2):564–573. doi:10.1103/PhysRev.100.564.

[66] Grotz, B., Hauf, M. V., Dankerl, M., Naydenov, B., Pezzagna, S., Meijer, J., Jelezko, F., Wrachtrup, J., Stutzmann, M., Reinhard, F., and Garrido, J. A. (2012). Charge state manipulation of qubits in diamond. *Nature Communications*, 3:729. doi:10.1038/ncomms1729.

[67] Gruber, A., Dräbenstedt, A., Tietz, C., Fleury, L., Wrachtrup, J., and von Borczyskowski, C. (1997). Scanning confocal optical microscopy and magnetic resonance on single defect centers. *Science*, 276(5321):2012–2014. doi:10.1126/science.276.5321.2012.

[68] Gruen, D. M., Shenderova, O. A., and Vul', A. Y., editors (2005). *Synthesis, properties and applications of ultrananocrystalline diamond*, volume 192 of *Proceedings of the NATO Advanced Research Workshop on Synthesis, Properties and Applications of Ultrananocrystalline Diamond St. Petersburg*. Springer-Verlag, Berlin/Heidelberg. ISBN:978-1-4020-3320-9.

[69] Häberle, T., Schmid-Lorch, D., Reinhard, F., and Wrachtrup, J. (2015). Nanoscale nuclear magnetic imaging with chemical contrast. *Nature Nanotechnology*, 10(2):125–128. doi:10.1038/nnano.2014.299.

[70] Haghiri-Gosnet, A.-M. and Renard, J.-P. (2003). CMR manganites: Physics, thin films and devices. *Journal of Physics D*, 36(8):R127–R150. doi:10.1088/0022-3727/36/8/201.

[71] Haghiri-Gosnet, A. M., Wolfman, J., Mercey, B., Simon, C., Lecoeur, P., Korzenski, M., Hervieu, M., Desfeux, R., and Baldinozzi, G. (2000). Microstructure and magnetic properties of strained $La_{0.7}Sr_{0.3}MnO_3$ thin films. *Journal of Applied Physics*, 88(7):4257. doi:10.1063/1.1309040.

[72] Hanson, R., Dobrovitski, V. V., Feiguin, A. E., Gywat, O., and Awschalom, D. D. (2008). Coherent dynamics of a single spin interacting with an adjustable spin bath. *Science*, 320(5874):352–355. doi:10.1126/science.1155400.

[73] Hensen, B., Bernien, H., Dréau, A. E., Reiserer, A., Kalb, N., Blok, M. S., Ruitenberg, J., Vermeulen, R. F. L., Schouten, R. N., Abellán, C., Amaya, W., Pruneri, V., Mitchell, M. W., Markham, M., Twitchen, D. J., Elkouss, D., Wehner, S., Taminiau, T. H., and Hanson, R. (2015). Loophole-free Bell inequality violation using electron spins separated by 1.3 kilometres. *Nature*, 526(7575):682–686. doi:10.1038/nature15759.

[74] Hoang, T. M., Ahn, J., Bang, J., and Li, T. (2016a). Electron spin control of optically levitated nanodiamonds in vacuum. *Nature Communications*, 7:12250. doi:10.1038/ncomms12250.

[75] Hoang, T. M., Ma, Y., Ahn, J., Bang, J., Robicheaux, F., Yin, Z.-Q., and Li, T. (2016b). Torsional optomechanics of a levitated nonspherical nanoparticle. *Physical Review Letters*, 117(12):123604. doi:10.1103/PhysRevLett.117.123604.

[76] Hofheinz, M., Wang, H., Ansmann, M., Bialczak, R. C., Lucero, E., Neeley, M., O'Connell, A. D., Sank, D., Wenner, J., Martinis, J. M., and Cleland, A. N. (2009). Synthesizing arbitrary quantum states in a superconducting resonator. *Nature*, 459(7246):546–549. doi:10.1038/nature08005.

[77] Hong, S., Grinolds, M. S., Pham, L. M., Le Sage, D., Luan, L., Walsworth, R. L., and Yacoby, A. (2013). Nanoscale magnetometry with NV centers in diamond. *Materials Research Society Bulletin*, 38(02):155–161. doi:10.1557/mrs.2013.23.

[78] Hopper, D. A., Grote, R. R., Exarhos, A. L., and Bassett, L. C. (2016). Near-infrared-assisted charge control and spin readout of the nitrogen-vacancy center in diamond. *Physical Review B*, 94(24):241201. doi:10.1103/PhysRevB.94.241201.

[79] Hotta, T. and Dagotto, E. (2000). Competition between ferromagnetic and charge-orbital ordered phases in $Pr_{1-x}Ca_xMnO_3$ for $x = 1/4$, $3/8$, and $1/2$. *Physical Review B*, 61(18):R11879–R11882. doi:10.1103/PhysRevB.61.R11879.

[80] Hsu, J.-F., Ji, P., Lewandowski, C. W., and D'Urso, B. (2016). Cooling the motion of diamond nanocrystals in a magneto-gravitational trap in high vacuum. *Scientific Reports*, 6(1):30125. doi:10.1038/srep30125.

[81] Hwang, H. Y., Palstra, T. T. M., Cheong, S.-W., and Batlogg, B. (1995). Pressure effects on the magnetoresistance in doped manganese perovskites. *Physical Review B*, 52(21):15046–15049. doi:10.1103/PhysRevB.52.15046.

[82] Inam, F. A., Gaebel, T., Bradac, C., Stewart, L., Withford, M. J., Dawes, J. M., Rabeau, J. R., and Steel, M. J. (2011). Modification of spontaneous emission from nanodiamond colour centres on a structured surface. *New Journal of Physics*, 13(7):073012. doi:10.1088/1367-2630/13/7/073012.

[83] Ithier, G., Collin, E., Joyez, P., Meeson, P. J., Vion, D., Esteve, D., Chiarello, F., Shnirman, A., Makhlin, Y., Schriefl, J., and Schön, G. (2005). Decoherence in a superconducting quantum bit circuit. *Physical Review B*, 72(13):134519. doi:10.1103/PhysRevB.72.134519.

[84] Ivády, V., Szász, K., Falk, A. L., Klimov, P. V., Christle, D. J., Janzén, E., Abrikosov, I. A., Awschalom, D. D., and Gali, A. (2015). Theoretical model of dynamic spin polarization of nuclei coupled to paramagnetic point defects in diamond and silicon carbide. *Physical Review B*, 92(11):115206. doi:10.1103/PhysRevB.92.115206.

[85] Iwasaki, T., Ishibashi, F., Miyamoto, Y., Doi, Y., Kobayashi, S., Miyazaki, T., Tahara, K., Jahnke, K. D., Rogers, L. J., Naydenov, B., Jelezko, F., Yamasaki, S., Nagamachi, S., Inubushi, T., Mizuochi, N., and Hatano, M. (2015). Germanium-vacancy single color centers in diamond. *Scientific Reports*, 5(1):12882. doi:10.1038/srep12882.

[86] Jacques, V., Neumann, P., Beck, J., Markham, M., Twitchen, D., Meijer, J., Kaiser, F., Balasubramanian, G., Jelezko, F., and Wrachtrup, J. (2009). Dynamic polarization of single nuclear spins by optical pumping of nitrogen-vacancy color centers in diamond at room temperature. *Physical Review Letters*, 102(5):057403. doi:10.1103/PhysRevLett.102.057403.

[87] Jaklevic, R. C., Lambe, J., Silver, A. H., and Mercereau, J. E. (1964). Quantum interference effects in Josephson tunneling. *Physical Review Letters*, 12(7):159–160. doi:10.1103/PhysRevLett.12.159.

[88] Janotti, A. and Van de Walle, C. G. (2008). Sources of unintentional conductivity in InN. *Applied Physics Letters*, 92(3):032104. doi:10.1063/1.2832369.

[89] Jarausch, D.-D. H. (2016). *Studies of magnetism in thin films with spins in diamond nanocrystals*. PhD thesis, University of Cambridge.

[90] Jelezko, F., Gaebel, T., Popa, I., Gruber, A., and Wrachtrup, J. (2004). Observation of coherent oscillations in a single electron spin. *Physical Review Letters*, 92(7):076401. doi:10.1103/PhysRevLett.92.076401.

[91] Jiang, L., Hodges, J. S., Maze, J. R., Maurer, P., Taylor, J. M., Cory, D. G., Hemmer, P. R., Walsworth, R. L., Yacoby, A., Zibrov, A. S., and Lukin, M. D. (2009). Repetitive readout of a single electronic spin via quantum logic with nuclear spin ancillae. *Science*, 326(5950):267–72. doi:10.1126/science.1176496.

[92] Josephson, B. (1962). Possible new effects in superconductive tunnelling. *Physics Letters*, 1(7):251–253. doi:10.1016/0031-9163(62)91369-0.

[93] Kanki, T., Tanaka, H., and Kawai, T. (2001). Anomalous strain effect in $La_{0.8}Ba_{0.2}MnO_3$ epitaxial thin film: Role of the orbital degree of freedom in stabilizing ferromagnetism. *Physical Review B*, 64(22):224418. doi:10.1103/PhysRevB.64.224418.

[94] Karaveli, S., Gaathon, O., Wolcott, A., Sakakibara, R., Shemesh, O. A., Peterka, D. S., Boyden, E. S., Owen, J. S., Yuste, R., and Englund, D. (2016). Modulation of nitrogen vacancy charge state and fluorescence in nanodiamonds using electrochemical potential. *Proceedings of the National Academy of Sciences*, 113(15):3938–3943. doi:10.1073/pnas.1504451113.

[95] Kennedy, T. A., Colton, J. S., Butler, J. E., Linares, R. C., and Doering, P. J. (2003). Long coherence times at 300 K for nitrogen-vacancy center spins in diamond grown by chemical vapor deposition. *Applied Physics Letters*, 83(20):4190–4192. doi:10.1063/1.1626791.

[96] Kim, M., Mamin, H. J., Sherwood, M. H., Ohno, K., Awschalom, D. D., and Rugar, D. (2015). Decoherence of near-surface nitrogen-vacancy centers due to electric field noise. *Physical Review Letters*, 115(8):087602. doi:10.1103/PhysRevLett.115.087602.

[97] King, J. P., Coles, P. J., and Reimer, J. A. (2010). Optical polarization of ^{13}C nuclei in diamond through nitrogen vacancy centers. *Physical Review B*, 81:1–4. doi:10.1103/PhysRevB.81.073201.

[98] King, J. P., Jeong, K., Vassiliou, C. C., Shin, C. S., Page, R. H., Avalos, C. E., Wang, H.-J., and Pines, A. (2015). Room-temperature in situ nuclear spin hyperpolarization from optically-pumped nitrogen vacancy centers in diamond. *ArXiv*, page 8. arXiv:1501.2897.

[99] Kittel, C. (1946). Theory of the structure of ferromagnetic domains in films and small particles. *Physical Review*, 70(11-12):965–971. doi:10.1103/PhysRev.70.965.

[100] Klauder, J. R. and Anderson, P. W. (1962). Spectral diffusion decay in spin resonance experiments. *Physical Review*, 125(3):912–932. doi:10.1103/PhysRev.125.912.

[101] Knowles, H. S., Kara, D. M., and Atatüre, M. (2013). Observing bulk diamond spin coherence in high-purity nanodiamonds. *Nature Materials*, 13(1):21–25. doi:10.1038/nmat3805.

[102] Knowles, H. S., Kara, D. M., and Atatüre, M. (2016). Demonstration of a coherent electronic spin cluster in diamond. *Physical Review Letters*, 117(10):100802. doi:10.1103/PhysRevLett.117.100802.

[103] Koehl, W. F., Buckley, B. B., Heremans, F. J., Calusine, G., and Awschalom, D. D. (2011). Room temperature coherent control of defect spin qubits in silicon carbide. *Nature*, 479(7371):84–87. doi:10.1038/nature10562.

[104] Kost, M., Cai, J., and Plenio, M. B. (2015). Resolving single molecule structures with Nitrogen-vacancy centers in diamond. *Scientific Reports*, 5:11007. doi:10.1038/srep11007.

[105] Kowarsky, M. A., Hollenberg, L. C. L., and Martin, A. M. (2014). Non-Abelian geometric phase in the diamond nitrogen-vacancy center. *Physical Review A*, 90(4):042116. doi:10.1103/PhysRevA.90.042116.

[106] Kraus, H., Soltamov, V. A., Riedel, D., Väth, S., Fuchs, F., Sperlich, A., Baranov, P. G., Dyakonov, V., and Astakhov, G. V. (2013). Room-temperature quantum microwave emitters based on spin defects in silicon carbide. *Nature Physics*, 10(2):157–162. doi:10.1038/nphys2826.

[107] Kucsko, G., Maurer, P. C., Yao, N. Y., Kubo, M., Noh, H. J., Lo, P. K., Park, H., and Lukin, M. D. (2013). Nanometre-scale thermometry in a living cell. *Nature*, 500(7460):54–8. doi:10.1038/nature12373.

[108] Kwon, C., Robson, M., Kim, K.-C., Gu, J., Lofland, S., Bhagat, S., Trajanovic, Z., Rajeswari, M., Venkatesan, T., Kratz, A., Gomez, R., and Ramesh, R. (1997). Stress-induced effects in epitaxial $(La_{0.7}Sr_{0.3})MnO_3$ films. *Journal of Magnetism and Magnetic Materials*, 172(3):229–236. doi:10.1016/S0304-8853(97)00058-9.

[109] Laraoui, A., Dolde, F., Burk, C., Reinhard, F., Wrachtrup, J., and Meriles, C. A. (2013). High-resolution correlation spectroscopy of ^{13}C spins near a nitrogen-vacancy centre in diamond. *Nature Communications*, 4:1651. doi:10.1038/ncomms2685.

[110] Laraoui, A., Hodges, J. S., and Meriles, C. A. (2012). Nitrogen-vacancy-assisted magnetometry of paramagnetic centers in an individual diamond nanocrystal. *Nano Letters*, 12(7):3477–3482. doi:10.1021/nl300964g.

[111] Laraoui, A., Hodges, J. S., Ryan, C. A., and Meriles, C. A. (2011). Diamond nitrogen-vacancy center as a probe of random fluctuations in a nuclear spin ensemble. *Physical Review B*, 84(10):104301. doi:10.1103/PhysRevB.84.104301.

[112] Lawson, S. C., Fisher, D., Hunt, D. C., and Newton, M. E. (1998). On the existence of positively charged single-substitutional nitrogen in diamond. *Journal of Physics: Condensed Matter*, 10(27):6171–6180. doi:10.1088/0953-8984/10/27/016.

[113] Lazariev, A. and Balasubramanian, G. (2015). A nitrogen-vacancy spin based molecular structure microscope using multiplexed projection reconstruction. *Scientific Reports*, 5(1):14130. doi:10.1038/srep14130.

[114] Ledbetter, M. P., Jensen, K., Fischer, R., Jarmola, A., and Budker, D. (2012). Gyroscopes based on nitrogen-vacancy centers in diamond. *Physical Review A*, 86(5):052116. doi:10.1103/PhysRevA.86.052116.

[115] Lenef, A. and Rand, S. C. (1996). Electronic structure of the N-V center in diamond: Theory. *Physical Review B*, 53(20):13441–13455. doi:10.1103/PhysRevB.53.13441.

[116] Lesik, M., Plays, T., Tallaire, A., Achard, J., Brinza, O., William, L., Chipaux, M., Toraille, L., Debuisschert, T., Gicquel, A., Roch, J., and Jacques, V. (2015). Preferential orientation of NV defects in CVD diamond films grown on (113)-oriented substrates. *Diamond and Related Materials*, 56:47–53. doi:10.1016/j.diamond.2015.05.003.

[117] Liu, G.-Q., Jiang, Q.-Q., Chang, Y.-C., Liu, D.-Q., Li, W.-X., Gu, C.-Z., Po, H. C., Zhang, W.-X., Zhao, N., and Pan, X.-Y. (2014). Protection of centre spin coherence by dynamic nuclear spin polarization in diamond. *Nanoscale*, 6(17):10134. doi:10.1039/C4NR02007C.

[118] Loretz, M., Boss, J. M., Rosskopf, T., Mamin, H. J., Rugar, D., and Degen, C. L. (2015). Spurious harmonic response of multipulse quantum sensing sequences. *Physical Review X*, 5(2):021009. doi:10.1103/PhysRevX.5.021009.

[119] Loubser, J. H. N. and Van Wyk, J. A. (1977). Optical spin-polarisation in a triplet state in irradiated and annealed type 1b diamonds. *Diamond Research*, 9(05):11–14.

[120] Loubser, J. H. N. and van Wyk, J. A. (1978). Electron spin resonance in the study of diamond. *Reports on Progress in Physics*, 41(8):1201–1248. doi:10.1088/0034-4885/41/8/002.

[121] Lovchinsky, I., Sushkov, A. O., Urbach, E., de Leon, N. P., Choi, S., De Greve, K., Evans, R., Gertner, R., Bersin, E., Muller, C., McGuinness, L., Jelezko, F., Walsworth, R. L., Park, H., and Lukin, M. D. (2016). Nuclear magnetic resonance detection and spectroscopy of single proteins using quantum logic. *Science*, 351(6275):836–841. doi:10.1126/science.aad8022.

[122] Maletinsky, P., Hong, S., Grinolds, M. S., Hausmann, B., Lukin, M. D., Walsworth, R. L., Loncar, M., and Yacoby, A. (2012). A robust scanning diamond sensor for nanoscale imaging with single nitrogen-vacancy centres. *Nature Nanotechnology*, 7(5):320–4. doi:10.1038/nnano.2012.50.

[123] Manson, N., Harrison, J., and Sellars, M. (2006). Nitrogen-vacancy center in diamond: Model of the electronic structure and associated dynamics. *Physical Review B*, 74(10):104303. doi:10.1103/PhysRevB.74.104303.

[124] Marín, L., Rodríguez, L. A., Magén, C., Snoeck, E., Arras, R., Lucas, I., Morellón, L., Algarabel, P. A., De Teresa, J. M., and Ibarra, M. R. (2015). Observation of the strain induced magnetic phase segregation in manganite thin films. *Nano Letters*, 15(1):492–497. doi:10.1021/nl503834b.

[125] Matsuzaki, Y., Shimooka, T., Tanaka, H., Tokura, Y., Semba, K., and Mizuochi, N. (2016). Hybrid quantum magnetic field sensor with an electron spin and a nuclear spin in diamond. *ArXiv*, pages 1–5. arXiv:1608.06717.

[126] Matsuzaki, Y., Zhu, X., Kakuyanagi, K., Toida, H., Shimooka, T., Mizuochi, N., Nemoto, K., Semba, K., Munro, W. J., Yamaguchi, H., and Saito, S. (2015). Improving the lifetime of the nitrogen-vacancy-center ensemble coupled with a superconducting flux qubit by applying magnetic fields. *Physical Review A*, 91(4):042329. doi:10.1103/PhysRevA.91.042329.

[127] Maurer, P. C., Kucsko, G., Latta, C., Jiang, L., Yao, N. Y., Bennett, S. D., Pastawski, F., Hunger, D., Chisholm, N., Markham, M., Twitchen, D. J., Cirac, J. I., and Lukin, M. D. (2012). Room-temperature quantum bit memory exceeding one second. *Science*, 336(6086):1283–6. doi:10.1126/science.1220513.

[128] Maze, J. R., Gali, A., Togan, E., Chu, Y., Trifonov, A., Kaxiras, E., and Lukin, M. D. (2011). Properties of nitrogen-vacancy centers in diamond: The group theoretic approach. *New Journal of Physics*, 13(2):025025. doi:10.1088/1367-2630/13/2/025025.

[129] Maze, J. R., Stanwix, P. L., Hodges, J. S., Hong, S., Taylor, J. M., Cappellaro, P., Jiang, L., Dutt, M. V. G., Togan, E., Zibrov, A. S., Yacoby, A., Walsworth, R. L., and Lukin, M. D. (2008). Nanoscale magnetic sensing with an individual electronic spin in diamond. *Nature*, 455(7213):644–7. doi:10.1038/nature07279.

[130] McElfresh, M. (1994). *Fundamentals of magnetism and magnetic measurements featuring quantum design's magnetic property measurement system*. Perdue University.

[131] McLellan, C. A., Myers, B. A., Kraemer, S., Ohno, K., Awschalom, D. D., and Bleszynski Jayich, A. C. (2016). Patterned formation of highly coherent nitrogen-vacancy centers using a focused electron irradiation technique. *Nano Letters*, 16(4):2450–2454. doi:10.1021/acs.nanolett.5b05304.

[132] Michl, J., Teraji, T., Zaiser, S., Jakobi, I., Waldherr, G., Dolde, F., Neumann, P., Doherty, M. W., Manson, N. B., Isoya, J., and Wrachtrup, J. (2014). Perfect alignment and preferential orientation of nitrogen-vacancy centers during chemical vapor deposition diamond growth on (111) surfaces. *Applied Physics Letters*, 104(10):102407. doi:10.1063/1.4868128.

[133] Millis, A. J., Darling, T., and Migliori, A. (1998). Quantifying strain dependence in "colossal" magnetoresistance manganites. *Journal of Applied Physics*, 83(3):1588–1591. doi:10.1063/1.367310.

[134] Mita, Y. (1996). Change of absorption spectra in type-Ib diamond with heavy neutron irradiation. *Physical Review B*, 53(17):11360–11364. doi:10.1103/PhysRevB.53.11360.

[135] Mochalin, V. N., Shenderova, O., Ho, D., and Gogotsi, Y. (2011). The properties and applications of nanodiamonds. *Nature Nanotechnology*, 7(1):11–23. doi:10.1038/nnano.2011.209.

[136] Müller, C., Kong, X., Cai, J.-M., Melentijević, K., Stacey, A., Markham, M., Twitchen, D., Isoya, J., Pezzagna, S., Meijer, J., Du, J. F., Plenio, M. B., Naydenov, B., McGuinness, L. P., and Jelezko, F. (2014). Nuclear magnetic resonance spectroscopy with single spin sensitivity. *Nature Communications*, 5:4703. doi:10.1038/ncomms5703.

[137] Myers, B. A., Das, A., Dartiailh, M. C., Ohno, K., Awschalom, D. D., and Bleszynski Jayich, A. C. (2014). Probing surface noise with depth-calibrated spins in diamond. *Physical Review Letters*, 113(2):027602. doi:10.1103/PhysRevLett.113.027602.

[138] Nath, T. K., Rao, R. A., Lavric, D., Eom, C. B., Wu, L., and Tsui, F. (1999). Effect of three-dimensional strain states on magnetic anisotropy of $La_{0.8}Ca_{0.2}MnO_3$ epitaxial thin films. *Applied Physics Letters*, 74(11):1615–1617. doi:10.1063/1.123634.

[139] Naydenov, B., Dolde, F., Hall, L. T., Shin, C., Fedder, H., Hollenberg, L. C. L., Jelezko, F., and Wrachtrup, J. (2011). Dynamical decoupling of a single-electron spin at room temperature. *Physical Review B*, 83(8):081201. doi:10.1103/PhysRevB.83.081201.

[140] Neu, E., Steinmetz, D., Riedrich-Möller, J., Gsell, S., Fischer, M., Schreck, M., and Becher, C. (2011). Single photon emission from silicon-vacancy colour centres in chemical vapour deposition nano-diamonds on iridium. *New Journal of Physics*, 13(2):025012. doi:10.1088/1367-2630/13/2/025012.

[141] Neumann, P., Beck, J., Steiner, M., Rempp, F., Fedder, H., Hemmer, P. R., Wrachtrup, J., and Jelezko, F. (2010). Single-shot readout of a single nuclear spin. *Science*, 329(5991):542–544. doi:10.1126/science.1189075.

[142] Neumann, P., Jakobi, I., Dolde, F., Burk, C., Reuter, R., Waldherr, G., Honert, J., Wolf, T., Brunner, A., and Shim, J. H. (2013). High-precision nanoscale temperature sensing using single defects in diamond. *Nano Letters*, 13(6):2738–42. doi:10.1021/nl401216y.

[143] Neumann, P., Kolesov, R., Jacques, V., Beck, J., Tisler, J., Batalov, a., Rogers, L., Manson, N. B., Balasubramanian, G., Jelezko, F., and Wrachtrup, J. (2009). Excited-state spectroscopy of single NV defects in diamond using optically detected magnetic resonance. *New Journal of Physics*, 11(1):013017. doi:10.1088/1367-2630/11/1/013017.

[144] Neumann, P., Mizuochi, N., Rempp, F., Hemmer, P., Watanabe, H., Yamasaki, S., Jacques, V., Gaebel, T., Jelezko, F., and Wrachtrup, J. (2008). Multipartite entanglement among single spins in diamond. *Science*, 320(5881):1326–9. doi:10.1126/science.1157233.

[145] Ohashi, K., Rosskopf, T., Watanabe, H., Loretz, M., Tao, Y., Hauert, R., Tomizawa, S., Ishikawa, T., Ishi-Hayase, J., Shikata, S., Degen, C. L., and Itoh, K. M. (2013). Negatively charged nitrogen-vacancy centers in a 5∼nm thin ^{12}C diamond film. *Nano Letters*, 13(10):4733–4738. doi:10.1021/nl402286v.

[146] Ohno, K., Joseph Heremans, F., Bassett, L. C., Myers, B. A., Toyli, D. M., Bleszynski Jayich, A. C., Palmstrøm, C. J., and Awschalom, D. D. (2012). Engineering shallow spins in diamond with nitrogen delta-doping. *Applied Physics Letters*, 101(8):082413. doi:10.1063/1.4748280.

[147] Ohno, K., Joseph Heremans, F., de las Casas, C. F., Myers, B. A., Alemán, B. J., Bleszynski Jayich, A. C., and Awschalom, D. D. (2014). Three-dimensional localization of spins in diamond using ^{12}C implantation. *Applied Physics Letters*, 105(5):052406. doi:10.1063/1.4890613.

[148] Osswald, S., Havel, M., Mochalin, V., Yushin, G., and Gogotsi, Y. (2008). Increase of nanodiamond crystal size by selective oxidation. *Diamond and Related Materials*, 17(7-10):1122–1126. doi:10.1016/j.diamond.2008.01.102.

[149] Osterkamp, C., Lang, J., Scharpf, J., Müller, C., McGuinness, L. P., Diemant, T., Behm, R. J., Naydenov, B., and Jelezko, F. (2015). Stabilizing shallow color centers in diamond created by nitrogen delta-doping using SF_6 plasma treatment. *Applied Physics Letters*, 106(11):113109. doi:10.1063/1.4915305.

[150] Patel, R. N., Schröder, T., Wan, N., Li, L., Mouradian, S. L., Chen, E. H., and Englund, D. R. (2016). Efficient photon coupling from a diamond nitrogen vacancy center by integration with silica fiber. *Light: Science & Applications*, 5:e16032. doi:10.1038/lsa.2016.32.

[151] Petrov, I., Shenderova, O., Grishko, V., Grichko, V., Tyler, T., Cunningham, G., and McGuire, G. (2007). Detonation nanodiamonds simultaneously purified and modified by gas treatment. *Diamond and Related Materials*, 16(12):2098–2103. doi:10.1016/j.diamond.2007.05.013.

[152] Pfaff, W., Taminiau, T. H., Robledo, L., Bernien, H., Markham, M., Twitchen, D. J., and Hanson, R. (2012). Demonstration of entanglement-by-measurement of solid-state qubits. *Nature Physics*, 9(1):29–33. doi:10.1038/nphys2444.

[153] Pfender, M., Aslam, N., Sumiya, H., Onoda, S., Neumann, P., Isoya, J., Meriles, C., and Wrachtrup, J. (2016). Nonvolatile quantum memory enables sensor unlimited nanoscale spectroscopy of finite quantum systems. *ArXiv*. arXiv:1610.05675.

[154] Pham, L. M., DeVience, S. J., Casola, F., Lovchinsky, I., Sushkov, A. O., Bersin, E., Lee, J., Urbach, E., Cappellaro, P., Park, H., Yacoby, A., Lukin, M., and Walsworth, R. L. (2016). NMR technique for determining the depth of shallow nitrogen-vacancy centers in diamond. *Physical Review B*, 93(4):045425. doi:10.1103/PhysRevB.93.045425.

[155] Pingault, B., Becker, J. N., Schulte, C. H. H., Arend, C., Hepp, C., Godde, T., Tartakovskii, A. I., Markham, M., Becher, C., and Atatüre, M. (2014). All-Optical formation of coherent dark states of silicon-vacancy spins in diamond. *Physical Review Letters*, 113(26):263601. doi:10.1103/PhysRevLett.113.263601.

[156] Pingault, B., Jarausch, D.-D., Hepp, C., Klintberg, L., Becker, J. N., Markham, M., Becher, C., and Atatüre, M. (2017). Coherent control of the silicon-vacancy spin in diamond. *ArXiv*. arXiv:1701.06848.

[157] Plakhotnik, T. and Gruber, D. (2010). Luminescence of nitrogen-vacancy centers in nanodiamonds at temperatures between 300 and 700 K: perspectives on nanothermometry. *Physical Chemistry Chemical Physics*, 12(33):9751–6. doi:10.1039/c001132k.

[158] Poggiali, F., Cappellaro, P., and Fabbri, N. (2016). Measurement of the excited-state transverse hyperfine coupling in NV centers via dynamic nuclear polarization. *ArXiv*. arXiv:1612.04783.

[159] Prellier, W., Simon, C., Haghiri-Gosnet, A. M., Mercey, B., and Raveau, B. (2000). Thickness dependence of the stability of the charge-ordered state in $Pr_{0.5}Ca_{0.5}MnO_3$ thin films. *Physical Review B*, 62(24):R16337–R16340. doi:10.1103/PhysRevB.62.R16337.

[160] Redman, D., Brown, S., Sands, R., and Rand, S. (1991). Spin dynamics and electronic states of N-V centers in diamond by EPR and four-wave-mixing spectroscopy. *Physical Review Letters*, 67(24):3420–3423. doi:10.1103/PhysRevLett.67.3420.

[161] Rej, E., Gaebel, T., Boele, T., Waddington, D. E., and Reilly, D. J. (2015). Hyperpolarized nanodiamond with long spin-relaxation times. *Nature Communications*, 6:8459. doi:10.1038/ncomms9459.

[162] Reserbat-Plantey, A., Schädler, K. G., Gaudreau, L., Navickaite, G., Güttinger, J., Chang, D., Toninelli, C., Bachtold, A., and Koppens, F. H. L. (2016). Electromechanical control of nitrogen-vacancy defect emission using graphene NEMS. *Nature Communications*, 7:10218. doi:10.1038/ncomms10218.

[163] Rios, J. M. (2010). *Quantum manipulation of nitrogen-vacancy centers in diamond: From basic properties to applications*. PhD thesis, Harvard University.

[164] Robledo, L., Bernien, H., Sar, T. V. D., and Hanson, R. (2011a). Spin dynamics in the optical cycle of single nitrogen-vacancy centres in diamond. *New Journal of Physics*, 13(2):025013. doi:10.1088/1367-2630/13/2/025013.

[165] Robledo, L., Bernien, H., van Weperen, I., and Hanson, R. (2010). Control and coherence of the optical transition of single nitrogen vacancy centers in diamond. *Physical Review Letters*, 105(17):177403. doi:10.1103/PhysRevLett.105.177403.

[166] Robledo, L., Childress, L., Bernien, H., Hensen, B., Alkemade, P. F. A., and Hanson, R. (2011b). High-fidelity projective read-out of a solid-state spin quantum register. *Nature*, 477(7366):574–8. doi:10.1038/nature10401.

[167] Rogers, L. J., McMurtrie, R. L., Sellars, M. J., and Manson, N. B. (2009). Time-averaging within the excited state of the nitrogen-vacancy centre in diamond. *New Journal of Physics*, 11(6):063007. doi:10.1088/1367-2630/11/6/063007.

[168] Romach, Y., Müller, C., Unden, T., Rogers, L. J., Isoda, T., Itoh, K. M., Markham, M., Stacey, A., Meijer, J., Pezzagna, S., Naydenov, B., McGuinness, L. P., Bar-Gill, N., and Jelezko, F. (2015). Spectroscopy of surface-induced noise using shallow spins in diamond. *Physical Review Letters*, 114(1):017601. doi:10.1103/PhysRevLett.114.017601.

[169] Rondin, L., Dantelle, G., Slablab, A., Grosshans, F., Treussart, F., Bergonzo, P., Perruchas, S., Gacoin, T., Chaigneau, M., Chang, H.-C., Jacques, V., and Roch, J.-F. (2010). Surface-induced charge state conversion of nitrogen-vacancy defects in nanodiamonds. *Physical Review B*, 82(11):115449. doi:10.1103/PhysRevB.82.115449.

[170] Rosskopf, T., Dussaux, A., Ohashi, K., Loretz, M., Schirhagl, R., Watanabe, H., Shikata, S., Itoh, K. M., and Degen, C. L. (2014). Investigation of surface magnetic noise by shallow spins in diamond. *Physical Review Letters*, 112(14):147602. doi:10.1103/PhysRevLett.112.147602.

[171] Rosskopf, T., Zopes, J., Boss, J. M., and Degen, C. L. (2016). A quantum spectrum analyzer enhanced by a nuclear spin memory. *ArXiv*. arXiv:1610.03253.

[172] Rugar, D., Budakian, R., Mamin, H. J., and Chui, B. W. (2004). Single spin detection by magnetic resonance force microscopy. *Nature*, 430(6997):329–332. doi:10.1038/nature02658.

[173] Saito, S., Zhu, X., Amsüss, R., Matsuzaki, Y., Kakuyanagi, K., Shimo-Oka, T., Mizuochi, N., Nemoto, K., Munro, W. J., and Semba, K. (2013). Towards realizing a quantum memory for a superconducting qubit: Storage and retrieval of quantum states. *Physical Review Letters*, 111(10):107008. doi:10.1103/PhysRevLett.111.107008.

[174] Sank, D., Chen, Z., Khezri, M., Kelly, J., Barends, R., Campbell, B., Chen, Y., Chiaro, B., Dunsworth, A., Fowler, A., Jeffrey, E., Lucero, E., Megrant, A., Mutus, J., Neeley, M., Neill, C., O'Malley, P. J. J., Quintana, C., Roushan, P., Vainsencher, A., White, T., Wenner, J., Korotkov, A. N., and Martinis, J. M. (2016). Measurement-induced state transitions in a superconducting qubit: Beyond the rotating wave approximation. *Physical Review Letters*, 117(19):190503. doi:10.1103/PhysRevLett.117.190503.

[175] Scarabelli, D., Trusheim, M., Gaathon, O., Englund, D., and Wind, S. J. (2016). Nanoscale engineering of closely-spaced electronic spins in diamond. *Nano Letters*, 16(8):4982–4990. doi:10.1021/acs.nanolett.6b01692.

[176] Shields, B. J., Unterreithmeier, Q. P., de Leon, N. P., Park, H., and Lukin, M. D. (2015). Efficient readout of a single spin state in diamond via spin-to-charge conversion. *Physical Review Letters*, 114(13):136402. doi:10.1103/PhysRevLett.114.136402.

[177] Sipahigil, A., Jahnke, K. D., Rogers, L. J., Teraji, T., Isoya, J., Zibrov, A. S., Jelezko, F., and Lukin, M. D. (2014). Indistinguishable photons from separated silicon-vacancy centers in diamond. *Physical Review Letters*, 113(11):113602. doi:10.1103/PhysRevLett.113.113602.

[178] Siyushev, P., Pinto, H., Vörös, M., Gali, A., Jelezko, F., and Wrachtrup, J. (2013). Optically controlled switching of the charge state of a single nitrogen-vacancy center in diamond at cryogenic temperatures. *Physical Review Letters*, 110(16):167402. doi:10.1103/PhysRevLett.110.167402.

[179] Slack, G. (1973). Nonmetallic crystals with high thermal conductivity. *Journal of Physics and Chemistry of Solids*, 34(2):321–335. doi:10.1016/0022-3697(73)90092-9.

[180] Smeltzer, B., McIntyre, J., and Childress, L. (2009). Robust control of individual nuclear spins in diamond. *Physical Review A*, 80(5):1–4. doi:10.1103/PhysRevA.80.050302.

[181] Song, W.-l., Yin, Z.-q., Yang, W.-l., Zhu, X.-b., Zhou, F., and Feng, M. (2015). One-step generation of multipartite entanglement among nitrogen-vacancy center ensembles. *Scientific Reports*, 5:7755. doi:10.1038/srep07755.

[182] Steiner, M., Neumann, P., Beck, J., Jelezko, F., and Wrachtrup, J. (2010). Universal enhancement of the optical readout fidelity of single electron spins at nitrogen-vacancy centers in diamond. *Physical Review B*, 81(3):035205. doi:10.1103/PhysRevB.81.035205.

[183] Stockill, R., Stanley, M. J., Huthmacher, L., Clarke, E., Hugues, M., Miller, A. J., Matthiesen, C., Gall, C. L., and Atatüre, M. (2017). Phase-tuned entangled state generation between distant spin qubits. *ArXiv*. arXiv:1702.03422.

[184] Sushkov, A. O., Lovchinsky, I., Chisholm, N., Walsworth, R. L., Park, H., and Lukin, M. D. (2014). Magnetic resonance detection of individual proton spins using quantum reporters. *Physical Review Letters*, 113(19):197601. doi:10.1103/PhysRevLett.113.197601.

[185] Svedberg, M., Majumdar, S., Huhtinen, H., Paturi, P., and Granroth, S. (2011). Optimization of $Pr_{0.9}Ca_{0.1}MnO_3$ thin films and observation of coexisting spin-glass and ferromagnetic phases at low temperature. *Journal of Physics: Condensed Matter*, 23(38):386005. doi:10.1088/0953-8984/23/38/386005.

[186] Takahashi, S., Hanson, R., van Tol, J., Sherwin, M., and Awschalom, D. (2008). Quenching spin decoherence in diamond through spin bath polarization. *Physical Review Letters*, 101(4):047601. doi:10.1103/PhysRevLett.101.047601.

[187] Tamarat, P., Manson, N. B., Harrison, J. P., McMurtrie, R. L., Nizovtsev, A., Santori, C., Beausoleil, R. G., Neumann, P., Gaebel, T., Jelezko, F., Hemmer, P., and Wrachtrup, J. (2008). Spin-flip and spin-conserving optical transitions of the nitrogen-vacancy centre in diamond. *New Journal of Physics*, 10(4):045004. doi:10.1088/1367-2630/10/4/045004.

[188] Taylor, J. M., Cappellaro, P., Childress, L., Jiang, L., Budker, D., Hemmer, P. R., Yacoby, A., Walsworth, R., and Lukin, M. D. (2008). High-sensitivity diamond magnetometer with nanoscale resolution. *Nature Physics*, 4(10):810–816. doi:10.1038/nphys1075.

[189] Tetienne, J.-P., Hingant, T., Rondin, L., Cavaillès, A., Mayer, L., Dantelle, G., Gacoin, T., Wrachtrup, J., Roch, J.-F., and Jacques, V. (2013). Spin relaxometry of single nitrogen-vacancy defects in diamond nanocrystals for magnetic noise sensing. *Physical Review B*, 87(23):235436. doi:10.1103/PhysRevB.87.235436.

[190] Tikkanen, J., Geilhufe, M., Frontzek, M., Hergert, W., Ernst, A., Paturi, P., and Udby, L. (2016). The low-temperature magnetostructure and magnetic field response of $Pr_{0.9}Ca_{0.1}MnO_3$: The roles of Pr spins and magnetic phase separation. *Journal of Physics: Condensed Matter*, 28(3):036001. doi:10.1088/0953-8984/28/3/036001.

[191] Tinkham (2003). *Group theory and quantum mechanics*. Dover.

[192] Tisler, J., Balasubramanian, G., Naydenov, B., Kolesov, R., Grotz, B., Reuter, R., Boudou, J.-P., Curmi, P. A., Sennour, M., Thorel, A., Börsch, M., Aulenbacher, K., Erdmann, R., Hemmer, P. R., Jelezko, F., and Wrachtrup, J. (2009). Fluorescence and spin properties of defects in single digit nanodiamonds. *ACS Nano*, 3(7):1959–1965. doi:10.1021/nn9003617.

[193] Togan, E., Chu, Y., Trifonov, A. S., Jiang, L., Maze, J., Childress, L., Dutt, M. V. G., Sørensen, A. S., Hemmer, P. R., Zibrov, A. S., and Lukin, M. D. (2010). Quantum entanglement between an optical photon and a solid-state spin qubit. *Nature*, 466(7307):730–4. doi:10.1038/nature09256.

[194] Tokura, Y., Tomioka, Y., Kuwahara, H., Asamitsu, A., Moritomo, Y., and Kasai, M. (1996). Origins of colossal magnetoresistance in perovskite-type manganese oxides. *Journal of Applied Physics*, 79(8):5288. doi:10.1063/1.361353.

[195] Toyli, D. M., Christle, D. J., Alkauskas, A., Buckley, B. B., Van de Walle, C. G., and Awschalom, D. D. (2012). Measurement and control of single nitrogen-vacancy center spins above 600 K. *Physical Review X*, 2(3):031001. doi:10.1103/PhysRevX.2.031001.

[196] Toyli, D. M., de las Casas, C. F., Christle, D. J., Dobrovitski, V. V., and Awschalom, D. D. (2013). Fluorescence thermometry enhanced by the quantum coherence of single spins in diamond. *Proceedings of the National Academy of Sciences*, 110(21):8417–21. doi:10.1073/pnas.1306825110.

[197] Tsui, F., Smoak, M. C., Nath, T. K., and Eom, C. B. (2000). Strain-dependent magnetic phase diagram of epitaxial $La_{0.67}Sr_{0.33}MnO_3$ thin films. *Applied Physics Letters*, 76(17):2421–2423. doi:10.1063/1.126363.

[198] Tzeng, Y.-K., Tsai, P.-C., Liu, H.-Y., Chen, O. Y., Hsu, H., Yee, F.-G., Chang, M.-S., and Chang, H.-C. (2015). Time-resolved luminescence nanothermometry with nitrogen-vacancy centers in nanodiamonds. *Nano Letters*, 15(6):3945–3952. doi:10.1021/acs.nanolett.5b00836.

[199] Van Oort, E. and Glasbeek, M. (1990). Electric-field-induced modulation of spin echoes of N-V centers in diamond. *Chemical Physics Letters*, 168(6):529–532. doi:10.1016/0009-2614(90)85665-Y.

[200] Vasyukov, D., Anahory, Y., Embon, L., Halbertal, D., Cuppens, J., Neeman, L., Finkler, A., Segev, Y., Myasoedov, Y., Rappaport, M. L., Huber, M. E., and Zeldov, E. (2013). A scanning superconducting quantum interference device with single electron spin sensitivity. *Nature Nanotechnology*, 8(9):639–644. doi:10.1038/nnano.2013.169.

[201] Waldherr, G., Beck, J., Neumann, P., Said, R. S., Nitsche, M., Markham, M. L., Twitchen, D. J., Twamley, J., Jelezko, F., and Wrachtrup, J. (2011a). High-dynamic-range magnetometry with a single nuclear spin in diamond. *Nature Nanotechnology*, 7(2):105–108. doi:10.1038/nnano.2011.224.

[202] Waldherr, G., Beck, J., Steiner, M., Neumann, P., Gali, A., Frauenheim, T., Jelezko, F., and Wrachtrup, J. (2011b). Dark states of single nitrogen-vacancy centers in diamond unraveled by single shot NMR. *Physical Review Letters*, 106(15):157601. doi:10.1103/PhysRevLett.106.157601.

[203] Wang, C., Kurtsiefer, C., Weinfurter, H., and Burchard, B. (2006). Single photon emission from SiV centres in diamond produced by ion implantation. *Journal of Physics B*, 39(1):37–41. doi:10.1088/0953-4075/39/1/005.

[204] Wang, P., Liu, B., and Yang, W. (2015). Strongly polarizing weakly coupled ^{13}C nuclear spins with optically pumped nitrogen-vacancy center. *Scientific Reports*, 5:15847. doi:10.1038/srep15847.

[205] Wang, Z.-H., de Lange, G., Ristè, D., Hanson, R., and Dobrovitski, V. V. (2012). Comparison of dynamical decoupling protocols for a nitrogen-vacancy center in diamond. *Physical Review B*, 85(15):155204. doi:10.1103/PhysRevB.85.155204.

[206] Wang, Z.-H. and Takahashi, S. (2013). Spin decoherence and electron spin bath noise of a nitrogen-vacancy center in diamond. *Physical Review B*, 87(11):115122. doi:10.1103/PhysRevB.87.115122.

[207] Wolters, J., Sadzak, N., Schell, A. W., Schröder, T., and Benson, O. (2013). Measurement of the ultrafast spectral diffusion of the optical transition of nitrogen vacancy centers in nano-size diamond using correlation interferometry. *Physical Review Letters*, 110(2):027401. doi:10.1103/PhysRevLett.110.027401.

[208] Woodhams, B. J., Knowles, H. S., Kara, D. M., Atatüre, M., and Bohndiek, S. E. (2017). Nanodiamond preparation and surface characterization for biological applications. In Achilefu, S. and Raghavachari, R., editors, *SPIE 10079, Reporters, Markers, Dyes, Nanoparticles, and Molecular Probes for Biomedical Applications IX*, volume 100790C. doi:10.1117/12.2252892.

[209] Wu, Y., Suzuki, Y., Rüdiger, U., Yu, J., Kent, A. D., Nath, T. K., and Eom, C. B. (1999). Magnetotransport and magnetic domain structure in compressively strained colossal magnetoresistance films. *Applied Physics Letters*, 75(15):2295–2297. doi:10.1063/1.124995.

[210] Yale, C. G., Buckley, B. B., Christle, D. J., Burkard, G., Heremans, F. J., Bassett, L. C., and Awschalom, D. D. (2013). All-optical control of a solid-state spin using coherent dark states. *Proceedings of the National Academy of Sciences*, 110(19):7595–7600. doi:10.1073/pnas.1305920110.

[211] Yamamoto, Y., Imai, T., Tanabe, K., Tsuno, T., Kumazawa, Y., and Fujimori, N. (1997). The measurement of thermal properties of diamond. *Diamond and Related Materials*, 6(8):1057–1061. doi:10.1016/S0925-9635(96)00772-8.

[212] Yuan, Y., Wang, X., Jia, G., Liu, J.-H., Wang, T., Gu, Y., Yang, S.-T., Zhen, S., Wang, H., and Liu, Y. (2010). Pulmonary toxicity and translocation of nanodiamonds in mice. *Diamond and Related Materials*, 19(4):291–299. doi:10.1016/j.diamond.2009.11.022.

[213] Zaiser, S., Rendler, T., Jakobi, I., Wolf, T., Lee, S.-Y., Wagner, S., Bergholm, V., Schulte-Herbrüggen, T., Neumann, P., and Wrachtrup, J. (2016). Enhancing quantum sensing sensitivity by a quantum memory. *Nature Communications*, 7:12279. doi:10.1038/ncomms12279.

[214] Zhu, X., Matsuzaki, Y., Amsüss, R., Kakuyanagi, K., Shimo-Oka, T., Mizuochi, N., Nemoto, K., Semba, K., Munro, W. J., and Saito, S. (2014). Observation of dark states in a superconductor diamond quantum hybrid system. *Nature Communications*, 5:3424. doi:10.1038/ncomms4524.

[215] Zhu, X., Saito, S., Kemp, A., Kakuyanagi, K., Karimoto, S.-i., Nakano, H., Munro, W. J., Tokura, Y., Everitt, M. S., Nemoto, K., Kasu, M., Mizuochi, N., and Semba, K. (2011). Coherent coupling of a superconducting flux qubit to an electron spin ensemble in diamond. *Nature*, 478(7368):221–224. doi:10.1038/nature10462.

[216] Ziese, M., Vrejoiu, I., Pippel, E., Nikulina, E., and Hesse, D. (2011). Magnetic properties of $Pr_{0.7}Ca_{0.3}MnO_3/SrRuO_3$ superlattices. *Applied Physics Letters*, 98(13):132504. doi:10.1063/1.3572027.